



Universitat Autònoma de Barcelona

ADVERTIMENT. L'accés als continguts d'aquesta tesi queda condicionat a l'acceptació de les condicions d'ús establertes per la següent llicència Creative Commons:  http://cat.creativecommons.org/?page_id=184

ADVERTENCIA. El acceso a los contenidos de esta tesis queda condicionado a la aceptación de las condiciones de uso establecidas por la siguiente licencia Creative Commons:  <http://es.creativecommons.org/blog/licencias/>

WARNING. The access to the contents of this doctoral thesis it is limited to the acceptance of the use conditions set by the following Creative Commons license:  <https://creativecommons.org/licenses/?lang=en>



Universitat Autònoma
de Barcelona

Nanobiosensors for diagnostics applications

Alejandro Zamora Gálvez

PhD Thesis

PhD in Chemistry

Directors

ICREA Prof. Arben Merkoçi

Dr. Carmen C. Mayorga Martínez

Dr. Edén Morales Narváez

Chemistry Department

Science Faculty

2017

Memòria presentada per aspirar al Grau de Doctor per Alejandro Zamora Gálvez

Alejandro Zamora Gálvez

Vist i plau



ICREA Prof. Arben Merkoçi Hyka
Nanobioelectronics & Biosensors Group
ICN2 Institut Català de Nanociència i Nanotecnologia

Dr. Carmen C Mayorga Martinez
School of Physical & Mathematical
Sciences, Division of Chemistry &
Biological Chemistry
Nanyang Technological University



Dr Edén Morales Narváez
Biophotonic Nanosensors
Laboratory, Photonics Department
Centro de Investigaciones en Óptica

Bellaterra, 20 de Juliol de 2017

Agradecimientos

In this part, I'm going to explain in my mother language the acknowledgments (Agradecimientos) for all the people that support me during this years.

Primero de todo quiero agradecer al Profesor Arben Merkoçi la oportunidad que me ha dado de realizar tanto mis estudios de Master como de Doctorado en su grupo, por ayudarme siempre que lo he necesitado y por guiarme en el mundo de la investigación. A Carmen Mayorga por todo lo que me ayudo cuando yo empezaba en este mundo, siempre estando pendiente de mí y por ser una postdoc que siempre intentaba saber cómo le va a sus alumnos y ayudarles. A Edén Morales, darle las gracias por todo lo que me ha enseñado respecto al mundo de los quantum dots y de la fluorescencia y por todo lo que me ha ayudado con la escritura de los artículos. Quiero también hacer una mención a Ruslán Alvarez, que a pesar de no ser mi director de tesis me ha aportado muchísimo tanto a nivel de trabajo como social, ayudándome siempre con mis dudas, dándome grandes ideas en las que trabajar juntos, pero sobre todo por ser un gran amigo con el que no puedo pasármelo mejor.

Quiero centrarme en la persona que me ha dado fuerzas siempre para continuar incluso en los momentos más difíciles, dándome su apoyo incondicional y ser siempre mi guía, y de la cual decir que esta tesis es en parte suya por todo lo que me ha dado siempre, y esa persona es mi esposa Nuria. Solo puedo decirle gracias por todas las horas que has dedicado ayudándome a corregir textos o intentando solucionar mis problemas de teoría, esta tesis no habría sido posible sin ti a mi lado.

Agradecer también a mis padres que siempre me hayan apoyado a que siguiera estudiando y que enriqueciera mi vida con conocimientos, dándome siempre todas las facilidades para continuar mis estudios y a pesar de no poder ayudarme en ellos, dándome el cariño que es más importante que cualquier otra cosa.

Quería también hablar de todos mis compañeros de trabajo, aunque ya no puedo llamarlos compañeros porque juntos somos una familia y grandes amigos, con los que puedo decir que he vivido de los mejores momentos de mi vida. Siempre recordare las conversaciones absurdas durante la hora de comer, nuestras cervezas juntos, todas las noches de fiesta donde siempre acaba pasando algo que recordamos por meses. Me gustaría acordarme de Dani, con el cual me une una amistad de más de diez años y que hemos pasado juntos por todas las penurias de la carrera, master y doctorado, y siempre ha sido un gran amigo con el que se puede contar y que aguanta mis locuras. A Amadeo, una persona que esta tan loca como yo y con la que siempre puedo contar para pasar un buen rato , a Juan por sus chistes horribles y por hacer el grupo más divertido, a José Fran porque es una persona con la que puedes hablar de todo tanto cosas absurdas como serias y siempre te lo pasas bien, a Anna porque aparte de ser una persona increíble sin ella seguramente estaríamos muertos, a Pablo y sus conversaciones profundas e interminables y de sus intentos por querer jugar siempre a las películas conmigo, también acordarme de Ruslan, Enric, Denise, Yef, Gina, Marc, por hacerme disfrutar las horas de trabajo, por todo lo que reímos juntos y todas fiestas que hemos hecho y disfrutado. A gente que a pesar de ya no estar en el grupo han sido muy importantes para mí como Irene; de la que siempre echaré de menos nuestros desayunos en

mi mesa, de las risas y de los grandes momentos juntos, a Luiza y Jahir, dos personas a las que admiro profesionalmente y considero dos de las mejores personas que conozco. Recordar también a miembros antiguos del grupo que significaron algo para mí como Marisol; que siempre me ayudó con todo y es una persona estupenda, Alex, Luis, Sandrine, Lourdes, Natalia, Alessandra, Flavio, Thiago, Fabio, Abdellatif, Monica, Maria Luiza, Nopchulee, Hector, Aida, Adrià, Alfredo, Carme, Erhan, Livia, Andrzej, Emma, Guilia, Recep, Esma y todos los restantes, por todo lo que me han aportado.

Acordarme también de la gente de Química, Ana, M^a Angels, Javi, Dani, Marta, con los que tantos años hemos pasado juntos desde que empezamos la carrera, por todas las cosas que hemos hecho juntos que siempre hace que disfrutes más de la vida, por todas las risas, por todas las cenas raras y cafés tomados.

Finalmente dar las gracias a los servicios técnicos del ICN como los departamentos de Microscopia, sobre todo a Marcos y Belén, de Rayos X a Guillaume y Common Services a Javier Saiz.

Acknowledgment for the economic and logistic support:



Universitat Autònoma
de Barcelona



Institut Català
de Nanociència
i Nanotecnologia



Detection of PTHrP using magneto sand



immuno@



Generalitat
de Catalunya

done by ICN group as a contribution to the project:

*evaluation of the calcium sensing receptor as a potential new tumor su
gene and therapeutic target in neuroblastoma".*

ELISA: enzyme linked immunosorbent assay

Fab: antigen-binding fragment

AuNPs: gold nanoparticles

MWCNT: multi walled carbon nanotubes

CNTs: carbon nanotubes

CFU: colony forming units

HPLC: high pressure liquid chromatography

ATRP: atom transfer radical polymerization

MIP: molecularly imprinted polymer

MNPs: magnetic nanoparticles

SMX: sulfamethoxazole

SEM: scanning electron microscopy

TEM: transmission electron microscopy

FT-IR: Fourier transform infrared spectroscopy

XPS: X-ray photoelectron spectroscopy

SPCE: screen printed carbon electrodes.

DMSO: dimethyl sulfoxide

MAA: methacrylic acid

PVP: polyvinylpyrrolidone

Py: pyrrole

NIP: non imprinted polymer

EIS: electrochemical impedance spectroscopy

SDZ: sulfadiazine

SCT: sulfacetamine

LOD: limit of detection

LOQ: limit of quantification

TBT: tributyltin

MBT: monobutyltin

DBT: dibutyltin

APTS: aminopropyltriethoxysilane

EGDMA: ethylene glycol dimethacrylate

IF: imprinting factor

GO: graphene oxide

IgG: immunoglobulin G

QDs: quantum dots

LFA: lateral flow immunoassay

Ab: antibody

TL: test line

CL: control line

ppb: parts per billion

PBS: phosphate buffer saline

BSA: bovine serum albumin

This PhD thesis describes the development of innovative nanomaterials-based platforms with interest for environment as well as other diagnostics applications. The first platform takes advantages of molecularly imprinted polymers (MIPs) and magnetic nanoparticles for electrochemical detection of contaminants. The second one consists in a lateral flow immunoassay, where quantum dots (QDs) are used as photoluminescence source and graphene oxide as quencher to perform fluorescence measurements.

Chapter 1 is an introduction in the topic and shows the state of the art of nanomaterials connected to biological and non-biological receptors for bio/sensing applications. This chapter discusses how antibodies (biological receptor) and molecularly imprinted polymers (non-biological-receptors) can improve the sensitivity, stability and specificity of the bio/sensing systems for a large number of analytes and different transducer methods, ranging from optical to electrochemical techniques.

In **Chapter 2**, the objectives of the thesis are explained.

In **Chapter 3 and Chapter 4**, two different sensors based on magnetic nanoparticles decorated with molecularly imprinted polymer (MIP) as non-biological receptor for sulfonamide and tributyltin detection are presented. In both sensors, the electrochemical impedance spectroscopy is used as a transduction method. The first sensor (chapter 3) has a related paper in "Anal. Chem. 2016, 88, 3578–3584" and the second sensor (chapter 4) is related to the paper published in "Electrochem. Commun. 2017, 10.1016/j.elecom.2017.07.007. Two MIPs are fabricated using: (i) pyrrole and methacrylic acid for sulfonamide, and (ii) EGDMA and APTS selective to tributyltin. Moreover, the fabrication methods as well as the analytical performance including their application in real samples are explained in detail in each chapter.

In **Chapter 5**, is presented a lateral flow immunoassay whose photoluminescent properties can be modulated upon protein recognition via the photoluminescence quenching capabilities of graphene oxide (GO). The assay is intended for the detection of a model protein in human serum, that is, human immunoglobulin G, with the aim to demonstrate a virtually universal protein detection platform. The proposed system shows a low limit of detection improving the conventional lateral flow with gold nanoparticles for the detection of the same

analyte in standard buffer. Also the system is able to achieve excellent limits of detection in a complex matrix such as human serum.

Finally, in **Chapter 6**, the general conclusions and the future perspectives are discussed.

In addition, annex reports all the publications resulted during the development of this PhD thesis.

1. **CHAPTER 1 INTRODUCTION**, Nanomaterials connected to bio/receptors for bio/sensor applications
 - 1.1. Biological receptors: Antibodies
 - 1.1.1. Antibody and nanomaterials connection for biosensors applications.
 - 1.1.2. Antibodies for point of care applications: Lateral flow immunoassay
 - 1.2. Non-biological receptors: Molecularly imprinted polymers (MIPs)
 - 1.2.1. Current trends in MIPs-based biosensing applications
 - 1.2.2. Nanomaterials and Molecularly Imprinted technology.
 - 1.2.3. Electrochemical sensing applications
 - 1.2.4. Optical applications of Molecularly imprinted polymers
 - 1.3. Conclusions
 - 1.4. References
2. **CHAPTER 2**: Thesis objectives
3. **CHAPTER 3**: Development of a molecularly imprinted polymer decorated with magnetite nanoparticles for selective sulfonamide detection.
 - 3.1. Introduction
 - 3.2. Experimental section
 - 3.2.1. Reagents and materials
 - 3.2.2. Screen printed carbon electrodes
 - 3.2.3. Synthesis Magnetite nanoparticles
 - 3.2.4. Synthesis of Molecularly Imprinted Polymer-Decorated Magnetite Nanoparticles
 - 3.2.5. Binding Experiments
 - 3.3. Results and discussion
 - 3.3.1. Characterization of Fe₃O₄ MNPs and MIP-Decorated Fe₃O₄ MNPs
 - 3.3.2. Electrochemical Impedance Responses of the MIP-Decorated Fe₃O₄ MNPs toward SMX
 - 3.3.3. Characterization of the NIP-Composite and Selectivity Studies
 - 3.3.4. Real samples measurements
 - 3.3.5. Size effect study
 - 3.4. Conclusions
 - 3.5. References
4. **CHAPTER 4**: Magnetic nanoparticle-molecular imprinted polymer: A new impedimetric sensor for tributyltin detection.
 - 4.1. Introduction
 - 4.2. Experimental section
 - 4.2.1. Reagents and materials
 - 4.2.2. Synthesis of molecular imprinted MIP-Fe₃O₄NPs composite
 - 4.2.3. Electrochemical measurements
 - 4.3. Results and discussion
 - 4.3.1. Characterization
 - 4.3.2. Impedance measurements in buffer and sea water

- 4.3.3. Study of the selectivity
- 4.4. Conclusions
- 4.5. References
- 5. **CHAPTER 5:** Development of a photoluminescent lateral flow flow based on non-radiative energy transfer for protein detection in human serum.
 - 5.1. Introduction
 - 5.2. Experimental Section
 - 5.2.1. Reagents and materials
 - 5.2.2. Lateral flow strip preparation
 - 5.2.3. Overall measurement procedure
 - 5.3. Results and discussion.
 - 5.3.1. System optimization
 - 5.3.2. Characterization
 - 5.3.3. Protein measurements in buffer and human serum
 - 5.4. Conclusion
 - 5.5. References
- 6. **CHAPTER 6:** General conclusions and future perspectives
 - 6.1. General conclusions
 - 6.2. Future perspectives
- 7. Annex
 - 7.1. Compendium of publications

CHAPTER 1

Introduction

Nowadays nanomaterials are considered a pivotal tool for different fields such as textiles, energy, environment, electronics, photonics, food, agriculture, biomedicine and health care. This is due to their advantageous properties coming from their high surface area, among other physicochemical properties, compared to their respective bulk forms. Nanomaterials, while used in (bio)detection systems, have shown to be extremely valuable to improve the analytical performance of conventional/laboratory methods and move forward biosensing technology. The usage of nanomaterials has been widely spread over the last few years mainly thanks to the great advantages that they offer in the development of conceptually new biosensors or improving the existing ones. This review focus on how the usage of different nanomaterials have impacted biosensing research underscoring two different types of receptors, including biological receptors and non-biological receptors. The performance of relevant biosensing platforms including lateral flow devices as well as other optical and electrochemical approaches integrating nanomaterials and (bio) receptors are also discussed.

1. Nanomaterials connected to bio/receptors for bio/sensor applications.

Currently the biosensing field represents an emergent technology with high capabilities and versatility to detect a myriad of analytes in different mediums, for instance pesticides in food^{1,2} and water samples^{3,4}, toxics in food^{5,6} and clinically relevant (bio)molecules in urine or blood (e.g. the pregnancy test and glucose sensors beside others).^{7,8} Given the importance of this application field, the research and development of biosensing technology has been continuously increasing during the last decade. Above all, this has been supported by the rise of nanomaterials, which offer interesting building blocks to design innovative biosensors or improving those existing ones.^{9,10}

Nanomaterials are nanometric structures that have outstanding physicochemical properties and display a size of 100 nanometers or smaller in at least one dimension, which is extremely useful in many areas such as food, agriculture or biomedicine. Regarding the environmental field, nanomaterials have shown the potential for highly efficient removal of pollutants¹¹⁻¹⁴ and detection as well. In food processing, the usage of nanomaterials is also valuable for the removal of biological contaminants; likewise in agricultural applications for plants protection this class of materials lead to improve the productivity and minimize losses.¹⁵⁻¹⁸ Furthermore, nanomaterials are finding excellent opportunities in the medicine

field, including various biomedical applications such as diagnostics, point of care devices, theranostics, bioimaging, drug delivery and cancer therapy.^{19–21,22–25}

During the last years, there has been an increase of the improvement in the synthesis and characterization of different nanomaterials, such as magnetic nanoparticles^{26,27}, hydrogels^{28,29}, polymeric nanoparticles³⁰, carbon-based nanomaterials.^{31,32} and two dimensional materials.^{33,34} However, advances related to nanomaterials biofunctionalization are crucial to achieve and further high specificity in biosensing. To this end, depending on the target analyte, nanomaterials can be decorated with different (bio)receptors such as peptides,^{35,36} synthetic oligonucleotides/aptamers,^{37,38} antibodies,^{39,40} enzymes^{41,42} or molecularly imprinted polymers.⁴³ These (bio)receptors offer different capabilities and specific recognition ability, with the possibility to apply them in biosensing

As it is well-known, nanomaterials have many advantages, being their high specific surface area one of the most important features enabling a better efficiency of the immobilization of host materials and thus a rich and advantageous amount of (bio)receptor units. Performing the right immobilization strategy onto the explored nanomaterial represents a challenge that allows for the conjugation of the nanomaterial and the (bio)receptor^{44–46}. Covalent binding is one of the most common strategies to immobilize (bio)receptors onto nanomaterials. Depending on the surface chemistry of the involved materials, this type of linking can be carried out by a classical amide reaction^{47,48} or a cross-linking process^{49,50}. Though, its main drawback is that the anchoring of the biomolecule is uncontrolled and the sensing surface can be negatively affected hindering the biorecognition phenomenon targeted by the biosensing system. Another strategy can be the immobilization of biomolecules due to supramolecular or coordinative interactions. Regarding this strategy one of the most utilized is the biotin/streptavidin system, whose simple – albeit effective- process is also used in the field of biosensors.^{51,52}

In biosensing technology, the signal of interest is generated by correlating a transducing signal with the capture of the analyte using a (bio)receptor. Then, the transducer translates this signal into a quantifiable parameter (piezoelectric, optical, electrochemical, etc.), which is the output signal. This review is focused on the usage of nanomaterials connected to specific (bio)receptors for biosensor applications. Particularly, we are going to focus on two classes of (bio)receptors for nanomaterials functionalization, including antibodies, which are

biological receptors, and molecularly imprinted polymers, which are biomimetic receptors that are excellent candidates to be used in lieu of other biological receptors such as antibodies, especially when the target analyte is not an immunogenic agent.

1.1 Biological receptors antibodies.

Antibodies represent a very common bioreceptor for different kind of analysis based on immunoassays, which are exploited in different techniques being the most common the enzyme linked immunosorbent assay (ELISA) or western blot (WB) assays.

On the other hand it is important to remember that the conjugation of nanoparticles with antibodies combines the outstanding properties of nanomaterials with the highly specific and selective recognition ability of the antibodies targeting a myriad of antigens.⁵³⁻⁵⁵

Antibodies are proteins with Y shape, with the ability to recognize a specific molecule; that is the antigen, via the antigen-binding (Fab) fragment variable region. This region is highly specific and can be tailored, thus each antibody can be produced with a completely different specificity. Antibodies have two light chains; exactly the same, and two heavy chain, also identical, each component chain contains one NH₂-terminal and one or more COOH-terminal, both chains are linked by disulphide bridges. Different changes in heavy chain produces different immunoglobulins.⁵⁶ Such immunoglobulins are glycoproteins of 150 kDa and they are synthesized by the plasma cells as immune response to neutralize pathogens such as bacteria and viruses. There are five immunoglobulin classes found in serum: IgG, IgM, IgA, IgE and IgD, the difference between them are the type of heavy chain they contain. IgG have γ -chains; IgMs μ -chains; IgAs α -chains; IgEs ϵ -chains; and IgDs δ -chains. The variations in heavy chain polypeptides allows each immunoglobulin class to work as a different type of immune response or during a different stage of the body's defense.^{57,58}

IgA (see structure in Figure 1.1) exists in two forms, as a monomeric form found in serum and as a dimeric form. Dimeric IgA is often produced by plasma cells that act near epithelial surfaces and other areas where complement is not highly active. IgA can act as a neutralizing antibody but commonly can function by blocking pathogens from entering certain tissues. IgE is present in the lowest levels and is not really effective except binding mast cells with good efficiency. Mast cells secrete a variety of cytokines and other inflammatory compounds useful during an immune response. IgE are thought to be useful in combating larger, extracellular

pathogens, and are responsible for secreting histamine, which is commonly known to provoke allergic responses. The function of circulating IgD is unclear, as it is not known to participate in the major antibody effector mechanisms.^{59–61}

IgM forms large pentamers with 10 antigen binding sites per molecule, allowing it to bind antigens with high avidity even during the early immune response when antibody affinity use to be low. Due to its large size and structure it is mainly present in the blood and not in intercellular spaces, is also very effective at activating the complement system because provides a large “target” for the C1 protein to bind. IgG is the main type of antibody found in circulation, is much smaller than IgM and is only found in monomers. IgG is generally great for opsonizing pathogens and activating complement. IgG is sort of like an all-purpose workhorse.

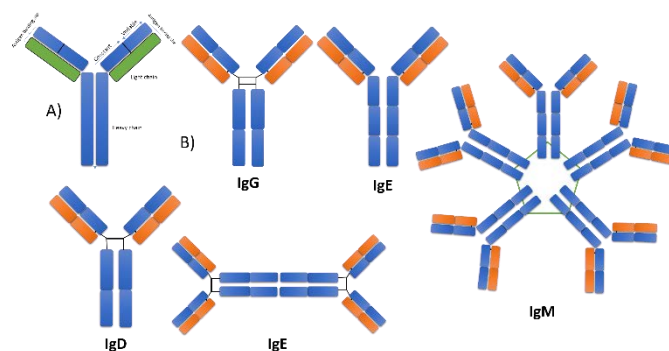


Figure 1.1. Antibody structure (a) and types of immunoglobulin (b)

IgG is the immunoglobulin most used in biosensing among all the different classes. We can find two different kind of this antibody, the monoclonal one and the polyclonal, which can be differently exploited for hundreds of different analysis, depending conditions and needs. The characteristics of each one are summarized in Table 1.1.

Table 1.1. Comparison between monoclonal and polyclonal antibodies.

Monoclonal Antibodies	Polyclonal Antibodies
Expensive to produce	Inexpensive to produce
Skills required for production are low	Training is required for the technology used
Relatively quick to produce	Hybridomas take a relatively long time to produce
Generate large amounts of non-specific antibodies	Generate large amounts of specific antibodies
Recognize multiple epitopes on any one antigen	Recognize only one epitope on an antigen
Can have batch-to-batch variability	Once a hybridoma is made, it is a constant and renewable source
-	No or low batch-to-batch variability

1.1.1 Antibody and nanomaterials connection for biosensors applications.

Antibodies are widely used in biosensing^{62,63} for pollutants , ^{12,64} biomarkers, pathogens, ^{65,66} cancer cells detection,^{67–69} where antibodies act as highly specific capture probe. Actually, the identification and posterior quantification of different biological molecules have high relevance in biomedical applications and environmental control.

Literature reports a great variety of systems that combine antibodies with nanomaterials for their usage in biosensors to detect clinically relevant analytes, for example the work developed by *Shao et al* ⁷⁰, in which they use nanotube-antibody biosensor arrays for the detection of circulating breast cancer cells. They report a novel system based on a single

nanotube and a single field effect transistor array, which is functionalized with IGF1 (insulin growth factor) and Her2 (protein present in cancer cells) specific antibodies (see Figure 1.2). This system exhibits a high sensitivity and selectivity for human breast cancer cells in human blood. The device created by this group represents a new technology in cancer cell detection, which use a single carbon nanotube as a sensitive platform. Interestingly, the system shows a single cell sensitivity, high reproducibility, and high selectivity. Furthermore, compared with other methods like nanoscale top-down manufacturing, it is easy to fabricate and with lower cost. It should be remarked that immune sensing approaches can be tailored to detect other molecules by simply changing the respective antibody.

Human influenza virus is another example of a clinically relevant target.^{11,71} An innovative biosensor for the recognition of this virus was developed by *Arya et al.*⁷² The authors use a specific antibody for hemagglutinin detection and a coiled-coil peptide modifying a microelectrode array platform. In this system, the influenza virus was measured using electrochemical impedance spectroscopy (EIS) and cyclic voltammetry. The use of coiled-coil peptides with HA-antibody creates a platform for the detection of an immunoglobulin specific for influenza virus, with a detection range from 1 pg mL⁻¹ to 100 ng mL⁻¹, showing a detection limit of 1 pg mL⁻¹, which is a detection limit extremely low in comparison with other different techniques such as MDCK cell culture, complement fixation, hemagglutinin-inhibition, and RT-PCR.^{73,74} Detection and prevention of different diseases is crucial in our society,^{75,76} consequently disease-related proteins need a critical sensitive detection in order to help in early detection and facilitate the possibility of successful treatment. In this regard, immunoassays using surface plasmon resonance (SPR) represent important advantages, including a label free detection, small samples size, reusable sensors chips, suitable reproducibility and the involved measurements allow for the real time monitoring.^{77,78} Importantly, it is also amenable to combining with nanomaterials so as to improve its sensibility. In the work developed by *J. Zhang et al*⁷⁹, they use surface plasmon resonance combined with graphene oxide (GO) and gold nanorods (AuNRs) conjugated with antibodies for transferrin detection. Interestingly, the GO properties were smartly used in this approach as this carbon-based material is richly oxygenated and is endowed with high specific surface area, long-term stability and a hydrophilic character, which enables GO to interact with different types of biomolecules by covalent, non-covalent or electrostatic interactions.

Moreover, gold is known as an excellent material for bioassays design. In this case, AuNRs are used to provide the system for transferrin detection with nanoplasmonic properties. It is worth mentioning that the nanoplasmonic properties of AuNRs are more sensitive than those of their spherical counterpart, especially in biosensing approaches.^{80,81} A concentration range between 0.0375 and 40.00 $\mu\text{g mL}^{-1}$ was obtained for transferrin detection using this system. The combination of the highly sensitive nanoplasmonic properties of AuNRs in synergy with the high loading capacity for biomolecules of GO was proven valuable for improving the SPR performance.

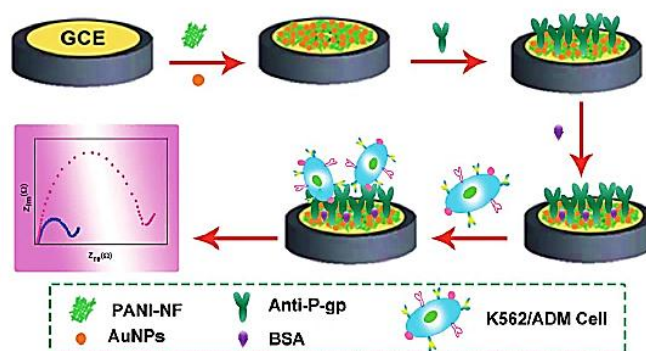


Figure 1.2. Illustration of the preparation process of a label-free electrochemical cytosensor biosensor designed by S.Zhang et al. Reprinted with permission from S. Zhang et al. (2014), Copyright 2014 American Chemical Society.

Another application based on the usage of nanomaterials and antibodies for biosensing applications with an important purpose in medicine, is the sensitive recognition of drug-resistant leukemia cells.^{82,83} Probably one of the hot topics during the last years in clinical and biomedical areas is the efficient diagnosis and therapy of cancer.^{84–86} In this regard, it is theorized that a key point in this field is the detection of P-glycoprotein overexpression because it can cause the failure of chemotherapy. There are several conventional methods for the detection of this molecule such as flow cytometry,⁸⁷ immunohistochemistry, ELISA⁸⁸ and fluorescence,⁸⁹. Though, most of them need multiple steps and are time-consuming assays. Moreover, they need highly qualified technical staff. Due to these drawbacks, electrochemical methods have been recently applied in cancer cell detection. S Zhang et al. developed an electrochemical cytosensor based on P-glycoprotein expression level on a cell membrane.⁹⁰

The idea developed by Zhang (see Figure 1.2) and his group relies on the combination of gold nanoparticles with polyaniline nanofibers conjugated with anti-p-glycoprotein. This molecule can provide a biomimetic interface for the immunosensing of cell surface P-glycoprotein and then can capture the overexpression of this protein. Finally, the sensor reported by S Zhang and colleagues was demonstrated to be simple, efficient and can be sensitive to the recognition of drug resistant leukemia cells with a low limit of detection (80 cells/mL). Moreover, this technique does not present the drawbacks of the conventional methods for the detection of this kind of analyte.

1.1.2 Antibodies for point of care applications: Lateral flow immunoassay.

Lateral flow immunoassays (LFA) can be catalogued within paper-based devices.^{91–93} Its characteristics like the low-cost technology, good robustness, specificity and low limit of detection make them interesting for biosensing applications.

Lateral flow technique (see structure in Figure 1.3) is mostly used for semi-quantitative and qualitative assays, including pathogens detection⁹⁴, drugs⁹⁵, hormones⁹⁶ and metabolites in biomedical, phytosanitary, veterinary, feed/food and environmental monitoring⁹⁷.

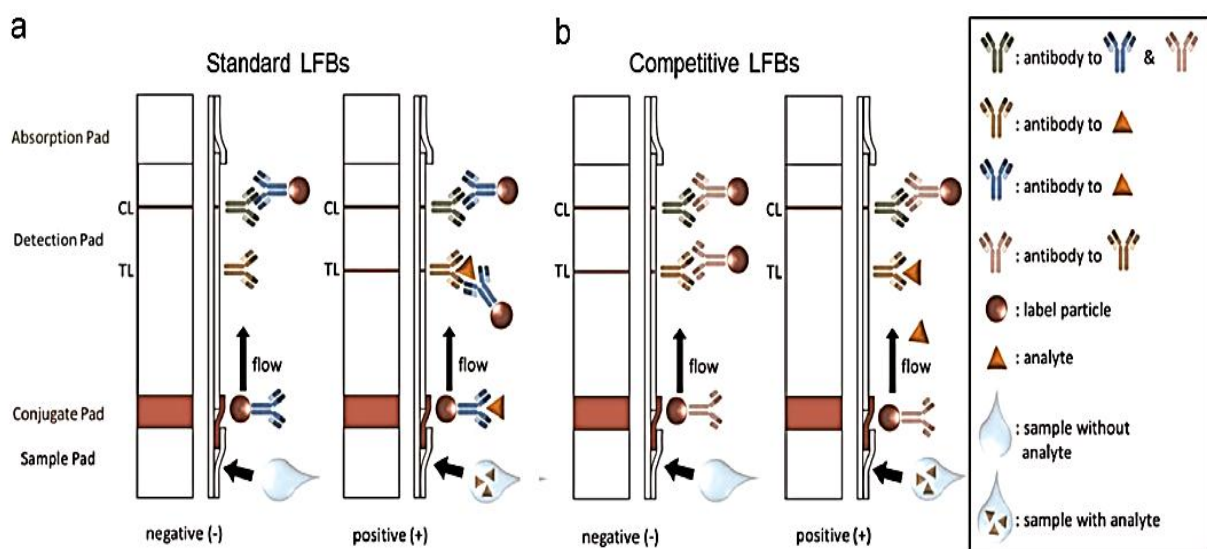


Figure 1.3. Schematic representation of the different parts of lateral flow strip and movement of an analyte and label particles across it with (a) standard and (b) competitive design. Reprinted with permission from Quesada et al.(2015), Copyright 2015 Elsevier.

However, LFA has some drawbacks as the qualitative response with naked eye, that it can be solved with some reading devices which transform the qualitative response in a semi-quantitative signal, or the fact that the samples has to be in liquid state to avoid the clogged of the pores size in the lateral flow membrane, that in some cases can be a problem due to unspecific absorptions in the membrane

Nowadays there are different lateral flow assays, the most common and widely used is that based-on gold nanoparticles for colorimetric detection.⁹⁸⁻¹⁰⁰ This kind of nanoparticles are employed in this technique due to their easy synthesis and manipulation, their stability and biocompatibility.

Moreover, their intense red colour contrasting the typical white background on to the nitrocellulose strip makes them perfect for visually detectable assays, such as LFA

Currently LFA are reaching new goals by integrating more complex nanomaterials. In this regard, the work developed by *Tang et al.* gives a new step forward for the detection of an interesting analyte; aflatoxin, this compound represents a high dangerous problem for humans due to is carcinogenic effect and are produced by certain kinds of molds, being easily to be found in the environment. The idea developed by this group is based on magnetic nanogold microspheres (see Figure 1.4), with nano- Fe_2O_3 as a core and gold nanoparticles (16nm) as a shell and biofunctionalized with monoclonal anti-AFB₂ antibodies.¹⁰¹

This kind of technique is really useful for food monitoring, and the results obtained by this group in different samples such us peanuts, hazelnuts, pistachio and almonds, gives a visual limit of detection that is threefold lower than that obtained by the conventional lateral flow (using simple gold nanoparticles as reporters).

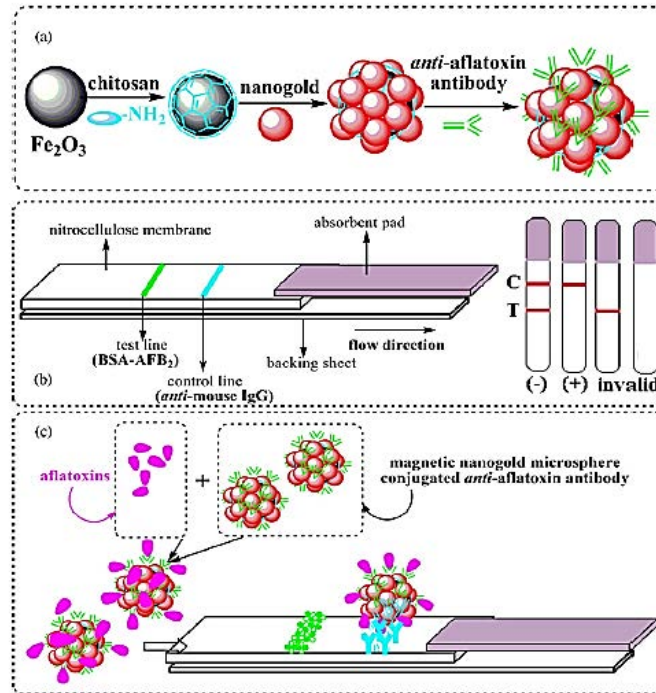


Figure 1.4. (a) Fabrication process of the synthesized magnetic nanogold microspheres, (b) schematic illustration of the lateral flow strip and (c) principle of the detection method. Reprinted with permission from Thang et al. (2009), Copyright 2009 Elsevier.

We can find different nanomaterials involved in lateral flow-based assays, including carbon nanotubes (CNT). The use of this kind of nanomaterial is not really common in lateral flow but it has an enormous potential, and exhibits better detection limits in comparison with common lateral flow with gold nanoparticles. A relevant example of this approach was developed by Qiu et al.¹⁰² The authors achieved a detection limit for DNA sequence 12.5 times lower than that of the conventional gold nanoparticle-based LFA (see Figure 1.5)

A sandwich-type DNA hybridization reaction was performed onto the lateral flow strip, to be reported by the multi-walled carbon nanotubes (MWCNTs) on the respective test and control lines, obtaining a characteristic black band. Moreover, this system has another great advantage in comparison with the gold LFA, it can avoid the aggregation conjugates thanks to the MWCNTs. This kind of LFA open a new door to point of care diagnosis of genetic diseases and infectious agents detection.

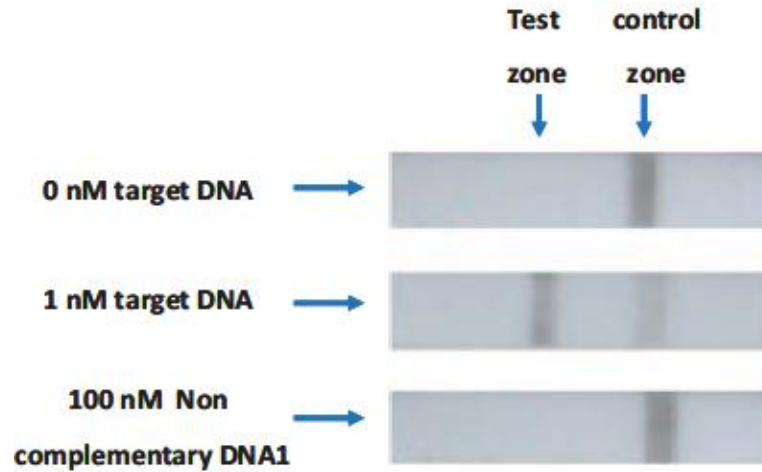


Figure 1.5. Typical images of MWCNT-based LFB in the absence and presence of 1 nM target DNA and 100nM non-complementary DNA. Reprinted with permission from Qui *et al.*(2015), Copyright 2015 Elsevier

Aside from this, it is possible to combine lateral flow with fluorescent particles such as quantum dots (QDs). QDs have been intensively used in different immunoassays for its properties; broad and strong excitation spectra, size-tuneable emission, narrow, symmetric and strong photoluminescence and robust photo-stability. It is possible to use QDs in LFA in two different forms; the addition of this particles in the test and control line to detect the amount of analyte indirectly by quenching effect, or directly conjugating them with antibodies or aptamers. An example of that first case is the one developed by *Morales-Narvaez et al.* The authors report how it is possible to detect *E. coli* using a LF system with QDs conjugated with antibodies, printed in the test line, and revealed with graphene oxide (GO) as quencher to obtain a detection system for of *E. coli* present in liquid samples (see Figure 1.6). The system can be read in terms of fluorescence quenching effect over the test/control line. The novelty of this lateral flow is based on a test line with CdSe@ZnS QDs conjugated with antibody (in this case anti-*E. coli*), the control line made of bare QDs, and the use of GO as revealing-agent added after adding the sample to the LF strip. The sensing principle of the system is related with the absence/presence of the analyte, if there is no presence of the analyte in the analyzed sample, the test and control line are efficiently quenched by GO, due to the small distance between QDs-Ab and GO (OFF state). Otherwise, if the sample contains the analyte

it is going to be recognized and attached for the antibody present in the test line, in this case after addition of GO the distance between this and QDs exceeds the distance where resonance energy transfer is observable (around 20nm), leading to an ON state. With this assay, the authors are able to achieve detection limits of up to 10^4 CFU mL⁻¹. This results represent a really good improvement in comparison with other methods, such as microarray technique that obtains 10^4 CFU mL⁻¹,¹⁰³ immunofiltration assay with 100 CFU mL⁻¹,¹⁰⁴, or a conductimetric biosensor; between 0.5 - 10^4 CFU mL⁻¹ depending the system used . Moreover, the key point of this photoluminescence lateral flow is that it is a cost-effective device being also easy-to-use.

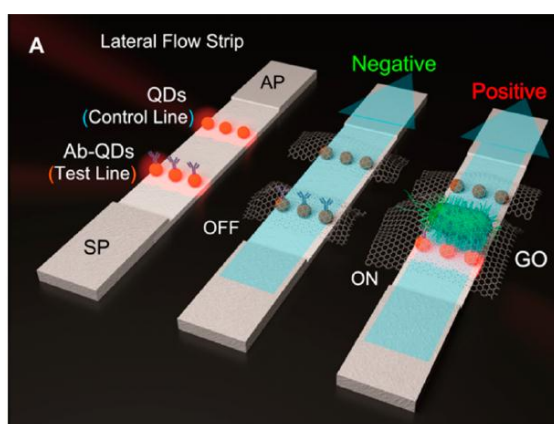


Figure 1.6. Schematic representation of photoluminescent lateral flow test revealed by graphene oxide (GO) for pathogen detection. Reprinted with permission from Morales Narvaez et al. (2015), Copyright2015 American Chemical Society

A lateral flow strip reported by QDs was developed by Yang et al.¹⁰⁵ This research team performed a QD-based point-of-care device for syphilis detection (see Figure 1.7). To obtain a complete strip, they just have to print a mixture of recombinant antigen for syphilis (*Treponema pallidum*) in the test line and IgG as control line, letting both dry and block, and then add the conjugate pad with the mixture of colloidal gold and quantum dots. This mixture presents better results if we compare it with lateral flow with only colloidal gold, in terms of sensitivity, and selectivity. This LF has advantageous features as it is an inexpensive technique, it is also easy to fabricate and has been demonstrated to be suitable for in situ syphilis screening. Overall, integrating different nanomaterials into LF strips also represents an

improvement in conventional LF strips, showing better limits of detection (LODs), reducing manufacture costs, and keep the original features of LF strips as they do not need highly qualified staff, they are portable and easy to manipulate.

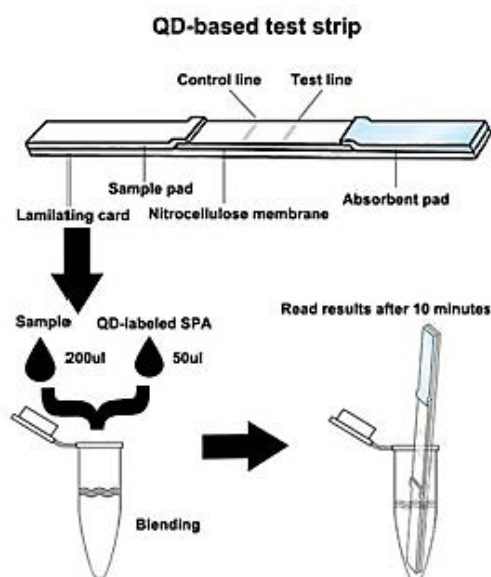


Figure 1.7. Schematic representation of QD-based lateral flow strips. Reprinted with permission from Yang et al. (2010), Copyright 2010 Springer

1.2 Non biological receptors: Molecularly imprinted polymers (MIPs)

Molecularly imprinted polymers are a group of compounds in which the functional and crosslinking monomer are copolymerized in the presence of a target analyte, after this, during the final step the analyte is removed and the cavities (acting as non-biological receptor) are ready (Figure 1.8).^{106–108} These cavities are a kind of mould complementary in terms of size and shape regarding the imprinted analyte. MIPs also have the ability to recognize and bind specific target molecules;^{109,110} however, in comparison with those techniques that employ antibodies in their systems, molecularly imprinted polymer technique has a great advantage as MIPs are highly stable and resistant to physical and chemical treatment, including heating, acids, bases and organic acids – these polymers are physicochemically stable at extreme pH and temperatures levels.^{111,112} MIPs are also easy to synthesize and handle, and they have a low fabrication cost, high specificity, and excellent reproducibility. The application of MIPs

may face major limitations in certain fields, including heterogeneous binding, small binding capacity with the analyte, lower selectivity, and poor site accessibility. These factors appear as a result of total insertion of the template and binding site into the polymer matrix, which depends on the designed synthesis process. Surface imprinting onto a solid support and surface-imprinted core-shell particles can be used to reduce the drawbacks of these mechanisms, fabricating surface-imprinted materials which can effectively recognize template molecules. Situation of the imprinting sites at or near the polymer surface may also further improve recognition in these molecules.^{113–115}

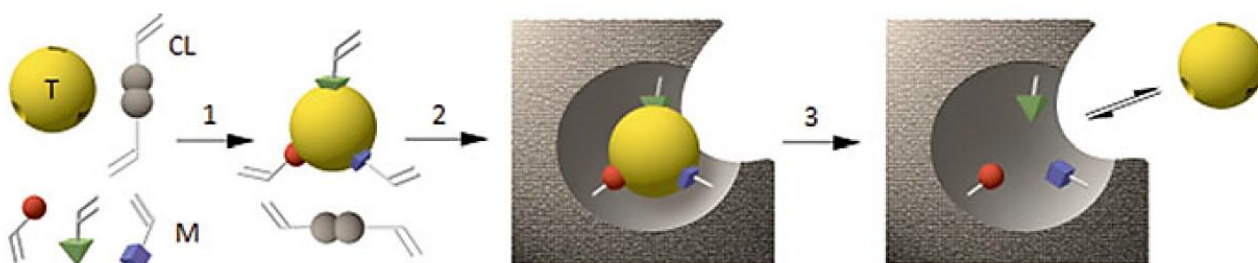


Figure 1.8. Scheme of molecularly imprinted polymer preparation. (1). The polymerization of the resulting system produces a rigid structure bearing imprinted sites (2). Finally, removal of the template liberates cavities that can specifically recognize and bind the target molecule (3). Reprinted with permission from Haupt et al. (2003), Copyright 2003 American Chemical Society

The characteristics of MIPs mainly depend on the selected functional monomer as this defines the polymer matrix structure, its functionality and crosslinking process.^{116,117} The rigidity and flexibility of the supporting polymer is important in the process since the polymer structure enables the cavities to retain a specific shape after removing the template, giving more selectivity. Some flexibility is necessary to allow a fast binding and splitting of the template within the cavities. Other pivotal factors affecting the template are the ratio between the monomer and the guest molecule and the polymerisation temperature. In fact there are several methods to synthesize MIPs, including covalent, non-covalent and semi-covalent approaches.¹⁰⁶ The covalent approach, involves the formation of covalent bonds

between the template and monomers before polymerization. After the polymerization step, the template is separated from the polymer by removing the covalent bonds, for then form new covalent bonds again upon rebinding of the analyte. The high stability of the interaction between the template and the monomer gives to the system a homogenous population of binding sites, and reduces the presence of non-specific sites. However, the design of a template-monomer complex in which covalent bond formation and cleavage are readily reversible under mild conditions makes this approach somewhat restrictive. An intermediate option is the semi-covalent approach. In this case, the template is also covalently bound to a functional monomer, but the template rebinding is based only on non-covalent interactions. The non-covalent approach is based on the formation of relatively weak non-covalent interactions (for example, hydrogen bonds or ionic interactions) between the template molecule and the selected monomer before polymerization. The non-covalent approach is probably the most used method for the preparation of MIPs.¹¹⁸

1.2.1 Current trends in MIPs-based biosensing applications.

Instead of a biomolecule (antibodies, enzyme, etc), MIPs can be used as a recognition element in biosensing.^{119,120} Certain general properties of the analyte; as stability, solvents in which can be used, size, conductivity...etc, or changes in one or more physicochemical parameters of the system upon analyte binding can be smartly employed as a detection principle. Biomolecules; such as antibodies or enzymes, are widely employed in biosensing, environmental monitoring and food safety. However, this kind of molecules have some drawbacks, including their poor stability at high temperatures, pH or in the presence of organic solvents. MIPs represent an effective alternative to conventional biosensors as they are cheaper and easy to manipulate in comparison with enzymes or antibodies and depending on their size. MIPs can bear thousands or millions of binding sites, whereas biological receptors have a few binding sites.¹²⁰

Regarding the synthesis of MIPs as protein-recognizing agents,¹²¹ there are only few functional monomers; for example methacrylic acid , 2-(dimethylamino)-ethyl-methacrylate, N,N-dimethylaminopropyl-acrylamide and others, reported in the synthesis of MIPs for proteins. If we compare this with the protein-based receptors this can be a drawback, because only a few monomers can be used to synthesize MIP for proteins. Regarding protein imprinted

MIPs in Figure 1. 9 we can see the evolution in this field comparing them with other MIPs, and how is increasing the use of this kind of receptors for proteins.

Imprinting techniques for protein detection (see Figure 1. 9 on this field is evolving in terms of publications) are challenging and are under active research.^{122,123}. This kind of MIPs with a high specificity for proteins are a valuable tool in environmental analysis, sensors, diagnostics, proteomics and drug delivery and the biomedical field.

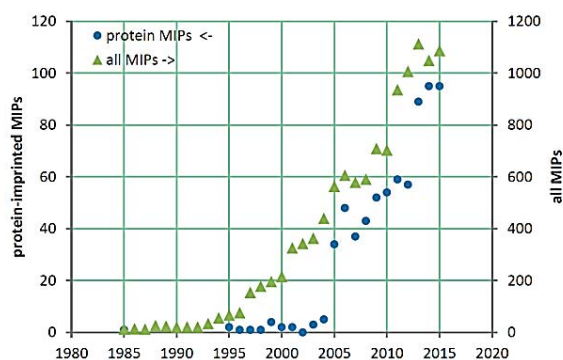


Figure 1.9. Number of publications on protein-imprinted (circles) and all MIPs (triangles) until 2015. Reprinted with permission from Menger et al. (2016), Copyright 2016 MDPI

Bulk imprinting of proteins or surface imprinting are probably the most important approaches for MIPs synthesis aiming at detecting proteins. The technique of bulk imprinting is well established in MIPs synthesis,^{124,125} but this technique is designed for low molecular-weight compounds, and their extrapolation to the macromolecules imprinting process represents a challenge due to their mobility in the polymeric network. It is possible for macromolecule to be entrapped within the polymeric network, and due to the high size the removal or rebinding of the protein is impossible. But, nowadays bulk imprinted hydrogels with low density and bigger pores has been developed as MIPs precursor in protein detection^{126,127}. On the other hand, surface imprinting represents a technique with greater advantages and promising results in MIPs production. The key-point to perform this process relies on controlling the binding site generation only onto the surface of the polymer, which can be easily accomplished using highly cross-linked polymer films. The resulting MIP presents an extremely thin layer that is comparable with the hydrodynamic radius of the protein, then

only half part of the cavities is filled and presents in the MIP and thus complete entrapment of the guest molecule is avoided. Consequently, these nanofilms have the potential of a successful removal and rebinding for a specific analyte.

Literature reports two approaches related to surface imprinting, including top-down and bottom-up approaches (see Figure 1.10).¹²⁸ In the top-down approach the target protein is attached onto a support or template, and then the analyte is removed to obtain a polymer layer over the surface. In the bottom-up approach, first of all the protein is immobilized onto the substrate in which the polymer is going to be deposited, then next steps occur in the same conditions as top down, adding the template and functional monomer to proceed with the polymerization.

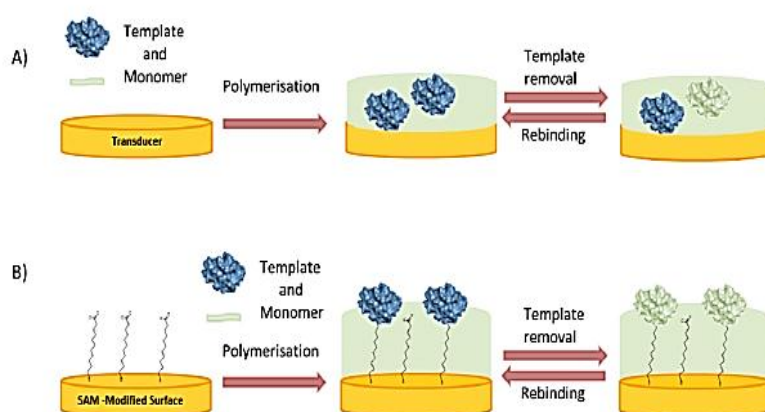


Figure 1.10. Surface imprinting approaches for the synthesis of MIPs films. A) Polymerization of a mixture of monomer/protein. B) Binding of the protein to a self-assembled anchor layer.

Reprinted with permission from Menger et al. (2016), Copyright 2016 MDPI.

MIPs preparation is also reaching new possibilities using techniques like photopolymerization,¹²⁹ Comparing this technique with other conventional techniques, such as classic thermal polymerization,^{130,131} photopolymerization has more versatility as it can be much more easily controlled, it has softer conditions and is easy to manipulate.

Regarding this new MIP tendency, photoinitiated atom-transfer radical polymerization (ATRP) has been limited thus far, because it has an incompatibility with acidic monomers, such as methacrylic acid,¹³² and this is still a great challenge. ATRP is widely used to obtain

MIP nano and microstructures, and there are developed work probed to be good synthesis even solving the problem with acidic monomers. For example the group of *Hawker et al*¹³³ employed fac-[Ir(ppy)₃] (ppy=2-phenylpyridine) as a photoredox catalyst, maintaining an excellent control over the polymerization reaction of methacrylates even in the presence of methacrylic acid in the media, solving with this the biggest drawback of this kind of reaction.

Another work in which ATRP is employed was reported by *Zeynep et al.*¹³⁴. The authors describe a new method to synthesize MIP nanomaterials using this procedure at room temperature. The method has a wide range of different monomers with diverse possibilities avoiding higher temperatures and giving the possibility to increase the stability of the template complex letting us obtain multiple composite forms (monoliths, nanoparticles, and surface-bound films). The possibility to obtain different MIPs with different shapes and forms gives a high variety of opportunities in sensing field. Thanks to this new method for MIPs production, it is possible to solve the problems regarding acidic monomers with softer conditions if we compare with traditional thermal polymerization.

After the synthesis process, the last parameter to be considered is the imprinting factor (IF). This factor is the ratio of the signal between the MIP and the non-imprinted polymer (NIP) after the conjugation with the analyte present in the sample. IF reflects the ratio of specific binding of the MIP in comparison with the non-specific binding of the NIP, and is affected by the preparation method of the imprinted polymer. All in all, the conditions of the template removal mechanism are crucial in order to obtain a good imprinting factor in the MIP.

The critical part in MIPs-based biosensing is the integration with the transducer, this part can be achieved by different ways; for instance, polymerization,^{135,136} spin coating,¹³⁷ electropolymerization,¹³⁸ open sandwich MIP (using antibodies combined with MIP technology),¹³⁹ and other procedures, with excellent results. The most MIP-based biosensing approaches are fluorimetry,¹⁴⁰ conductometry,¹⁴¹ chromatography,¹⁴² or different electrochemical techniques.¹⁴³ A common example found in literature can be glucose detection. Glucose is one of the most common analytes targeted with MIPs.^{144,145} These approaches can be performed with electropolymerization techniques for the imprinted material fabrication. Nowadays, modification of electrode surfaces seems to be a current trend in glucose detection based on MIPs. Capacitance, impedance, voltammetry or other

electrochemical tools are used to quantify the involved signal. Moreover, other innovative tools have been developed for glucose sensors, which are based on electrodeposition of molecularly imprinted polymeric micelles.¹⁴⁶

Regarding environmental applications, MIPs also represent a useful tool in prevention, extraction and detection of harmful compounds, such as pesticides.^{147,148} The typical methods to detect pesticides are based on chromatography separation,¹⁴⁹ gas chromatography,¹⁵⁰ electron-capture detector,¹⁵¹ flame ionization detector,¹⁵² and mass spectrometry.¹⁵³ These techniques reach low LODs with a high reproducibility, but require extensive purification, expensive equipment and trained staff. During the last few years, electrochemical sensors have been reported to be a user-friendly and miniaturized alternative for pesticides detection. Nevertheless, they normally use bio-receptors (aptamers, antibodies, enzymes), which can be instable, non-specific, and expensive. However, new and active fields devoted to biosensing are evolving and using MIPs for the development of specific, stable and low cost pesticide detection systems, for instance fenitrothiol,¹⁵⁴ organochlorine,¹⁵⁵ tributyltin[43] and heptachlor¹⁵⁶ detection systems showing excellent results.

Solid phase extraction represents one of the most common methods for pre-concentration and purification of pesticides contained in a complex matrix using MIPs. *Binsalom et al.* reported the synthesis of different MIPs for solid phase extraction of chlorpyrifos using various pyrogens (such as acetonitrile, and toluene among others), a thermal polymerization, methacrylic acid as monomer and ethylene glycol dimethacrylate as cross linker.¹⁵⁷ The preparation of the composite requires a couple of days, that in fact represents a normal synthesis time for MIPs, including purification step of the bulk material. They studied different solvents in different conditions in order to obtain optimized conditions for the solid phase extraction. Finally, they were able to confirm that MIP prepared with acetonitrile has the highest affinity to chlorpyrifos when tested in water, and in comparison, with MIPs made with other organic solvents. In this investigation, they test how the type of solvent used during polymerization step effects on the affinity of the polymers. Successful extraction and pre-concentration of the pesticide in real samples of water were achieved by this team using MIP and acetonitrile as solvent. Finally, the MIP was tested with other pesticides and achieved good results in terms of selectivity, demonstrating that the developed MIP with the

appropriate solvent is a good candidate for solid phase extraction of this pesticide. This work developed by *Binsalom et al.* has an enormous potential in terms of selectivity and sensibility for a given analyte.

Organophosphorus pesticides are one of the most problematic and common compounds we can find in the environment. *Zhu et al.* have developed a method in which a MIP is used for organophosphorus detection in water and soil using solid phase extraction.¹⁵⁸ The MIP used in this work is a conventional template obtained with the analyte, methacrylic acid and ethilenglycoldimethacrylate using azobisisobutyronitrile as radical initiator. They obtained interesting results in extraction of the analyte from water-based samples (77.5–99.1%) and soil (79.3–93.5%).

Liu et al create a MIP combined with fluorescence properties and magnetic nanoparticles for detection of atrazine.¹⁵⁹ Atrazine is an herbicide of the triazine class, after 2001,¹⁶⁰ was the most commonly detected pesticide contaminating in drinking water on the United States. Liu's method for the detection of atrazine in tap water relies on the direct competition between atrazine and 5-(4,6-dichlorotriazinyl) using MIP technology to selective recognition of atrazine. The limit of detection (LOD) of atrazine determined in spiked tap water was 0.86 $\mu\text{mol/L}$, this limit is within the range of contaminant of this type that can be present in drinking water. The method is user friendly and is easy to manipulate in terms of equipment and techniques.

MIPs can be extrapolated to be used in other classical analytical methods, including high pressure liquid chromatography (HPLC). In fact, *Bakas et al.* developed a MIP for the detection of fenthion in olive oil using HPLC as detection system and they are able to achieve detection limits of 0,41 $\text{ng}\cdot\text{g}^{-1}$.¹⁶¹ If we compare the LOD obtained by *Bakas et al.* with other methods, for example, with square wave voltammetry it is possible to achieve until 78,8 $\text{ng}\cdot\text{g}^{-1}$, whereas gas chromatography achieves detection limits of 0.002 $\text{ng}\cdot\text{g}^{-1}$. Although the detection limit achieved by analytical methods such as gas chromatography are lower than those obtained with MIP technique, the usage of MIPs in HPLC decreases the cost and it becomes easy to handle given other advantageous points to considerer, as for example stability, can be used for different analyte size, and stronger to extreme conditions; as pH, temperature.

1.2.2 Nanomaterials and Molecularly Imprinted technology.

Molecular imprinted nanomaterials are excellent candidates to fabricate sensing layers. There are two great advantages to considerer using this couple of materials, including high surface area and small size. In fact, precipitation, emulsion, free radical polymerization and core-shell approaches are the most common techniques for synthesizing MIPs at the nanoscale.

If we move on to a practical example, it is worth mentioning that currently the fabrication of imprinted nanospheres can be achieved via precipitation polymerization. In fact, Wei *et al.* were able to synthesize micro and nanospheres in a one-step reaction for the detection of 17 β -estradiol (see Figure 1.11). Wei *et al.*, controlled the size of the sphere (ranging from 3 μ m to 400 nm) during the polymerization reaction, with different monomer concentration and temperature¹⁶². They also demonstrated the potential of the nanomaterial in HPLC separation and achieved sufficient molecular selectivity for the separation of optical isomers and analogue structures. Moreover, the developed imprinted microspheres demonstrated a better behavior compared to other conventional methods to prepare bulk polymers or microspheres, for instance they use the multi- step polymerization. The microspheres developed by Wei *et al* represent a perfect alternative for separation of estradiol, and can be extrapolated to other compounds.

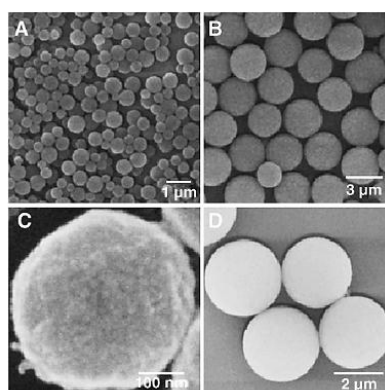


Figure 1.11. Scanning electron microscopy images, of micro (A) and nanospheres (B).

Reprinted with permission from Wei *et al.* (2006), Copyright 2006 Elsevier

Other alternative to combine nanomaterials with MIPs is the surface imprinting technique, where it is possible to print the complex over surfaces such as screen printed electrodes,¹⁶³ plastics,¹⁶⁴ or other biological/inorganic particles.¹⁶⁵

Surface imprinting is also an emerging technology in chemical sciences, with applications in many different fields, ranging from medical diagnostic to environmental monitoring. The work developed by *Cumbo et al.* (see Figure 1.12) established a novel imprinted polymer by using a strategy starting from an artificial organic-inorganic nanoparticle material which possesses the virus imprinted on to the surface (silica nanoparticles), thus creating a virus imprinted polymer.¹⁶⁶ The developed MIP has an excellent selectivity through its recognition elements for icosahedral plant viruses. The MIP also has a sensitivity at the pM order and the possibility to export this technique to all the icosahedral viruses.

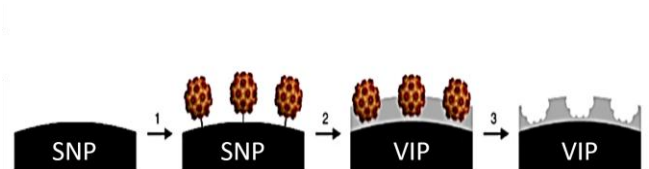


Figure 1.12. Scheme of composite preparation imprinted over silica nanoparticles. Reprinted with permission from *Cumbo et al. (2013)*, Copyright 2013 Nature Publishing Group

All these examples show us how nanomaterials involved with MIPs technique represent a great advantage for many fields, thanks to its great sensibility and selectivity. Nowadays MIPs can be improved in so many aspects, regarding monomers, temperature, solvents...etc, and use more broadly with biological compounds to go one step further in detection, separation, etc.

1.2.3 Electrochemical sensing applications.

Taking advantages of the previously discussed features, the usage of MIPs combined with electrochemistry can give excellent results in terms of detection limits. Furthermore, electrochemistry is a low cost technique and can be easily miniaturized.^{167–169} In fact, compounds representing a risk for human health such as pesticides, pollutants, food contaminants, proteins or different chemical compounds can also be detected using electrochemistry as a detection technique and MIPs as biomimetic receptors with excellent results. For instance, *Lakshmi et al.* reported the detection of catechol and dopamine using an electrochemical sensor based in a catalytic molecular imprinted polymer (see Figure 1.13).¹⁷⁰ Combining a catalytic MIP with a conductive polymer they were able to solve the lack of a direct path for the conduction of electrons from active sites to the electrode. In the scheme of the preparation of this novel MIP, the monomer NPEDMA (N-phenylethylene diamine methacrylamide, used as the interface between the MIP catalyst and gold electrode, is electrochemically deposited onto the electrode surface. With this technique, the LOD obtained by this group was 228 nM of catechol, which is an impressive improvement if we compare this LOD with others obtained by different methods, generally in a range of μM .

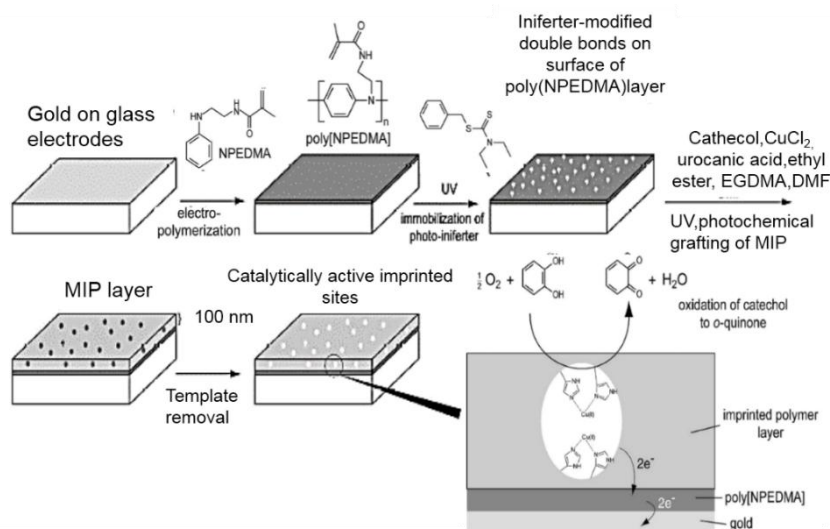


Figure 1.13. Schematic representation of Catalytic MIP-Hybrid Electrodes Imprinted with Catechol. Reprinted with permission from Lakshmi et al. (2009), Copyright 2009 American Chemical Society.

The exposition by short/long term periods to explosive compounds has consequences in health, environment and security risk. Hence, there is also a need to measure and quantify

these compounds. *Alizadeh et al.* reported an electrochemical approach for the detection of 2,4,6-trinitrotoluene.¹⁷² Common techniques for the detection of this molecule relies on the use of chemically modified electrodes (with moderate selectivity) or electrochemical immunosensors, but this kind of sensors have the problem of a high cost for antibodies and poor stability. As discussed above, in order to solve these drawbacks, MIPs are introduced instead of antibodies. The MIP developed by this group was formed onto a carbon paste electrode by conventional methods using methacrylic acid, ethylene glycol dimethacrylate and AIBN (azobisisobutyronitrile) as radical initiator to start the polymerization reaction.

This method has a LOD of 0.3 ppb and compared with other approaches based on chemiluminescent immunoassays (with a LOD of 1 µg/mL, that is, 1000ppb) or wave fiber optic (with a LOD of 8 ppb), one can note the contribution of MIPs in biosensing.

MIPs related to electrochemical methods can be applied for pesticide detection. There are different families inside pesticides, such us fungicides, herbicides, insecticides.... etc. Inside each type of the pesticide family, exist hundreds of different categories, one of the most common are organophosphorus, chlorinated or phenoxy groups. These three classes are present in a wide range of pesticides spectra and an environmental/health necessity to control this kind of compounds exists.

Regarding chlorinated pesticides, one of the most common is dicloran. This molecule is used as fungicide, inhibiting the fungal spore germination. An exposition to dicloran can produce hyperpyrexia, liver damage and corneal opacities. One example for dicloran detection was developed by *Khadem et al*¹⁷³. The MIP synthesized by this group is made of MAA, EGDMA and AIBN as radical initiator, mixing this with different parts of graphite and introducing it onto the surface of a carbon paste electrode and without any special pretreatment being directly measured by voltammetry technique. The detection limit obtained by this method was $4.8 \cdot 10^{-10} \text{ mol} \cdot \text{L}^{-1}$. Comparing this LOD with other methods this represent an improvement in terms of selectivity and handling/cost effectiveness.

There are many examples of organophosphorus detection using MIPs and electrochemistry. For example glyphosate detection, maybe the most used herbicide in the world; the group of *Huy Do et al*¹⁷⁴ developed a MIP with a high sensitivity for glyphosate, being able to quantify 0.8 pg/L even in real samples.

Methodathion, is another insecticide really common nowadays. This kind of compounds has the ability to inhibit the action of acetylcholinesterase, in consequence may result in respiratory malfunctions. *Idriss Bakas et al*¹⁷⁵ developed an impedimetric sensor based on molecular imprinted polymer/sol-gel chemistry. They combine the MIP and sol-gel technique with screen printed carbon electrodes; an inexpensive, portable and disposable technology. The developed sensor of this group exhibits excellent analytical performances in terms of selectivity and sensibility and possess high stability.

Continuing with organophosphorus compounds, diazinon pesticide is a non-synthetic organophosphate used as insecticide in agriculture. The problem with this pesticide is the inhibition of acetylcholinesterase and causes headache, dizziness, convulsion, delirium and depression. *Motaharian et al*¹⁷⁶synthetize a conventional MIP using MAA and EGDMA and mixed with carbon paste electrodes. The experiment was performed by square wave voltammetry and tested in real samples as well water and apple fruit. The sensor presented by Motaharian et al has long term stability, easy preparation and electrode regeneration providing rapid and economical method to measure.

The last example of organophosphorus we are going to present is methyl parathion. This pesticide is widely used in agriculture production, and has a high toxicity, and the regulations for maximum amount of this compound are 0,1 mg/kg in the case of China. The group of *Lijuan Zhao et al*¹⁷⁷develop a composite of graphene/ MIP in coated electrode for electrochemical detection. The glassy carbon electrode combines advantages of MIP, ionic liquid and graphene oxide. The composite was tested in two ways, cyclic voltammograms (CV) and differential pulse voltammograms (DPV) exhibiting excellent reproducibility, sensibility and high stability, in buffer and in real samples, and for the last one they tested cabbage and apple peel and the recovery obtained for each one is acceptable.

1.2.4 Optical applications of molecularly imprinted polymers.

Optical techniques involving MIPs-based sensors are scarcely explored. However, they also have some important advantages, such as cost-effectiveness, they are fast and do not necessarily need well-trained staff, while they can also be easily converted in portable devices.

Zhor et al. designed a composite material incorporating nanomaterials such as graphene quantum dots embedded in a MIP matrix coating magnetic silica beads (see Figure 1.14).¹⁷⁸ The composite was created to detect tributyltin, which is a hazardous antifouling compound (see Figure 1.14).

The sensing principle of this analytical approach is based on energy transfer. Tributyltin, an organometallic compound, quenches the photoluminescence of the graphene quantum dots, upon binding on the MIP, thus obtaining an off state in the presence of the analyte and an on state in absence of the target. Based on this, high concentrations of the analyte present a lower photoluminescent intensity, whereas low concentrations of the analyte yield a weak quenching phenomenon. The composite was also tested in real sample analysis, including seawater with good recovery (between 92-114%) and without any sample pretreatment process. With the aim to investigate the specificity and selectivity, the analytical system was tested using possible interferences, including monobutyltin and dibutyltin, observing that the composite offers excellent selectivity. This approach achieved a LOD of 12.78 ppb in water and 42.56 ppb in seawater. This is also an excellent example of how the integration of (optically active) nanomaterials and MIPs into biosensing technology leads to outstanding analytical approaches.

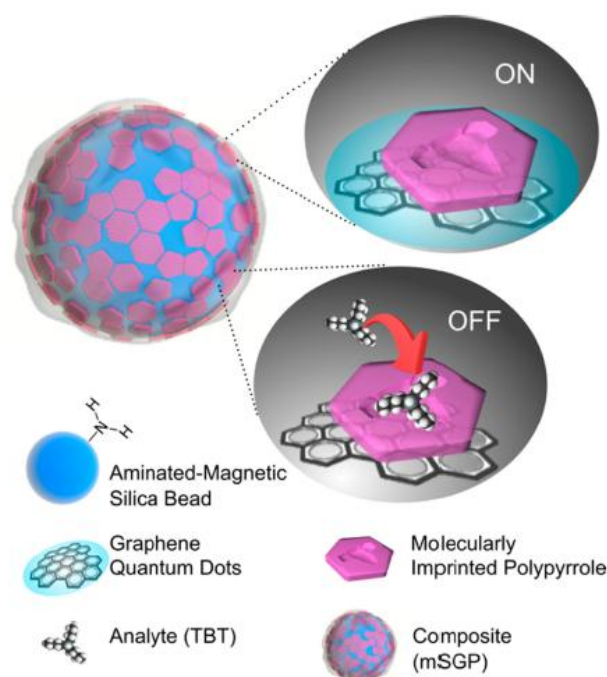


Figure 1.14. Schematic representation of the mSGP composite and its sensing mechanism.

MIPs can be used as substitutive for antibodies or enzymes in ELISA measurements, as an example of this idea is the work developed by *Piletsky et al*¹⁷⁹ for detection of atrazine in

which they perform an oxidative polymerization, in the presence of template; monomers: 3-aminophenylboronic acid (APBA), 3-thiopheneboronic acid (TBA) and aniline were polymerized in water and the polymers were grafted onto the polystyrene surface of the microplates. With this system they use the MIP grafted on to microplate to perform fluorescence measurements, the idea is that the atrazine binding was measured using a competitive reaction between fluorescent triazine derivative 5-(4,6-dichlorotriazinyl)amino fluorescein (FT) conjugate and free analyte. The LOD of this developed system was 0.7 μM , this limit of detection not represents and improvement in this field, but is possible to say that is a beginning of a really promising technique.

It is possible to say that the use of MIPs with optical techniques, as it could be the fluorescence, is not very exploited, however combining these two techniques can obtain very interesting results, being a technique of future.

1.4. Conclusions

This chapter gives a brief overview of the usage of nanomaterials combined with different receptors with interest in building sensors and biosensors. Two important receptors, antibodies and MIPs, and their connection with some interesting nanomaterials are discussed. The synergy between nanomaterials and mentioned receptors is clearly shown in the improvement of different existing detection systems in terms of reproducibility, selectivity and sensibility in addition of the design of brand new detection systems with certain advantages.

In the chapter are described two main technologies that have been already combining nanomaterials and receptors, lateral flow immunoassay and molecular imprinting polymers. LFA is an excellent biosensing technology to be used as a point of care device. It represents a cost efficient platform as it is related to a rather cheap technology, quick assay in addition of being robust enough and doesn't need washing steps. In parallel MIPs has one important advantage compared to antibodies or enzymes, because these non-biological receptors are cheaper in comparison to antibodies, stable and robust.

The developed LFA and MIPs-based detection systems are applied in different areas that include health and environment diagnostics as well as safety and security. Although results in the lab are satisfactory further efforts must be shown in the integration of all the sensing

components so as to achieve compact and easy to use devices. Issues related to sensors reproducibility are strongly related to nanometrology affecting nanomaterials in addition to biometrology that control the quality of receptors. All these aspects are critical for further industrialization/mass production of these devices.

1.5 References

- (1) Liu, S.; Zheng, Z.; Wei, F.; Ren, Y.; Gui, W.; Wu, H.; Zhu, G. *J. Agric. Food Chem.* **2010**, *58* (6), 3271–3278.
- (2) Medina-sánchez, M.; Mayorga-martinez, C. C.; Watanabe, T.; Ivandini, T. A.; Honda, Y.; Pino, F.; Nakata, K.; Fujishima, A.; Einaga, Y.; Merkoçi, A. *Biosens. Bioelectron.* **2016**, *79*, 946.
- (3) Zamora-Gálvez, A.; Ait-Lahcen, A.; Mercante, L. A.; Morales-Narváez, E.; Amine, A.; Merkoçi, A. *Anal. Chem.* **2016**, *88* (7), 3578–3584.
- (4) Mayorga-Martinez, C. C.; Pino, F.; Kurbanoglu, S.; Rivas, L.; Ozkan, S. A.; Merkoçi, A. *J. Mater. Chem. B* **2014**, *2* (16), 2233.
- (5) Rivas, L.; Mayorga-Martinez, C. C.; Quesada-González, D.; Zamora-Gálvez, A.; de la Escosura-Muñiz, A.; Merkoçi, A. *Anal. Chem.* **2015**, *87* (10), 5167–5172.
- (6) Arora, P.; Sindhu, A.; Dilbaghi, N.; Chaudhury, A. *Biosens. Bioelectron.* **2011**, *28* (1), 1–12.
- (7) Mehrotra, P. J. *Oral Biol. Craniofacial Res.* **2016**, *6* (2), 153–159.
- (8) Turner, A. P. F. *Chem. Soc. Rev.* **2013**, *42* (8), 3184–3196.
- (9) Zhu, C.; Yang, G.; Li, H.; Du, D.; Lin, Y. *Anal. Chem.* **2015**, *87* (1), 230–249.
- (10) Vikesland, P. J.; Wigginton, K. R. *Environ. Sci. Technol.* **2010**, *44* (10), 3656–3669.
- (11) Amano, Y.; Cheng, Q. *Anal. Bioanal. Chem.* **2005**, *381* (1), 156–164.
- (12) Alvarez, M.; Calle, A.; Tamayo, J.; Lechuga, L. M.; Abad, A.; Montoya, A. *Biosens. Bioelectron.* **2003**, *18* (5–6), 649–653.
- (13) Colvin, V. L. *Nat. Biotechnol.* **2003**, *21* (10), 1166–1170.
- (14) Grieger, K. D.; Linkov, I.; Hansen, S. F.; Baun, A.; Grieger, K. D.; Linkov,

- I.; Hansen, S. F.; Baun, A. **2016**, 5390 (November).
- (15) Dimetry, N. Z.; Hussein, H. M. *Int. J. PharmTech Res.* **2016**, 9 (10), 121–144.
- (16) Navrotsky, A. *J. Nanoparticle Res.* **2000**, 321–323.
- (17) Jain, A.; Ranjan, S.; Dasgupta, N.; Ramalingam, C. *Crit. Rev. Food Sci. Nutr.* 0 (ja), 0.
- (18) Khot, L. R.; Sankaran, S.; Maja, J. M.; Ehsani, R.; Schuster, E. W. *Crop Prot.* **2012**, 35, 64–70.
- (19) Holzinger, M.; Le Goff, A.; Cosnier, S. *Front. Chem.* **2014**, 2 (August), 63.
- (20) Klaine, S. J.; Alvarez, P. J. J.; Batley, G. E.; Fernandes, T. F.; Handy, R. D.; Lyon, D. Y.; Mahendra, S.; McLaughlin, M. J.; Lead, J. R. *Environ. Toxicol. Chem.* **2008**, 27 (9), 1825–1851.
- (21) Wang, J. **2005**, No. i, 421–426.
- (22) Solanki, A.; Kim, J. D.; Lee, K.-B. *Nanomedicine* **2008**, 3 (4), 567–578.
- (23) Salata, O. V. *J. Nanobiotechnology* **2004**, 6 (3), 1–6.
- (24) Yao, J.; Yang, M.; Duan, Y. **2014**.
- (25) Chen, T.; Shukoor, M. I.; Chen, Y.; Yuan, Q.; Zhu, Z.; Zhao, Z.; Gulbakan, B.; Tan, W. *Nanoscale* **2011**, 3 (2), 546–556.
- (26) Hsing, I. M.; Xu, Y.; Zhao, W. *Electroanalysis* **2007**, 19 (7–8), 755–768.
- (27) Connolly, J.; St Pierre, T. G. *J. Magn. Magn. Mater.* **2001**, 225 (1–2), 156–160.
- (28) Russell, R. J.; Pishko, M. V.; Gefrides, C. C.; McShane, M. J.; Cote, G. L. *Anal. Chem.* **1999**, 71 (15), 3126–3132.
- (29) Brahim, S.; Narinesingh, D.; Guiseppi-Elie, A. *Biosens. Bioelectron.* **2002**, 17 (1–2), 53–59.
- (30) Slowing, I. I.; Trewyn, B. G.; Giri, S.; Lin, V. S. Y. *Adv. Funct. Mater.* **2007**, 17 (8), 1225–1236.
- (31) Besteman, K.; Lee, J. O.; Wiertz, F. G. M.; Heering, H. A.; Dekker, C. *Nano Lett.* **2003**, 3 (6), 727–730.
- (32) Wang, J.; Musameh, M.; Lin, Y. J. *Am. Chem. Soc.* **2003**, 125 (9), 2408–2409.
- (33) Raston, C. L. **2013**, 49 (12).

- (34) Narayanan, T. N.; Gupta, B. K.; Vithayathil, S. A.; Aburto, R. R.; Mani, S. A.; Taha-Tijerina, J.; Xie, B.; Kaipparettu, B. A.; Torti, S. V.; Ajayan, P. M. *Adv. Mater.* **2012**, *24* (22), 2992–2998.
- (35) Malmsten, M. *Curr. Opin. Colloid Interface Sci.* **2013**, *18* (5), 468–480.
- (36) Zelzer, M.; Ulijn, R. V. *Chem. Soc. Rev.* **2010**, *39* (9), 3351–3357.
- (37) Lee, J. H.; Yigit, M. V.; Mazumdar, D.; Lu, Y. *Adv. Drug Deliv. Rev.* **2010**, *62* (6), 592–605.
- (38) Wang, G.; Wang, Y.; Chen, L.; Choo, J. *Biosens. Bioelectron.* **2010**, *25* (8), 1859–1868.
- (39) Yang, W.; Liu, S.; Bai, T.; Keefe, A. J.; Zhang, L.; Ella-Menye, J. R.; Li, Y.; Jiang, S. *Nano Today* **2014**, *9* (1), 10–16.
- (40) Cheng, F.-Y.; Chen, C.-T.; Yeh, C.-S. *Nanotechnology* **2009**, *20* (42), 425104.
- (41) Lin, Y.; Ren, J.; Qu, X. *Acc. Chem. Res.* **2014**, *47* (4), 1097–1105.
- (42) Wei, H.; Wang, E. *Chem. Soc. Rev.* **2013**, *42* (14), 6060.
- (43) Chen, X.; Mao, S. S. **2007**.
- (44) Wu, H.; Wang, J.; Kang, X.; Wang, C.; Wang, D.; Liu, J.; Aksay, I. A.; Lin, Y. *Talanta* **2009**, *80* (1), 403–406.
- (45) Kang, X.; Mai, Z.; Zou, X.; Cai, P.; Mo, J. *Anal. Biochem.* **2007**, *369* (1), 71–79.
- (46) Chen, S.; Yuan, R.; Chai, Y.; Zhang, L.; Wang, N.; Li, X. *Biosens. Bioelectron.* **2007**, *22* (7), 1268–1274.
- (47) Sharma, R. K.; Sharma, S.; Dutta, S.; Zboril, R.; Gawande, M. B. *Green Chem.* **2015**, *17* (6), 3207–3230.
- (48) Biju, V. *Chem. Soc. Rev.* **2014**, *43* (3), 744–764.
- (49) Zou, J.; Hew, C. C.; Themistou, E.; Li, Y.; Chen, C.-K.; Alexandridis, P.; Cheng, C. *Adv. Mater.* **2011**, *23* (37), 4274–4277.
- (50) Zamani, M.; Prabhakaran, M. P.; Ramakrishna, S. *Int. J. Nanomedicine* **2013**, *8*, 2997–3017.
- (51) Takahashi, S.; Sato, K.; Anzai, J. *Anal. Bioanal. Chem.* **2012**, *402* (5), 1749–1758.
- (52) Choi, A.; Kim, K.; Jung, H.-I.; Lee, S. Y. *Sensors Actuators B Chem.* **2010**, *148* (2), 577–582.

- (53) Withers, G. S.; Zoback, M. D.; Apel, R.; Baumgartner, J.; Brudy, M.; Emmermann, R.; Engeser, B.; Fuchs, K.; Kessels, W.; Rischmuller, H.; Rummel, F.; Vernlk, L. *Nat. Lett.* **1993**, 363.
- (54) Galfrè, G.; Milstein, C. 1981; pp 3–46.
- (55) Milstein, C.; Introduction, I. [1] *Preparation of Monoclonal Antibodies: Strategies and Procedures* By G. GALFRÌ ~ and C. MILSTEIN I. Introduction The derivation of cell lines capable of permanent production of specific antibody directed against a pred; 1981; Vol. 73.
- (56) Orange, J. S.; Hossny, E. M.; Weiler, C. R.; Ballow, M.; Berger, M.; Bonilla, F. A.; Buckley, R.; Chinen, J.; El-Gamal, Y.; Mazer, B. D.; Nelson, R. P.; Patel, D. D.; Secord, E.; Sorensen, R. U.; Wasserman, R. L.; Cunningham-Rundles, C. J. *Allergy Clin. Immunol.* **2006**, 117 (4 SUPPL.), 525–553.
- (57) HARBOE, N.; INGILD, A. *Scand. J. Immunol.* **1973**, 2, 161–164.
- (58) Chothia, C.; Lesk, A. M. *J. Mol. Biol.* **1987**, 196 (4), 901–917.
- (59) Potter, M.; Lieberman, R. *Adv. Immunol.* **1967**, 7, 91–145.
- (60) Schroeder, H. W.; Cavacini, L. J. *Allergy Clin. Immunol.* **2010**, 125 (2), S41–S52.
- (61) Chan, M. K.; Chan, K. W.; Jones, B. *Nephron* **1987**, 47 (2), 125–130.
- (62) Cooper, M. A. *Nat Rev Drug Discov* **2002**, 1 (7), 515–528.
- (63) Keusgen, M. *Naturwissenschaften* **2002**, 89 (10), 433–444.
- (64) Marty, J. L.; Garcia, D.; Rouillon, R. *Trends Anal. Chem.* **1995**, 14 (7), 329–333.
- (65) Ivnitski, D.; Abdel-Hamid, I.; Atanasov, P.; Wilkins, E. *Biosens. Bioelectron.* **1999**, 14 (7), 599–624.
- (66) Lazcka, O.; Campo, F. J. Del; Mu??oz, F. X. *Biosens. Bioelectron.* **2007**, 22 (7), 1205–1217.
- (67) Maltez-da Costa, M.; de la Escosura-Muñiz, A.; Nogués, C.; Barrios, L.; Ibáñez, E.; Merkoçi, A. *Nano Lett.* **2012**, 12 (8), 4164–4171.
- (68) Thakur, A.; Norkina, O.; Lum, L. G. *Cancer Immunol. Immunother.* **2011**, 60 (12), 1707–1720.
- (69) Weiner, L. M.; Surana, R.; Wang, S.

- Nat Rev Immunol* **2010**, *10* (5), 317–327.
- (70) Shao, N.; Wickstrom, E.; Panchapakesan, B. *Nanotechnology* **2008**, *19* (46), 465101.
- (71) Xu, J.; Suarez, D.; Gottfried, D. S. *Anal. Bioanal. Chem.* **2007**, *389* (4), 1193–1199.
- (72) Arya, S. K.; Kongsuphol, P.; Wong, C. C.; Polla, L. J.; Park, M. K. *Sensors Actuators, B Chem.* **2014**, *194*, 127–133.
- (73) Spackman, E.; Suarez, D. L. In *Avian Influenza Virus*; Spackman, E., Ed.; Humana Press: Totowa, NJ, 2008; pp 19–26.
- (74) Reichert, A.; Nagy, J. O.; Spevak, W.; Charych, D. *J. Am. Chem. Soc.* **1995**, *117* (2), 829–830.
- (75) Pejicic, B.; Marco, R. De; Parkinson, G. *Analyst* **2006**, *131* (10), 1079–1090.
- (76) Haes, A. J.; Chang, L.; Klein, W. L.; Van Duyne, R. P. *J. Am. Chem. Soc.* **2005**, *127* (7), 2264–2271.
- (77) Jain, P. K.; Huang, X.; El-Sayed, I. H.; El-Sayed, M. A. *Plasmonics* **2007**, *2* (3), 107–118.
- (78) Homola, J.; Yee, S. S.; Gauglitz, G. *Sensors Actuators B Chem.* **1999**, *54* (1–2), 3–15.
- (79) Zhang, J.; Sun, Y.; Xu, B.; Zhang, H.; Gao, Y.; Zhang, H.; Song, D. *Biosens. Bioelectron.* **2013**, *45* (1), 230–236.
- (80) Chen, C.-D.; Cheng, S.-F.; Chau, L.-K.; Wang, C. R. C. *Biosens. Bioelectron.* **2007**, *22* (6), 926–932.
- (81) Yu, C.; Irudayaraj, J. *Anal. Chem.* **2007**, *79* (2), 572–579.
- (82) Kerman, K.; Saito, M.; Tamiya, E.; Yamamura, S.; Takamura, Y. *TrAC - Trends Anal. Chem.* **2008**, *27* (7), 585–592.
- (83) Yun, Y. H.; Eteshola, E.; Bhattacharya, A.; Dong, Z.; Shim, J. S.; Conforti, L.; Kim, D.; Schulz, M. J.; Ahn, C. H.; Watts, N. *Sensors* **2009**, *9* (11), 9275–9299.
- (84) Wang, J. *Biosens. Bioelectron.* **2006**, *21* (10), 1887–1892.
- (85) Tothill, I. E. *Semin. Cell Dev. Biol.* **2009**, *20* (1), 55–62.
- (86) Yang, W.; Ratinac, K. R.; Ringer, S. R.; Thordarson, P.; Gooding, J. J.; Braet, F. *Angew. Chemie - Int. Ed.* **2010**, *49* (12), 2114–2138.

- (87) Wang, E.; Casciano, C. N.; Clement, R. P.; Johnson, W. W. **2000**, *28* (5), 522–528.
- (88) Tsai, C. E.; Daood, M. J.; Lane, R. H.; Hansen, T. W. R.; Gruetzmacher, E. M.; Watchko, J. F. *Neonatology* **2002**, *81* (1), 58–64.
- (89) Chaudhary, P. M.; Roninson, I. B. *Cell* **1991**, *66* (1), 85–94.
- (90) Zhang, S.; Zhang, L.; Zhang, X.; Yang, P.; Cai, J. *Analyst* **2014**, *139* (14), 3629.
- (91) Quesada-González, D.; Merkoçi, A. *Biosens. Bioelectron.* **2015**, *73*, 47–63.
- (92) Posthuma-Trumpie, G. A.; Korf, J.; Van Amerongen, A. *Anal. Bioanal. Chem.* **2009**, *393* (2), 569–582.
- (93) Ngom, B.; Guo, Y.; Wang, X.; Bi, D. *Anal. Bioanal. Chem.* **2010**, *397* (3), 1113–1135.
- (94) Danks, C.; Barker, I. *EPPO Bull.* **2000**, *30* (3–4), 421–426.
- (95) Taranova, N. A.; Byzova, N. A.; Zaiko, V. V.; Starovoitova, T. A.; Vengerov, Y. Y.; Zherdev, A. V.; Dzantiev, B. B. *Microchim. Acta* **2013**, *180* (11), 1165–1172.
- (96) You, D. J.; Park, T. S.; Yoon, J.-Y. *Biosens. Bioelectron.* **2013**, *40* (1), 180–185.
- (97) Richter, B. D.; Warner, A. T.; Meyer, J. L.; Lutz, K. *River Res. Appl.* **2006**, *22* (3), 297–318.
- (98) Rong-Hwa, S.; Shiao-Shek, T.; Der-Jiang, C.; Yao-Wen, H. *Food Chem.* **2010**, *118* (2), 462–466.
- (99) Mao, X.; Ma, Y.; Zhang, A.; Zhang, L.; Zeng, L.; Liu, G. *Anal. Chem.* **2009**, *81* (4), 1660–1668.
- (100) Hu, J.; Wang, L.; Li, F.; Han, Y. L.; Lin, M.; Lu, T. J.; Xu, F. *Lab Chip* **2013**, *13* (22), 4352–4357.
- (101) Tang, D.; Saucedo, J. C.; Lin, Z.; Ott, S.; Basova, E.; Goryacheva, I.; Biselli, S.; Lin, J.; Niessner, R.; Knopp, D. *Biosens. Bioelectron.* **2009**, *25* (2), 514–518.
- (102) Qiu, W.; Xu, H.; Takalkar, S.; Gurung, A. S.; Liu, B.; Zheng, Y.; Guo, Z.; Baloda, M.; Baryeh, K.; Liu, G. *Biosens. Bioelectron.* **2015**, *64*, 367–372.
- (103) Radke, S. M.; Alocilja, E. C. *Biosens. Bioelectron.* **2005**, *20* (8 SPEC. ISS.), 1662–1667.
- (104) Abdel-Hamid, I.; Ivnitski, D.;

- Atanasov, P.; Wilkins, E. *Biosens. Bioelectron.* **1999**, *14* (3), 309–316.
- (105) Yang, H.; Li, D.; He, R.; Guo, Q.; Wang, K.; Zhang, X.; Huang, P.; Cui, D. *Nanoscale Res. Lett.* **2010**, *5* (5), 875–881.
- (106) Turiel, E.; Martín-Esteban, A. *Anal. Chim. Acta* **2010**, *668* (2), 87–99.
- (107) Haupt, K. *Anal. Chem.* **2003**, *75* (17), 376 A–383 A.
- (108) I. The, S. li, *Molecular Imprinted Polymers : a Review*, (n.d.).
- (109) Pichon, V.; Chapuis-Hugon, F. *Anal. Chim. Acta* **2008**, *622* (1–2), 48–61.
- (110) Tokonami, S.; Shiigi, H.; Nagaoka, T. *Anal. Chim. Acta* **2009**, *641* (1–2), 7–13.
- (111) Mahony, J. O.; Nolan, K.; Smyth, M. R.; Mizaikoff, B. *Anal. Chim. Acta* **2005**, *534* (1), 31–39.
- (112) Mayes, A. G.; Mosbach, K. *TrAC - Trends Anal. Chem.* **1997**, *16* (6), 321–332.
- (113) Kempe, M.; Glad, M.; Mosbach, K. *J. Mol. Recognit.* **1995**, *8* (1–2), 35–39.
- (114) Gao, B.; Wang, J.; An, F.; Liu, Q. *Polymer (Guildf)*. **2008**, *49* (5), 1230–1238.
- (115) Tan, C. J.; Tong, Y. W. *Anal. Bioanal. Chem.* **2007**, *389* (2), 369–376.
- (116) Cormack, P. A. .; Elorza, A. Z. *J. Chromatogr. B* **2004**, *804* (1), 173–182.
- (117) Haupt, K. *Analyst* **2001**, *126* (6), 747–756.
- (118) Caro, E.; Masqué, N.; Marcé, R. M.; Borrull, F.; Cormack, P. A. G.; Sherrington, D. C. *J. Chromatogr. A* **2002**, *963* (1–2), 169–178.
- (119) Haupt, K.; Mosbach, K. *Chem. Rev.* **2000**, *100* (7), 2495–2504.
- (120) Yano, K.; Karube, I. *TrAC - Trends Anal. Chem.* **1999**, *18* (3), 199–204.
- (121) Menger, M.; Yarman, A.; Erdőssy, J.; Yildiz, H. B.; Gyurcsányi, R. E.; Scheller, F. W. *Biosensors* **2016**, *6* (3).
- (122) Bossi, A.; Bonini, F.; Turner, A. P. F.; Piletsky, S. A. *Biosens. Bioelectron.* **2007**, *22* (6), 1131–1137.
- (123) Hansen, D. E. *Biomaterials* **2007**, *28* (29), 4178–4191.
- (124) Mayes, A. G.; Mosbach, K. *Anal. Chem.* **1996**, *68* (21), 3769–3774.
- (125) Ansell, R. J.; Mosbach, K. *Analyst*

- 1998**, 123 (7), 1611–1616.
- (126) Hua, Z.; Zhou, S.; Zhao, M. *Biosens. Bioelectron.* **2009**, 25 (3), 615–622.
- (127) Kimhi, O.; Bianco-Peled, H. *Langmuir* **2007**, 23 (11), 6329–6335.
- (128) Biswas, A.; Bayer, I. S.; Biris, A. S.; Wang, T.; Dervishi, E.; Faupel, F. *Adv. Colloid Interface Sci.* **2012**, 170 (1–2), 2–27.
- (129) Fuchs, Y.; Soppera, O.; Haupt, K. *Anal. Chim. Acta* **2012**, 717, 7–20.
- (130) Moad, G.; Rizzardo, E.; Solomon, D. H. *Polym. Bull.* **1982**, 6 (11), 589–593.
- (131) Hui, A. W.; Hamielec, A. E. *J. Appl. Polym. Sci.* **1972**, 16 (3), 749–769.
- (132) Dadashi-Silab, S.; Atila Tasdelen, M.; Yagci, Y. *J. Polym. Sci. Part A Polym. Chem.* **2014**, 52 (20), 2878–2888.
- (133) Living radical polymerizations ,(n.d.) 8850.
- (134) Adali-Kaya, Z.; Tse Sum Bui, B.; Falcimaigne-Cordin, A.; Haupt, K. *Angew. Chemie - Int. Ed.* **2015**, 54 (17), 5192–5195.
- (135) De Barros, L. A.; Martins, I.; Rath, S. *Anal. Bioanal. Chem.* **2010**, 397 (3), 1355–1361.
- (136) Tappura, K.; Vikholm-Lundin, I.; Albers, W. M. *Biosens. Bioelectron.* **2007**, 22 (6), 912–919.
- (137) Blanco-López, M. C.; Gutiérrez-Fernández, S.; Lobo-Castañón, M. J.; Miranda-Ordieres, A. J.; Tuñón-Blanco, P. *Anal. Bioanal. Chem.* **2004**, 378 (8), 1922–1928.
- (138) Pernites, R.; Ponnappati, R.; Felipe, M. J.; Advincola, R. *Biosens. Bioelectron.* **2011**, 26 (5), 2766–2771.
- (139) Minami, K.; Ihara, M.; Kuroda, S.; Tsuzuki, H.; Ueda, H. *Bioconjug. Chem.* **2012**, 23 (7), 1463–1469.
- (140) Subrahmanyam, S.; Piletsky, S. A.; Piletska, E. V.; Chen, B.; Karim, K.; Turner, A. P. F. *Biosens. Bioelectron.* **2001**, 16 (9–12), 631–637.
- (141) Kriz, D.; Kempe, M.; Mosbach, K. *Sensors Actuators B Chem.* **1996**, 33 (1–3), 178–181.
- (142) Ansell, R. J.; Kriz, D.; Mosbach, K. *Curr. Opin. Biotechnol.* **1996**, 7 (1), 89–94.
- (143) Turner, A.; Piletsky, S. *Electroanalysis* **2002**, 14, 317–323.

- (144) Cheng, Z.; Wang, E.; Yang, X. *Biosens. Bioelectron.* **2001**, *16* (3), 179–185.
- (145) Malitesta, C.; Losito, I.; Zambonin, P. G. *Anal. Chem.* **1999**, *71* (7), 1366–1370.
- (146) Yang, Y.; Yi, C.; Luo, J.; Liu, R.; Liu, J.; Jiang, J.; Liu, X. *Biosens. Bioelectron.* **2011**, *26* (5), 2607–2612.
- (147) Baggiani, C.; Trotta, F.; Giraudi, G.; Giovannoli, C.; Vanni, A. *Anal. Commun.* **1999**, *36* (7), 263–266.
- (148) Jenkins, A. L.; Yin, R.; Jensen, J. L. *Analyst* **2001**, *126* (6), 798–802.
- (149) Wu, J.; Mester, Z.; Pawliszyn, J. J. *Anal. At. Spectrom.* **2001**, *16* (2), 159–165.
- (150) Song, X.; Li, J.; Xu, S.; Ying, R.; Ma, J.; Liao, C.; Liu, D.; Yu, J.; Chen, L. *Talanta* **2012**, *99*, 75–82.
- (151) Rissato, S. R.; Galhiane, M. S.; Knoll, F. R. N.; Apon, B. M. *J. Chromatogr. A* **2004**, *1048* (2), 153–159.
- (152) Delgado, M. J. S.; Barroso, S. R.; Fernández-Tostado, G. T.; Polo-Díez, L. M. *J. Chromatogr. A* **2001**, *921* (2), 287–296.
- (153) Sarkar, P. K.; Prajapati, P. K.; Shukla, V. J.; Ravishankar, B.; Choudhary, A. K. *Indian J. Exp. Biol.* **2009**, *47* (12), 987–992.
- (154) Tamayo, F. G.; Casillas, J. L.; Martín-Esteban, A. *J. Chromatogr. A* **2005**, *1069* (2), 173–181.
- (155) Garcia, R.; Cabrita, M. J.; Maria, A.; Freitas, C. *Am. J. Anal. Chem.* **2011**, *2*, 16–25.
- (156) Mena, M. L.; Martínez-Ruiz, P.; Reviejo, A. J.; Pingarrón, J. M. *Anal. Chim. Acta* **2002**, *451* (2), 297–304.
- (157) A, B.; I, C.; K, C.; M, Z. *J. Chromatogr. Sep. Tech.* **2016**, *7* (6).
- (158) Zhu, X.; Yang, J.; Su, Q.; Cai, J.; Gao, Y. *J. Chromatogr. A* **2005**, *1092* (2), 161–169.
- (159) Pan, J.; Xu, L.; Dai, J.; Li, X.; Hang, H.; Huo, P.; Li, C.; Yan, Y. *Chem. Eng. J.* **2011**, *174* (1), 68–75.
- (160) Solomon, K. R.; Carr, J. A.; Du Preez, L. H.; Giesy, J. P.; Kendall, R. J.; Smith, E. E.; Van Der Kraak, G. J. *Crit. Rev. Toxicol.* **2008**, *38* (9), 721–772.
- (161) A, B.; I, C.; K, C.; M, Z. *J. Chromatogr. Sep. Tech.* **2016**, *7* (6).
- (162) Wei, S.; Molinelli, A.; Mizaiakoff, B.

- Biosens. Bioelectron.* **2006**, *21* (10), 1943–1951.
- (163) Renedo, O. D.; Alonso-Lomillo, M. A.; Martínez, M. J. A. *Talanta* **2007**, *73* (2), 202–219.
- (164) Martynova, L.; Locascio, L. E.; Gaitan, M.; Kramer, G. W.; Christensen, R. G.; MacCrehan, W. a. *Anal. Chem.* **1997**, *69* (23), 4783–4789.
- (165) Fang, G. Z.; Tan, J.; Yan, X. P. *Anal. Chem.* **2005**, *77* (6), 1734–1739.
- (166) Cumbo, A.; Lorber, B.; Corvini, P. F.-X.; Meier, W.; Shahgaldian, P. *Nat. Commun.* **2013**, *4*, 1503.
- (167) Yang, G.; Zhao, F. *Biosens. Bioelectron.* **2015**, *64*, 416–422.
- (168) Zhang, X.; Peng, Y.; Bai, J.; Ning, B.; Sun, S.; Hong, X.; Liu, Y.; Liu, Y.; Gao, Z. *Sensors Actuators B Chem.* **2014**, *200*, 69–75.
- (169) Li, Y.; Liu, Y.; Liu, J.; Liu, J.; Tang, H.; Cao, C.; Zhao, D.; Ding, Y. *Sci. Rep.* **2015**, *5*, 7699.
- (170) Lakshmi, D.; Bossi, A.; Whitcombe, M. J.; Chianella, I.; Fowler, S. a.; Subrahmanyam, S.; Piletska, E. V.; Piletsky, S. a. *Anal. Chem.* **2009**, *81* (9), 3576–3584.
- (171) Zamora-G??lvez, A.; Ait-Lahcen, A.; Mercante, L. A.; Morales-Narv??ez, E.; Amine, A.; Merko??i, A. *Anal. Chem.* **2016**, *88* (7), 3578–3584.
- (172) Alizadeh, T.; Zare, M.; Ganjali, M. R.; Norouzi, P.; Tavana, B. *Biosens. Bioelectron.* **2010**, *25* (5), 1166–1172.
- (173) Khadem, M.; Faridbod, F.; Norouzi, P.; Foroushani, A. R.; Ganjali, M. R.; Shahtaheri, S. J. *J. Iran. Chem. Soc.* **2016**, *13* (11), 2077–2084.
- (174) Do, M. H.; Florea, A.; Farre, C.; Bonhomme, A.; Bessueille, F.; Vocanson, F.; Tran-Thi, N.-T.; Jaffrezic-Renault, N. *Int. J. Environ. Anal. Chem.* **2015**, *95* (15), 1489–1501.
- (175) Bakas, I.; Hayat, A.; Piletsky, S.; Piletska, E.; Chehimi, M. M.; Noguier, T.; Rouillon, R. *Talanta* **2014**, *130*, 294–298.
- (176) Motaharian, A.; Motaharian, F.; Abnous, K.; Hosseini, M. R. M.; Hassanzadeh-Khayyat, M. *Anal. Bioanal. Chem.* **2016**, *408* (24), 6769–6779.
- (177) Zhao, L.; Zhao, F.; Zeng, B. *Sensors Actuators, B Chem.* **2013**, *176*, 818–

- 824.
- (178) Zor, E.; Morales-Narváez, E.; Zamora-Gálvez, A.; Bingol, H.; Ersoz, M.; Merkoçi, A. *ACS Appl. Mater. Interfaces* **2015**, *7* (36), 20272–20279.
- (179) Piletsky, S. A.; Piletska, E. V.; Bossi, A.; Karim, K.; Lowe, P.; Turner, A. P. *F. Biosens. Bioelectron.* **2001**, *16* (9–12), 701–707.

CHAPTER 2

Thesis Objectives

The main objective of this PhD thesis is the development of innovative electrochemical and optical sensing platforms through the use of nanoparticles (Fe_3O_4 NPs and quantum dots, QDs) and 2D materials (graphene oxide, GO) connected to non-biological and biological receptors with interest for diagnostics applications.

More in details the objectives of this thesis can be summarized as following:

- Synthesis and characterization of magnetic nanoparticles to be used as template for molecularly imprinted polymers (MIPs) production.
- Fabrication and study of two different MIPs specific for tributyltin and sulfonamide.
- Implementation of tributyltin and the sulfonamide electrochemical sensors using the corresponding MIPs and electrochemical impedance spectroscopy (EIS) as a transduction method.
- Study and evaluation of the analytical performance of tributyltin and the sulfonamide electrochemical sensors in terms of reproducibility, range of response, selectivity, and sensitivity including their applicability in real samples.
- Development of an innovative lateral flow immunoassay (LFA) based on the use of QDs, GO and photoluminescence measurements for protein detection.
- Optimization and evaluation of the developed LFA in a complex matrix including a human serum

CHAPTER 3

Development of a molecularly imprinted polymer decorated with magnetite nanoparticles for selective sulfonamide detection.

Related publication

1) *Anal. Chem.* 2016, 88, 3578–3584

3.1 Introduction

Since the mid-twentieth century, sulfonamides have been extensively exploited as antimicrobial agents in humans and animals.¹⁻³ On the one hand, it is well-known that the use of antibiotics leads to antimicrobial resistance, which is an international serious concern.⁴ On the one hand, sulfonamides have been reported not only to elicit dermatological eruptions,⁵ but also to be potentially carcinogenic among other health consequences.^{2,3} On the other hand, medical treatments, livestock and aquaculture operations of an exponentially growing human population have a great demand for sulfonamides compounds, which may reach the environment through wastewater from pharmaceutical or food chains involving human and animal waste. In fact, it is estimated that every year more than 20 thousand tons of sulfonamides reach the global environment.¹ Therefore, as a potential health threat, highly sensitive monitoring of sulfonamide residues is relevant to enforce food safety and environmental quality.

Dmitrienko et al. have recently performed a broad study on the recent trends towards sulfonamides detection.¹ Sulfonamide residues are generally screened using time-consuming but highly sensitive, robust and reliable methods involving complex apparatus operated by skilled personnel; for instance, liquid chromatography,^{6,7} mass spectrometry^{8,9} or capillary electrophoresis.^{10,11} Consequently, alternative antibiotic residues screening methods such as immunoassays and biosensing platforms are rising considerably.³ These alternatives are leading to a promising analytical performance in terms of sensitivity; for example, they bear limits of detection of up to 5×10^{-2} ppb.¹ However, they have not been reported to be as sensitive and have limits of detection as those achieved by solid-phase extraction working in synergy with liquid chromatography/mass spectrometry, which has been reported to be up to 9×10^{-5} ppb.¹

Biosensing technology incorporates biorecognition elements integrated with a transducing system that leads to a specific signal upon analyte recognition. The signal can be optical, electrochemical or mechanical among others; whereas enzymes, antibodies, oligonucleotides or other biomolecules can be exploited as biorecognition elements. However, biosensing technology is also taking advantage of biomimetic recognition elements such as molecularly imprinted polymers (MIPs),^{12,13} for example when biorecognition elements targeting small molecules are technically difficult to obtain.¹⁴ MIPs are synthetic polymers typically obtained

by copolymerization of a monomer with a cross-linker in the presence of a template molecule.¹⁵ The shape, size, and functionalities of MIPs are complementary to the target analyte, which is used as template molecule. Consequently, they can selectively recognize and bind specific target molecules through non-covalent strength interactions between the host matrix and the guest molecule, including Van der Waals force, hydrogen bonding, electrostatic features, hydrophobic phenomena and metal-ion coordination.¹⁶

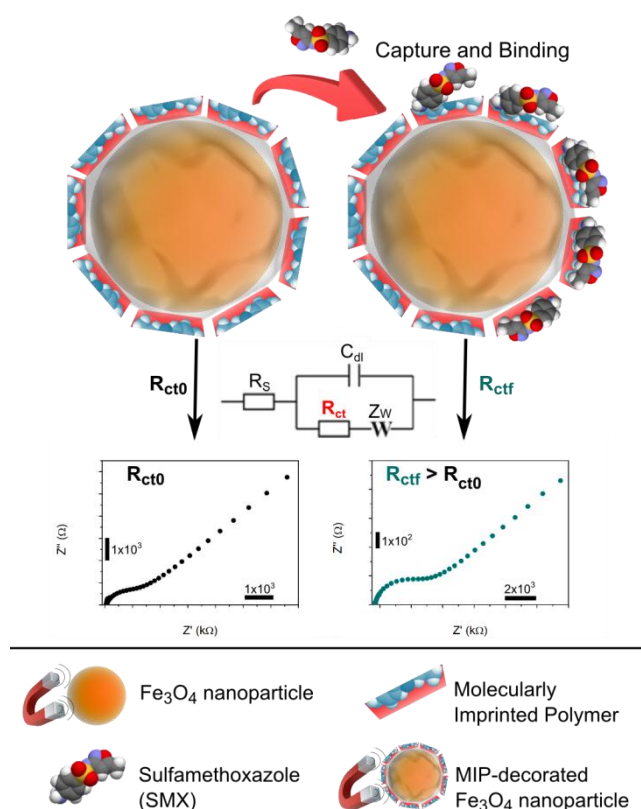


Figure 3.1. Schematic representation of the proposed nano-enabled sensing system. The proposed system operates via electrochemical impedance spectroscopy. Abbreviations: R_s is the electrolyte resistance, C_{dl} is the interface capacitance, R_{ct} is the charge (electron) transfer resistance and Z_w is the Warburg impedance.

Herein, a composite material based on molecularly imprinted polymer (MIP) and Fe_3O_4 superparamagnetic nanoparticles (MNPs) that is designed to specifically detect sulfamethoxazole^{17–21} (SMX) with extraordinary sensitivity is reported. Scanning electron

microscopy (SEM), transmission electron microscopy (TEM), X-ray photoelectron spectroscopy (XPS) and Fourier transform infrared spectroscopy (FT-IR) have been utilized to characterize the proposed hybrid material. The superparamagnetic properties of the composite are utilized to pre-concentrate, separate and manipulate the analyte which is selectively captured by the MIP onto the surface of the composite. On the other hand, disposable screen printed electrodes, have been used to monitor the impedance levels of the whole material, which is related to the amount of the captured analyte via electrochemical impedance spectroscopy, facilitating a simple and label-free sensing platform (see Figure 3.1).

3.2 Experimental section.

3.2.1 Reagents and materials

Sulfamethoxazole, sulfadiazine, sulfacetamide, dimethyl sulfoxide, acetic acid, methacrylic acid, iron chloride (II), iron chloride (III), ammonium hydroxide, polyvinylpyrrolidone, oleic acid, 2,5-Bis(tertbutylperoxy)-2,5dimethylhexane, potassium hexacyanoferrate (II) and potassium hexacyanoferrate (III) were purchased from Sigma-Aldrich (Madrid, Spain). Methanol was purchased from Labbox (Vilassar de Dalt, Barcelona, Spain). Stock solutions of sulfamethoxazole, sulfadiazine and sulfacetamide were prepared in methanol/water (1:1, v/v). Seawater samples were extracted from Poblenou Beach (Barcelona, Spain). Seawater samples were filtered using filter paper and then a nitrocellulose membrane (0.025 μm , Millipore, Billerica, Massachusetts, USA). TEM analysis was performed using a FEI TECNAI G2 F20 (Hillsboro, Oregon, USA). XPS analysis was carried out with a Phoibos 150 analyzer (SPECS GmbH, Berlin, Germany) in ultrahigh vacuum conditions (1×10^{-10} mbar) with a monochromatic aluminum K-alpha ($K\alpha$) X-ray source (1486.74 eV). The energy resolution (0.58 eV) was measured by the full width at half-maximum intensity of the Ag 3d_{5/2} peak for a sputtered silver foil. SEM analysis was performed using a FEI Magellan (Hillsboro, Oregon, USA) and FT-IR analysis was carried out by IR-ATR (attenuated total reflectance) for direct measuring, model IR Tensor 27 (Bruker, Billerica, Massachusetts, USA). A computer-controlled Autolab PGSTAT-12 (302N-High performance) (potentiostat/galvanostat) with a general purpose electrochemical impedance software operating system (Frequency Response Analysers, FRA, v.4.9.006, Solartron Metrology, Leicester, England) was used for impedance measurements. BET (Brunauer–Emmett– Teller) measurements were performed with an

ASAP-2000 instrument from Micromeritics and were carried out for N₂ relative vapor pressure of 0.05–0.3 at 77 K.

3.2.2 Screen printed carbon electrodes (SPCE).

The SPEs consist of a single plastic strip containing three electrodes: working, reference and counter electrode. They were produced by screen-printed technology using a screen-printed machine (DEK 248). Masks galvanized steel frames (580 x 580 x 35 x 25 mm) with 4xM6, photolithograph masks, polyester substrate and thermostatic oven were also utilized. Three different inks were used: graphite ink for the working and counter electrode, silver/silver chloride for the reference electrode layer and finally an insulating layer to define the working electrode area and avoid the undesirable contacts of the liquid with the internal connections. The fabrication procedure involves three printing process. In the first process, the graphite layer was printed onto a polyester sheet by using the first stencil and the graphite ink. After this, the ink was cured at 60 °C for 15 minutes. The silver ink layer was printed and cured at the same conditions, to be used as the reference electrode. Then, an insulating ink printing process was carried out. After this step the SPEs were stored in dry environment prior to be used. It is noteworthy that the graphite ink, is a conductive screen printable ink containing carbon nanoparticles dispersed in a thermoplastic resin.

3.2.3 Synthesis of magnetite nanoparticles.

Magnetite nanoparticles were prepared by co-precipitation method,^{22–25} mixing 0.05 mol of FeCl₃·6H₂O and 0.025 mol FeCl₂·4H₂O in 250 mL of ultrapure water, using a 500 mL three neck flask. The mixture was stirred under nitrogen atmosphere and heated until 80°C, and then 20 mL of NH₄OH from the stock solution, was added (drop by drop). The reaction remained under reflux for 40 min and was cooled down at room temperature. The black product was separated and washed with ultrapure water three times. Lastly, the product was dried under vacuum at 45°C. In order to evaluate the influence of the nanoparticles size on the sensing properties of MIPs, bigger magnetite nanoparticles were also synthesized following the same experimental conditions, but changing the molar ratio between Fe²⁺/Fe³⁺ from 1:2 to 1:0.25.^{26,27}

3.2.4 Synthesis of molecularly imprinted polymer-decorated magnetite nanoparticles.

To synthesize the MIP-decorated MNPs for SMX detection, two solutions were prepared. Firstly, 1 mL of sulfamethoxazole (10 mmol) was solubilized with 10 mL of DMSO and 4 mmol

of methacrylic acid (MAA) and the solution was stirred for 30 min. Fe₃O₄ MNPs were mixed with 1 mL of oleic acid and 10 mmol of pyrrole (Py). Secondly, the solution made of DMSO, MAA and SMX was added to the Fe₃O₄ MNPs/Py solution and immersed in an ultrasound bath for 30 min. Under nitrogen atmosphere, 150 mL of DMSO/water (9:1, v/v), 1g of PVP (polyvinylpyrrolidone), the Fe₃O₄ MNPs/Py/SMX solution and 0.3 mmol of radical initiator (2,5-Bis(tertbutylperoxy)-2,5 dimethylhexane) were added in a two neck flask. The mixture was allowed to react for 24 h at 60°C. The final product was separated and washed with a mixture of methanol/acetic acid (4:1, v/v) and purified using a Soxhlet extractor with methanol/water (1:1, v/v), and dried under vacuum. The non-imprinted polymer (NIP) was synthesized using the same method in the absence of the analyte (SMX).

3.2.5 Binding experiments.

A range of different concentrations of SMX, starting from 1×10^{-2} mol L⁻¹ until 1×10^{-10} mol L⁻¹ was prepared in a mixture of methanol and water (1:1, v/v), and then 20 mg of MIP-decorated Fe₃O₄ MNPs was added into each sample. The solutions were incubated for 2 hours at 700 rpm. After that, three successive centrifugation processes were made during 5 min at 10000 rpm, removing the supernatant and replacing the solvent with new methanol/water solution. The final solution was reconstituted in ultrapure water. Seawater samples were collected from Barcelona Mediterranean Sea (Poblenou Beach) and treated through filtration to remove potential interfering species contained within the original matrix. Various seawater sample solutions containing SMX with concentrations from 1×10^{-2} to 1×10^{-10} mol L⁻¹ were prepared by spiking method. Then, 0.5 mL of extraction media (methanol/acetic acid 1:1, v/v) was added in each sample in order to extract interfering compounds presents in the matrix of the sample, and incubated for 10 min at 650 rpm. In each pre-treated sample to be analyzed, 20 mg of MIP-decorated Fe₃O₄ MNPs was added, and then 2-hour incubation was performed at 25°C and 700 rpm. Finally, in order to remove the template, a centrifugation step was done. Three successive centrifugations were carried out, each one during 5 min at 10000 rpm, removing the supernatant and replacing for methanol/water solution. The final solution was reconstituted in 2 mL ultrapure water. The electroanalytical performance of the proposed sensing system was investigated using electrochemical impedance spectroscopy (EIS). The measurements were performed using home-made screen printed carbon electrodes (SPCE) and 1 mmol L⁻¹ [Fe(CN)₆]^{3-/4-} with 0.1 mol L⁻¹ KCl as redox probe. MIP-decorated MNPs were

fixed over the working electrode using a magnet underneath the SPCE to perform impedance measurements. The resulting data was fitted in a regular Randles circuit to extract the value of charge transfer resistance (R_{ct}) using FRA (v.4.9.006) software.

3.3 Results and discussion.

3.3.1 Characterization of Fe_3O_4 MNPs and MIP-decorated Fe_3O_4 MNPs.

Fe_3O_4 MNPs and MIP-decorated Fe_3O_4 MNPs were first characterized by TEM. As shown in Figure 3.2A, the magnetite nanoparticles have a sphere-like shape and an average size of 11 ± 2 nm (Figure 3.3A). After being coated with the MIP, due to the polymerization process, the resulted MIP-decorated Fe_3O_4 MNPs were observed to be arranged in clusters with an average diameter of 30-50 nm (Figure 3.2B and Figure 3.3B), suggesting that the MIP was successfully deposited onto the surface of the nanoparticles.

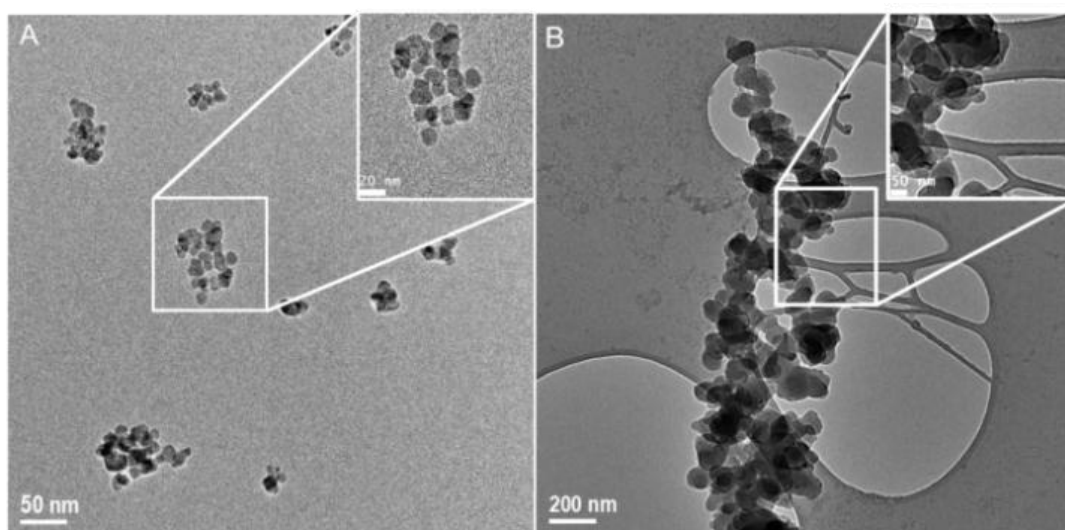


Figure 3.2. TEM images of (A) Fe_3O_4 MNPs and (B) MIP-decorated Fe_3O_4 MNPs.

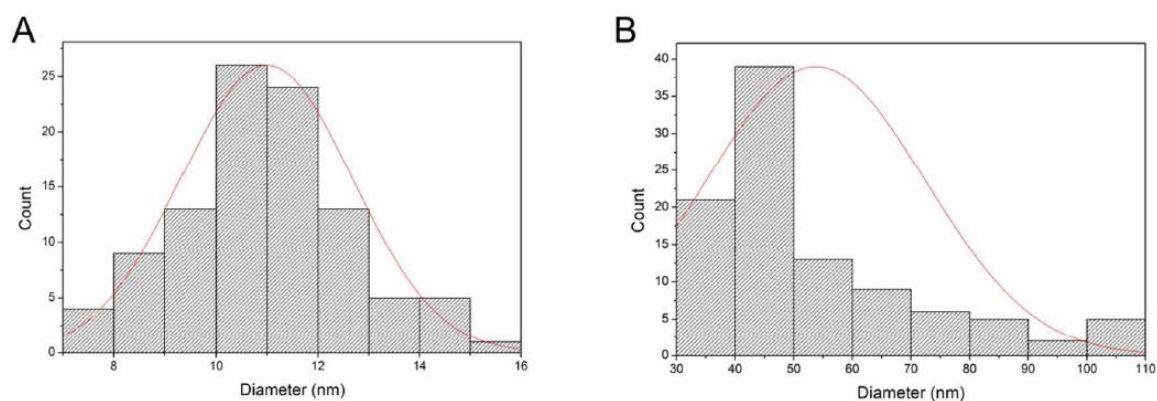


Figure 3.3. Sizes distributions of (A) Fe_3O_4 MNPs and (B) MIP-decorated Fe_3O_4 MNPs.

Aiming at confirming the composition of the synthesized materials, XPS analysis was performed. The spectrum presented in Figure 3.4A shows two peaks at 711 and 725 eV corresponding to $\text{Fe}2p_{3/2}$ and $\text{Fe}2p_{1/2}$. The $\text{Fe}2p$ doublet peaks involve the presence of typical magnetite Fe–O bonds, confirming the formation of the magnetite. The spectra of the MIP-decorated Fe_3O_4 MNPs (Figure 3.4B) do not display the iron signals; this is probable due to the fact that the polymeric layer surrounding the magnetite exceeds the maximum depth that XPS can analyze (around 20 nm). Knowing that, it is possible to see on Figure 3B the signal for C_{1s} at 277 eV, corresponding to C–C signal, and another smaller peak at 281 eV, related to the C–O–C bond from the different compounds used in the synthesis process. The peaks at 525 eV and 392 eV are ascribed to O_{1s} and N_{1s} , respectively.

FT-IR experiments were also carried out to investigate the formation of MIP-decorated Fe_3O_4 MNPs. Figure 3.4C shows the FT-IR spectra of Fe_3O_4 MNPs (black line) and MIP-decorated Fe_3O_4 MNPs (red line). Fe_3O_4 MNPs display a main absorption band at 539 cm^{-1} assigned to Fe–O stretching. Regarding the spectra of MIP-decorated Fe_3O_4 MNPs, it is possible to observe a broad band centered at 3300 cm^{-1} ascribed to the stretching vibration of –OH and –NH groups from the methanol. The peaks at 1636 cm^{-1} and 949 cm^{-1} are related to C=C from the pyrrole aromatic ring. The multiple peaks from 1457 to 1320 cm^{-1} belong to the pyrrole backbone ring. The peak at 3400 cm^{-1} corresponds to N–H, the peak 1248 cm^{-1} corresponds to C–N, and the peak at 1145 cm^{-1} is ascribed to S=O bonds, these groups belong to sulfamethoxazole. These results confirm that the MIP was successfully imprinted on the surface of the Fe_3O_4 MNPs.

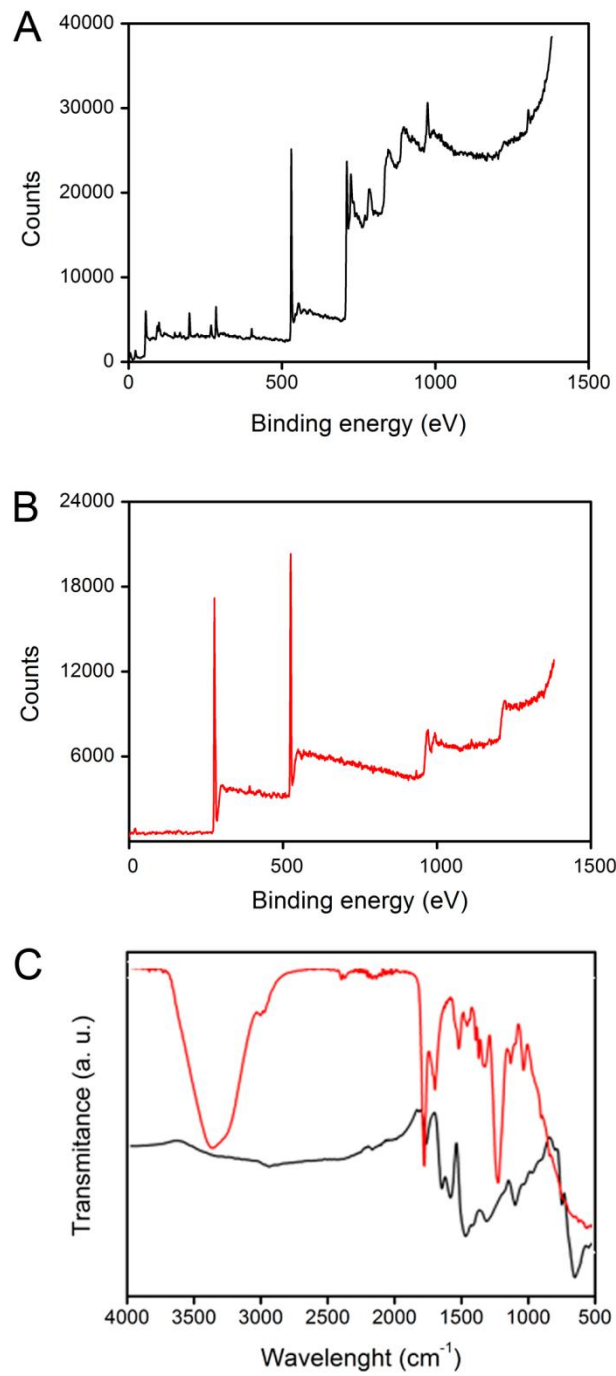


Figure 3.4. X-ray photoelectron spectroscopy, (A) Fe₃O₄ MNPs, (B) MIP-decorated Fe₃O₄ MNPs and (C) FTIR spectra of Fe₃O₄ MNPs (black line) and MIP-decorated Fe₃O₄ MNPs (red line).

3.3.2 Electrochemical impedance responses of the MIP-decorated Fe₃O₄ MNPs toward SMX.

Electrochemical impedance spectroscopy (EIS) is an effective tool to analyze changes that take place at an interface during a recognition event.²⁸ In brief, EIS measurements can be performed in two ways: Faradaic EIS and non-Faradaic method. Faradaic impedance measurements were usually carried out by using a reversible redox probe while non-Faradaic impedance measurements are done without using any redox probe.²⁹ Both Faradic^{30,31} and non-Faradic^{32,33} impedance spectroscopy have been applied for the studies of the recognition events involved in MIP. The typical impedance data are presented in the form of the Nyquist plot and relies on a semicircular region at higher frequencies corresponding to the interfacial charge-transfer process and a linear part at lower frequency range representing the diffusion process. The semicircle diameter in the Nyquist plot corresponds to the charge transfer resistance (R_{ct}), which reflects the electron-transfer kinetics of the redox probe at the electrode surface.²⁹ EIS measurements were performed through SPCEs in a 1 mmol L⁻¹ [Fe(CN)₆]^{3-/4-} solution containing 0.1 mol L⁻¹ KCl using a potential of 0.24 V over the frequency range from 0.1 Hz to 100 kHz and a voltage amplitude of 50 mV. Comprising MIP-decorated Fe₃O₄ MNPs was carried out in ultrapure water in the absence and presence of different concentrations of SMX (from 1 x 10⁻² mol L⁻¹ to 1 x 10⁻¹⁰ mol L⁻¹) in the frequency range from 0.1 Hz to 100 kHz (Figure 3.5). The obtained results were analyzed using a Randles equivalent circuit (see Figure 3.4 inset *i*), where: R_s is the electrolyte resistance, C_{dl} is the interface capacitance, R_{ct} is the charge (electron) transfer resistance and Z_w is the Warburg impedance. Different R_{ct} values were obtained for each SMX concentration. The R_{ct} of the electrode in the absence of SMX is 68 Ω ; this relatively small R_{ct} value can be attributed to the free electron transfer from the electrode surface to the solution.³⁰ The R_{ct} value increases due to the presence of the analyte, as the SMX molecule present in the solution gets bound via the recognition sites or cavities of the MIP. The magnitude of the change in R_{ct} increases as a function of SMX concentration in a logarithmic way in a wide range between 1 x 10⁻² mol L⁻¹ to 1 x 10⁻¹⁰ mol L⁻¹, as displayed in the inset. The linear regression equation was adjusted to R_{ct} (k Ω) = 0.01 log [SMX] (mol L⁻¹) + 0.31 (R^2 = 0.98), with an estimated detection limit of 1 x 10⁻¹² mol L⁻¹ (2.8 x 10⁻⁴ ppb), calculated as the concentration of SMX corresponding to the 3 times "S/N" ratio, where "S" is the standard deviation of the blank impedance signal (three

replicates) and “*N*” is the slope of the related calibration curve. This sensing platform offers an advantageous performance in terms of limit of detection when compared to other methods for SMX determination (see Table 3.1).

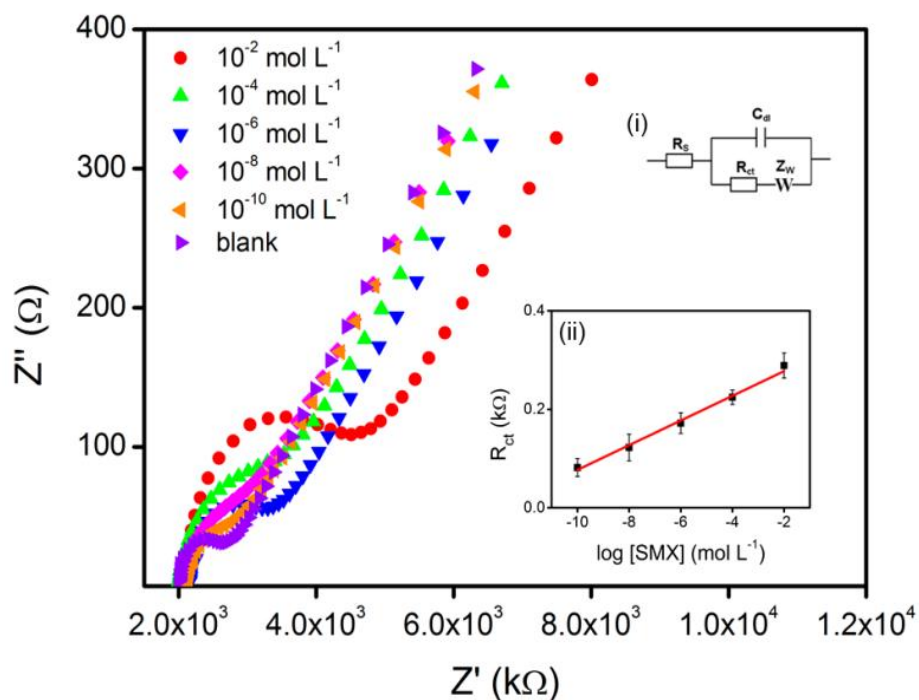


Figure 3.5. Nyquist plots of EIS of MIP-decorated Fe₃O₄ MNP-modified SPCE electrode in the presence of different SMX concentrations. EIS measurements were performed in a 1 mmol L⁻¹ [Fe(CN)₆]^{3-/4-} containing 0.1 mol L⁻¹ KCl at a potential of 0.24 V over the frequency range from 0.1 Hz to 100 kHz, using a voltage amplitude of 50 mV. The insets are related to: (i) the Randles equivalent circuit model for the impedance data and (ii) the calibration curve obtained by plotting the R_{ct} values vs \log of SMX concentration in the range of 1×10^{-2} mol L⁻¹ to 1×10^{-10} mol L⁻¹.

Table 3.1. Comparison of Composition, Detection Limit and Linear Range of Different Modified Electrodes for Determination of SMX.

Method	Detection Limit	Linear range	Reference
MMIP (Fe ₃ O ₄)	1.5 ng g ⁻¹	1.5 - 4.3 ng g ⁻¹	17
MIP-OPPy ^a	3.59 x 10 ⁻⁴ mM	25 x 10 ⁻³ - 0.75 mM	18
MIP-EDMA ^b	3.0 x 10 ⁻⁷ mol L ⁻¹	3.0 x 10 ⁻⁷ - 4.0 x 10 ⁻⁴ mol L ⁻¹	19
Broad specific immunoassay	65.2 µg L ⁻¹	0.2 - 65.2 µg L ⁻¹	20
LC-MS	5–10 ng g ⁻¹	50 - 200 ppb	21
MIP-decorated Fe ₃ O ₄ MNPs	1 x 10 ⁻¹² mol L ⁻¹	1 x 10 ⁻² - 1 x 10 ⁻¹⁰ mol L ⁻¹	This work

a OPpy - Overoxidized polypyrrole.

b EDMA - Ethylene glycol dimethacrylat

The electrode reproducibility and stability were also investigated by impedimetric responses of sample solutions containing 10⁻⁶ mol L⁻¹ SMX. The relative standard deviations (RSDs) of the same sensor for five successive measurements were found to be 3.6% and for three different electrodes it was 6.8%. These results confirm the electrode reproducibility. The imprinted sensor also exhibited satisfactory stability. In fact, the results show that after 3 weeks 82% of the initial response was preserved.

3.3.3 Characterization of the NIP-composite and selectivity studies.

To confirm the specificity of the MIP-decorated Fe₃O₄ MNPs, its performance was compared with the performance of a non-imprinted polymer (NIP)-composite.^{31–33} Figure 3.6A shows the R_{ct} values obtained for both materials in the absence and presence of 1 x 10⁻² mol L⁻¹ SMX. The difference observed on R_{ct} values for the imprinted sensor (160 Ω) and non-imprinted sensor (110 Ω) is related to the imprinted cavities presented on the MIP-composite, which facilitate the diffusion of the [Fe(CN)₆]^{3-/4-} probes into the electrode surface, decreasing the charge transfer resistance.³⁴ Analyzing the R_{ct} values corresponding to the sample containing SMX, the MIP-composite shows a value that is 3 times higher than the blank, whereas the NIP-composite displays a value that is 1.4 times higher than the blank. These large separation factors suggest that the MIP-composite possesses a high specificity towards SMX when compared with the NIP-composite behavior.

Interferences of other sulfonamides were also studied aiming at exploring the selectivity of the sensing system based on the proposed MIP-decorated Fe_3O_4 MNPs. In particular, the performance of the sensing system was evaluated in the presence of two kinds of structurally similar sulfonamides such as sulfadiazine (SDZ) and sulfacetamide (SCT). In a typical experiment, the electrochemical impedance of the electrode modified with the composite was measured in the presence of 1×10^{-8} mol L^{-1} of each analyte. As shown in Figure 3.6B, the R_{ct} values obtained for SDZ and SCT show practically no difference between them and the blank. These results suggest that the sensor exhibits good selectivity, which is attributed to the specificity of the MIP toward SMX.

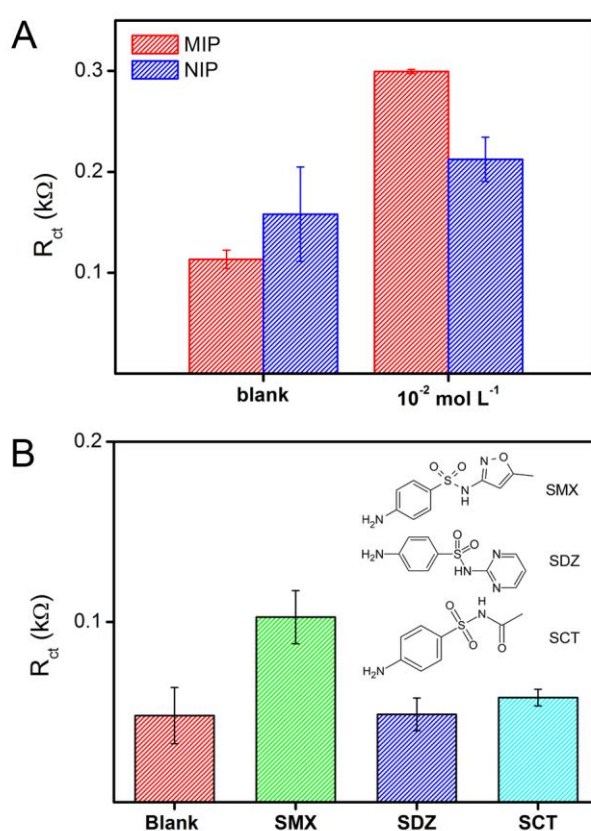


Figure 3.6. R_{ct} values obtained for (A) imprinted (MIP) and non-imprinted (NIP) sensor and (B) the MIP-decorated Fe_3O_4 MNPs in the presence of SMX, SDZ and SCT. Results obtained from the EIS measurements performed in a 1 mmol L^{-1} $[\text{Fe}(\text{CN})_6]^{3-/4-}$ containing 0.1 mol L^{-1} KCl at a potential of 0.24 V over the frequency range from 0.1 Hz to 100 kHz, using a voltage amplitude of 50

3.3.4 Real sample measurements.

In order to evaluate the applicability of the proposed sensor in real environmental samples, determination of SMX was carried out in spiked seawater samples. Prior to the analysis, the samples were mixed with extraction media (see experimental description) in order to minimize matrix complexity and spike the samples with different SMX concentrations. It was observed from the EIS data (Figure 3.7) that the R_{ct} value increased on spiking with SMX. Hence, from the R_{ct} values obtained for three different SMX concentrations (10^{-4} , 10^{-6} and 10^{-8} mol L⁻¹), recovery was calculated and the results obtained are given in Table 3.2. The recoveries of the samples are 87 - 106 % with the RSD in the range of 1.2 - 4.5 %, which indicates that the developed assay can be performed for the accurate determination of SMX in real samples analysis.

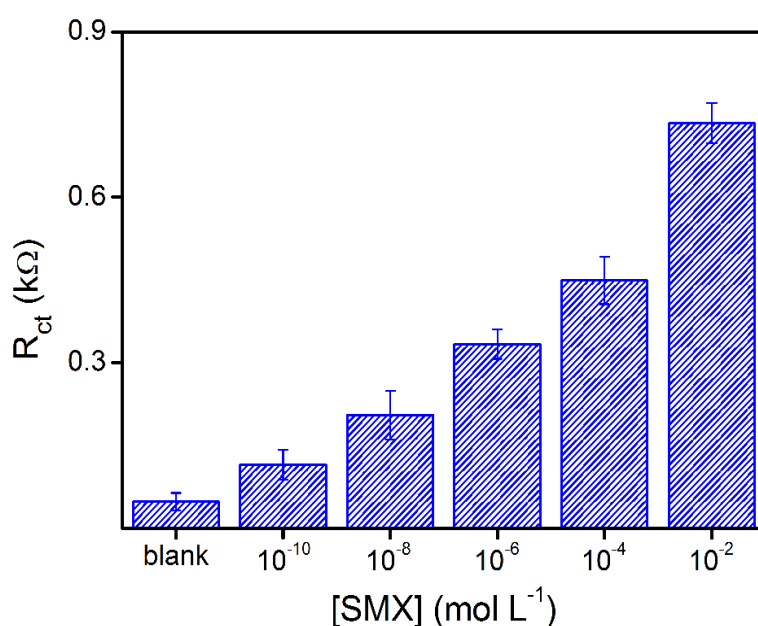


Figure 3.7. R_{ct} values obtained for MIP-decorated Fe_3O_4 MNPs in seawater in the absence and presence of different spiked SMX concentrations. Results obtained from the EIS measurements performed in a 1 mmol L⁻¹ $[Fe(CN)_6]^{3-/4-}$ containing 0.1 mol L⁻¹ KCl at a potential of 0.24 V over the frequency range from 0.1 Hz to 100 kHz, using a voltage amplitude of 50 mV.

Table 3.2. Determination of SMX in seawater.

SMX Spiked (mol L^{-1})	R_{ct} ($\text{k}\Omega$)	Recovery (%)	RSD (%)
10^{-4}	0.233	92	1.2
10^{-6}	0.174	87	4.5
10^{-8}	0.115	106	2.3

3.3.5 Fe_3O_4 MNPs size effect study.

MIP-composite was also synthesized using bigger magnetite nanoparticles. The new magnetite nanoparticles were characterized using TEM, which shows the formation of nanoparticles with diameter around 27 nm (Figure 3.8A).

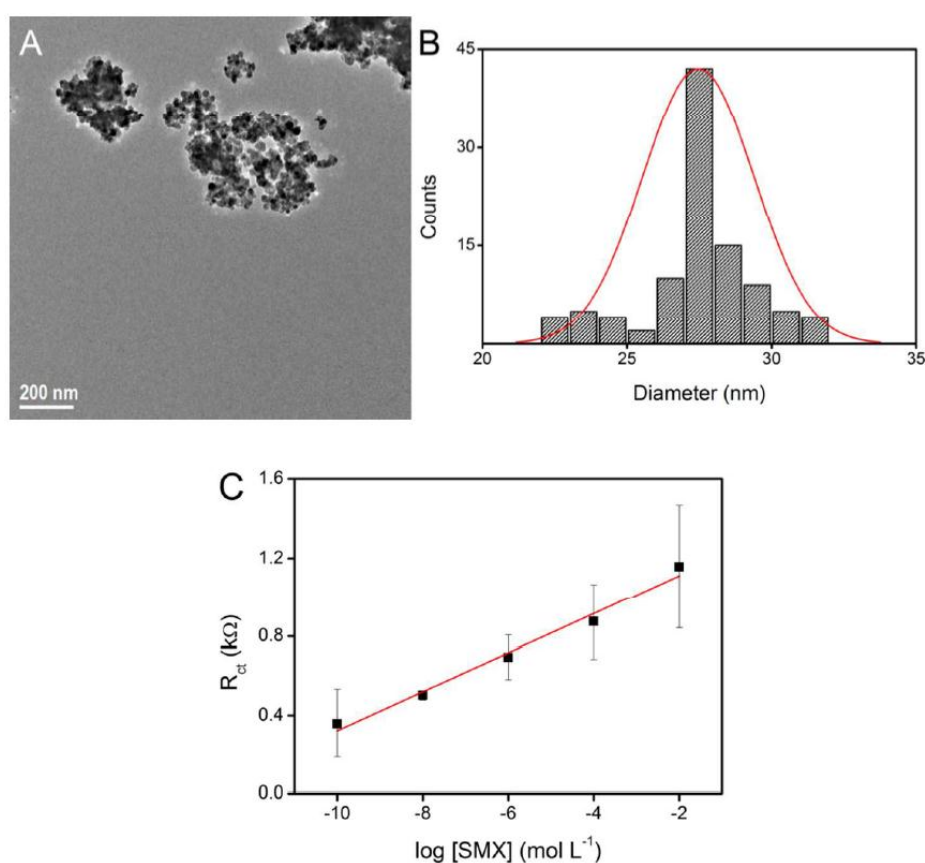


Figure 3.8. (A) TEM image and (B) size distribution of 27nm- Fe_3O_4 MNPs. (C) Calibration curve obtained by plotting the R_{ct} values vs log of SMX concentration in the range of $1 \times 10^{-2} \text{ mol L}^{-1}$ to $1 \times 10^{-10} \text{ mol L}^{-1}$ for the MIP-composite based on particles of an average diameter of 27 nm.

Binding experiments for the new MIP was carried out following the same procedure. From the EIS data obtained for the composite containing Fe₃O₄ MNPs of 27 nm, a new calibration curve was constructed (Figure 3.8B) and a new limit of detection was also determined (S/N = 3). The LOD for the new MIP-composite shows a different performance when compared with that of the original one, obtaining $5 \times 10^{-12} \text{ mol L}^{-1}$ ($1.4 \times 10^{-3} \text{ ppb}$), being 5 times higher than that obtained with the composite based on particles of an average diameter of 11 nm ($1 \times 10^{-12} \text{ mol L}^{-1}$).

Since the new-proposed sensing system was found to offer a different performance in terms of limit of detection by changing the size of the particles embedded in the composite, the specific surface area of both composites was explored via Brunauer-Emmett-Teller (BET) technique in order to verify the influence of this parameter in the limit of detection of the developed sensing system. Hence, the limit of detection of the proposed sensing system using the MIP-decorated Fe₃O₄ MNPs containing two different sizes of particles, 11 and 27 nm respectively, was systematically studied in parallel with the BET analysis. The composite decorated with 27 nm Fe₃O₄ NPs showed a surface area of $64 \text{ m}^2\text{g}^{-1}$, whereas the composite of 11 nm displayed a larger surface area of $184 \text{ m}^2\text{g}^{-1}$ due to the smaller size of MNPs. From this data, it can be concluded that smaller nanoparticles can improve the surface area, increasing the number of the recognition sites for SMX which improves the electrochemical response of the sensing system. Table 3.3 summarizes the obtained results.

Table 3.3. The influence of the specific surface area on the limit of detection of the proposed sensing system.

Particle size (nm)	LOD (mol L^{-1}) ^a	SSA ($\text{m}^2 \text{g}^{-1}$) ^b
11	1×10^{-12}	64
27	5×10^{-12}	184

a. Limit of detection (S/N = 3), b. Specific surface area

3.4 Conclusions.

A selective, specific and highly sensitive composite-based sensing system has been engineered aiming at detecting the potentially hazardous chemotherapeutic agent SMX in a label-free fashion via electrochemical impedance spectroscopy. The proposed sensing system (i) bears selectivity and specificity, due to its biomimetic receptor; (ii) facilitates pre-concentration, separation and manipulation of the analyte, due to its magnetic properties; (iii) showing a high surface area ($184 \text{ m}^2 \text{ g}^{-1}$), this composite-based sensing system exhibits a high sensitivity (LOD around $1 \times 10^{-12} \text{ mol L}^{-1} \approx 2.8 \times 10^{-4} \text{ ppb}$), which is comparable with that of sulfonamides monitoring using liquid chromatography/mass spectrometry. Moreover, this sensing system has been proved to be useful in seawater monitoring, where sulfonamides content is minimum compared to other environmental samples and may be extended to other compounds by changing the MIP.

3.5 References

- (1) Dmitrienko, S. G.; Kochuk, E. V; Apyari, V. V; Tolmacheva, V. V; Zolotov, Y. A. *Anal. Chim. Acta* 2014, 850, 6–25.
- (2) Wang, S.; Zhang, H. Y.; Wang, L.; Duan, Z. J.; Kennedy, I. *Food Addit. Contam.* 2006, 23 (4), 362–384.
- (3) Cháfer-Pericás, C.; Maquieira, Á.; Puchades, R. *TrAC Trends Anal. Chem.* 2010, 29 (9), 1038–1049.
- (4) O’Neill, J. *Rev. Antimicrob. Resist.* 2014, No. December, 1–16.
- (5) Meltzer, L. J. *Invest. Dermatol.* 1949, 13 (4), 213–216.
- (6) Hela, W.; Brandtner, M.; Widek, R.; Schuh, R. *Food Chem.* 2003, 83 (4), 601–608.
- (7) Nebot, C.; Regal, P.; Miranda, J. M.; Fente, C.; Cepeda, A. *Food Chem.* 2013, 141 (3), 2294–2299.
- (8) Lindsey, M. E.; Meyer, T. M.; Thurman, E. M. *Anal. Chem.* 2001, 73 (19), 4640–4646.
- (9) Rodriguez, M.; Orescan, D. B. *Anal. Chem.* 1998, 70 (13), 2710–2717.

- (10) Fuh, M. R. S.; Chu, S. Y. *Anal. Chim. Acta* 2003, 499 (1-2), 215–221.
- (11) Santos, B.; Lista, A.; Simonet, B. M.; Ríos, A.; Valcárcel, M. *Electrophoresis* 2005, 26 (7-8), 1567–1575.
- (12) Merkoçi, A.; Alegret, S. *TrAC Trends Anal. Chem.* 2002, 21 (11), 717–725.
- (13) Schirhagl, R. *Anal. Chem.* 2014, 86 (1), 250–261.
- (14) Zor, E.; Morales-Narváez, E.; Zamora-Gálvez, A.; Bingol, H.; Ersoz, M.; Merkoçi, A. *ACS Appl. Mater. Interfaces* 2015, 7 (36), 20272–20279.
- (15) Chantada-Vázquez, M. P.; Sánchez-González, J.; Peña-Vázquez, E.; Taberner, M. J.; Bermejo, A. M.; Bermejo-Barrera, P.; Moreda-Piñeiro, A. *Biosens. Bioelectron.* 2016, 75, 213–221.
- (16) Wan, Y.; Ma, H.; Lu, B. *Adv. Biochem. Eng. Biotechnol.* 2015, 150, 131–166.
- (17) Chen, L.; Zhang, X.; Sun, L.; Xu, Y.; Zeng, Q.; Wang, H.; Xu, H.; Yu, A.; Zhang, H.; Ding, L. *J. Agric. Food Chem.* 2009, 57 (21), 10073–10080.
- (18) Ozkorucuklu, S. P.; Sahin, Y.; Alsancak, G. *Sensors* 2008, 8 (12), 8463–8478.
- (19) Guzm, A.; Prada, D.; Mart, P.; Reviejo, A. J.; Pingarr, J. M. 2005, 539, 125–132.
- (20) Franek, M.; Diblikova, I.; Cernoch, I.; Vass, M.; Hruska, K. 2006, 78 (5), 1559–1567.
- (21) Heller, D. N.; Ngoh, M. A.; Donoghue, D.; Podhorniak, L.; Righter, H.; Thomas, M. H. 2002, 774, 39–52.
- (22) Machala, L.; Zboril, R.; Gedanken, A. *J. Phys. Chem. B* 2007, 111 (16), 4003–4018.
- (23) Lee, Y.; Lee, Y.; Lee, J.; Lee, J.; Bae, C. J.; Bae, C. J.; Park, J.-G.; Park, J.-G.; Noh, H.-J.; Noh, H.-J.; Park, J.-H.; Park, J.-H.; Hyeon, T.; Hyeon, T. *Adv. Funct. Mater.* 2005, 15 (3), 503–509.
- (24) Prozorov, T.; Mallapragada, S. K.; Narasimhan, B.; Wang, L.; Palo, P.; Nilsen-Hamilton, M.; Williams, T. J.; Bazylinski, D. a.; Prozorov, R.; Canfield, P. C. *Adv. Funct. Mater.* 2007, 17 (6), 951–957.

- (25) Huynh, T.-P.; Wojnarowicz, A.; Sosnowska, M.; Srebniak, S.; Benincori, T.; Sannicolò, F.; Souza, F. D.; Kutner, W. *Biosens. Bioelectron.* 2015, 70, 153–160.
- (26) Herea, D.-D.; Chiriac, H.; Lupu, N. J. *Nanoparticle Res.* 2011, 13 (9), 4357–4369.
- (27) Sun, S.; Zeng, H. J. *Am. Chem. Soc.* 2002, 124 (28), 8204–8205.
- (28) Mayorga-Martinez, C. C.; Chamorro-Garcia, A.; Merkoçi, A. *Biosens. Bioelectron.* 2015, 67, 53–58.
- (29) Gautier, C.; Esnault, C.; Cougnon, C.; Pilard, J.; Casse, N.; Chénais, B. J. *Electroanal. Chem.* 2007, 610, 227–233.
- (30) Uygun, Z. O.; Dilgin, Y. *Sensors Actuators, B Chem.* 2013, 188, 78–84.
- (31) Wu, B.; Wang, Z.; Zhao, D.; Lu, X. *Talanta* 2012, 101, 374–381.
- (32) Apodaca, D. C.; Pernites, R. B.; Ponnampati, R.; Del Mundo, F. R.; Advincula, R. C. *Macromolecules* 2011, 44 (17), 6669–6682.
- (33) Reddy, K. K.; Gobi, K. V. *Sensors Actuators, B Chem.* 2013, 183, 356–363.
- (34) Yao, G.; Liang, R.; Huang, C.; Wang, Y.; Qiu, J. 2013.
- (35) Reddy, K. K.; Gobi, K. V. *Sensors Actuators B Chem.* 2013, 183, 356–363.
- (36) Nishad, P. A.; Bhaskarapillai, A.; Velmurugan, S.; Narasimhan, S. V. *Carbohydr. Polym.* 2012, 87 (4), 2690–2696.
- (37) Sergeeva, T. A.; Piletsky, S. a.; Panasyuk, T. L.; El'skaya, a. V.; Brovko, a. a.; Slinchenko, E. a.; Sergeeva, L. M. *Analyst* 1999, 124 (3), 331–334.
- (38) Pan, G.; Zu, B.; Guo, X.; Zhang, Y.; Li, C.; Zhang, H. *Polymer (Guildf)*. 2009, 50 (13), 2819–2825.
- (39) Zhu, L.; Cao, Y.; Cao, G. *Biosens. Bioelectron.* 2014, 54, 258–261.

CHAPTER 4

Magnetic molecularly imprinted polymer as an impedimetric sensor for tributyltin detection

Related publication

1) *Electrochem. Commun.* 2017, 10.1016/j.elecom.2017.07.007

4.1 Introduction

For decades, the pesticide tributyltin (TBT) has been an important additive in antifoulant paints to prevent the growth of marine organisms on the hulls of large ships. Eventually, this highly toxic pesticide leaks in the aquatic environment causing immuno-suppression and imposex in snails and bivalves, inhibiting the growth of several marine organisms, and inducing immunotoxic, hepatotoxic, and neurotoxic effects in fish and mammals, with potential effects even for humans ¹⁻³.

Nowadays, the typical methods to detect pesticides, including TBT, are chromatography separation ⁴⁻⁶, gas chromatography ⁷⁻⁹, electron-capture detector ¹⁰, flame ionization detector and mass spectrometry ¹¹. These techniques reach low limits of detections (LOD) and have high reproducibility, but require extensive purification, expensive equipment and trained users ¹². During the past few years, electrochemical sensors showed to be a user-friendly and miniaturized alternative for pesticides detection.¹³ Nevertheless, they normally use bio-receptors (aptamers, antibodies, enzymes) ¹³⁻¹⁵, which can be instable, non-specific, and expensive. Recently, our group and others used molecular imprinting polymers (MIPs) for the development of specific methods for the detection of different kinds of molecules such as fenitrothiol, organochlorine, and heptachlor ¹⁴⁻¹⁶.

Here a new sensing platform for the detection of TBT based on MIP technology is presented. Our system is based on the use of screen printing electrodes in conjunction with MIP-Fe₃O₄ nanoparticles (NPs) composite ¹⁵⁻¹⁷ as a specific receptor for TBT. Thanks to the use of electrochemical impedance spectroscopy, TBT was detected qualitatively in fresh and sea water (see scheme in Figure 4.1A) ^{14,16-18}.

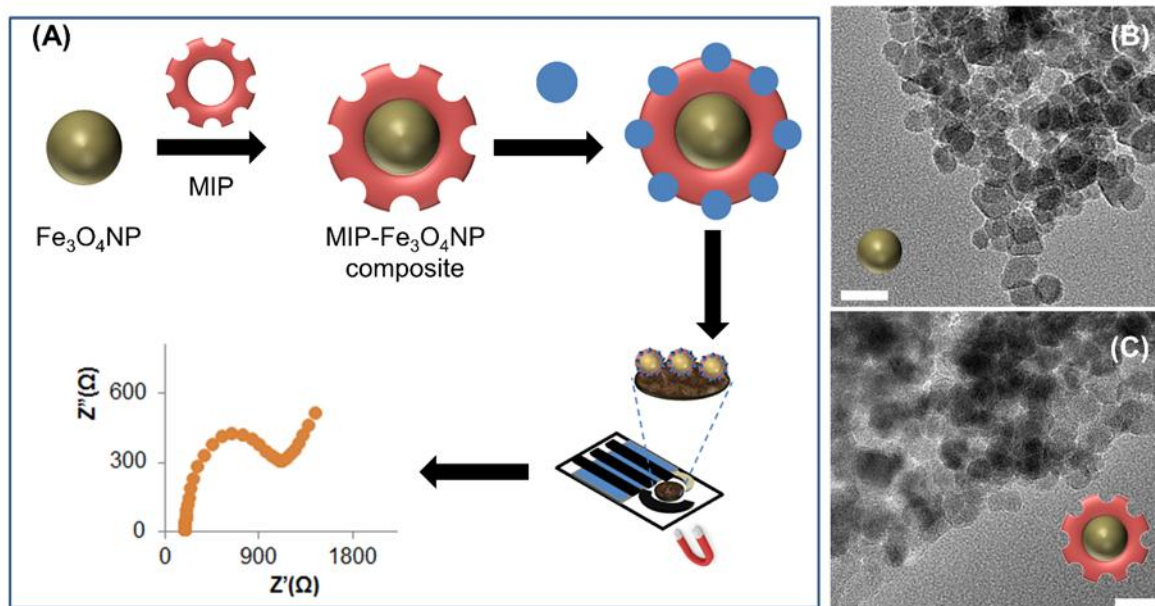


Figure 4.1. Schematic representation of the proposed TBT sensor (A). TEM images of Fe₃O₄NPs (B) and MIP-Fe₃O₄NPs (C). Scale bar: 20 nm.

4.2 Experimental section.

4.2.1 Reagents and materials

Tributyltin hydride, (3-Aminopropyl) trimethoxysilane, acryloyl chloride (C₃H₃ClO), FeCl₂•4H₂O, FeCl₃•6H₂O, ammonium hydroxide (NH₄OH), toluene anhydrous, potassium carbonate (KCO₃), ethanol, acetonitrile, ethylene glycol dimethacrylate 98%, 2,5-Bis(tert-butylperoxy)-2,5-dimethylhexane 90%, sodium hydroxide and methanol were purchased from Sigma Aldrich. Transmission electron microscope (TEM) FEI TECNAI G2 F20 (USA), X-ray photoelectron spectrometer Phoibos 150 analyzer (SPECS GmbH, Berlin, Germany) in ultra-high vacuum conditions (base pressure 1x 10⁻¹⁰ mbar). The infrared spectroscopy was performed by IR-ATR model IR Tensor 27 (Bruker). Homemade SPE, which fabrication method was reported previously¹⁴.

4.2.2 Synthesis of molecular imprinted MIP-Fe₃O₄NPs composite.

For the synthesis of the MIP-Fe₃O₄NPs composite, modification of a protocol previously reported by Zhu et al.¹⁹ was performed. A mixture of FeCl₂•4H₂O 0.02 g/mL and FeCl₃•6H₂O 0.054 g/mL was prepared and stirred under nitrogen to prevent the formation of Fe₂O₃. After that, 20 mL of ammonium hydroxide 25 M was added and the reaction was refluxed at 80 °C for 40 min. The solution was decanted and washed three times with MilliQ water to remove any unreacted reagent. The Fe₃O₄NPs were dried in a vacuum at 45 °C. All the next steps were performed under Schlenk line, to increase the stability of the compounds. Then, 0.1 g of Fe₃O₄ NPs was dissolved in 150 mL ethanol/water 14:1 and 50 µL 4.27 mM of amino propyl triethoxysilane (APTS) was added drop by drop, under continuous stirring during 7 h at room temperature and nitrogen ambient. Following by washing steps with absolute ethanol (5 times), and dried in vacuum. 0.1 mg of APTS- Fe₃O₄NPs and 0.5 g of K₂CO₃ were dispersed in 50 mL of toluene under ultrasonic ice bath during 30 min and 1 mL 0.012 M of acryloyl chloride was added and the flask was sealed, the mixture was under vigorous stirring for 12 h at room temperature. Next, the product was collected by application of an external magnetic field and rinsed three times with toluene, ethanol and acetonitrile, then the product was dried in vacuum conditions.

The modified Fe₃O₄ NPs (0.1 g) and 269 µL of tributyltin hydride (TBTH) were dissolved in 40 mL 19 M of acetonitrile and stirred for 6 h until the template-monomer was formed. Then 4.14 mL at 5.3 M of ethylene glycol dimethacrylate (EGDMA) and 9.35 µL 3M of 2,5-bis(tertbutyl peroxy)-2,5 dimethyl hexane were added in the solution. The solution was placed in the ultrasonic ice-bath for 5 min then was heated at 50 °C for 5 h and polymerized at 65 °C for 20 h. Finally the mixture was heated at 85°C for 5 h to assure complete polymerization. The reaction was purged with nitrogen and stirred. The resultant product was rinsed five times with a mixture of methanol-dichloromethane (4:1) and finally the resulted product was extracted using Soxhlet for 60 hours in presence of 0.3 M NaOH dissolved in methanol, the final product was dried under vacuum conditions. Although the synthesis of the MIP-Fe₃O₄NPs composite requires long time, the final amount that is obtained (ca. 5 grams) is enough to perform over 100 measurements.

4.2.3 Electrochemical measurements.

For TBT detection, different TBT concentrations were incubated with 10 mg/mL of MIP-Fe₃O₄NPs composite under stirring conditions for 2 h at room temperature. Afterward, 10 µL of the above suspension was drop casted onto the working electrode area of the SPE and TBT/MIP-Fe₃O₄NPs composite was accumulated onto the working electrode area with the help of a permanent magnet placed underneath. Then electrochemical impedance spectroscopy (EIS) was performed in 1 mM [Fe(CN)₆]^{3/4} with 0.1 M KCl adding 50 µL of this solution over the working electrode. A sinusoidal potential modulation of ±20 mV amplitude in the 0.1 Hz to 100 kHz frequency range was superimposed onto the formal potential (0.24 V vs. Ag/AgCl) of the redox couple, [Fe(CN)₆]^{3/4}. For sea water measurements, samples were filtered using a 0.05 µm VMWP filter to extract bigger compounds and impurities.

4.3 Results and discussion.

4.3.1 Characterization of the composite

Before applying MIP-Fe₃O₄NPs composite for TBT detection, was characterized using TEM, IR, XPS. TEM was used to study the synthesized Fe₃O₄NPs, which had a diameter of 20.05 ± 4.37 nm and a good homogeneity (as shown in Fig. 4.1B), in line with previously reported synthesis^{20,21}. Upon modification with the MIP, some Fe₃O₄NPs aggregation was observed (probably due to the polymerization process)²², which increased the apparent diameter of the Fe₃O₄NPs to 59.77±7.15 nm (Fig. 4.1C). The aggregation of Fe₃O₄ NPs should not negatively affect the sensor behavior, since their only role is to accumulate the MIP on the working electrode surface (upon inducing a magnetic field with a permanent magnet), for this reason we refer to MIP-Fe₃O₄NPs composite, rather than just MIP-Fe₃O₄NPs. In order to confirm the incorporation of the Fe₃O₄NPs into the MIP, it was magnetically separated the samples from their solutions before characterizing them with IR spectroscopy. Figure 4.2A shows how the characteristic peaks of the MIP in the IR spectra (i.e. C-H, C=O, Si-O, C=C-H δ and Si-CH) appeared just in the MIP- Fe₃O₄NPs composite spectrum and not in the one of bare Fe₃O₄NPs, suggesting that the Fe₃O₄NPs were included into the polymer structure. Composite and the bare nanoparticles was also characterized with X-ray spectroscopy. The survey spectrum (Fig. 4.2B) of MIP- Fe₃O₄NPs composite shows the enhanced signals from O 1s, C 1s and Si 2p peaks in comparison of survey spectrum of Fe₃O₄NPs, confirming the formation of

MIP- Fe₃O₄NPs composite. Fig. 4.2C shown the high resolution signals for the regions of O 1s, C 1s, Si 2p, Fe 2p and Ni 1s of MIP- Fe₃O₄NPs composite. Moreover, the specific surface was investigated by BET analysis and the obtained surface area for the MIP- Fe₃O₄NPs (59.77±7.15 nm) is 65 m²/g (see Fig. 4.2D).

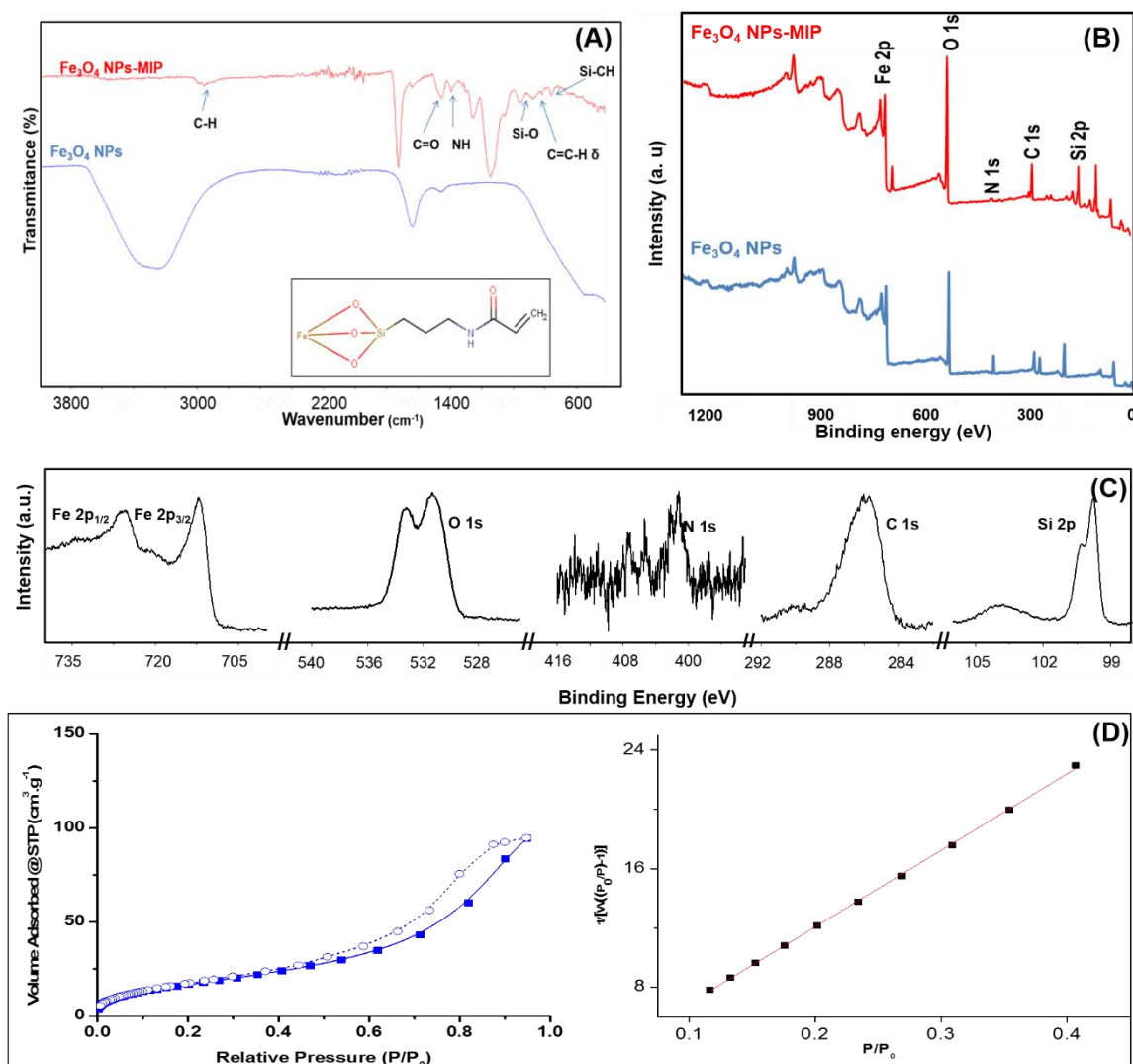


Figure 4.2. Comparison of the IR (A) and wide-scan X ray photoelectron (B) spectra of Fe₃O₄NPs (blue) and MIP-Fe₃O₄NPs composite (red). High-resolution X-ray photoelectron spectra of Fe 2p, O 1s, N 1s, C 1s and Si 2p regions of the MIP-Fe₃O₄NPs (C). N₂ adsorption isotherms (left) and dynamic curve (right) of MIP-Fe₃O₄NPs (D). Inset: MIP-Fe₃O₄NPs structure.

4.3.2 Impedance measurements in buffer and sea water.

Once proved the formation of the MIP- Fe₃O₄NPs composite, MIP was verified that it could bind the TBT using EIS. Figure 4.3A shows the Nyquist spectra of bare (SPE), MIP- Fe₃O₄NPs and MIP- Fe₃O₄NPs incubated with 5 μM TBT. The resulted R_{ct} for the MIP- Fe₃O₄NPs composite is 0.65 kΩ, which indicates a low resistivity compared with the R_{ct} of the bare electrode of 15-20 kΩ. We think that there are two main components inducing this low R_{ct} : the catalytic activity of Fe₃O₄NPs^{23,24} and the enhanced electrode effective area due to the presence of Fe₃O₄NPs. After the incubation of MIP-Fe₃O₄NPs with 5 μM TBT, the recorded signal is 1.66 kΩ. This enhanced R_{ct} confirms the binding between of MIP-Fe₃O₄NPs and TBT, because the negative charge from the tributyltin hydride²⁵ acts as an electrostatic barrier between SPE and the redox mediator. This was confirmed by Zeta-potential experiments (Fig. 4.3B). A gradual shift to negative values was observed when the MIP-Fe₃O₄NPs is connect with TBT.

After proving that the sensors responded to the presence of TBT, it was challenged with different TBT concentrations. The calibration curve of the R_{ct} values as a function of TBT concentration is shown in Figure 4.3D, a linear range spanning 6 orders of magnitude, from 5 pM to 5 μM ($r^2=0.97$) with a limit of detection (LOD) of 5.37 pM and a limit of quantification (LOQ) of 17.9 pM are obtained. The LOD and the LOQ was calculated by 3 times or 10 times the s/m criteria respectively, where s is the standard deviation of the R_{ct} of the lowest concentration of the TBT (3 repetitions) and m is the slope of the corresponding calibration graph. Both the LOD and LOQ of our sensor are smaller than the values recommended by the US Environmental Protection Agency: 1.45 nM (acute criterion) and 25 pM (chronic criterion)²⁶. Moreover, the high concentration tested is 100 times upper than the maximum allowable concentration indicated by international agencies.

On the other hand, the sensor revealed high reproducibility with a relative standard deviation (RSD) of 17.8%, calculated as the mean of RSD obtained from five TBT concentrations and three replicates for each concentration. The selectivity of our sensor is tested using 5 μM monobutyltin dichloride (MTB) and dibutyltin dichloride (DTB). MTB and DTB represent a potential interference in the detection of TBT. The R_{ct} values for MBT and DBT are considerably lower than the one obtained using TBT, respectively: 0.44 ± 0.176 and $0.81 \pm$

0.066 k Ω . The TBT produced a signal 377% and 200% higher than the ones obtained using MBT and DTB, proving the high selectivity of our sensor for TBT (see Fig.4.3E).

Finally, MIP-Fe₃O₄NPs composite was challenged with a recovery test. Two different concentrations was compared of TBT (5 pM and 5 μ M) in pre-filtered sea water samples (n = 3 for each sample) with the same concentrations of TBT in MilliQ water. The recovery percentages (eqn. 2) were 110.33% and 78.18%, respectively for 5 pM and 5 μ M. The recovery percentages were particularly good considering the complexity of sea water matrix.

$$\text{Recovery percentage} = \frac{[TBT]_{\text{Sea water}}}{[TBT]_{\text{MilliQ water}}} \times 100 \quad (2)$$

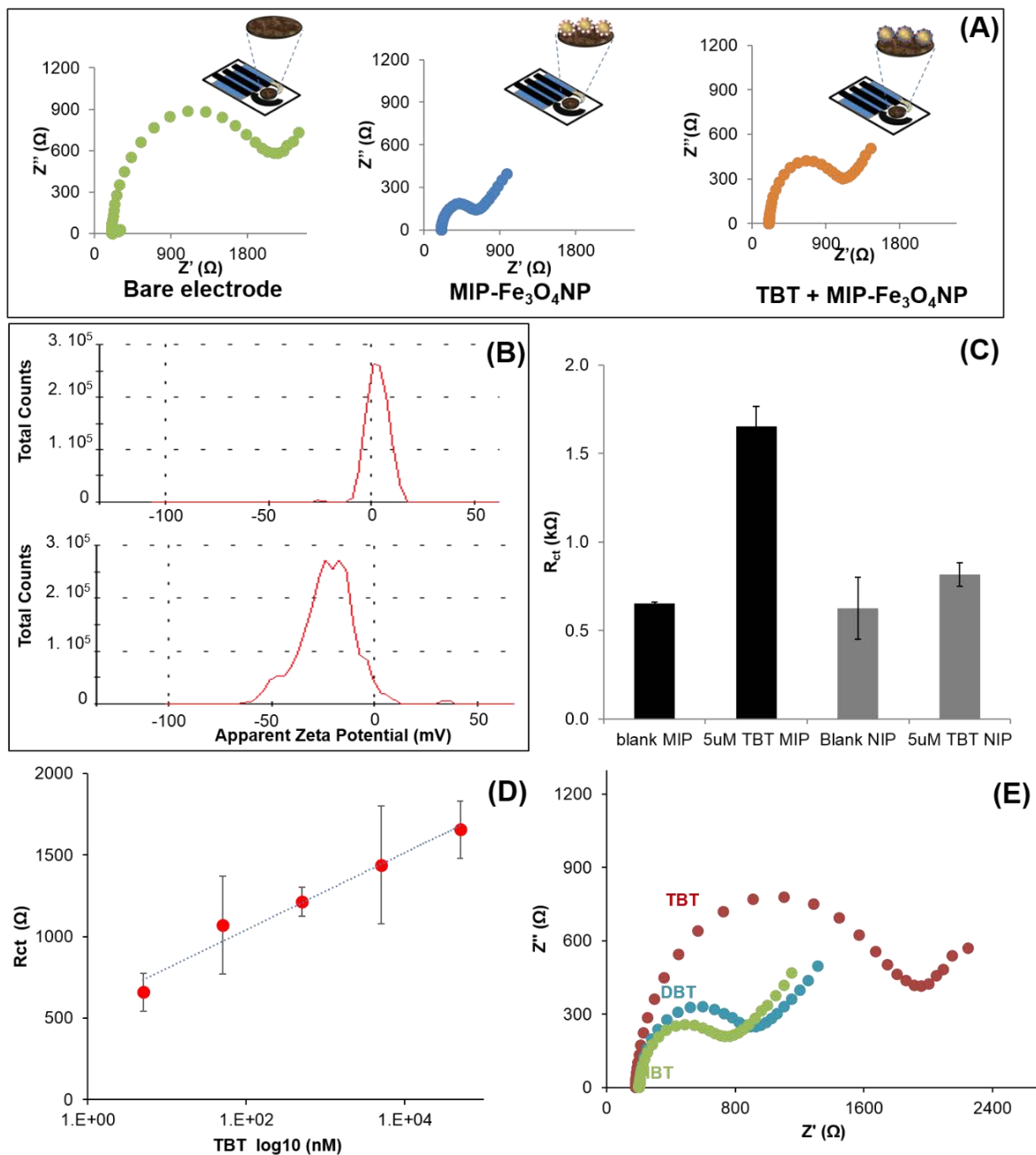


Figure 4.3. Nyquist plot of bare SPE, SPEs modified with MIP-Fe₃O₄NPs and MIP-Fe₃O₄NPs + 5 μ M TBT (A). Zeta-potential diagram from the dispersion of MIP-Fe₃O₄NPs and MIP-Fe₃O₄NPs + TBT (B). R_{ct} values obtained for MIP-Fe₃O₄NPs and NIP-Fe₃O₄NPs with and without 5 μ M TBT (C). Calibration curve for R_{ct} values as a function of the TBT concentration (D). Nyquist plot of TBT, MBT and DBT at the same concentration (5 μ M) (E).

4.3.3 Study of the selectivity

To verify that the signal change upon addition of TBT was specific, the same measurements were performed using NIP- Fe₃O₄NPs composite (non-imprinted polymer). Our sensor was challenged with four different solutions: MIP- Fe₃O₄NPs composite, NIP- Fe₃O₄NPs composite, MIP- Fe₃O₄NPs composite with 5 μM TBT, and NIP- Fe₃O₄NPs composite with 5 μM TBT (see Figure 4.3C). The R_{ct} obtained using NIP- Fe₃O₄NPs composite, both in the absence (0.63 ± 0.176 kΩ) and presence (0.82 ± 0.066 kΩ) of 5 μM TBT, were very similar to the one obtained using MIP- Fe₃O₄NPs composite in the absence of TBT (Fig. 4.3C) and the imprinted factor using the equation (1) is 5.315. These observations suggest that the change observed is induced by the specific binding of TBT to the MIP and not by non-specific adsorption of the TBT onto the working electrode or the composite. The R_{ct} is obtained using Randles model modified with Warburg impedance (Zw).

$$IF = \frac{R_{ct_{MIP+TBT}} - R_{ct_{MIP}}}{R_{ct_{NIP+TBT}} - R_{ct_{NIP}}} \quad (1)$$

4.4 Conclusions

We presented the development of the first impedimetric sensor for detection of TBT based on MIP-Fe₃O₄NPs composite. This low cost and user-friendly sensor shows excellent analytical performance thanks to the synergy between magnetic nanoparticles and MIPs. Such coupling allowed an efficient separation and preconcentration of the analyte. On one side, it responded specifically to TBT, in comparison to similar compounds (MBT and DBT), on the other its LOD (5 pM) and LOQ (18 pM) were below the values recommended by the US Environmental Protection Agency: 1.45 nM (acute criterion) and 25 pM (chronic criterion). Compared to other TBT detection systems, it showed the widest range of response and one of the lowest LOD found in the literature^{27,28]}. The high sensitivity of this system is attributed to high selectivity of MIP implemented previously by Zhu et.al¹⁹ and the high sensitivity of the EIS as reported before²⁹⁻³³. The results demonstrate that the MIP-Fe₃O₄NPs composite is a robust and stable receptor for the electrochemical detection of pesticides.

4.5 References

- [1] M.A. Farajzadeh, B. Feriduni, M.R.A. Mogaddam, *J. Sep. Sci.* 38 (2015) 1002–1009.
- [2] S. Murata, S. Takahashi, T. Agusa, N.J. Thomas, K. Kannan, S. Tanabe, *Mar. Pollut. Bull.* 56 (2008) 641–649.
- [3] B. Antizar-Ladislao, A review, *Environ. Int.* 34 (2008) 292–308.
- [4] M. Astruc, A. Astruc, R. Pinel, *Mikrochimica Acta*, 109 (1992) 83–86.
- [5] I.R. Pereiro, V.O. Schmitt, J. Szpunar, O.F. Donard, R. Lobiński, *Anal. Chem.* 68 (1996) 4135–40.
- [6] E. Turiel, A. Martin-Esteban, *Anal. Bioanal. Chem.* 378 (2004) 1876–1886.
- [7] X. Song, J. Li, S. Xu, R. Ying, J. Ma, C. Liao, D. Liu, J. Yu, L. Chen, *Talanta*. 99 (2012) 75–82.
- [8] J. Carpinteiro, I. Rodríguez, R. Cela, *Anal. Bioanal. Chem.* 380 (2004) 853–857.
- [9] S.C. Cunha, J.O. Fernandes, *J. Chromatogr. A.* 1218 (2011) 7748–7757.
- [10] S.R. Rissato, M.S. Galhiane, F.R.N. Knoll, B.M. Apon, *J. Chromatogr. A.* 1048 (2004) 153–159.
- [11] M.G. Cahill, G. Caprioli, M. Stack, S. Vittori, K.J. James, *Anal. Bioanal. Chem.* 400 (2011) 587–594.
- [12] D.B. Barr, L.L. Needham, *J. Chromatogr. B.* 778 (2002) 5–29.
- [13] G. Aragay, F. Pino, A. Merkoçi, *Chem. Rev.* 112 (2012) 5317–38.
- [14] C.C. Mayorga-martinez, F. Pino, S. Kurbanoglu, L. Rivas, S.A. Ozkan, *J. Mater. Chem. B* (2014) 2233–2239.
- [15] M. Medina-sánchez, C.C. Mayorga-martinez, T. Watanabe, T.A. Ivandini, Y. Honda, F. Pino, K. Nakata, A. Fujishima, Y. Einaga, A. Merkoçi, *Biosens. Bioelectron.* 08/75 (2015) 365–374.
- [16] A. Zamora-Gálvez, A. Ait-Lahcen, L.A. Mercante, E. Morales-Narváez, A. Amine, A. Merkoçi, *Anal. Chem.* 88 (2016) 3578–3584.

- [17] C.C. Mayorga Martinez, E.F. Treo, R.E. Madrid, C.C. Felice, *Biosensors and Bioelectronics* Biosens. Bioelectron. 26 (2010) 1239–1244.
- [18] L. Rivas, C.C. Mayorga-martinez, *Anal. Chem.* 87 (2015) 5167-5172.
- [19] S. Zhu, N. Gan, D. Pan, Y. Li, T. Yang, F. Hu, Y. Cao, D. Wu, *Microchim. Acta.* 180 (2013) 545–553.
- [20] J. He, J. An, D. Zhao, *Magn.* 48 (2012) 4293–4296.
- [21] K. Petcharoen, A. Sirivat, *Mater. Sci. Eng. B.* 177 (2012) 421–427.
- [22] L. Chen, J. Liu, Q. Zeng, H. Wang, A. Yu, H. Zhang, L. Ding, *J. Chromatogr. A.* 1216 (2009) 3710–3719.
- [23] H. Jung, J.-W. Kim, H. Choi, J.-H. Lee, H.-G. Hur, *Appl. Catal. B Environ.* 83 (2008) 208–213.
- [24] X. Liang, S. Zhu, Y. Zhong, J. Zhu, P. Yuan, H. He, J. Zhang, *Appl. Catal. B Environ.* 97 (2010) 151–159.
- [25] T. Braunbeck, D.E. Hinton, B. Streit. *Fish Ecotoxicology.* Basel; Boston: Birkhäuser Verlag, 1998
- [26] U.S. Epa, *Ambient Aquatic Life Water Quality Criteria for Tributyltin (TBT) - Final,* (2003).
- [27] M.D. Mueller, *Anal. Chemie.* 317 (1984) 32–36.
- [28] J. Wu, Z. Mester, J. Pawliszyn, *D J. Anal. At. Spectrom.* 16 (2001) 159–165.
- [29] M. Xu, X. Luo, J. J. Davis, *Biosens. Bioelectron.* 39 (2012) 21–25.
- [30] R.-M. Kong, Z.-L. Song, H.-M. Meng, X.-B. Zhang, G.-L. Shen, R.-Q. Yu, *Biosens. Bioelectron.* 54 (2014) 442–447.
- [31] M. Medina-Sánchez, B. Ibarlucea, N. Pérez, D. D. Karnaushenko, S. M. Weiz, L. Baraban, G. Cuniberti, O. G. Schmidt, *Nano Letters,* 16 (2016) 4288-4296.
- [32] A. Benvidi, N. Rajabzadeh, H. Molaye Zahedi, M. Mazloum Ardakani, M. M. Heidari, L, *Talanta* 137 (2015) 80-86.

- [33] A. Benvidi, M. D. Tezerjani, S. Jahanbani, M. Mazloun Ardakani, S. M. Moshtaghioun, Talanta 147 (2016) 621-627.

CHAPTER 5

Development of a photoluminescent lateral flow based on non-radiative energy transfer for protein detection in human serum.

5.1 Introduction

Lateral flow (LF) represents a powerful technique with high relevance in biosensing as it achieves the requirements needed for biosensor devices, including low cost, small amount of the sample, robustness and stability.

Taking into account that in lateral flow strips the samples are driven by capillary forces, lateral flow strips are generally built with four parts, (i) the sample pad in which the sample is added in the strip; (ii) the conjugate pad, where specific antibodies targeting the analyte are conjugated with nanoparticles (most commonly gold nanoparticles); the detection pad that includes two different lines where the main immunoreactions take place, that is to say the control and test line. The test line is typically printed with antibodies targeting the analyte, while the control line is printed with other antibodies that capture the antibody that is tagged with an optically active material and comes from the conjugate pad. (iv) The absorbent pad, which operates as the pump of the system. Thus, after adding the sample, the labeled antibodies of the conjugate pad flow throughout the detection pad until they reach the test line, where a sandwich immunocomplex is performed provided the analyte is present in the sample, giving a signal depending of the analyte concentration. On the other hand, as mentioned above, the antibodies coming from the conjugate pad are always captured onto the control line to report that the analysis has been carried out correctly. Consequently, this technology can perform fast measurements and does not need qualified staff to be manipulated.¹⁻³ However, LF has some drawbacks, for example at low concentrations of analyte this technology may present problems in terms of sensitivity. Furthermore, its membrane can saturate at high concentrations of the analyte and false negatives may appear as the membrane can be obstructed by different compounds presents in the analysed matrix and provoke unspecific absorptions. In this work, we strive to further LF technology by tackling the drawback of this technique related to its sensitivity.

There is a high demand for the rapid and low-cost determination of proteins,^{4,5} particularly for medical applications. In this context, the most widely used tests are based on colorimetric procedures in which proteins react to produce colorimetric complexes, but nowadays other methods such as fluorimetry,^{6,7} chemiluminescence⁸ and spectrophotometry⁹ are being implemented for protein detection. These techniques represent an improvement in terms of sensitivity and selectivity in comparison with classical methods, such as colorimetric assays.

In particular, we focus on photoluminescence measurements for the detection of a model protein, that is human immunoglobulin G. Photoluminescence has great advantages,^{10,11} including a great sensitivity and excellent specificity, given that the devices intended for photoluminescence measurement are highly specific and less susceptible to interferences as few materials can absorb and emit light. Furthermore, this technique is simply to perform and is fast to measure.

Our research team possesses experience in the usage of photoluminescent techniques and lateral technology flow-based devices.^{12,13} In a previous work, our team reported a photoluminescent LF for the detection of *Escherichia coli* (*E. coli*) using graphene oxide (GO) as a pathogen-revealing agent¹⁴. In that work, *E. coli* was employed as a spacer avoiding non-radiative energy transfer between photoexcited quantum dots (decorated with anti-*E. coli* antibodies and printed on the test line) and GO, which is known to be an excellent quencher of quantum dots.¹⁵ Importantly, using graphene related materials, non-radiative energy transfer is observable up to ~30 nm.¹⁶ In this regard, bacteria is an excellent spacer facilitating the successful operation of the previously reported LF,¹⁷ whereas this LF configuration is not applicable to protein detection since proteins are nanoscaled analytes (around 10 nm). Hence, in this research we engineered a new LF configuration and sought to achieve a highly sensitive photoluminescent lateral flow device for protein detection.

The proposed biosensor consist in a paper-based strip, this approach combines anti-human immunoglobulin G (IgG) antibodies with quantum dots nanocrystals (CdSe@ZnS) as a highly specific photoluminescence probe (Ab-QDs) onto the test line and bare QDs printed onto the control line. Aiming at designing an integrated device, we also employ SiO₂ beads functionalized with anti-human IgG antibodies (Ab-SiO₂) in the respective conjugated pad. Importantly, these SiO₂ beads are able to operate as a powerful spacer between photoexcited QDs and GO, avoiding non-radiative energy transfer as their diameter is greater than the nanoscale (300 – 600 nm). Once the sample is added in the strip, the analyte is selectively captured by the Ab-SiO₂ beads onto the conjugate pad and the sample flows by capillarity throughout the strip until reaching the test line, where a sandwich-like immunocomplex takes place due to the presence of Ab-QDs onto the test line. Eventually, GO is added as a revealing agent and the photoluminescence of those sites protected by the complex Ab-SiO₂/Antigen/Ab-QDs will not be quenched, whereas those photoluminescent sites directly

exposed are expected to be quenched by GO, including the control line reporting that the assay occurred successfully. Hence, the photoluminescence of the test line is modulated by the formation of sandwich-like immunocomplexes (see Figure 5.1).

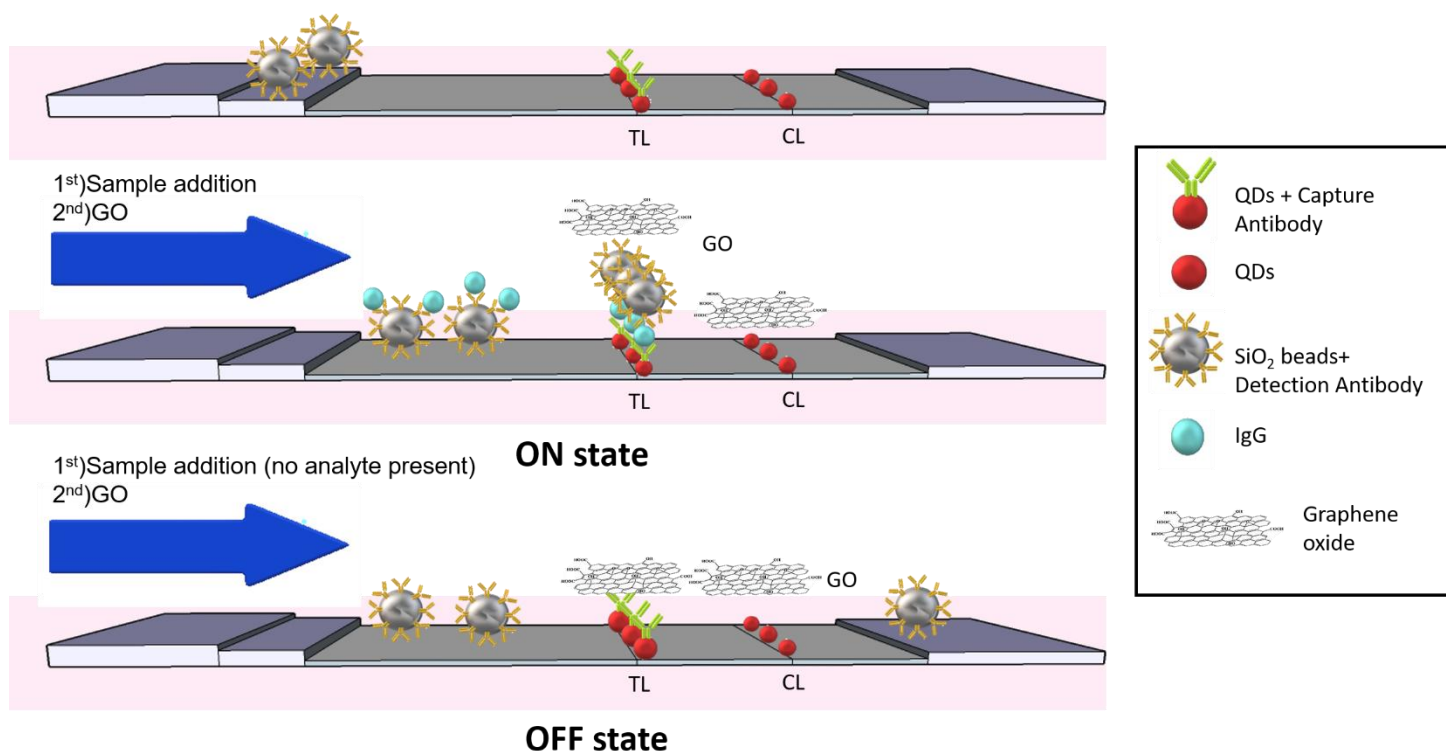


Figure 5.1. Scheme of the developed lateral flow

5.2 Experimental section

5.2.1 Reagents and materials

Streptavidin-Quantum dots 655 were purchased from Life Technologies (Eugene, OR, USA). Anti-human IgG (whole molecule, I1886), Human immunoglobulin depleted serum was purchased from Celprogen (Torrance, CA, USA), IgG (I4506), PBS tablets and Tween 20 were purchased from Sigma Aldrich (Madrid, Spain). Polyclonal antihuman IgG antibody conjugated with biotin (ab6869) and monoclonal Antihuman IgG antibody (ab99759) was purchased from Abcam (Cambridge, UK). SiO₂ beads were purchased from Microparticles GmbH (Berlin, Germany). Graphene oxide was purchased from Angstrom Materials (Dayton, OH, USA), bovine serum albumin, laminated cards (HF000MC100), nitrocellulose membranes

(SHF1800425), sample and adsorbent pads (CFSP001700) were purchased from Millipore (Billerica, MA, USA).

An ESEQuant lateral flow reader from Qiagen GmbH (Stockach, Germany) was used to perform measurements on the LF strips. Biospot Bt-500 reagent dispensing system from Biofluidix (Freiburg, Germany). TS-100 thermoshaker from Biosan (Riga, Latvia) was utilized to perform the conjugation of QDs with antibodies. JP Selecta 2000210 oven from JP selecta (Barcelona, Spain) was used to dry lateral flow strips. SEM analysis was performed using FEI Magellan (Hillsboro, Oregon, USA).

5.2.2. Lateral flow strip preparation.

Conjugation of QDs with antibodies. Biotinylated antibodies were easily conjugated with streptavidin-QDs. Streptavidin-QDs and biotinylated anti-IgG, were mixed at final concentrations of 8nM (QDs) and 300 $\mu\text{g mL}^{-1}$ (anti-IgG), respectively, using a thermoshaker set at 600 rpm and 4 °C for two hours. This conjugation was carried out in immunobuffer (that is, PBS + 1% BSA + Tween 20 0.5%).

The conjugate pad was impregnated with antibody-decorated SiO₂ beads with anti-IgG. Firstly, the conjugate is created by applying successive washing steps in a suspension the SiO₂ beads. To do that, 75 μL of the stock suspension of the beads was added in 925 μL of PBS buffer. The suspension was then shaken at 650 rpm during 10 minutes and centrifuged at 5000 rpm for 1min in order to precipitate the particles, and facilitate the subsequent removal of the supernatant. To complete the particle washing, the process is repeated three times using PBS, once using PBS supplemented with Tween 20 at 0.05% (PBST) and once with Immunobuffer. Next, 1 mL of anti-human IgG concentrated at 500 $\mu\text{g mL}^{-1}$ in Immunobuffer is added in the pellet of the previously washed particles and this suspension was shaken at 600 rpm for 2h at 4°C. After this process is finished, a glass fiber strip was soaked by drop casting with the Ab-SiO₂ beads conjugate suspension, and dried at room temperature overnight.

The fabrication of the strips is divided in three parts, (i) assemblage of the detection pad onto the laminated card and and printing of the test and control line onto the detection pad using the Isoflow reagent dispensing system. Antibody-decorated QDs are printed onto the test line, while bare QDs are printed onto the control line and these laminated cards are stored overnight in the fridge (at 8 °C). (ii) Blocking of the detection pad by adding 5 mL of immunobuffer in the laminated card and storing the strip for 15 min in the fridge. Next, the

strip is dried in an oven at 37°C for 90 min. (iii) Sample and absorbent pads are washed and assembled onto the laminated card. This washing procedure involves a washing procedure through ultrapure water, PBST and immunobuffer and a drying process overnight at room temperature. After that the sample and absorbent pads can be assembled onto the laminated card along with the conjugate pad. We normally manufacture strips that are 6 mm with size.

5.2.3 Overall measurement procedure

Human IgG protein was analyzed at different concentrations ranging from 65 ng mL⁻¹ to 1 µg mL⁻¹ in immunobuffer. The starting intensity of the lateral flow strip was determined using the ESEQuant lateral flow reader. After adding 100 µL of the sample onto the sample pad, 15 minutes are given for the sample to flow throughout the strip and arrive in the absorbent pad, which is the last part of strip. Next, the strip is dried using an oven at 37°C for 1 hour, and 100 µL of an aqueous dispersion of GO concentrated at 90 µg mL⁻¹ (see Figure S) was added in the sample pad as a revealing agent using the same aforementioned drying procedure (37 °C for 1 hour). Eventually, the strips are measured using the lateral flow reader. The assays implying human serum analysis may require a washing step before GO addition. To this end, 100 µL of immunobuffer were added in the sample pad in order to eliminate impurities and minimize the matrix effect.

5.3 Results and discussion.

5.3.1 System Optimization

As the assay depends on photoluminescent signals, we firstly optimized the concentration of the involved QDs. To this end, a strong photoluminescent signal hindering saturation of the LF reader should be chosen, whereas weak photoluminescent signals should be avoided. Consequently, as depicted in Figure 5.2, we printed different QD concentrations (from 4 to 11 nM) onto various strips and measured their intensities utilizing a lateral flow reader (excitation wavelength of 365 nm, emission filter centered at 670 nm). Through these experiments we determined that 8 nM was an optimal concentration of this reagent as it displays a strong intensity of up to 75% of the dynamic range of the LF reader, thus avoiding saturation.

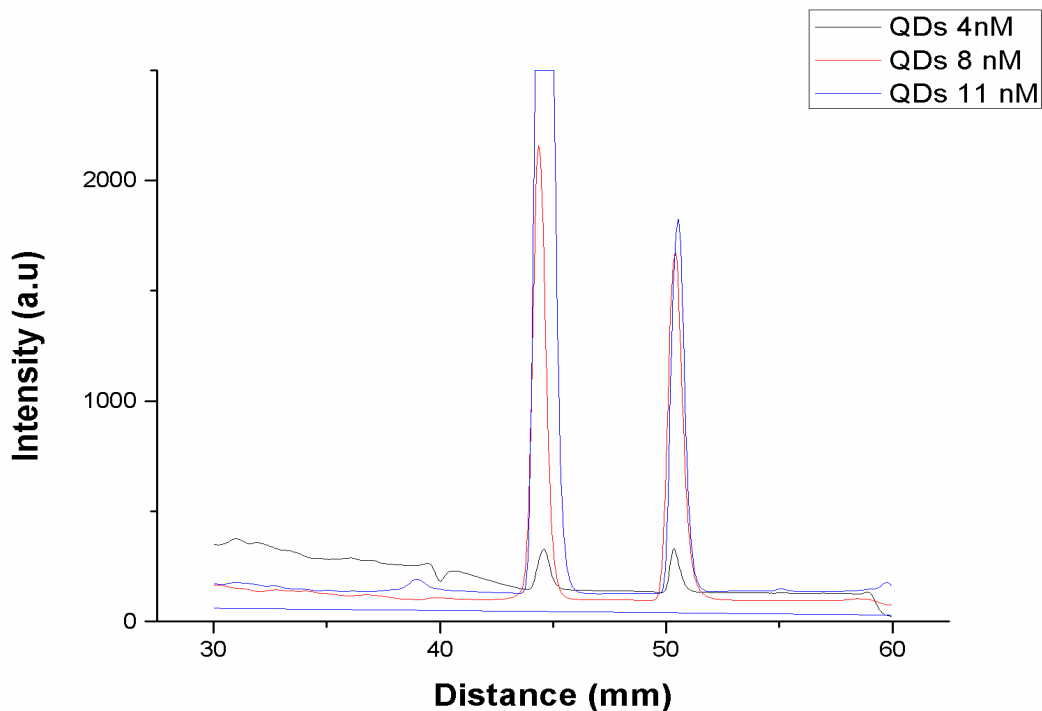


Figure 5.2. Optimization of QDs concentration.

We then explored different concentrations of GO so as to reach the maximum quenching of QDs in terms of the ratio initial intensity (before GO) / final intensity (after GO). To this end, different water-based suspensions of GO were directly added in the sample pad of several strips printed with QDs concentrated at 8 nM. Among several concentrations of GO, ranging from 70 to 120 $\mu\text{g mL}^{-1}$, a GO concentration of 90 $\mu\text{g mL}^{-1}$ was picked to yield a maximum quenching efficiency around 85% in both lines, test and control line, avoiding saturation of the flow due to a saturation of GO in the strip as it occurs with higher GO concentrations (see Figure 5.3). It is worth mentioning that according to the manufacturer's characterization, the GO monolayer we are employing has an average lateral size of 500 nm and a carbon / oxygen ratio around 1.

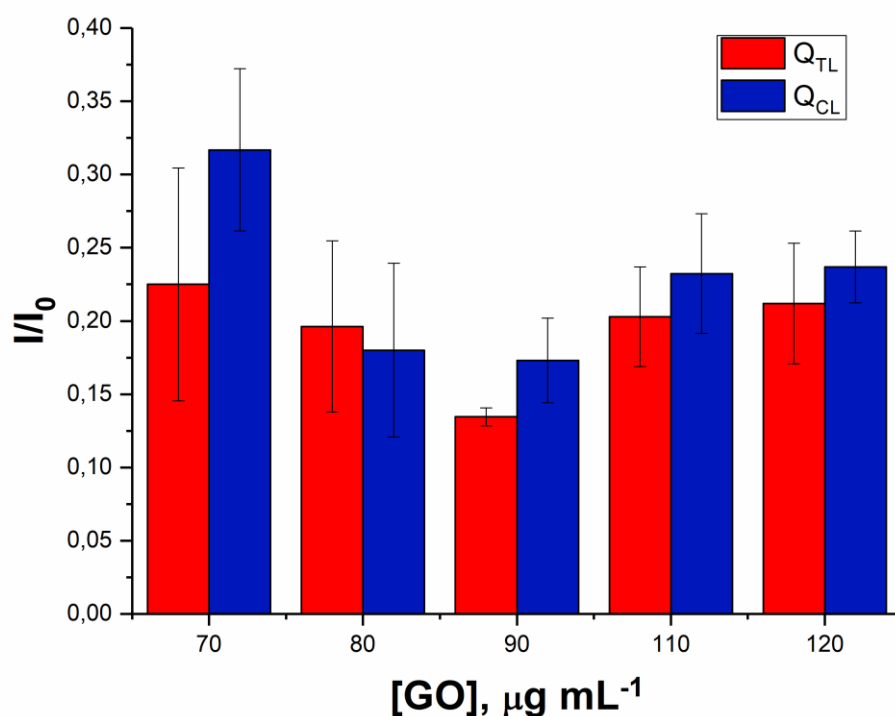


Figure 5.3. Optimization of graphene oxide concentration.

In order to optimize the spacer agent avoiding highly efficient non-radiative energy transfer, we also investigated two sizes of SiO_2 beads utilized as spacers between photoexcited QDs and GO, including monodispersed beads of 300 and 650 nm respectively (see Figure 5.4). To this end, SiO_2 beads were previously conjugated to anti human IgG antibodies and embedded into the conjugation pad as described in the experimental section. We carried out our LF approach using a standard buffer as a matrix, from now and the termed as immunobuffer, that is a mixture of phosphate-buffered saline 0.01M, bovine serum albumin 1% w/v, and Tween 20 0.5%, and different concentrations of the analyte, ranging from 65 to 1000 ng mL^{-1} . Blank samples were also analyzed.

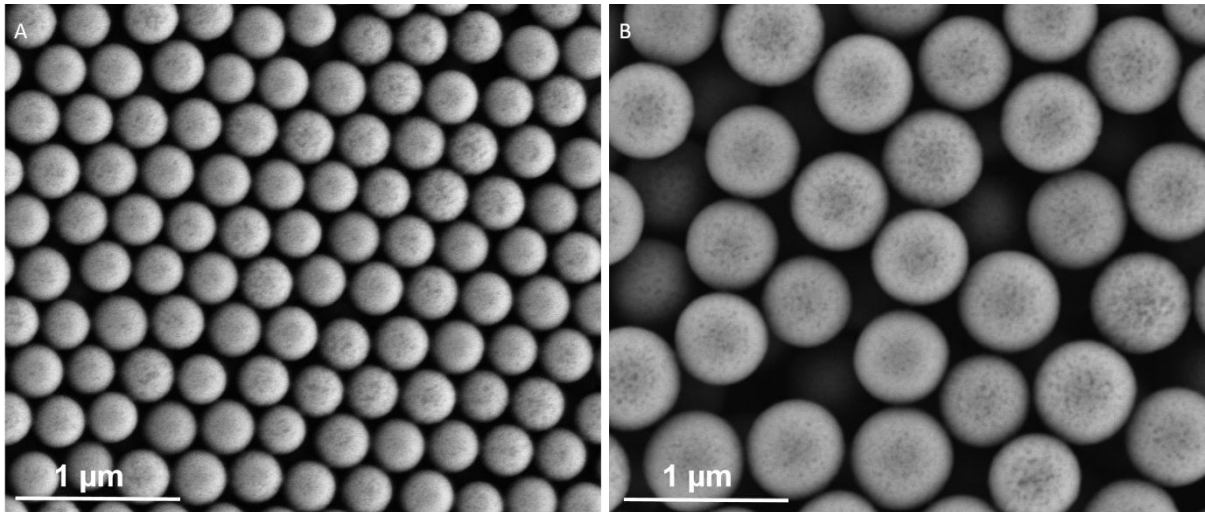


Figure 5.4. SEM micrographs of SiO₂ NPs of (A) 300nm and (B) 650 nm

Figure 5.5 Overall sensitivity achieved by these assays, shows that the usage of SiO₂ beads of 650 nm facilitates a better sensitivity in the assay probably due to its better efficiency as a bigger spacer that simultaneously amplifies the protected area that will not be quenched by GO.

Figure 5.6 shows the relationship between the analyte concentration and the quenching effect in the proposed LF approach, in where the highest concentrations of the analyte trigger the strongest photoluminescent signals, as quenching is avoided due to the operational principle of this biosensing approach. Hence, the quenching of the test line; Q_{TL} , defined as the final intensity of the test line divided by the initial intensity of the test line, has maximum values around 0.8 units, whereas the quenching of the control line; Q_{CL} , similarly defined as Q_{TL} , remains constant with values of less than 0.2 units. On the contrary, the lowest concentrations of the analyte give rise to highly efficient non-radiative energy transfer since SiO₂ beads are scarcely present and thus GO is able to interact directly with the photoluminescent probes, mainly by physical adsorption forces, pi-pi stacking interactions and hydrogen bonding forces that can occur between GO and biomolecules such as proteins¹⁷. Consequently, the Q_{TL} values tend to approximate to those values of the Q_{CL} .

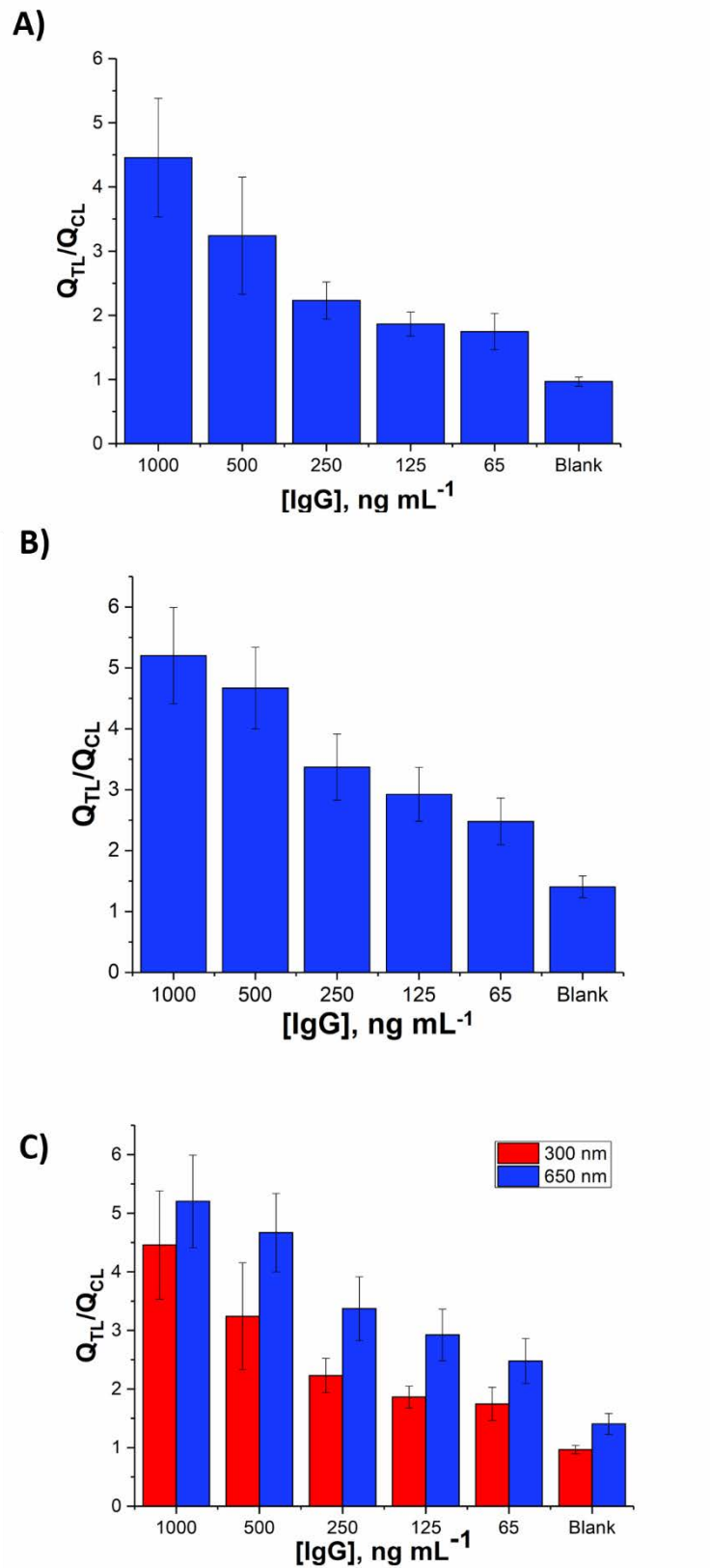


Figure 5.5. Optimization of SiO₂ NPs size, a) 300 nm, b) 650nm and c) comparative graphic

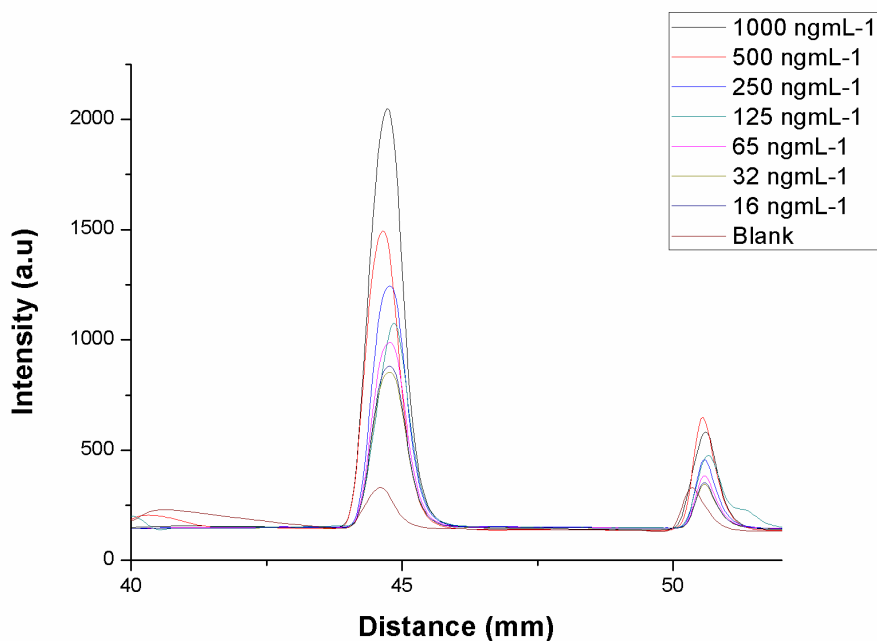


Figure 5.6. Profile of the photoluminescent intensity of the explored lateral flow strips at different concentrations of IgG.

5.3.2 Characterization

In order to confirm the operational principle of the proposed LF strip, we investigated its different components via scanning electron microscopy (SEM). The SEM micrographs in Figure 5.3 reveal how SiO₂ beads are efficiently anchored onto the test line (Figure 5.7A) and absent onto the control line (Figure 5.7B) due to the highly specific aforementioned immunoreaction. Panels B and D in Figure 5.7 display GO-coated LF strips, confirming that GO is able to flow throughout the strip and interact with the control and test line.

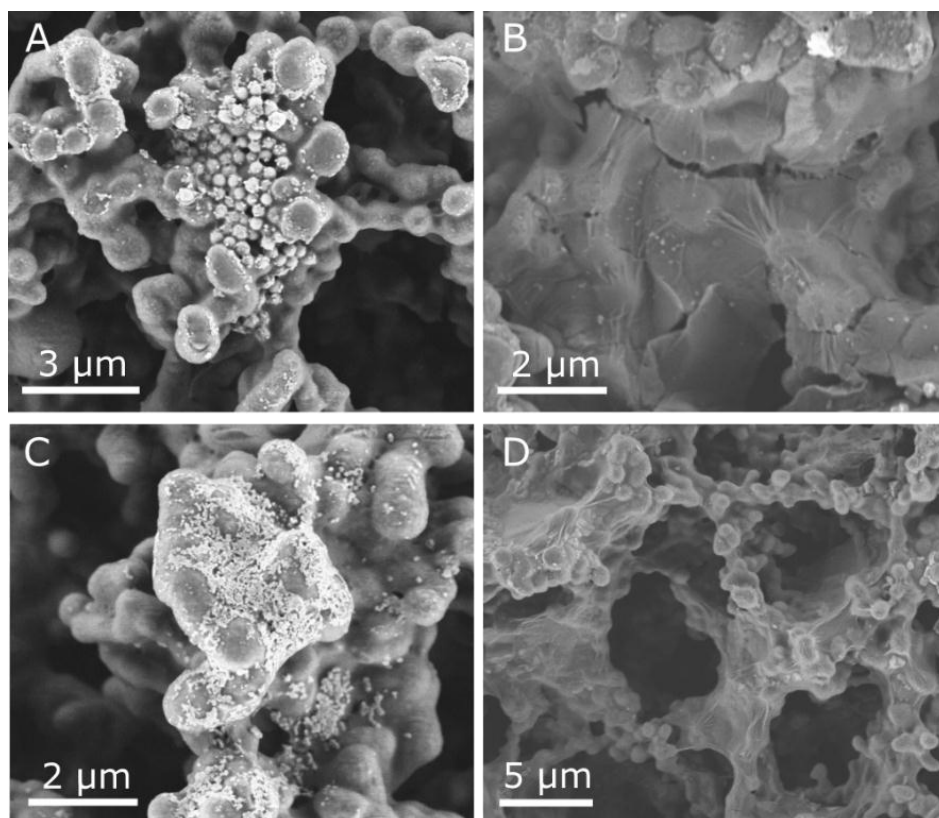


Figure 5.7. SEM micrographs of the lateral flow strip. Test line before adding GO (A) and after GO addition (B). Control line before adding GO (C) and after GO addition (D).

5.3.3 Protein measurement in buffer and in real samples.

Figure 5.8B displays a normalization in terms of the Q_{TL}/Q_{CL} ratio and the limit of detection (LOD) was calculated using this ratio in the analyzed blank sample plus 3 times its standard deviation. The LOD was determined to be c.a. 3.64 ng mL^{-1} (Figure 5.10A). At this point, this LF approach starts becoming advantageous in terms of LOD when compared with other LF approaches targeting IgG as it can be observed in Table 5.1. However, we sought to improve the LOD of the LF approach even further. To this end, we replaced the capture polyclonal antibody of the test line by a monoclonal antibody. It is well-known that monoclonal antibodies are able to improve both, sensitivity and specificity in immunoassays.¹⁸ Hence, we tested this new configuration following the methods detailed in the experimental section and found that the usage of such a monoclonal antibody benefited the LOD of the LF approach. Figure 5.8C-D depicts the overall biosensing performance of this

new configuration exhibiting a LOD of c.a. 1.35 ng mL^{-1} , obtaining a significant improvement in the system sensitivity compared with the conventional methods. Figure 5.10B displays the corresponding calibration curve.

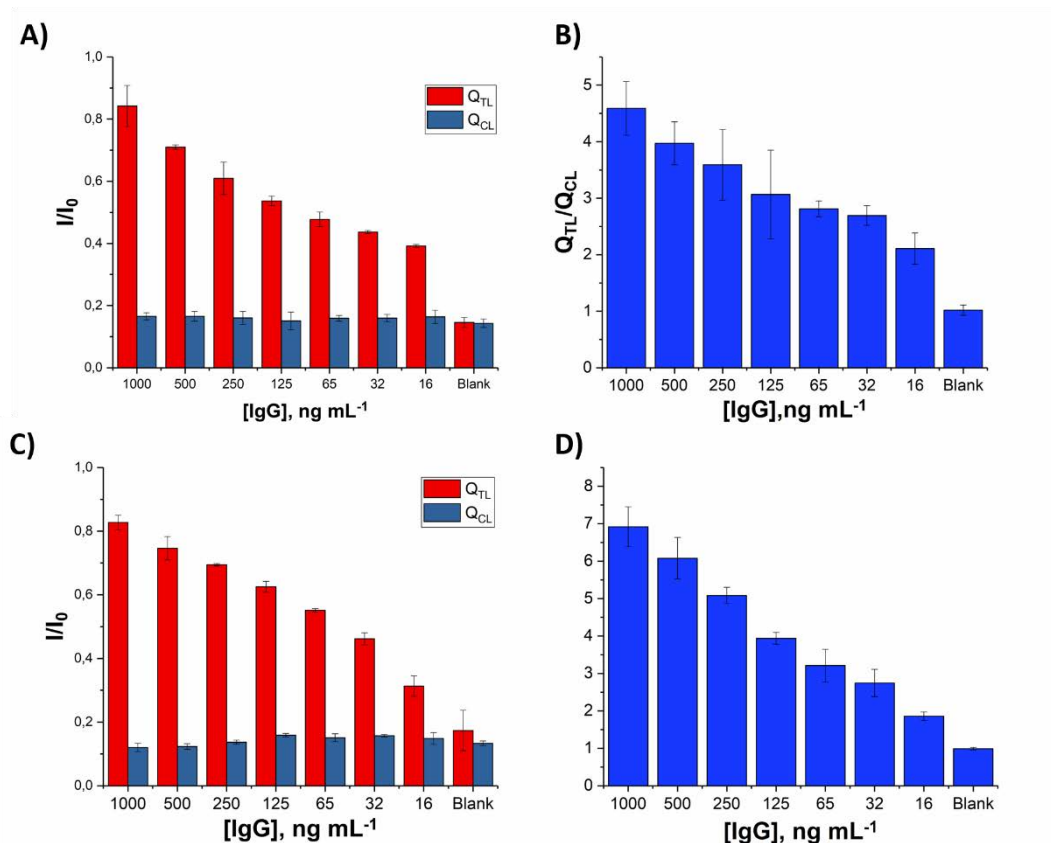


Figure 5.8. Representation of measurements in standard buffer for test and control line of each concentration of IgG (a), the bars represents % of quenching (coefficient of final intensity and initial), (b) normalized values (Q_{TL}/Q_{CL}) and (c) same experiment using monoclonal antibody, (d) normalized values.

Moreover, in order to prove that this approach can be applied in real sample analyses, the resulting LF strip was also employed in human serum analysis. We employed human immunoglobulin (IgG/IgM/IgE)-depleted serum as a complex matrix that we spiked with different concentrations of IgG, ranging from 1000 ng mL^{-1} until 16 ng mL^{-1} (see Figure 5.9). Blank samples of this matrix were also analyzed. The prepared solutions can be directly added in the strip, though a washing step is necessary in order to remove possible interferences

contained in such a complex matrix. This washing process was performed by adding 100 μL of immunobuffer once the sample is dried in the strip. After performing a calibration curve, the limit of detection this approach in human serum was 6.30 ng mL^{-1} , calculated using the aforementioned definition of LOD (see Figure 5.10C). It is obvious that the matrix effect affects the overall analytical performance; however, this effect is well known in immunoassays,¹⁹ and these experiments demonstrate the high sensitivity and selectivity of the proposed lateral flow approach even in a complex matrix.

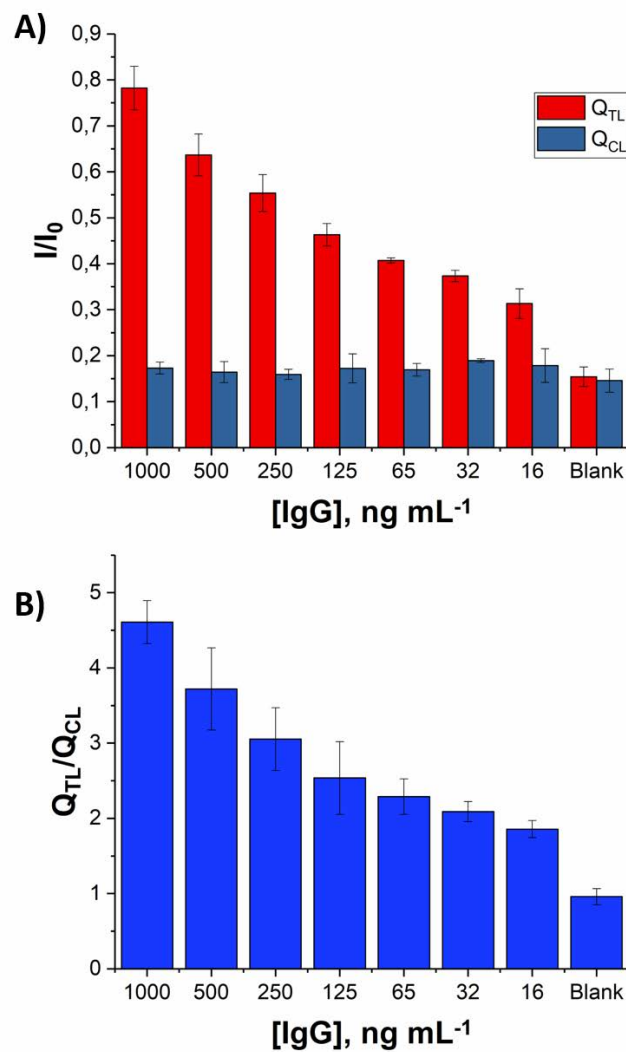


Figure 5.9. Results of measurements in human serum. (A) Comparison of TL and CL of each strip (B) normalized values

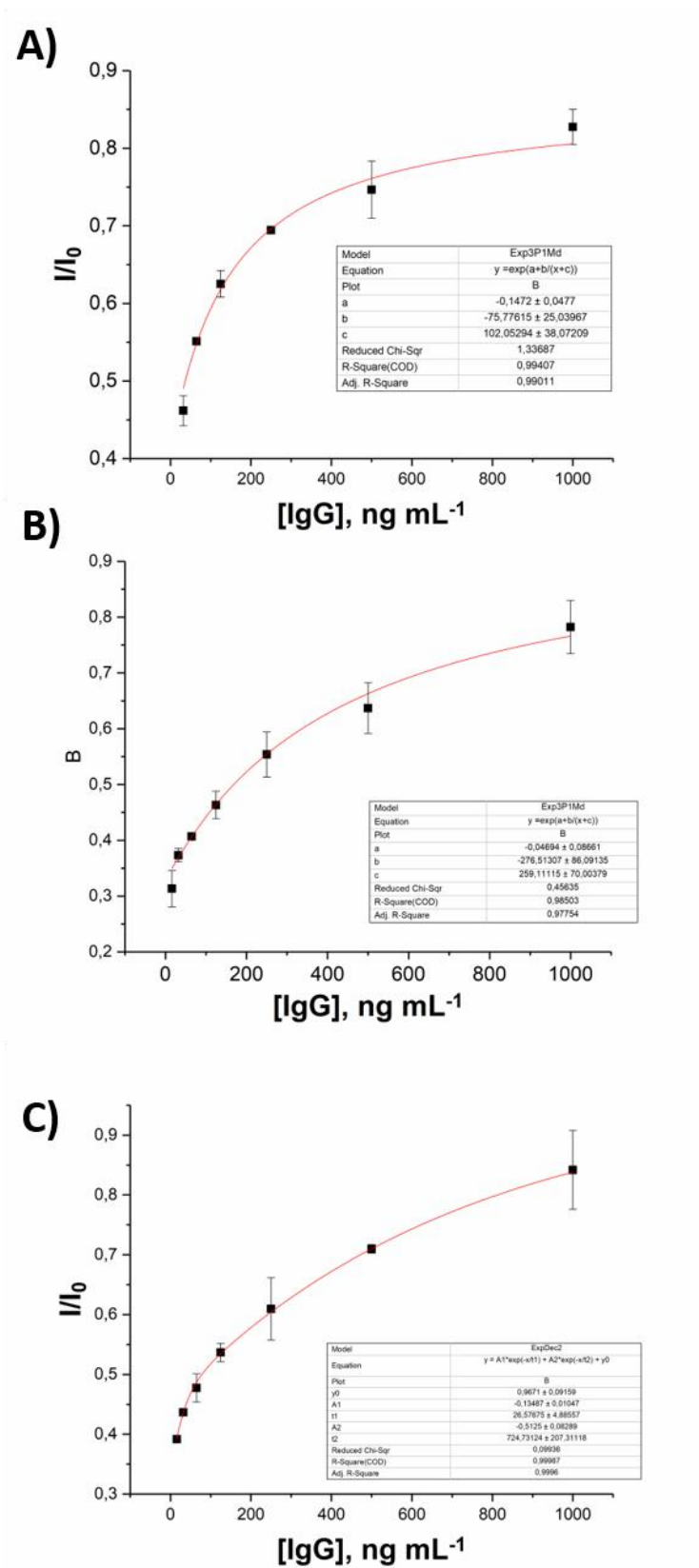


Figure 5.10. Calibration curve of IgG measurements with polyclonal (a) and monoclonal (b) antibody and in human serum (c).

Table 5.1. Comparison of LOD for IgG detection.

LF strategy	Range	LOD	Technique	REF
Conventional LF	5-500 ng mL ⁻¹	8-12 ng/mL	Colorimetric	20
LF with wax pillars onto the detection pad	5-500 ng mL ⁻¹	6,6 ng/mL	Colorimetric	21
gold nanoparticles loaded with enzymes	2-10 ng mL ⁻¹	2 ng mL ⁻¹	Colorimetric	20
LF QDs-GO (this work)	1-20 ng mL ⁻¹	1,35 ng mL ⁻¹	Fluorescence	-

5.4 Conclusions.

A novel design based on lateral flow technology in combination with quantum dots and the usage of graphene oxide as revealing agent for specific, selective and highly sensitive protein detection has been explored. The overall analytical performance of the system was successfully explored in different matrices, including standard buffer and human serum, showing an advantageous limit of detection of 1.35 ng mL⁻¹ and 6.30 ng mL⁻¹, respectively. In comparison with other lateral flow immunoassays targeting human IgG, the developed biosensor presents excellent results in terms of LOD and its adequate behavior in human serum analysis proves that it can be a valuable tool in real sample analysis.

Besides, LFA is a versatile and easy adaptable technique. Each component of the system can be easily modified with the aim of adapting the assay to a different target, obtaining the possibility of a multidetection platform. The good point of paper-based diagnostics is that there are suitable for large scale production, making them a very cheap and efficient technology. This result could open the way to the use this LF in more diagnostics applications, especially in a medical or laboratory context, due to the lower limit of quantification obtained and improvement of the actual techniques for immunoglobulins detection with lateral flow.

5.5 References.

- (1) Posthuma-Trumpie, G. A.; Korf, J.; Van Amerongen, A. *Anal. Bioanal. Chem.* **2009**, *393* (2), 569–582.
- (2) Quesada-González, D.; Merkoçi, A. *Biosens. Bioelectron.* **2015**, *73*, 47–63.
- (3) Sajid, M.; Kawde, A. N.; Daud, M. J. *Saudi Chem. Soc.* **2015**, *19* (6), 689–705.
- (4) Fredriksson, S.; Gullberg, M.; Jarvius, J.; Olsson, C.; Pietras, K.; Gústafsdóttir, S. M.; Östman, A.; Landegren, U. *Nat. Biotechnol.* **2002**, *20* (5), 473–477.
- (5) Vollmer, F.; Braun, D.; Libchaber, A.; Khoshsim, M.; Teraoka, I.; Arnold, S. *Appl. Phys. Lett.* **2002**, *80* (21), 4057–4059.
- (6) Zhang, Z.; Sharon, E.; Freeman, R.; Liu, X.; Willner, I. *Anal. Chem.* **2012**, *84* (11), 4789–4797.
- (7) Xue, L.; Zhou, X.; Xing, D. *Anal. Chem.* **2012**, *84* (8), 3507–3513.
- (8) Roda, A.; Guardigli, M. *Anal. Bioanal. Chem.* **2012**, *402* (1), 69–76.
- (9) Boja, E. S.; Rodriguez, H. *Proteomics* **2012**, *12* (8), 1093–1110.
- (10) Wang, Y.; Ni, Y. *Anal. Chem.* **2014**, *86* (15), 7463–7470.
- (11) Yi, Y.; Deng, J.; Zhang, Y.; Li, H.; Yao, S. *Chem. Commun.* **2013**, *49* (6), 612–614.
- (12) Zor, E.; Morales-Narváez, E.; Zamora-Gálvez, A.; Bingol, H.; Ersoz, M.; Merkoçi, A. *ACS Appl. Mater. Interfaces* **2015**, *7* (36), 20272–20279.
- (13) Gravagnuolo, A. M.; Morales-Narváez, E.; Matos, C. R. S.; Longobardi, S.; Giardina, P.; Merkoçi, A. *Adv. Funct. Mater.* **2015**, *25* (38), 6084–6092.
- (14) Morales-Narváez, E.; Naghdi, T.; Zor, E.; Merkoçi, A. *Anal. Chem.* **2015**, *87* (16), 8573–8577.
- (15) Morales-Narváez, E.; Pérez-López, B.; Pires, L. B.; Merkoçi, A. *Carbon N. Y.* **2012**, *50* (8), 2987–2993.
- (16) Gaudreau, L.; Tielrooij, K. J.; Prawiroatmodjo, G. E. D. K.; Osmond, J.; de Abajo, F. J. G.; Koppens, F. H. L. *Nano Lett.* **2013**, *13* (5), 2030–2035.
- (17) Morales-Narváez, E.; Hassan, A.-R.; Merkoçi, A. *Angew. Chemie Int. Ed.* **2013**, *52* (51), 13779–13783.
- (18) Deguchi, R.; Matsushima, M.; Suzuki, T.; Mine, T.; Fukuda, R.; Nishina, M.; Ozawa, H.;

Takagi, A. *J. Gastroenterol.* **2009**, *44* (7), 713–716.

- (19) Morales-Narváez, E.; Guix, M.; Medina-Sánchez, M.; Mayorga-Martinez, C. C.; Merkoçi, A. *Small* **2014**, *10* (13), 2542–2548.
- (20) Parolo, C.; de la Escosura-Muñiz, A.; Merkoçi, A. *Biosens. Bioelectron.* **2013**, *40* (1), 412–416.
- (21) Rivas, L.; Medina-Sanchez, M.; de la Escosura-Muniz, A.; Merkoci, A. *Lab Chip* **2014**, *14* (22), 4406–4414.

CHAPTER 6

General conclusions and future perspectives

6.1 General conclusions.

Since the specific conclusions are exposed for each one of the different technologies / chapters, in this part some general conclusions are reported.

Different innovative and advantageous platforms for sensing different kinds of analytes such as pesticides, sulfonamides and proteins have been developed. First group of platforms is based on molecularly imprinted polymers (MIPs) for the detection of tributyltin and sulfamethoxazole. The detection system is based on screen printed carbon electrodes (SCPE) and electrochemical impedance spectroscopy (EIS) as transduction method. The resulted sensors based on MIPs have shown better analytical performance in terms of sensitivity, selectivity and stability in comparison to detection systems reported so far for the same analytes.

The other designed platform is a lateral flow immunoassay (LFA). This is based on an innovative detection principle combining quantum dots with the usage of graphene oxide as revealing agent for specific, selective and highly sensitive protein detection. The developed strategy represents an improvement regarding a conventional lateral flow method reported before using QDs and GO and restricted to rather big size analytes (ex. bacteria). The new LFA can now be applied to any kind of analyte, independently of its size, with interest for diagnostics (environment or health).

The platforms designed and fabricated during this thesis have been shown to be:

- Sensitive: Low limits of detection in ppb, pM and ng mL⁻¹ levels are obtained, which represent an important improvement in their respective research fields for the bio/sensors developed here.
- User friendly sensors: Each detection system requires only few steps.
- Cost efficient: given the relatively cheap materials used (plastic, paper etc.) the production cost of the developed bio/sensors may be too low (less than 1 €)
- Portability: The developed bio/sensors can be easily miniaturized and are related to hand held instruments.

6.2 Future perspectives.

Thanks to the unique properties that the nanomaterials exhibit, the possibility to develop new (bio)sensing strategies with improved analytical performance is continuously increasing. Combination of nanomaterials with chemical and biological receptors is offering unprecedented sensing systems with interest for various fields.

Of great interest are molecularly imprinted polymers that can be implemented in real time monitoring of pesticides in sea or river water. Currently these materials applied in chromatography separation^{1,2} or treatment of hazard compounds in sea water or direct determination³ also can be implemented in continuous monitoring⁴. This is related to the high benefits offered by these materials, their high stability, the resistance to elevated temperature and pressure, inertness toward acids, metal ions or organic solvents.

Another challenge to the future of molecular imprinted technology is their use in biomedical assays. Nowadays is not quite common the use of MIPs for biological purpose, but for example in the case of proteins, more publications showing the use of MIPs for proteins detection are appearing. Given the development of molecular computational techniques and the use of nanomaterials MIPs may be an alternative to expensive biological receptors (ex. antibodies) for future biomedical applications.

Regarding lateral flow platform for immunoglobulin detection its easy modification can be previewed with the aim of adapting the assay to different other targets. In addition the possibility exist to perform multidetection of proteins, cells etc. by using different receptors. This will open the way to interesting clinical and biotechnological applications.

The developed platforms still need further integration so as to be more compact, stable and easy to be applied reducing the necessary assay steps. This will require further efforts in nanomaterials immobilization (ex. graphene oxide in the paper-based platforms) in addition to materials standardization that is crucial for the mass production and commercialization of the developed devices. A deeper study of the interferences in real sample applications is another important issue that would deserve further efforts.

Annex

7.1 Compendium of publications

- 1) A. Zamora-Gálvez, A. Ait-Lahcen, L.A. Mercante, E. Morales-Narváez, A. Amine, A. Merkoçi, Molecularly Imprinted Polymer-Decorated Magnetite Nanoparticles for Selective Sulfonamide Detection, *Anal. Chem.* 88 (2016) 3578–3584. doi:10.1021/acs.analchem.5b04092.
- 2) A. Zamora-Gálvez, C.C. Mayorga-Matinez, C. Parolo, J. Pons, A. Merkoçi, Magnetic nanoparticle-molecular imprinted polymer: A new impedimetric sensor for tributyltin detection, *Electrochem. Commun.* (2017). doi:10.1016/j.elecom.2017.07.007.
- 3) Graphene quantum dots based photoluminescence sensor: a multifunctional composite for pesticide detection
- 4) E. Morales-Narváez, L. Baptista-Pires, A. Zamora-Gálvez, A. Merkoçi, Graphene-Based Biosensors: Going Simple, *Adv. Mater.* 29 (2017). doi:10.1002/adma.201604905.
- 5) L. Rivas, C.C. Mayorga-Martinez, D. Quesada-González, A. Zamora-Gálvez. Label-Free Impedimetric Aptasensor for Ochratoxin - A Detection Using Iridium Oxide Nanoparticles, (2015). doi:10.1021/acs.analchem.5b00890

Molecularly Imprinted Polymer-Decorated Magnetite Nanoparticles for Selective Sulfonamide Detection

Alejandro Zamora-Gálvez,^{†,§} Abdellatif Ait-Lahcen,^{†,‡,§} Luiza A. Mercante,^{†,||} Eden Morales-Narváez,[†] Aziz Amine,[‡] and Arben Merkoçi^{*,†,⊥}

[†]Catalan Institute of Nanoscience and Nanotechnology (ICN2), CSIC and The Barcelona Institute of Science and Technology, Campus UAB, Bellaterra, 08193 Barcelona, Spain

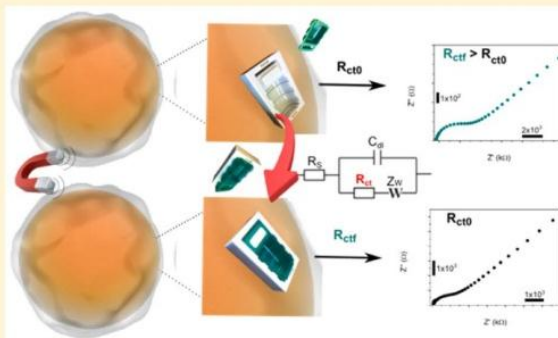
[‡]Faculty of Science and Techniques, Hassan II University of Casablanca, B.P.146, 20650, Mohammedia, Morocco

^{||}National Laboratory for Nanotechnology in Agribusiness (LNNA), Embrapa Instrumentation, 13560-970, São Carlos, São Paulo Brazil

[⊥]ICREA—Catalan Institution for Research and Advanced Studies, Barcelona, 08010, Spain

Supporting Information

ABSTRACT: Sulfonamides are known not only to be antimicrobial drugs that lead to antimicrobial resistance but also to be chemotherapeutic agents that may be allergenic and potentially carcinogenic, which represents a potentially hazardous compound once present in soil or water. Herein, a hybrid material based on molecularly imprinted polymer (MIP)-decorated magnetite nanoparticles for specific and label-free sulfonamide detection is reported. The composite has been characterized using different spectroscopic and imaging techniques. The magnetic properties of the composite are used to separate, preconcentrate, and manipulate the analyte which is selectively captured by the MIP onto the surface of the composite. Screen printed electrodes have been employed to monitor the impedance levels of the whole material, which is related to the amount of the captured analyte, via electrochemical impedance spectroscopy. This composite-based sensing system exhibits an extraordinary limit of detection of $1 \times 10^{-12} \text{ mol L}^{-1}$ ($2.8 \times 10^{-4} \text{ ppb}$) ($S/N = 3$), which is close to those obtained with liquid chromatography and mass spectrometry, and it was demonstrated to screen sulfamethoxazole in a complex matrix such as seawater, where according to the literature sulfonamides content is minimum compared with other environmental samples.



Since the midtwentieth century, sulfonamides have been extensively exploited as antimicrobial agents in humans and animals.^{1–3} On the one hand, it is well-known that the use of antibiotics leads to antimicrobial resistance, which is an international serious concern.⁴ On the one hand, sulfonamides have been reported not only to elicit dermatological eruptions,⁵ but also to be potentially carcinogenic among other health consequences.^{2,3} On the other hand, medical treatments, livestock and aquaculture operations of an exponentially growing human population have a great demand for sulfonamides compounds, which may reach the environment through wastewater from pharmaceutical or food chains involving human and animal waste. In fact, it is estimated that every year more than 20 thousand tons of sulfonamides reach the global environment.¹ Therefore, as a potential health threat, highly sensitive monitoring of sulfonamide residues is relevant to enforce food safety and environmental quality.

Dmitrienko et al. have recently performed a broad study on the recent trends toward sulfonamides detection.¹ Sulfonamide residues are generally screened using time-consuming but

highly sensitive, robust and reliable methods involving complex apparatus operated by skilled personnel; for instance, liquid chromatography,^{6,7} mass spectrometry^{8,9} or capillary electrophoresis.^{10,11} Consequently, alternative antibiotic residues screening methods such as immunoassays and biosensing platforms are rising considerably.³ These alternatives are leading to a promising analytical performance in terms of sensitivity; for example, they bear limits of detection of up to $5 \times 10^{-2} \text{ ppb}$.¹ However, they have not been reported to be as sensitive and have limits of detection as those achieved by solid-phase extraction working in synergy with liquid chromatography/mass spectrometry, which has been reported to be up to $9 \times 10^{-5} \text{ ppb}$.¹

Biosensing technology incorporates biorecognition elements integrated with a transducing system that leads to a specific signal upon analyte recognition. The signal can be optical,

Received: October 28, 2015

Accepted: March 2, 2016

Published: March 3, 2016

electrochemical or mechanical among others; whereas enzymes, antibodies, oligonucleotides or other biomolecules can be exploited as biorecognition elements. However, biosensing technology is also taking advantage of biomimetic recognition elements such as molecularly imprinted polymers (MIPs),^{12,13} for example when biorecognition elements targeting small molecules are technically difficult to obtain.¹⁴ MIPs are synthetic polymers typically obtained by copolymerization of a monomer with a cross-linker in the presence of a template molecule.¹⁵ The shape, size, and functionalities of MIPs are complementary to the target analyte, which is used as template molecule. Consequently, they can selectively recognize and bind specific target molecules through noncovalent strength interactions between the host matrix and the guest molecule, including van der Waals force, hydrogen bonding, electrostatic features, hydrophobic phenomena and metal-ion coordination.¹⁶

Herein, a composite material based on molecularly imprinted polymer (MIP) and Fe₃O₄ superparamagnetic nanoparticles (MNPs) that is designed to specifically detect sulfamethoxazole (SMX)^{17–21} (SMX) with extraordinary sensitivity is reported. Scanning electron microscopy (SEM), transmission electron microscopy (TEM), X-ray photoelectron spectroscopy (XPS) and Fourier transform infrared spectroscopy (FT-IR) have been utilized to characterize the proposed hybrid material. The superparamagnetic properties of the composite are utilized to preconcentrate, separate and manipulate the analyte which is selectively captured by the MIP onto the surface of the composite. On the other hand, disposable screen printed electrodes, have been used to monitor the impedance levels of the whole material, which is related to the amount of the captured analyte via electrochemical impedance spectroscopy, facilitating a simple and label-free sensing platform (see Figure 1).

EXPERIMENTAL SECTION

Chemicals and Materials. Sulfamethoxazole, sulfadiazine, sulfacetamide, dimethyl sulfoxide, acetic acid, methacrylic acid, iron chloride (II), iron chloride (III), ammonium hydroxide, polyvinylpyrrolidone, oleic acid, 2,5-Bis(tertbutylperoxy)-2,5-dimethylhexane, potassium hexacyanoferrate (II) and potassium hexacyanoferrate (III) were purchased from Sigma-Aldrich (Madrid, Spain). Methanol was purchased from Labbox (Vilassar de Dalt, Barcelona, Spain). Stock solutions of sulfamethoxazole, sulfadiazine and sulfacetamide were prepared in methanol/water (1:1, v/v). Seawater samples were extracted from Poblenou Beach (Barcelona, Spain). Seawater samples were filtered using filter paper and then a nitrocellulose membrane (0.025 μm, Millipore, Billerica, Massachusetts, USA).

TEM analysis was performed using a FEI TECNAI G2 F20 (Hillsboro, Oregon, USA). XPS analysis was carried out with a Phoibos 150 analyzer (SPECS GmbH, Berlin, Germany) in ultrahigh vacuum conditions (1×10^{-10} mbar) with a monochromatic aluminum K-alpha (K α) X-ray source (1486.74 eV). The energy resolution (0.58 eV) was measured by the full width at half-maximum intensity of the Ag 3d^{5/2} peak for a sputtered silver foil. SEM analysis was performed using a FEI Magellan (Hillsboro, Oregon, USA) and FT-IR analysis was carried out by IR-ATR (attenuated total reflectance) for direct measuring, model IR Tensor 27 (Bruker, Billerica, Massachusetts, USA). A computer-controlled Autolab PGSTAT-12 (302N-High performance) (potentiostat/galvano-

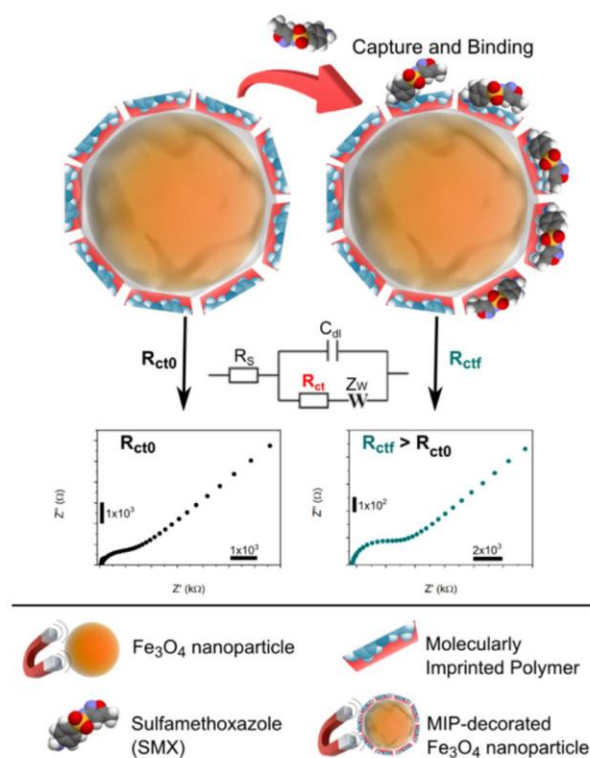


Figure 1. Schematic representation of the proposed nanoenabled sensing system. The proposed system operates via electrochemical impedance spectroscopy. Abbreviations: R_s is the electrolyte resistance, C_{dl} is the interface capacitance, R_{ct} is the charge (electron) transfer resistance, and Z_w is the Warburg impedance.

stat) with a general purpose electrochemical impedance software operating system (Frequency Response Analysers, FRA, v.4.9.006, Solartron Metrology, Leicester, England) was used for impedance measurements. BET (Brunauer–Emmett–Teller) measurements were performed with an ASAP-2000 instrument from Micromeritics and were carried out for N₂ relative vapor pressure of 0.05–0.3 at 77 K.

Screen Printed Carbon Electrodes (SPCE). The SPEs consist of a single plastic strip containing three electrodes: working, reference, and counter electrode. They were produced by screen-printed technology using a screen-printed machine (DEK 248). Masks galvanized steel frames (580 × 580 × 35 × 25 mm) with 4xM6 holes (Pantur, Sabadell, Spain), photolithograph masks (P1000 + ENT5060P110 Entelar 54 × 58 P-110 + INDZ5060 Exposure diazo 54 × 58, Paimser, Cerdanola del Valles, Spain), polyester substrate (Autostat HT5, McDermid Autotype, UK) and thermostatic oven (J.P. Selecta, Abrera, Barcelona, Spain) were also utilized. Three different inks were used: graphite ink for the working and counter electrode (Electrodag 423SS ink), silver/silver chloride for the reference electrode layer (Electrodag 6037SS ink), and finally an insulating layer (Minico M-7000 Blue) to define the working electrode area and avoid the undesirable contacts of the liquid with the internal connections. All the inks were purchased from Gwent Group, (Mamhilad Pk Est, Pontypool, UK). The fabrication procedure involves three printing process. In the first process the graphite layer was printed onto a polyester sheet by using the first stencil and the graphite ink. After this, the ink was cured at 60 °C for 15 min. The silver ink layer was

printed and cured at the same conditions, to be used as the reference electrode. Then, an insulating ink printing process was carried out. After this step the SPEs were stored in dry environment prior to be used. It is noteworthy that the graphite ink, C2030519P4, is a conductive screen printable ink containing carbon nanoparticles dispersed in a thermoplastic resin.

Synthesis of Magnetite Nanoparticles. Magnetite nanoparticles were prepared by coprecipitation method,^{22–25} mixing 0.05 mol of $\text{FeCl}_3 \cdot 6\text{H}_2\text{O}$ and 0.025 mol $\text{FeCl}_2 \cdot 4\text{H}_2\text{O}$ in 250 mL of ultrapure water, using a 500 mL three neck flask. The mixture was stirred under nitrogen atmosphere and heated until 80 °C, and then 20 mL of NH_4OH from the stock solution, was added (drop by drop). The reaction remained under reflux for 40 min and was cooled down at room temperature. The black product was separated and washed with ultrapure water three times. Lastly, the product was dried under vacuum at 45 °C. To evaluate the influence of the nanoparticles size on the sensing properties of MIPs, bigger magnetite nanoparticles were also synthesized following the same experimental conditions, but changing the molar ratio between $\text{Fe}^{2+}/\text{Fe}^{3+}$ from 1:2 to 1:0.25.^{26,27}

Synthesis of Molecularly Imprinted Polymer-Decorated Magnetite Nanoparticles. To synthesize the MIP-decorated MNPs for SMX detection, two solutions were prepared. First, 1 mL of sulfamethoxazole (10 mmol) was solubilized with 10 mL of DMSO and 4 mmol of methacrylic acid (MAA) and the solution was stirred for 30 min. Fe_3O_4 MNPs were mixed with 1 mL of oleic acid and 10 mmol of pyrrole (Py). Second, the solution made of DMSO, MAA and SMX was added to the Fe_3O_4 MNPs/Py solution and immersed in an ultrasound bath for 30 min. Under nitrogen atmosphere, 150 mL of DMSO/water (9:1, v/v), 1g of PVP (polyvinylpyrrolidone), the Fe_3O_4 MNPs/Py/SMX solution and 0.3 mmol of radical initiator (2,5-Bis(tertbutylperoxy)-2,5 dimethylhexane) were added in a two neck flask. The mixture was allowed to react for 24 h at 60 °C. The final product was separated and washed with a mixture of methanol/acetic acid (4:1, v/v) and purified using a Soxhlet extractor with methanol/water (1:1, v/v), and dried under vacuum. The nonimprinted polymer (NIP) was synthesized using the same method in the absence of the analyte (SMX).

Binding Experiments. A range of different concentrations of SMX, starting from 1×10^{-2} mol L^{-1} until 1×10^{-10} mol L^{-1} was prepared in a mixture of methanol and water (1:1, v/v), and then 20 mg of MIP-decorated Fe_3O_4 MNPs was added into each sample. The solutions were incubated for 2 h at 700 rpm. After that, three successive centrifugation processes were made during 5 min at 10000 rpm, removing the supernatant and replacing the solvent with new methanol/water solution. The final solution was reconstituted in ultrapure water. Seawater samples were collected from Barcelona Mediterranean Sea (Poblenou Beach) and treated through filtration to remove potential interfering species contained within the original matrix. Various seawater sample solutions containing SMX with concentrations from 1×10^{-2} to 1×10^{-10} mol L^{-1} were prepared by spiking method. Then, 0.5 mL of extraction media (methanol/acetic acid 1:1, v/v) was added in each sample to extract interfering compounds presents in the matrix of the sample, and incubated for 10 min at 650 rpm. In each pretreated sample to be analyzed, 20 mg of MIP-decorated Fe_3O_4 MNPs was added, and then 2-h incubation was performed at 25 °C and 700 rpm. Finally in order to remove

the template, a centrifugation step was done. Three successive centrifugations were carried out, each one during 5 min at 10000 rpm, removing the supernatant and replacing for methanol/water solution. The final solution was reconstituted in 2 mL ultrapure water. The electroanalytical performance of the proposed sensing system was investigated using electrochemical impedance spectroscopy (EIS). The measurements were performed using homemade screen printed carbon electrodes (SPCE) and 1 mmol L^{-1} $[\text{Fe}(\text{CN})_6]^{3-/4-}$ with 0.1 mol L^{-1} KCl as redox probe. MIP-decorated MNPs were fixed over the working electrode using a magnet underneath the SPCE to perform impedance measurements. The resulting data was fitted in a regular Randles circuit to extract the value of charge transfer resistance (R_{ct}) using FRA (v.4.9.006) software.

RESULTS AND DISCUSSION

Characterization of Fe_3O_4 MNPs and MIP-Decorated Fe_3O_4 MNPs. Fe_3O_4 MNPs and MIP-decorated Fe_3O_4 MNPs were first characterized by TEM. As shown in Figure 2A, the

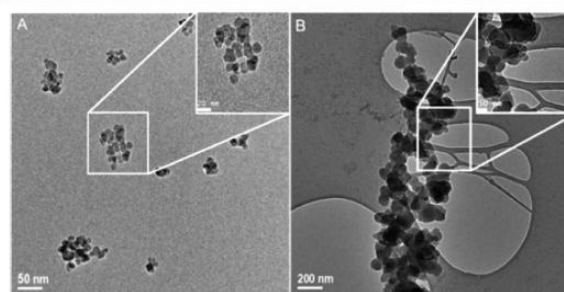


Figure 2. TEM images of (A) Fe_3O_4 MNPs and (B) MIP-decorated Fe_3O_4 MNPs.

magnetite nanoparticles have a sphere-like shape and an average size of 11 ± 2 nm (Figure S1A). After being coated with the MIP, due to the polymerization process, the resulted MIP-decorated Fe_3O_4 MNPs were observed to be arranged in clusters with an average diameter of 30–50 nm (Figure 2B and Figure S1B), suggesting that the MIP was successfully deposited onto the surface of the nanoparticles.

Aiming at confirming the composition of the synthesized materials, XPS analysis was performed. The spectrum presented in Figure 3A shows two peaks at 711 and 725 eV corresponding to Fe 2p_{3/2} and Fe 2p_{1/2}. The Fe 2p doublet peaks involve the presence of typical magnetite Fe–O bonds, confirming the formation of the magnetite. The spectra of the MIP-decorated Fe_3O_4 MNPs (Figure 3B) do not display the iron signals; this is probable due to the fact that the polymeric layer surrounding the magnetite exceeds the maximum depth that XPS can analyze (around 20 nm). Knowing that, it is possible to see on Figure 3B the signal for C_{1s} at 277 eV, corresponding to C–C signal, and another smaller peak at 281 eV, related to the C–O–C bond from the different compounds used in the synthesis process. The peaks at 525 and 392 eV are ascribed to O_{1s} and N_{1s}, respectively.

FT-IR experiments were also carried out to investigate the formation of MIP-decorated Fe_3O_4 MNPs. Figure 3C shows the FT-IR spectra of Fe_3O_4 MNPs (black line) and MIP-decorated Fe_3O_4 MNPs (red line). Fe_3O_4 MNPs display a main absorption band at 539 cm^{-1} assigned to Fe–O stretching. Regarding the spectra of MIP-decorated Fe_3O_4 MNPs, it is

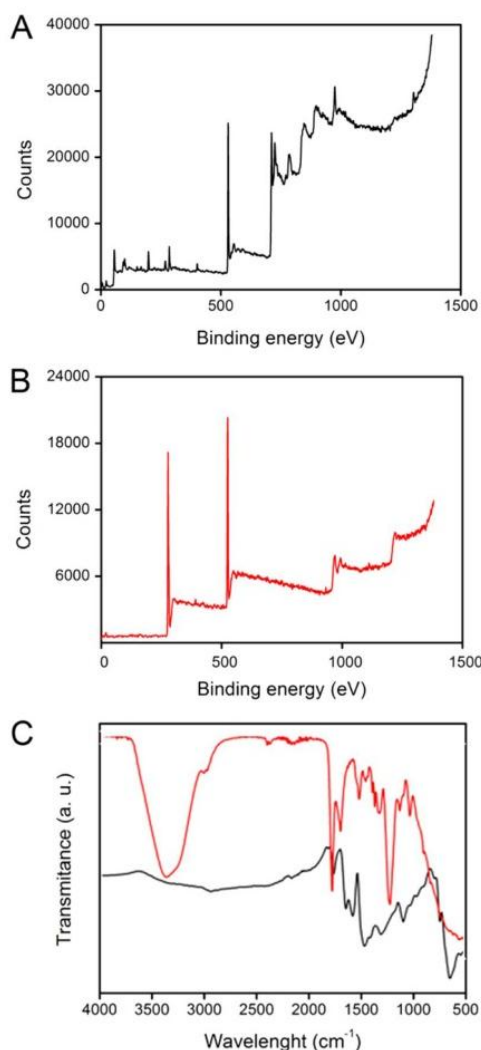


Figure 3. X-ray photoelectron spectroscopy, (A) Fe_3O_4 MNPs, (B) MIP-decorated Fe_3O_4 MNPs and (C) FTIR spectra of Fe_3O_4 MNPs (black line) and MIP-decorated Fe_3O_4 MNPs (red line).

possible to observe a broad band centered at 3300 cm^{-1} ascribed to the stretching vibration of $-\text{OH}$ and $-\text{NH}$ groups from the methanol. The peaks at 1636 and 949 cm^{-1} are related to $\text{C}=\text{C}$ from the pyrrole aromatic ring. The multiple peaks from 1457 to 1320 belong to the pyrrole backbone ring. The peak at 3400 cm^{-1} corresponds to $\text{N}-\text{H}$, the peak 1248 cm^{-1} corresponds to $\text{C}-\text{N}$, and the peak at 1145 cm^{-1} is ascribed to $\text{S}=\text{O}$ bonds, these groups belong to sulfamethoxazole (see figure S2). These results confirm that the MIP was successfully imprinted on the surface of the Fe_3O_4 MNPs.

Electrochemical Impedance Responses of the MIP-Decorated Fe_3O_4 MNPs toward SMX. Electrochemical impedance spectroscopy (EIS) is an effective tool to analyze changes that take place at an interface during a recognition event.²⁸ In brief, EIS measurements can be performed in two ways: Faradaic EIS and non-Faradaic method. Faradaic impedance measurements are usually carried out by using a reversible redox probe while non-Faradaic impedance measurements are done without using any redox probe.^{29,30} Both Faradaic^{31,32} and non-Faradaic^{33,34} impedance spectroscopy

have been applied for the studies of the recognition events involved in MIP. Importantly, improved sensitivity has been reported for Faradaic measurements.³⁰ The typical impedance data are presented in the form of the Nyquist plot and relies on a semicircular region at higher frequencies corresponding to the interfacial charge-transfer process and a linear part at lower frequency range representing the diffusion process. The semicircle diameter in the Nyquist plot corresponds to the charge transfer resistance (R_{ct}), which reflects the electron-transfer kinetics of the redox probe at the electrode surface.³⁵ In this work, Faradaic EIS measurements were performed through SPCEs in a 1 mmol L^{-1} $[\text{Fe}(\text{CN})_6]^{3-/4-}$ solution containing 0.1 mol L^{-1} KCl using a potential of 0.24 V over the frequency range from 0.1 Hz to 100 kHz and a voltage amplitude of 50 mV . Comprising MIP-decorated Fe_3O_4 MNPs was carried out in ultrapure water in the absence and presence of different concentrations of SMX (from $1 \times 10^{-2}\text{ mol L}^{-1}$ to $1 \times 10^{-10}\text{ mol L}^{-1}$) in the frequency range from 0.1 Hz to 100 kHz (Figure 4). The obtained results were analyzed using a Randles

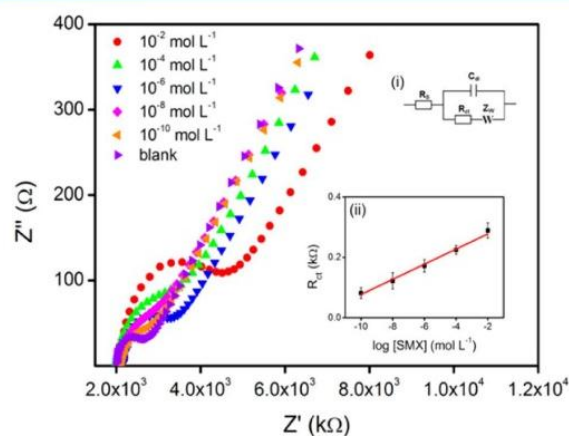


Figure 4. Nyquist plots of EIS of MIP-decorated Fe_3O_4 MNP-modified SPCE electrode in the presence of different SMX concentrations. EIS measurements were performed in a 1 mmol L^{-1} $[\text{Fe}(\text{CN})_6]^{3-/4-}$ -containing 0.1 mol L^{-1} KCl at a potential of 0.24 V over the frequency range from 0.1 Hz to 100 kHz , using a voltage amplitude of 50 mV . The insets are related to (i) the Randles equivalent circuit model for the impedance data and (ii) the calibration curve obtained by plotting the R_{ct} values vs log of SMX concentration in the range of 1×10^{-2} to $1 \times 10^{-10}\text{ mol L}^{-1}$.

equivalent circuit (see Figure 4 inset i), where R_s is the electrolyte resistance, C_{dl} is the interface capacitance, R_{ct} is the charge (electron) transfer resistance and Z_w is the Warburg impedance. Different R_{ct} values were obtained for each SMX concentration. The R_{ct} of the electrode in the absence of SMX is $68\text{ }\Omega$; this relatively small R_{ct} value can be attributed to the free electron transfer from the electrode surface to the solution.³⁶ The R_{ct} value increases due to the presence of the analyte, as the SMX molecule present in the solution gets bound via the recognition sites or cavities of the MIP. The magnitude of the change in R_{ct} increases as a function of SMX concentration in a logarithmic way in a wide range between $1 \times 10^{-2}\text{ mol L}^{-1}$ to $1 \times 10^{-10}\text{ mol L}^{-1}$, as displayed in the inset. The linear regression equation was adjusted to $R_{\text{ct}}(\text{k}\Omega) = 0.01 \log [\text{SMX}] (\text{mol L}^{-1}) + 0.31$ ($R^2 = 0.98$), with an estimated detection limit of $1 \times 10^{-12}\text{ mol L}^{-1}$ ($2.8 \times 10^{-4}\text{ ppb}$), calculated as the concentration of SMX corresponding to the 3

Table 1. Comparison of Composition, Detection Limit and Linear Range of Different Modified Electrodes for Determination of SMX

method	detection limit	linear range	ref
MMIP (Fe ₃ O ₄)	1.5 ng g ⁻¹	1.5–4.3 ng g ⁻¹	17
MIP-OPPy ^a	3.59 × 10 ⁻⁴ mM	2.5 × 10 ⁻³ –0.75 mM	18
MIP-EDMA ^b	3.0 × 10 ⁻⁷ mol L ⁻¹	3.0 × 10 ⁻⁷ –4.0 × 10 ⁻⁴ mol L ⁻¹	19
broad specific immunoassay	65.2 μg L ⁻¹	0.2–65.2 μg L ⁻¹	20
LC-MS	5–10 ng g ⁻¹	50–2 00 ppb	21
MIP-decorated Fe ₃ O ₄ MNPs	1 × 10 ⁻¹² mol L ⁻¹	1 × 10 ⁻² –1 × 10 ⁻¹⁰ mol L ⁻¹	this work

^aOPPy = overoxidized polypyrrole. ^bEDMA = ethylene glycol dimethacrylate.

times *S/N* ratio, where *S* is the standard deviation of the blank impedance signal (three replicates) and *N* is the slope of the related calibration curve. This sensing platform offers an advantageous performance in terms of limit of detection when compared to other methods for SMX determination (see Table 1).

The electrode reproducibility and stability were also investigated by impedimetric responses of sample solutions containing 10⁻⁶ mol L⁻¹ SMX. The relative standard deviations (RSDs) of the same sensor for five successive measurements were found to be 3.6% and for three different electrodes it was 6.8%. These results confirm the electrode reproducibility. The imprinted sensor also exhibited satisfactory stability. In fact, the results show that after 3 weeks 82% of the initial response was preserved.

Characterization of the NIP-Composite and Selectivity Studies. To confirm the specificity of the MIP-decorated Fe₃O₄ MNPs, its performance was compared with the performance of a nonimprinted polymer (NIP)-composite.^{37–39} Figure 5A shows the *R*_{ct} values obtained for both materials in the absence and presence of 1 × 10⁻² mol L⁻¹ SMX. The difference observed on *R*_{ct} values for the imprinted sensor (160 Ω) and nonimprinted sensor (110 Ω) is related to the imprinted cavities presented on the MIP-composite, which facilitate the diffusion of the [Fe(CN)₆]^{3-/4-} probes into the electrode surface, decreasing the charge transfer resistance.⁴⁰ Analyzing the *R*_{ct} values corresponding to the sample containing SMX, the MIP-composite shows a value that is 3 times higher than the blank, whereas the NIP-composite displays a value that is 1.4 times higher than the blank. These large separation factors suggest that the MIP-composite possesses a high specificity toward SMX when compared with the NIP-composite behavior.

Interferences of other sulfonamides were also studied aiming at exploring the selectivity of the sensing system based on the proposed MIP-decorated Fe₃O₄ MNPs. In particular, the performance of the sensing system was evaluated in the presence of two kinds of structurally similar sulfonamides such as sulfadiazine (SDZ) and sulfacetamide (SCT). In a typical experiment, the electrochemical impedance of the electrode modified with the composite was measured in the presence of 1 × 10⁻⁸ mol L⁻¹ of each analyte. As shown in Figure 5B, the *R*_{ct} values obtained for SDZ and SCT show practically no difference between them and the blank. These results suggest that the sensor exhibits good selectivity, which is attributed to the specificity of the MIP toward SMX.

Real Sample Analysis. To evaluate the applicability of the proposed sensor in real environmental samples, determination of SMX was carried out in spiked seawater samples. Prior to the analysis, the samples were mixed with extraction media (see experimental description) to minimize matrix complexity and

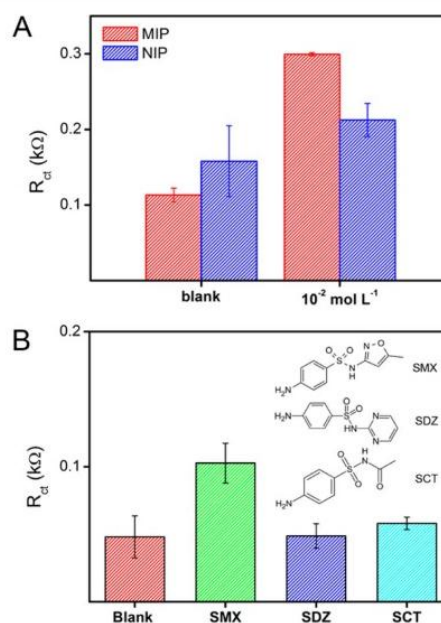


Figure 5. *R*_{ct} values obtained for (A) imprinted (MIP) and nonimprinted (NIP) sensor and (B) the MIP-decorated Fe₃O₄ MNPs in the presence of SMX, SDZ and SCT. Results obtained from the EIS measurements performed in a 1 mmol L⁻¹ [Fe(CN)₆]^{3-/4-} containing 0.1 mol L⁻¹ KCl at a potential of 0.24 V over the frequency range from 0.1 Hz to 100 kHz, using a voltage amplitude of 50 mV.

spike the samples with different SMX concentrations. It was observed from the EIS data (Figure 6) that the *R*_{ct} value increased on spiking with SMX. Hence, from the *R*_{ct} values obtained for three different SMX concentrations (10⁻⁴, 10⁻⁶, and 10⁻⁸ mol L⁻¹), recovery was calculated and the results obtained are given in Table 2. The recoveries of the samples are 87–106% with the RSD in the range of 1.2–4.5%, which indicates that the developed assay can be performed for the accurate determination of SMX in real samples analysis.

Fe₃O₄ MNPs Size Effect Study. MIP-composite was also synthesized using bigger magnetite nanoparticles. The new magnetite nanoparticles were characterized using TEM, which shows the formation of nanoparticles with diameter around 27 nm (Figure S3A). Binding experiments for the new MIP was carried out following the same procedure. From the EIS data obtained for the composite containing Fe₃O₄ MNPs of 27 nm, a new calibration curve was constructed (Figure S3B) and a new limit of detection was also determined (*S/N* = 3). The LOD for the new MIP-composite shows a different performance when compared with that of the original one, obtaining 5

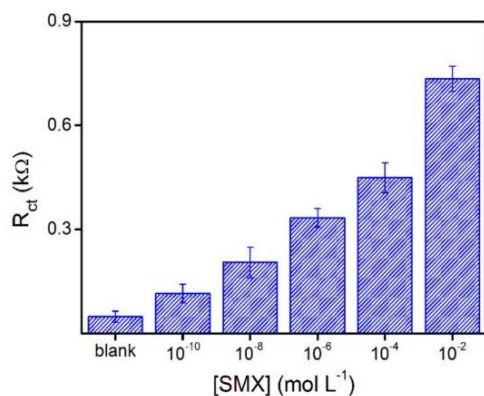


Figure 6. R_{ct} values obtained for MIP-decorated Fe_3O_4 MNPs in seawater in the absence and presence of different spiked SMX concentrations. Results obtained from the EIS measurements performed in a $1 \text{ mmol L}^{-1} [\text{Fe}(\text{CN})_6]^{3-/4-}$ containing 0.1 mol L^{-1} KCl at a potential of 0.24 V over the frequency range from 0.1 Hz to 100 kHz , using a voltage amplitude of 50 mV .

Table 2. Determination of SMX in Seawater

SMX spiked (mol L^{-1})	R_{ct} ($\text{k}\Omega$)	recovery (%)	RSD (%)
10^{-4}	0.233	92	1.2
10^{-6}	0.174	87	4.5
10^{-8}	0.115	106	2.3

$\times 10^{-12} \text{ mol L}^{-1}$ ($1.4 \times 10^{-3} \text{ ppb}$), being 5 times higher than that obtained with the composite based on particles of an average diameter of 11 nm ($1 \times 10^{-12} \text{ mol L}^{-1}$).

Since the new-proposed sensing system was found to offer a different performance in terms of limit of detection by changing the size of the particles embedded in the composite, the specific surface area of both composites was explored via Brunauer–Emmett–Teller (BET) technique to verify the influence of this parameter in the limit of detection of the developed sensing system. Hence, the limit of detection of the proposed sensing system using the MIP-decorated Fe_3O_4 MNPs containing two different sizes of particles, 11 and 27 nm , respectively, was systematically studied in parallel with the BET analysis (Figure S4). The composite decorated with 27 nm Fe_3O_4 NPs showed a surface area of $64 \text{ m}^2 \text{ g}^{-1}$, whereas the composite of 11 nm displayed a larger surface area of $184 \text{ m}^2 \text{ g}^{-1}$ because of the smaller size of MNPs. From this data, it can be concluded that smaller nanoparticles can improve the surface area, increasing the number of the recognition sites for SMX which enhances the electrochemical response of the sensing system. Table 3 summarizes the obtained results.

CONCLUSIONS

A selective, specific and highly sensitive composite-based sensing system has been engineered aiming at detecting the potentially hazardous chemotherapeutic agent SMX in a label-

Table 3. Influence of the Specific Surface Area on the Limit of Detection of the Proposed Sensing System

particle size (nm)	LOD (mol L^{-1}) ^a	SSA ($\text{m}^2 \text{ g}^{-1}$) ^b
11	1×10^{-12}	64
27	5×10^{-12}	184

^aLimit of detection ($S/N = 3$). ^bSpecific surface area.

free fashion via electrochemical impedance spectroscopy. The proposed sensing system (i) bears selectivity and specificity, due to its biomimetic receptor; (ii) facilitates preconcentration, separation and manipulation of the analyte, due to its magnetic properties; (iii) showing a high surface area ($184 \text{ m}^2 \text{ g}^{-1}$), this composite-based sensing system exhibits a high sensitivity (LOD around $1 \times 10^{-12} \text{ mol L}^{-1} \approx 2.8 \times 10^{-4} \text{ ppb}$), which is comparable with that of sulfonamides monitoring using liquid chromatography/mass spectrometry. Moreover, this sensing system has been proved to be useful in seawater monitoring, where sulfonamides content is minimum compared to other environmental samples and may be extended to other compounds by changing the MIP.

ASSOCIATED CONTENT

Supporting Information

The Supporting Information is available free of charge on the ACS Publications website at DOI: 10.1021/acs.analchem.5b04092.

Sizes distributions of Fe_3O_4 MNPs MIP-decorated Fe_3O_4 MNPs, detailed FT-IR, TEM image, and size distribution of 27 nm - Fe_3O_4 MNPs, calibration curve for the MIP-composite based on particles of an average diameter of 27 nm , and N_2 adsorption isotherms (PDF)

AUTHOR INFORMATION

Corresponding Author

*E-mail: arben.merkoçi@icn.cat.

Author Contributions

[§]A.Z.-G. and A.A.-L. contributed equally to this work.

Notes

The authors declare no competing financial interest.

ACKNOWLEDGMENTS

This work was supported by The European Commission Program, FP7-OCEAN, SMS Project (613844). ICN2 acknowledges support from the Severo Ochoa Program (MINECO, Grant SEV-2013-0295). Nanobiosensors and Bioelectronics Group acknowledges Supramolecular Nano-Chemistry and Materials group (Dr. Carlos Carbonell and Prof. Daniel Maspoch at ICN2) for BET measurements, and the support from Secretaria d'Universitats i Recerca del Departament d'Economia i Coneixement de la Generalitat de Catalunya (2014 SGR 260). L.A.M acknowledges financial support from FAPESP-BEPE (2014/26088-4) project.

REFERENCES

- (1) Dmitrienko, S. G.; Kochuk, E. V.; Apyari, V. V.; Tolmacheva, V. V.; Zolotov, Y. A. *Anal. Chim. Acta* **2014**, *850*, 6–25.
- (2) Wang, S.; Zhang, H. Y.; Wang, L.; Duan, Z. J.; Kennedy, I. *Food Addit. Contam.* **2006**, *23*, 362–384.
- (3) Cháfer-Pericás, C.; Maquieira, Á.; Puchades, R. *TrAC, Trends Anal. Chem.* **2010**, *29*, 1038–1049.
- (4) O'Neill, J. *Antimicrobial Resistance: Tackling a Crisis for the Health and Wealth of Nations*; Review on Antimicrobial Resistance: London, 2014; http://amr-review.org/sites/default/files/AMR%20Review%20Paper%20-%20Tackling%20a%20crisis%20for%20the%20health%20and%20wealth%20of%20nations_1.pdf.
- (5) Meltzer, L. J. *Invest. Dermatol.* **1949**, *13*, 213–216.
- (6) Hela, W.; Brandtner, M.; Widek, R.; Schuh, R. *Food Chem.* **2003**, *83*, 601–608.

- (7) Nebot, C.; Regal, P.; Miranda, J. M.; Fente, C.; Cepeda, A. *Food Chem.* **2013**, *141*, 2294–2299.
- (8) Lindsey, M. E.; Meyer, T. M.; Thurman, E. M. *Anal. Chem.* **2001**, *73* (19), 4640–4646.
- (9) Rodriguez, M.; Orescan, D. B. *Anal. Chem.* **1998**, *70*, 2710–2717.
- (10) Fuh, M. R. S.; Chu, S. Y. *Anal. Chim. Acta* **2003**, *499*, 215–221.
- (11) Santos, B.; Lista, A.; Simonet, B. M.; Ríos, A.; Valcárcel, M. *Electrophoresis* **2005**, *26*, 1567–1575.
- (12) Merkoçi, a.; Alegret, S. *TrAC, Trends Anal. Chem.* **2002**, *21*, 717–725.
- (13) Schirhagl, R. *Anal. Chem.* **2014**, *86*, 250–261.
- (14) Zor, E.; Morales-Narváez, E.; Zamora-Gálvez, A.; Bingöl, H.; Ersoz, M.; Merkoçi, A. *ACS Appl. Mater. Interfaces* **2015**, *7*, 20272–20279.
- (15) Chantada-Vázquez, M. P.; Sánchez-González, J.; Peña-Vázquez, E.; Tabernero, M. J.; Bermejo, A. M.; Bermejo-Barrera, P.; Moreda-Piñeiro, A. *Biosens. Bioelectron.* **2016**, *75*, 213–221.
- (16) Wan, Y.; Ma, H.; Lu, B. *Adv. Biochem. Eng./Biotechnol.* **2015**, *150*, 131–166.
- (17) Chen, L.; Zhang, X.; Sun, L.; Xu, Y.; Zeng, Q.; Wang, H.; Xu, H.; Yu, A.; Zhang, H.; Ding, L. *J. Agric. Food Chem.* **2009**, *57*, 10073–10080.
- (18) Ozkorucuklu, S. P.; Sahin, Y.; Alsancak, G. *Sensors* **2008**, *8*, 8463–8478.
- (19) Guzmán-Vázquez de Prada, A.; Martínez-Ruiz, P.; Reviejo, A. J.; Pingarrón, J. M. *Anal. Chim. Acta* **2005**, *539*, 125–132.
- (20) Franek, M.; Diblikova, I.; Cernoch, I.; Vass, M.; Hruska, K. *Anal. Chem.* **2006**, *78*, 1559–1567.
- (21) Heller, D. N.; Ngoh, M. A.; Donoghue, D.; Podhorniak, L.; Righter, H.; Thomas, M. H. *J. Chromatogr. B: Anal. Technol. Biomed. Life Sci.* **2002**, *774*, 39–52.
- (22) Machala, L.; Zboril, R.; Gedanken, A. *J. Phys. Chem. B* **2007**, *111*, 4003–4018.
- (23) Lee, Y.; Lee, J.; Bae, C. J.; Park, J.-G.; Noh, H.-J.; Park, J.-H.; Hyeon, T. *Adv. Funct. Mater.* **2005**, *15*, 503–509.
- (24) Prozorov, T.; Mallapragada, S. K.; Narasimhan, B.; Wang, L.; Palo, P.; Nilsen-Hamilton, M.; Williams, T. J.; Bazylinski, D. a.; Prozorov, R.; Canfield, P. C. *Adv. Funct. Mater.* **2007**, *17*, 951–957.
- (25) Huynh, T.-P.; Wojnarowicz, A.; Sosnowska, M.; Srebnik, S.; Benincori, T.; Sannicolò, F.; D'Souza, F.; Kutner, W. *Biosens. Bioelectron.* **2015**, *70*, 153–160.
- (26) Herea, D.-D.; Chiriac, H.; Lupu, N. *J. Nanopart. Res.* **2011**, *13*, 4357–4369.
- (27) Sun, S.; Zeng, H. *J. Am. Chem. Soc.* **2002**, *124*, 8204–8205.
- (28) Mayorga-Martinez, C. C.; Chamorro-Garcia, A.; Merkoçi, A. *Biosens. Bioelectron.* **2015**, *67*, 53–58.
- (29) Gautier, C.; Esnault, C.; Cougnon, C.; Pilard, J.; Casse, N.; Chénais, B. *J. Electroanal. Chem.* **2007**, *610*, 227–233.
- (30) Patil, A. V.; Bedatty Fernandes, F. C.; Bueno, P. R.; Davis, J. J. *Anal. Chem.* **2015**, *87*, 944–950.
- (31) Uygun, Z. O.; Dilgin, Y. *Sens. Actuators, B* **2013**, *188*, 78–84.
- (32) Wu, B.; Wang, Z.; Zhao, D.; Lu, X. *Talanta* **2012**, *101*, 374–381.
- (33) Apodaca, D. C.; Pernites, R. B.; Ponnampati, R.; Del Mundo, F. R.; Advincula, R. C. *Macromolecules* **2011**, *44*, 6669–6682.
- (34) Reddy, K. K.; Gobi, K. V. *Sens. Actuators, B* **2013**, *183*, 356–363.
- (35) Yao, G.; Liang, R.; Huang, C.; Wang, Y.; Qiu, J. *Anal. Chem.* **2013**, *85*, 11944–11951.
- (36) Reddy, K. K.; Gobi, K. V. *Sens. Actuators, B* **2013**, *183*, 356–363.
- (37) Nishad, P. A.; Bhaskarapillai, A.; Velmurugan, S.; Narasimhan, S. *V. Carbohydr. Polym.* **2012**, *87*, 2690–2696.
- (38) Sergeeva, T. A.; Piletsky, S. a.; Panasyuk, T. L.; El'skaya, a. V.; Brovko, a. a.; Slinchenko, E. a.; Sergeeva, L. M. *Analyst* **1999**, *124*, 331–334.
- (39) Pan, G.; Zu, B.; Guo, X.; Zhang, Y.; Li, C.; Zhang, H. *Polymer* **2009**, *50*, 2819–2825.
- (40) Zhu, L.; Cao, Y.; Cao, G. *Biosens. Bioelectron.* **2014**, *54*, 258–261.

Supporting Information

Molecularly Imprinted Polymer–decorated Magnetite Nanoparticles for Selective Sulfonamide Detection

Alejandro Zamora-Gálvez^{†,§}, Abdellatif Ait-Lahcen^{†,‡,§}, Luiza A. Mercante^{†,¶}, Eden Morales-Narváez[†], Aziz Amine[‡], Arben Merkoçi^{†,‡,*}

[†] *Catalan Institute of Nanoscience and Nanotechnology (ICN2), CSIC and The Barcelona Institute of Science and Technology, Campus UAB, Bellaterra, 08193 Barcelona, Spain*

[‡] *Faculty of Science and Technology, University Hassan II of Casablanca, B.P.146, 20650, Mohammedia, Morocco.*

[¶] *National Laboratory for Nanotechnology in Agribusiness (LNNA), Embrapa Instrumentation, 13560-970, São Carlos, SP, Brazil*

[‡] *ICREA – Catalan Institution for Research and Advanced Studies, Barcelona, 08010, Spain*

[§] *This authors contributed equally to this work.*

*E-mail: arben.merkoci@icn.cat

Table of Contents

Figure S1. Sizes distributions of (A) Fe₃O₄ MNPs and (B) MIP-decorated Fe₃O₄ MNPs.

Figure S2. Detailed FT-IR of (A) Fe₃O₄ MNPs and (B) MIP-decorated Fe₃O₄ MNPs.

Figure S3. (A) TEM image and (B) size distribution of 27nm-Fe₃O₄ MNPs. (C) Calibration curve obtained by plotting the R_{ct} values vs log of SMX concentration in the range of 1 x 10⁻² mol L⁻¹ to 1 x 10⁻¹⁰ mol L⁻¹ for the MIP-composite based on particles of an average diameter of 27 nm.

Figure S4. N₂ adsorption isotherms of MIP-composite based on magnetite nanoparticles of an average diameter of (A) 11 nm and (B) 27 nm.

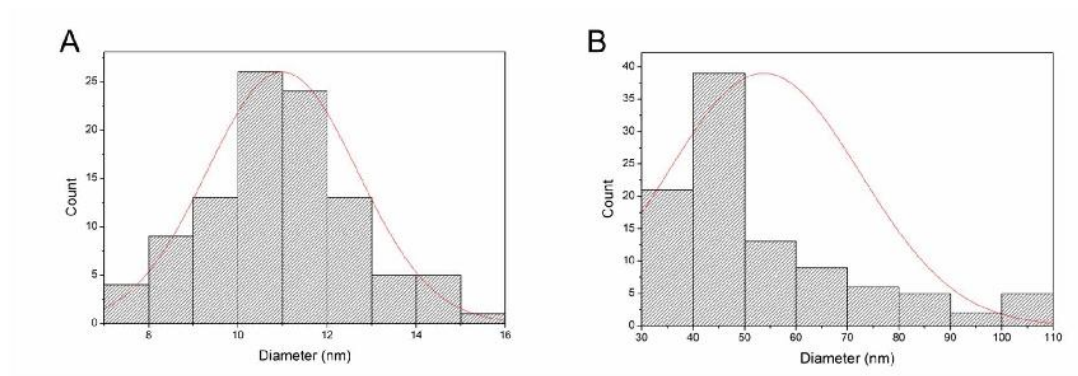


Figure S1. Sizes distributions of (A) Fe₃O₄ MNPs and (B) MIP-decorated Fe₃O₄ MNPs.

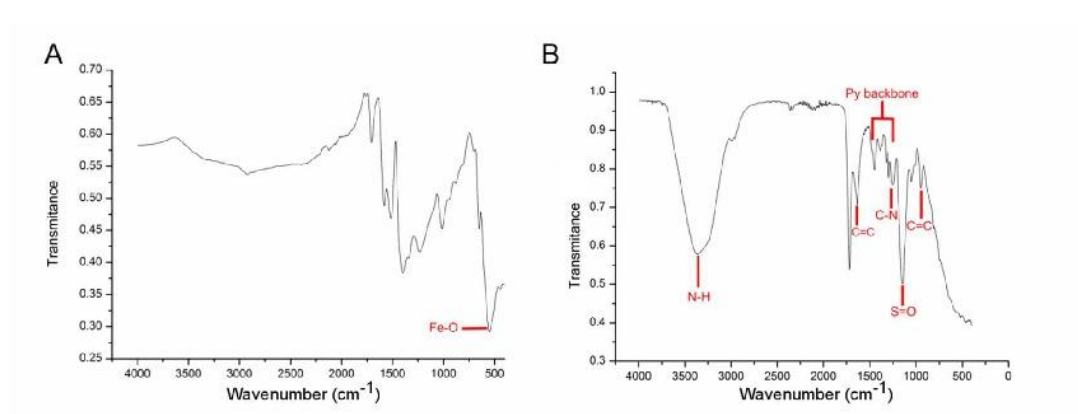


Figure S2. Detailed FT-IR of (A) Fe₃O₄ MNPs and (B) MIP-decorated Fe₃O₄ MNPs.

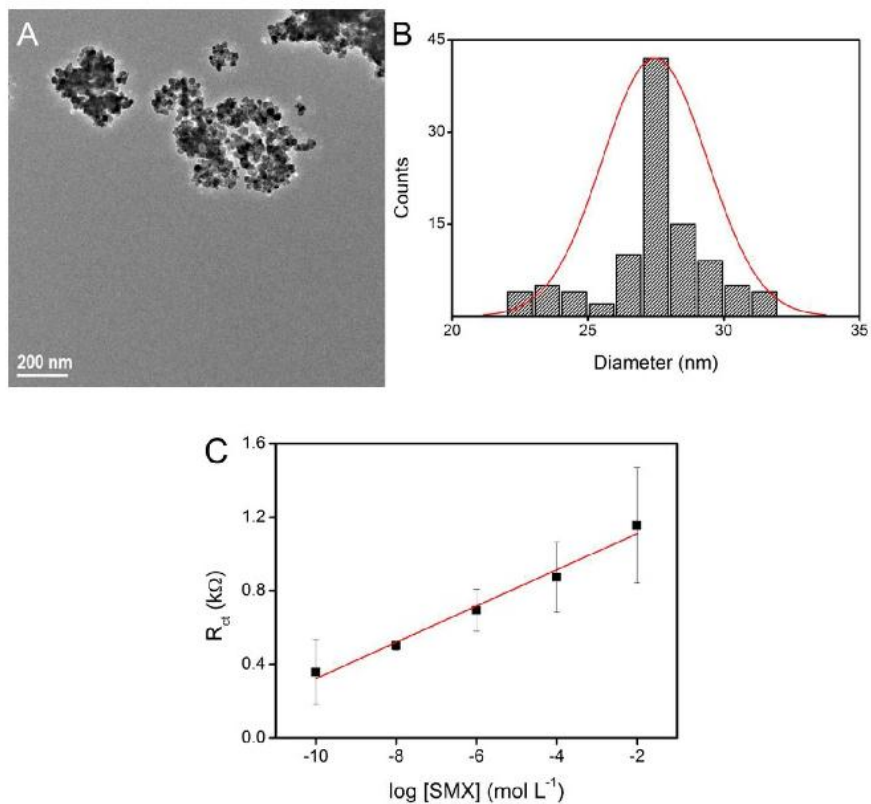


Figure S3. (A) TEM image and (B) size distribution of 27nm-Fe₃O₄ MNPs. (C) Calibration curve obtained by plotting the R_{ct} values vs log of SMX concentration in the range of 1×10^{-2} mol L⁻¹ to 1×10^{-10} mol L⁻¹ for the MIP-composite based on particles of an average diameter of 27 nm.

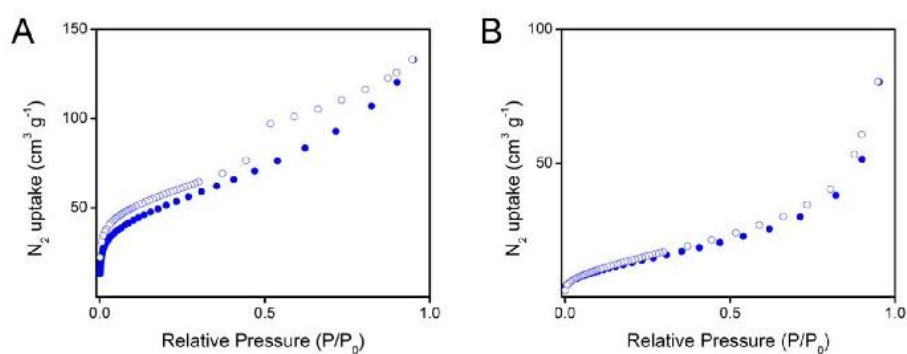


Figure S4. N₂ adsorption isotherms of MIP-composite based on magnetite nanoparticles of an average diameter of (A) 11 nm and (B) 27 nm.



Magnetic nanoparticle-molecular imprinted polymer: A new impedimetric sensor for tributyltin detection

Alejandro Zamora Gálvez^{a, b, 1}, Carmen C. Mayorga-Matínez^{a, 1}, Claudio Parolo^a, Josefina Pons^b, Arben Merkoçi^{a, c, *}

^a Nanobioelectronics & Biosensors Group, Catalan Institute of Nanoscience and Nanotechnology (ICN2), CSIC and The Barcelona Institute of Science and Technology, Campus UAB, Bellaterra, Barcelona 08193, Spain

^b Departament de Química, Universitat Autònoma de Barcelona, 08193 Bellaterra, Barcelona, Spain

^c ICREA, Pg. Lluís Companys 23, 08010 Barcelona, Spain

ARTICLE INFO

Keywords:

Electrochemical impedance spectroscopy
Pollutants
Electrochemical sensor

ABSTRACT

Recently, molecular imprinted polymers (MIPs) were extensively used for separation and identification of specific molecules, replacing expensive and unstable biological receptors. Nonetheless, their application in electrochemical sensors has not been sufficiently explored. Here we report the use of a MIP as a specific receptor in a new highly sensitive tributyltin (TBT) electrochemical sensor. The sensor combines the specificity, pre-concentration capability and robustness of molecular imprinted polymer attached onto magnetic nanoparticles with the quantitative outputs of impedimetric measurements. The proposed device detects TBT in a concentration range of 5 pM to 5 μM with a low limit of detection (5.37 pM), which is lower than the one recommended for TBT in sea water by the US Environmental Protection Agency (EPA). We believe that this new electrochemical sensor can play an important role in the monitoring of the quality of sea and fresh waters worldwide.

1. Introduction

For decades, the pesticide tributyltin (TBT) has been an important additive in antifouling paints to prevent the growth of marine organisms on the hulls of large ships. Eventually, this highly toxic pesticide leaks in the aquatic environment causing immuno-suppression and imposex in snails and bivalves, inhibiting the growth of several marine organisms, and inducing immunotoxic, hepatotoxic, and neurotoxic effects in fish and mammals, with potential effects even for humans [1–3].

Nowadays, the typical methods to detect pesticides, including TBT, are chromatography separation [4–6], gas chromatography [7–9], electron-capture detector [10], flame ionization detector and mass spectrometry [11]. These techniques reach low limits of detections (LOD) and have high reproducibility, but require extensive purification, ex-

pensive equipment and trained users [12]. During the past few years, electrochemical sensors showed to be a user-friendly and miniaturized alternative for pesticides detection [13]. Nevertheless, they normally use bio-receptors (aptamers, antibodies, enzymes) [13–15], which can be instable, non-specific, and expensive. Recently, we and others used molecular imprinting polymers (MIPs) for the development of specific methods for the detection of different kinds of molecules such as fenitrothiol, organochlorine, and heptachlor [14–16].

In this paper we present a new sensing platform for the detection of TBT based on MIP technology. Our system is based on the use of screen printing electrodes in conjunction with MIP-Fe₃O₄ nanoparticles (NPs) composite [15–17] as a specific receptor for TBT. Thanks to the use of electrochemical impedance spectroscopy, we managed to quantitatively detect TBT in fresh and sea water (see scheme in Fig. 1A) [14,16–18].

* Corresponding author at: Nanobioelectronics & Biosensors Group, Catalan Institute of Nanoscience and Nanotechnology (ICN2), CSIC and The Barcelona Institute of Science and Technology, Campus UAB, Bellaterra, Barcelona 08193, Spain.

Email address: arben.merkoci@icn2.cat (A. Merkoçi)

¹ These authors contributed equally.

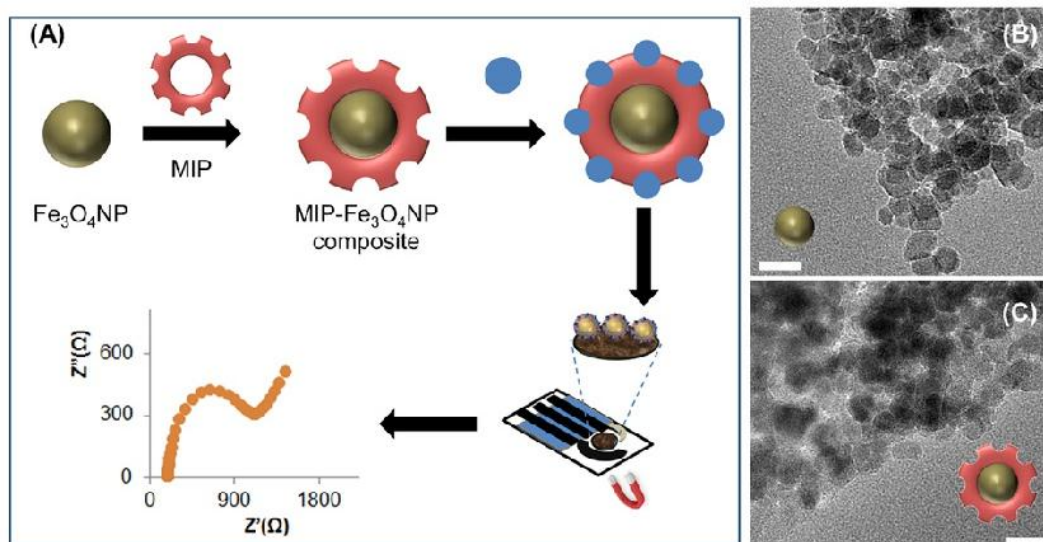


Fig. 1. Cartoon of the proposed TBT sensor (A). TEM images of $\text{Fe}_3\text{O}_4\text{NPs}$ (B) and $\text{MIP-Fe}_3\text{O}_4\text{NPs}$ (C). Scale bar: 20 nm.

2. Experimental

2.1. Chemicals and materials

Tributyltin hydride, (3-aminopropyl) trimethoxysilane, acryloyl chloride ($\text{C}_3\text{H}_3\text{ClO}$), $\text{FeCl}_2 \cdot 4\text{H}_2\text{O}$, $\text{FeCl}_3 \cdot 6\text{H}_2\text{O}$, ammonium hydroxide (NH_4OH), toluene anhydrous, potassium carbonate (K_2CO_3), ethanol, acetonitrile, ethylene glycol dimethacrylate 98%, 2,5-bis(*tert*-butyl peroxy)-2,5-dimethylhexane 90%, sodium hydroxide and methanol were purchased from Sigma Aldrich. Transmission electron microscope (TEM) FEI TECNAI G2 F20 (USA), X-ray photoelectron spectrometer Phoibos 150 analyzer (SPECS GmbH, Berlin, Germany) in ultra-high vacuum conditions (base pressure 1×10^{-10} mbar). The infrared spectroscopy was performed by IR-ATR model IR Tensor 27 (Bruker). Home-made SPE, which fabrication method was reported previously [14].

2.2. Synthesis of molecular imprinted $\text{MIP-Fe}_3\text{O}_4\text{NPs}$ composite

For the synthesis of the $\text{MIP-Fe}_3\text{O}_4\text{NPs}$ composite we modified a protocol previously reported by Zhu et al. [19]. A mixture of $\text{FeCl}_2 \cdot 4\text{H}_2\text{O}$ 0.02 g/mL and $\text{FeCl}_3 \cdot 6\text{H}_2\text{O}$ 0.054 g/mL was prepared and stirred under nitrogen to prevent the formation of Fe_2O_3 . After that, 20 mL of ammonium hydroxide 25 M was added and the reaction was refluxed at 80 °C for 40 min. The solution was decanted and washed three times with MilliQ water to remove any unreacted reagent. The $\text{Fe}_3\text{O}_4\text{NPs}$ were dried in a vacuum at 45 °C. All the next steps were performed under Schlenk line, to increase the stability of the compounds. Then, 0.1 g of Fe_3O_4 NPs was dissolved in 150 mL ethanol/water 14:1 and 50 μL 4.27 mM of amino propyl triethoxysilane (APTS) was added drop by drop, under continuous stirring during 7 h at room temperature and nitrogen ambient. Following by washing steps with absolute ethanol (5 times), and dried in vacuum. 0.1 mg of APTS- $\text{Fe}_3\text{O}_4\text{NPs}$ and 0.5 g of K_2CO_3 were dispersed in 50 mL of toluene under ultrasonic ice bath during 30 min and 1 mL 0.012 M of acryloyl chloride was added and the flask was sealed, the mixture was under vigorous stirring for 12 h at room temperature. Next, the product was collected by application of an external magnetic field and rinsed three times with toluene, ethanol and acetonitrile, then the product was dried in vacuum conditions.

The modified Fe_3O_4 NPs (0.1 g) and 269 μL of tributyltin hydride

(TBTH) were dissolved in 40 mL 19 M of acetonitrile and stirred for 6 h until the template-monomer was formed. Then 4.14 mL at 5.3 M of ethylene glycol dimethacrylate (EGDMA) and 9.35 μL 3 M of 2,5-bis(*tert*-butyl peroxy)-2,5 dimethyl hexane were added in the solution. The solution was placed in the ultrasonic ice-bath for 5 min then was heated at 50 °C for 5 h and polymerized at 65 °C for 20 h. Finally the mixture was heated at 85 °C for 5 h to assure complete polymerization. The reaction was purged with nitrogen and stirred. The resultant product was rinsed five times with a mixture of methanol-dichloromethane (4:1) and finally the resulted product was extracted using Soxhlet for 60 h in presence of 0.3 M NaOH dissolved in methanol, the final product was dried under vacuum conditions. Although the synthesis of the $\text{MIP-Fe}_3\text{O}_4\text{NPs}$ composite requires long time, the final amount that is obtained (ca. 5 g) is enough to perform over 100 measurements.

2.3. Electrochemical measurements

For TBT detection, we incubated solutions of different TBT concentrations with 10 mg/mL of $\text{MIP-Fe}_3\text{O}_4\text{NPs}$ composite under stirring conditions for 2 h at room temperature. Afterward, 10 μL of the above suspension was drop casted onto the working electrode area of the SPE and TBT/ $\text{MIP-Fe}_3\text{O}_4\text{NPs}$ composite was accumulated onto the working electrode area with the help of a permanent magnet placed underneath. Then electrochemical impedance spectroscopy (EIS) was performed in 1 mM $[\text{Fe}(\text{CN})_6]^{3/4-}$ with 0.1 M KCl adding 50 μL of this solution over the working electrode. A sinusoidal potential modulation of ± 20 mV amplitude in the 0.1 Hz to 100 kHz frequency range was superimposed onto the formal potential (0.24 V vs. Ag/AgCl) of the redox couple, $[\text{Fe}(\text{CN})_6]^{3/4-}$. For sea water measurements, we filtered the samples using a 0.05 μm VMWP filter to extract bigger compounds and impurities.

3. Results and discussion

Before applying $\text{MIP-Fe}_3\text{O}_4\text{NPs}$ composite for TBT detection, we characterized it using TEM, IR, XPS. We used TEM to study the synthesized $\text{Fe}_3\text{O}_4\text{NPs}$, which had a diameter of 20.05 ± 4.37 nm and a good homogeneity (as shown in Fig. 1B), in line with previously reported synthesis [20,21]. Upon modification with the MIP, we observed some $\text{Fe}_3\text{O}_4\text{NPs}$ aggregation (probably due to the polymerization process) [22], which increased the apparent diameter of the

Fe_3O_4 NPs to 59.77 ± 7.15 nm (Fig. 1C). The aggregation of Fe_3O_4 NPs should not negatively affect the sensor behavior, since their only role is to accumulate the MIP on the working electrode surface (upon inducing a magnetic field with a permanent magnet), for this reason we refer to MIP- Fe_3O_4 NPs composite, rather than just MIP- Fe_3O_4 NPs. In order to confirm the incorporation of the Fe_3O_4 NPs into the MIP, we magnetically separated the samples from their solutions before characterizing them with IR spectroscopy. Fig. 2A shows how the characteristic peaks of the MIP in the IR spectra (i.e. C—H, C=O, Si—O, C=C—H δ and Si—CH) appeared just in the MIP- Fe_3O_4 NPs composite spectrum and not in the one of bare Fe_3O_4 NPs, suggesting that the Fe_3O_4 NPs were included into the polymer structure. We also characterized the composite and the bare nanoparticles with X-ray spectroscopy. The survey spectrum (Fig. 2B) of MIP- Fe_3O_4 NPs composite shows the enhanced signals from O 1s, C 1s and Si 2p peaks in comparison of survey spectrum of Fe_3O_4 NPs, confirming the formation of MIP- Fe_3O_4 NPs composite. Fig. 2C shows the high resolution signals for the regions of O 1s, C 1s, Si 2p, Fe 2p and Ni 1s of MIP- Fe_3O_4 NPs composite. Moreover, the specific surface was investigated by BET analysis and the obtained surface area for the MIP- Fe_3O_4 NPs (59.77 ± 7.15 nm) is $65 \text{ m}^2/\text{g}$ (see Fig. 2D).

Once proved the formation of the MIP- Fe_3O_4 NPs composite, we verified that the MIP could actually bind the TBT using EIS. Fig. 3A shows

the Nyquist spectra of bare (SPE), MIP- Fe_3O_4 NPs and MIP- Fe_3O_4 NPs incubated with $5 \mu\text{M}$ TBT. The resulted R_{ct} for the MIP- Fe_3O_4 NPs composite is $0.65 \text{ k}\Omega$, which indicates a low resistivity compared with the R_{ct} of the bare electrode of $15\text{--}20 \text{ k}\Omega$. We think that there are two main components inducing this low R_{ct} : the catalytic activity of Fe_3O_4 NPs [23,24] and the enhanced electrode effective area due to the presence of Fe_3O_4 NPs. After the incubation of MIP- Fe_3O_4 NPs with $5 \mu\text{M}$ TBT, the recorded signal is $1.66 \text{ k}\Omega$. This enhanced R_{ct} confirms the binding between of MIP- Fe_3O_4 NPs and TBT, because the negative charge from the tributyltin hydride [25] acts as an electrostatic barrier between SPE and the redox mediator. This was confirmed by Zeta-potential experiments (Fig. 3B). A gradual shift to negative values was observed when the MIP- Fe_3O_4 NPs is connect with TBT.

To verify that the signal change upon addition of TBT was specific, we performed the same measurements using NIP- Fe_3O_4 NPs composite (non-imprinted polymer). We challenged our sensor with four different solutions: MIP- Fe_3O_4 NPs composite, NIP- Fe_3O_4 NPs composite, MIP- Fe_3O_4 NPs composite with $5 \mu\text{M}$ TBT, and NIP- Fe_3O_4 NPs composite with $5 \mu\text{M}$ TBT (see Fig. 3B). The R_{ct} obtained using NIP- Fe_3O_4 NPs composite, both in the absence ($0.63 \pm 0.176 \text{ k}\Omega$) and presence ($0.82 \pm 0.066 \text{ k}\Omega$) of $5 \mu\text{M}$ TBT, were very similar to the one obtained using MIP- Fe_3O_4 NPs composite in the absence of TBT (Fig. 3B) and the

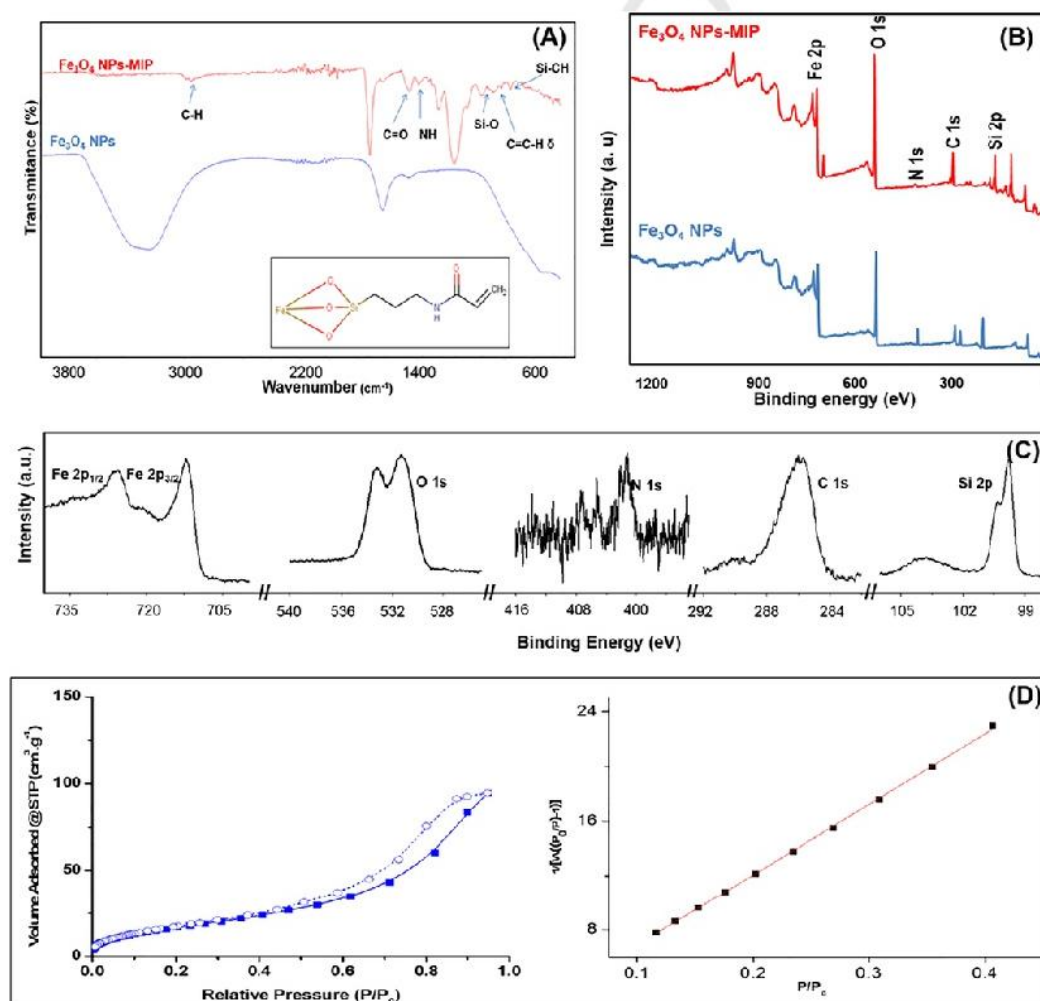


Fig. 2. Comparison of the IR (A) and wide-scan X ray photoelectron (B) spectra of Fe_3O_4 NPs (blue) and MIP- Fe_3O_4 NPs composite (red). High-resolution X-ray photoelectron spectra of Fe 2p, O 1s, N 1s, C 1s and Si 2p regions of the MIP- Fe_3O_4 NPs (C). N_2 adsorption isotherms (left) and dynamic curve (right) of MIP- Fe_3O_4 NPs (D). Inset: MIP- Fe_3O_4 NPs structure. (For interpretation of the references to color in this figure legend, the reader is referred to the web version of this article.)

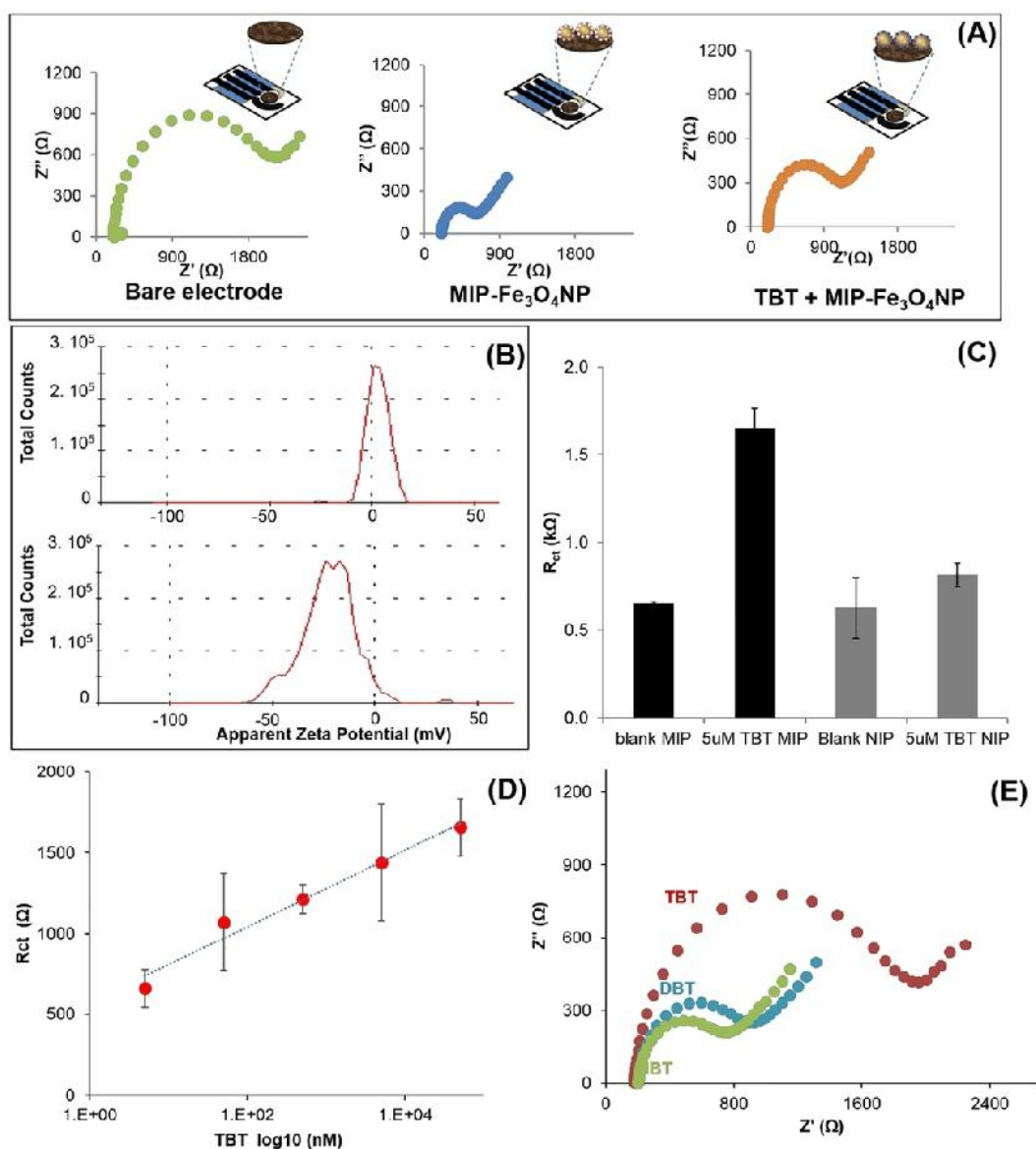


Fig. 3. Nyquist plot of bare SPE, SPEs modified with MIP- Fe_3O_4 NPs and MIP- Fe_3O_4 NPs + 5 μM TBT(A). Zeta-potential diagram from the dispersion of MIP- Fe_3O_4 NPs and MIP- Fe_3O_4 NPs + TBT (B). R_{ct} values obtained for MIP- Fe_3O_4 NPs and MIP- Fe_3O_4 NPs with and without 5 μM TBT (C). Calibration curve for R_{ct} values as a function of the TBT concentration (D). Nyquist plot of TBT, MBT and DBT at the same concentration (5 μM) (E).

imprinted factor using the Eq. (1) is 5.315. These observations suggest that the change observed is induced by the specific binding of TBT to the MIP and not by non-specific adsorption of the TBT onto the working electrode or the composite. The R_{ct} is obtained using Randles model modified with Warburg impedance (Z_w).

$$IF = \frac{R_{ct_{\text{MIP+TBT}}} - R_{ct_{\text{MIP}}}}{R_{ct_{\text{NIP+TBT}}} - R_{ct_{\text{NIP}}}} \quad (1)$$

After proving that the sensors responded to the presence of TBT, we challenged it with different TBT concentrations. The calibration curve of the R_{ct} values as a function of TBT concentration is shown in Fig. 3C, a linear range spanning 6 orders of magnitude, from 5 pM to 5 μM ($r^2 = 0.97$) with a limit of detection (LOD) of 5.37 pM and a limit of quantification (LOQ) of 17.9 pM are obtained. The LOD and the LOQ was calculated by 3 times or 10 times the s/m criteria respectively, where s is the standard deviation of the R_{ct} of the lowest concentration

of the TBT (3 repetitions) and m is the slope of the corresponding calibration graph. Both the LOD and LOQ of our sensor are smaller than the values recommended by the US Environmental Protection Agency: 1.45 nM (acute criterion) and 25 pM (chronic criterion) [26]. Moreover, the high concentration tested is 100 times upper than the maximum allowable concentration indicated by international agencies.

On the other hand, the sensor revealed high reproducibility with a relative standard deviation (RSD) of 17.8%, calculated as the mean of RSD obtained from five TBT concentrations and three replicates for each concentration. The selectivity of our sensor is tested using 5 μM monobutyltin dichloride (MTB) and dibutyltin dichloride (DTB). MTB and DTB represent a potential interference in the detection of TBT. The R_{ct} values for MBT and DBT are considerably lower than the one obtained using TBT, respectively: 0.44 ± 0.176 and 0.81 ± 0.066 k Ω . The TBT produced a signal 377% and 200% higher than the ones obtained using MBT and DTB, proving the high selectivity of our sensor for TBT (see Fig. 3E).

Finally, we challenged the MIP-Fe₃O₄NPs composite with a recovery test. We compared two different concentrations of TBT (5 pM and 5 μM) in pre-filtered sea water samples ($n = 3$ for each sample) with the same concentrations of TBT in MilliQ water. The recovery percentages (Eq. (2)) were 110.33% and 78.18%, respectively for 5 pM and 5 μM. The recovery percentages were particularly good considering the complexity of sea water matrix.

$$\text{Recovery percentage} = \frac{[\text{TBT}]_{\text{Sea water}}}{[\text{TBT}]_{\text{MilliQ water}}} \times 100 \quad (2)$$

4. Conclusions

We presented the development of the first impedimetric sensor for detection of TBT based on MIP-Fe₃O₄NPs composite. This low cost and user-friendly sensor shows excellent analytical performance thanks to the synergy between magnetic nanoparticles and MIPs. Such coupling allowed an efficient separation and preconcentration of the analyte. On one side, it responded specifically to TBT, in comparison to similar compounds (MBT and DBT), on the other its LOD (5 pM) and LOQ (18 pM) were below the values recommended by the US Environmental Protection Agency: 1.45 nM (acute criterion) and 25 pM (chronic criterion). Compared to other TBT detection systems, it showed the widest range of response and one of the lowest LOD found in the literature [27,28]. The high sensitivity of this system is attributed to high selectivity of MIP implemented previously by Zhu et al. [19] and the high sensitivity of the EIS as reported before [29–33]. The results demonstrate that the MIP-Fe₃O₄NPs composite is a robust and stable receptor for the electrochemical detection of pesticides.

Acknowledgment

This work was supported by: The European Commission Program, FP7-OCEAN, SMS Project (613844) and MINECO (Spain, MAT2014-52485-P). ICN2 acknowledges support from the Severo Ochoa Program (MINECO, Grant SEV-2013-0295). Nanobiosensors and Bioelectronics Group acknowledges the support from Secretaria d'Universitats i Recerca del Departament d'Economia i Coneixement de la Generalitat de Catalunya (2014 SGR 260).

References

- [1] M.A. Farajzadeh, B. Feriduni, M.R.A. Mogaddam, Determination of triazole pesticide residues in edible oils using air-assisted liquid-liquid microextraction followed by gas chromatography with flame ionization detection, *J. Sep. Sci.* 38 (2015) 1002–1009.
- [2] S. Muata, S. Takahashi, T. Agusa, N.J. Thomas, K. Kannan, S. Tanabe, Contamination status and accumulation profiles of organotins in sea otters (*Enhydra lutris*) found dead along the coasts of California, Washington, Alaska (USA), and Kamchatka (Russia), *Mar. Pollut. Bull.* 56 (2008) 641–649.
- [3] B. Antizar-Ladislao, Environmental levels, toxicity and human exposure to tributyltin (TBT)-contaminated marine environment. A review, *Environ. Int.* 34 (2008) 292–308.
- [4] M. Astruc, A. Astruc, R. Pinel, Speciation of butyltin compounds by on line HPLC-ETAAS, *Mikrochimica Acta* 109 (1992) 83–86.
- [5] I.R. Pereiro, V.O. Schmitt, J. Szpunar, O.F. Donard, R. Lubiński, Speciation analysis for organotin compounds in biomaterials after integrated dissolution, extraction, and derivatization in a focused microwave field, *Anal. Chem.* 68 (1996) 4135–4140.
- [6] E. Turiel, A. Martín-Esteban, Molecularly imprinted polymers: towards highly selective stationary phases in liquid chromatography and capillary electrophoresis, *Anal. Bioanal. Chem.* 378 (2004) 1876–1886.
- [7] X. Song, J. Li, S. Xu, R. Ying, J. Ma, C. Liao, D. Liu, J. Yu, L. Chen, Determination of 16 polycyclic aromatic hydrocarbons in seawater using molecularly imprinted solid-phase extraction coupled with gas chromatography-mass spectrometry, *Talanta* 99 (2012) 75–82.
- [8] J. Carpinteiro, I. Rodríguez, R. Cela, Applicability of solid-phase microextraction combined with gas chromatography atomic emission detection (GC-MIP AED) for the determination of butyltin compounds in sediment samples, *Anal. Bioanal. Chem.* 380 (2004) 853–857.
- [9] S.C. Cunha, J.O. Fernandes, Multipesticide residue analysis in maize combining acetonitrile-based extraction with dispersive liquid-liquid microextraction followed by gas chromatography-mass spectrometry, *J. Chromatogr. A* 1218 (2011) 7748–7757.
- [10] S.R. Rissato, M.S. Galhiane, F.R.N. Knoll, B.M. Apon, Supercritical fluid extraction for pesticide multiresidue analysis in honey: determination by gas chromatography with electron-capture and mass spectrometry detection, *J. Chromatogr. A* 1048 (2004) 153–159.
- [11] M.G. Cahill, G. Caprioli, M. Stack, S. Vittori, K.J. James, Semi-automated liquid chromatography-mass spectrometry (LC-MS/MS) method for basic pesticides in wastewater effluents, *Anal. Bioanal. Chem.* 400 (2011) 587–594.
- [12] D.B. Barr, L.L. Needham, Analytical methods for biological monitoring of exposure to pesticides: a review, *J. Chromatogr. B* 778 (2002) 5–29.
- [13] G. Aragay, F. Pino, A. Merkoçi, Nanomaterials for sensing and destroying pesticides, *Chem. Rev.* 112 (2012) 5317–5338.
- [14] C.C. Mayorga-Martínez, F. Pino, S. Kurbanoğlu, L. Rivas, S.A. Ozkan, Iridium oxide nanoparticle induced dual catalytic/inhibition based detection of phenol and pesticide compounds, *J. Mater. Chem. B* (2014) 2233–2239.
- [15] M. Medina-Sánchez, C.C. Mayorga-Martínez, T. Watanabe, T.A. Ivandini, Y. Honda, F. Pino, K. Nakata, A. Fujishima, Y. Einaga, A. Merkoçi, Corrigendum to 'Microfluidic platform for environmental contaminants sensing and degradation based on boron-doped diamond electrodes' [Biosens. Bioelectron. 08/75 (2015) 365–374], *Biosens. Bioelectron.* 79 (2016) 946.
- [16] A. Zamoza-Gálvez, A. Ait-Lahcen, L.A. Mercante, E. Morales-Narváez, A. Amine, A. Merkoçi, Molecularly imprinted polymer-decorated magnetite nanoparticles for selective sulfonamide detection, *Anal. Chem.* 88 (2016) 3578–3584.
- [17] C.C. Mayorga Martínez, E.F. Treo, R.E. Madrid, C.C. Felice, Biosensors and bioelectronics evaluation of chrono-impedance technique as transduction method for a carbon paste/glucose oxidase (CP/GO₂) based glucose biosensor, *Biosens. Bioelectron.* 26 (2010) 1239–1244.
- [18] L. Rivas, C.C. Mayorga-Martínez, Label-free impedimetric aptasensor for ochratoxin - a detection using iridium oxide nanoparticles, *Anal. Chem.* 87 (2015) 5167–5172.
- [19] S. Zhu, N. Gan, D. Pan, Y. Li, T. Yang, F. Hu, Y. Cao, D. Wu, Extraction of tributyltin by magnetic molecularly imprinted polymers, *Microchim. Acta* 180 (2013) 545–553.
- [20] J. He, J. An, D. Zhao, Synthesis and the characteristics of iron/iron oxide nanoparticles, *IEEE Trans. Magn.* 48 (2012) 4293–4296.
- [21] K. Petcharoen, A. Sirivat, Synthesis and characterization of magnetite nanoparticles via the chemical co-precipitation method, *Mater. Sci. Eng. B* 177 (2012) 421–427.
- [22] L. Chen, J. Liu, Q. Zeng, H. Wang, A. Yu, H. Zhang, L. Ding, Preparation of magnetic molecularly imprinted polymer for the separation of tetracycline antibiotics from egg and tissue samples, *J. Chromatogr. A* 1216 (2009) 3710–3719.
- [23] H. Jung, J.-W. Kim, H. Choi, J.-H. Lee, H.-G. Hur, Synthesis of nanosized biogenic magnetite and comparison of its catalytic activity in ozonation, *Appl. Catal. B Environ.* 83 (2008) 208–213.
- [24] X. Liang, S. Zhu, Y. Zhong, J. Zhu, P. Yuan, H. He, J. Zhang, The remarkable effect of vanadium doping on the adsorption and catalytic activity of magnetite in the decolorization of methylene blue, *Appl. Catal. B Environ.* 97 (2010) 151–159.
- [25] T. Braunbeck, D.E. Hinton, B. Streit, *Fish Ecotoxicology*. Basel, Birkhäuser Verlag, Boston, 1998.
- [26] U.S. EPA, Ambient Aquatic Life Water Quality Criteria for Tributyltin (TBT) - Final, 2003.
- [27] M.D. Mueller, Tributyltin detection at trace levels in water and sediments using GC with flame-photometric detection and GC-MS, *Presenius' Zeitschrift für Anal. Chemie.* 317 (1984) 32–36.
- [28] J. Wu, Z. Mester, J. Pawliszyn, Determination of tributyltin by automated in-tube solid-phase microextraction coupled with HPLC-ES-MS, *J. Anal. At. Spectrom.* 16 (2001) 159–165.
- [29] M. Xu, X. Luo, J.J. Davis, The label free picomolar detection of insulin in blood serum, *Biosens. Bioelectron.* 39 (2012) 21–25.
- [30] R.-M. Kong, Z.-L. Song, H.-M. Meng, X.-B. Zhang, G.-L. Shen, R.-Q. Yu, A label-free electrochemical biosensor for highly sensitive and selective detection of DNA via a dual-amplified strategy, *Biosens. Bioelectron.* 54 (2014) 442–447.

Graphene Quantum Dots-based Photoluminescent Sensor: A Multifunctional Composite for Pesticide Detection

Erhan Zor,^{†,‡,§,||,∇} Eden Morales-Narváez,^{†,∇} Alejandro Zamora-Gálvez,[†] Haluk Bingol,^{||} Mustafa Ersoz,[⊥] and Arben Merkoçi^{*,†,‡,§,||,∇}

[†]ICN2—Catalan Institute of Nanoscience and Nanotechnology, Campus de la UAB, 08193 (Bellaterra) Barcelona, Spain

[‡]Science and Technology Department, A.K. Faculty of Education, Necmettin Erbakan University, Konya, 42090, Turkey

[§]Department of Chemistry, Institute of Science, Selcuk University, Konya, 42030, Turkey

^{||}Department of Chemistry, A.K. Education Faculty, Necmettin Erbakan University, Konya, 42090, Turkey

[⊥]Advanced Technology Research and Application Center, Selcuk University, Konya, 42030, Turkey

[#]ICREA—Catalan Institution for Research and Advanced Studies, Barcelona, 08010, Spain

S Supporting Information

ABSTRACT: Due to their size and difficulty to obtain, cost/effective biological or synthetic receptors (e.g., antibodies or aptamers, respectively), organic toxic compounds (e.g., less than 1 kDa) are generally challenging to detect using simple platforms such as biosensors. This study reports on the synthesis and characterization of a novel multifunctional composite material, magnetic silica beads/graphene quantum dots/molecularly imprinted polypyrrole (mSGP). mSGP is engineered to specifically and effectively capture and signal small molecules due to the synergy among chemical, magnetic, and optical properties combined with molecular imprinting of tributyltin (291 Da), a hazardous compound, selected as a model analyte. Magnetic and selective properties of the mSGP composite can be exploited to capture and preconcentrate the analyte onto its surface, and its photoluminescent graphene quantum dots, which are quenched upon analyte recognition, are used to interrogate the presence of the contaminant. This multifunctional material enables a rapid, simple and sensitive platform for small molecule detection, even in complex mediums such as seawater, without any sample treatment.

KEYWORDS: graphene quantum dots, magnetic silica beads, molecularly imprinted polymer, multifunctional composite, small molecule detection



1. INTRODUCTION

Small molecules such as organic toxic compounds have raised serious concerns due to not only their persistent and bioaccumulative characteristics that impact wildlife and sensitive ecosystems,^{1–3} but also effects on human health, which include endocrine disruptive activity, carcinogenicity, genotoxicity, and irritancy.⁴ Typically, these hazardous compounds are detected through highly sensitive and robust techniques such as high-performance liquid chromatography and mass spectrometry. However, these techniques often require expensive equipment, time-consuming sample preparation procedures, and trained personnel. As a consequence, development of simple approaches for highly specific detection of organic toxic compounds is under active research, in particular using biosensing and nanotechnology.⁵

In biosensing, biological/synthetic sensing elements (or receptors), such as antibodies or aptamers, are crucial because they selectively interact with the analyte. Owing to their size (less than 1 kDa), organic toxic compounds are not immunogenic.⁶ Consequently, development of antibodies targeting these compounds is technically difficult to cope

with. On the other hand, aptamers targeting organic toxic compounds have been scarcely reported and usually imply high cost and long procedures. In this context, molecularly imprinted polymers (MIPs) represent a biomimetic alternative as sensing elements.^{7–10}

Moreover, nanomaterials such as graphene-related materials have received much attention in sensors and devices due to their unique electronic properties, mechanical flexibility, thermal/chemical stability, and optical properties.¹¹ A wide variety of optical and electrical sensing platforms based on graphene-related materials have been developed for the detection of ions, biomolecules, pathogens, and other species.^{11–15} However, small molecule detection has been scarcely explored in this context. Because graphene quantum dots (GQDs) have low toxicity and are chemically inert, biocompatible, and resistant to photobleaching,¹⁶ they are one of the emerging and promising optical nanomaterials for

Received: June 30, 2015

Accepted: August 27, 2015

Published: August 27, 2015

prospective applications in bioimaging,¹⁷ photovoltaics,¹⁸ chemical sensors,¹⁹ and bio/sensors.²⁰ Although the electrical properties have attracted continuous and tremendous interest, the use and investigation of the photoluminescent properties of graphene-related materials remain a challenge to be completely explored.²¹ Moreover, GQDs display high surface area and the carboxylic moieties at their edges provide them with water dispersibility and proper functional groups to be complexed with several compounds (including inorganic, polymeric, or biological compounds).²⁰ Recently, a nonmultifunctional GQDs-based composite targeting a toxic phenolic compound has been reported, however, it requires filtration procedures to assay real samples, which implies extra steps and materials during the proposed analysis.²²

Herein, the synthesis, characterization and performance of a multifunctional composite material (mSGP) designed to detect an organic toxic compound without any sample treatment is reported. The pesticide tributyltin (TBT, 291 Da), which is genotoxic and gives rise to endocrine disruptions,²³ has been chosen as a model analyte. This composite (mSGP) consists of magnetic silica beads encapsulated by GQDs embedded in molecularly imprinted polypyrrole. Thus, the mSGP composite displays: (1) magnetic properties, which are useful for separation and preconcentration of the toxic compound; (2) water dispersibility, which is important for its processing in aqueous phase; (3) selectivity, which is pivotal in terms of selectivity and specificity; and (4) photoluminescence as an optical transducing system that is quenched by energy transfer upon analyte binding. A schematic representation of the mSGP composite and its sensing mechanism is depicted in Figure 1.

2. MATERIALS AND METHODS

2.1. Chemical and Apparatus. All commercial reagents were of analytical grade and handled according to the material safety data



Figure 1. Schematic representation of the mSGP composite and its sensing mechanism. The concept is based on turn-off in photoluminescence of mSGP. Once pesticide (TBT) is selectively captured by the cavities of the molecularly imprinted polymer, photoluminescent GQDs lead to an optical transducing system, that is, GQDs are quenched upon analyte recognition.

sheets suggested by the suppliers. Citric acid, NaOH, pyrrole, monobutyltin (MBT), dibutyltin (DBT) and tributyltin (TBT) were purchased from Sigma-Aldrich (Madrid, Spain). A solution of NH_2 functionalized magnetic silica beads (mSB S-NH₂ 600) was purchased from MoBiTec (Göttingen, Germany). All aqueous solutions were freshly prepared in Milli-Q ultrapure water.

A Bruker PMA 50 (accessory coupled to Tensor 27) Fourier transformed infrared (FT-IR) spectrometer (Coventry, UK) was used to record spectra of the samples between 400 and 4000 cm^{-1} . X-ray photoelectron spectroscopy (XPS) measurements were performed using a PHOIBOS-150 analyzer/spectrometer (SPECS GmbH, Berlin, Germany). High-resolution scanning electron microscopy (SEM) images were taken on an FEI Magellan 400L SEM (Hillsboro, OR). High-resolution transmission electron microscopy (HR-TEM) images were taken with a FEI Tecnai F20 S/TEM (Hillsboro, OR). Confocal Raman measurements were performed on a Renishaw inVia Reflex (Gloucestershire, U.K.) equipped with CCD detector and a Leica microscope (Wetzlar, Germany). In order to obtain Raman images (3D-in a volume of $6 \times 6 \times 5 \mu\text{m}$; x, y, z), a thin layer of the samples was deposited onto a glass slide and spectra were recorded with a 100 \times objective creating a 532 nm DPSS laser. Zeta potentials were measured with a Malvern Zetasizer Nano Z (Malvern, U.K.). UV-vis absorbance and fluorescence measurements were carried out using a SpectraMax M2e microplate reader (Molecular Devices, Sunnyvale, CA). AFM micrographs were obtained using a Park XE7 instrument (Suwon, Korea).

2.2. Synthesis of Multifunctional Magnetic Silica Beads/Graphene Quantum Dots/Molecularly Imprinted Polypyrrole (mSGP).

Synthesis of magnetic silica beads/graphene quantum dots/molecularly imprinted polypyrrole (mSGP) was performed in three steps. As the first step, GQDs was prepared by directly pyrolysis of citric acid (CA).²⁴ Briefly, 2 g of CA was put into a 5 mL beaker and heated to 200 °C using an oil bath. After standing for 30 min at 200 °C in an oil bath, CA was liquated, the color of the liquid changed to pale yellow, and then orange, respectively. The resulting orange liquid was added drop by drop into 100 mL of 10 mg mL^{-1} NaOH solution under vigorous stirring to obtain the aqueous solution of GQDs. For the analysis processes, the GQDs solution was washed with ethanol/water (GQD solution; 80:20 v/v) and centrifuged for 10 min at 4000 rpm several times in order to remove NaOH to obtain GQDs and the precipitate was dried at 40 °C in oven for overnight. In the second step, 20 mL of GQDs solution, pyrrole (50 mM) and tributyltin (10 mM) as a template were added into the solution. Then, polypyrrole (PPy) was initiated with the addition of H₂O₂ (50 mM) under acidic conditions (pH 2) adjusted by HCl and mixed at room temperature for 24 h.²⁵ The color changed to pale green and then dark green indicating GQDs/PPy is obtained by in situ polymerization. The final step is the synthesis of the multifunctional mSGP composite material and removal of TBT. For this reason, after 1-ethyl-3-(3-dimethylaminopropyl)-carbodiimide (EDC; 25 mM) and *N*-hydroxysulfosuccinimide sodium salt (Sulfo-NHS; 25 mM) were added to the GQDs/PPy solution to activate the surface carboxylic group of GQDs and mixed for 30 min at room temperature with continuous stirring.²⁶ 10 mL of mSB S-NH₂ (0.5 mg mL^{-1}) was added into the solution and allowed to react for 72 h at room temperature with continuous stirring. After that, TBT is removed from the polymer by washing the composite with ethanol for several times using a magnet to separate the composite after the release of TBT into supernatant. The obtained multifunctional final mSGP composite is water-soluble, photoluminescent led by GQDs, selective for TBT due to the MIP and easy to remove from the solution by its magnetic property.

2.3. Procedure for Fluorescence Measurements and Real Sample Analysis. In a typical test, a suspension of as-prepared mSGP composite (200 μL , in Milli-Q water) and different amounts of TBT (usually from 10 ppb to 10 ppm) or the other possible interferences such as MBT and DBT were added into a 96-well fluorescence microplate and incubated during 45 min to capture the analyte. The excitation wavelength was 365 nm. For the real sample analysis measurements, TBT, MBT, and DBT were added into the seawater solution with suspended mSGP. Then, mSGP was separated from the

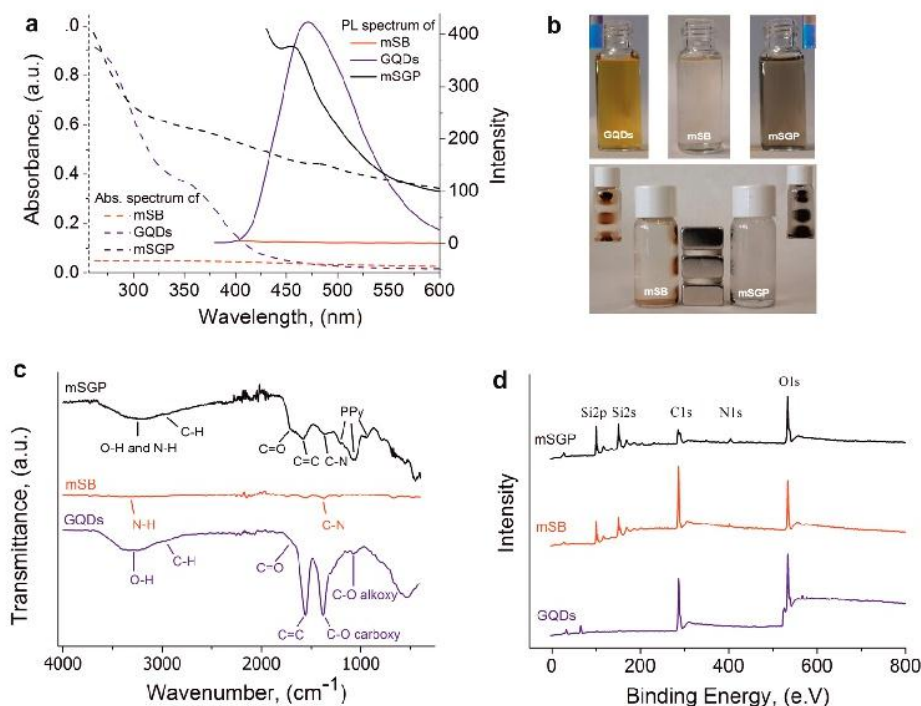


Figure 2. Spectroscopic characterization of the mSGP composite; (a) UV–vis and photoluminescent spectra, (b) the solutions and magnetic characters in water, (c) FT-IR spectra, and (d) XPS spectra of GQDs, mSB, and mSGP.

seawater solution using a magnet and resuspended in 200 μL of distilled water, and fluorescence spectra were recorded.

2.4. Quantum Yield Determination. The quantum yields (QYs) of the GQDs and mSGP were determined by using quinine sulfate (QY = 0.54 in 0.1 M H_2SO_4) as the standard sample²⁷ and were calculated according to the following equation;

$$Q_x = Q_{st} \frac{I_x A_{st} n_x^2}{I_{st} A_x n_{st}^2} \quad (1)$$

where Q refers to quantum yield, I is the measured emission intensity, A is the extinction, and n is the refractive index. The subscript “st” belongs to the standard solution, and “x” represents the sample.

3. RESULTS AND DISCUSSION

3.1. Characterization. The characterization of the composite material was performed by ultraviolet–visible spectroscopy (UV–vis), photoluminescent spectra, Fourier transform infrared spectroscopy (FT-IR), X-ray photoelectron spectroscopy (XPS), scanning electron microscopy (SEM), high resolution transmission electron microscopy (HR-TEM), and confocal Raman microscopy techniques.

3.1.1. UV–Vis Absorption, Photoluminescence Spectra, and Colloidal Stability. Figure 2a shows the UV–vis absorption and photoluminescence spectra of GQDs, magnetic silica beads (mSB) and mSGP. GQDs dispersion display a maximum absorption peak at 273 nm due to the π – π^* transition of aromatic C=C bonds and a typical absorption peak at 365 nm which corresponds to the n – π^* transition of the C=O bond.^{28,29} On the other hand, mSB is optically inactive, whereas mSGP shows two weak shoulders in absorption spectrum at 367 nm and at 485 nm which are respectively n – π^* transition of the C=O bond²⁹ and the characteristic absorption peak of PPy.³⁰

Figure 2b shows the solutions of GQDs (yellow), mSB (pale yellow-brown), and mSGP (dark green-black), which implies the final composite material is synthesized and completely different from the precursor materials. As it can be seen, both solutions of GQDs and mSGP emit blue light (at 470 and 460 nm, respectively) under 365 nm UV beam. Although both GQDs and mSGP have their maximum luminescence quantum yields (QYs) at emission wavelengths of 470 and 460 nm, the GQDs show much stronger luminescence than the mSGP under excitation of 365 nm light. The QYs of GQDs and mSGP at 365 nm were calculated to be about 3.9% and 1.1%, respectively. The drop in the QY of the composite can be attributed to the covalent functionalization of the GQDs with magnetic silica beads containing NH_2 groups, which modifies the original moieties in the GQDs. Additionally, the vials shown in Figure 2b display the magnetic properties of mSB and mSGP (applying a permanent magnetic field with the triple magnets).

It should be noted that this magnetic property not only is crucial to remove the template molecule after MIP synthesis (or subsequently capturing the analyte) but also may be used as a preconcentration process to enrich the concentration of samples with low content of analyte. Moreover, the zeta potential measurement (Figure S1a) indicates that the silica beads are positively charged in water with a zeta potential of $+22.60 \pm 0.86$ mV due to the amine groups on the surface of silica beads, whereas mSGP is negatively charged with a stable zeta potential value of -47.10 ± 2.23 mV due to the GQDs which have oxygen containing groups such as –OH and –COOH, as shown in Figure S1b.

3.1.2. Fourier Transform Infrared Spectroscopy (FT-IR) and X-ray Photoelectron Spectroscopy (XPS) Analysis. FT-IR analysis of GQDs, mSB and mSGP was represented in Figure 2c. The broad bands at 3243–3291 cm^{-1} are ascribed to –OH and –NH groups stretching vibration.²⁴ The peak at 2956

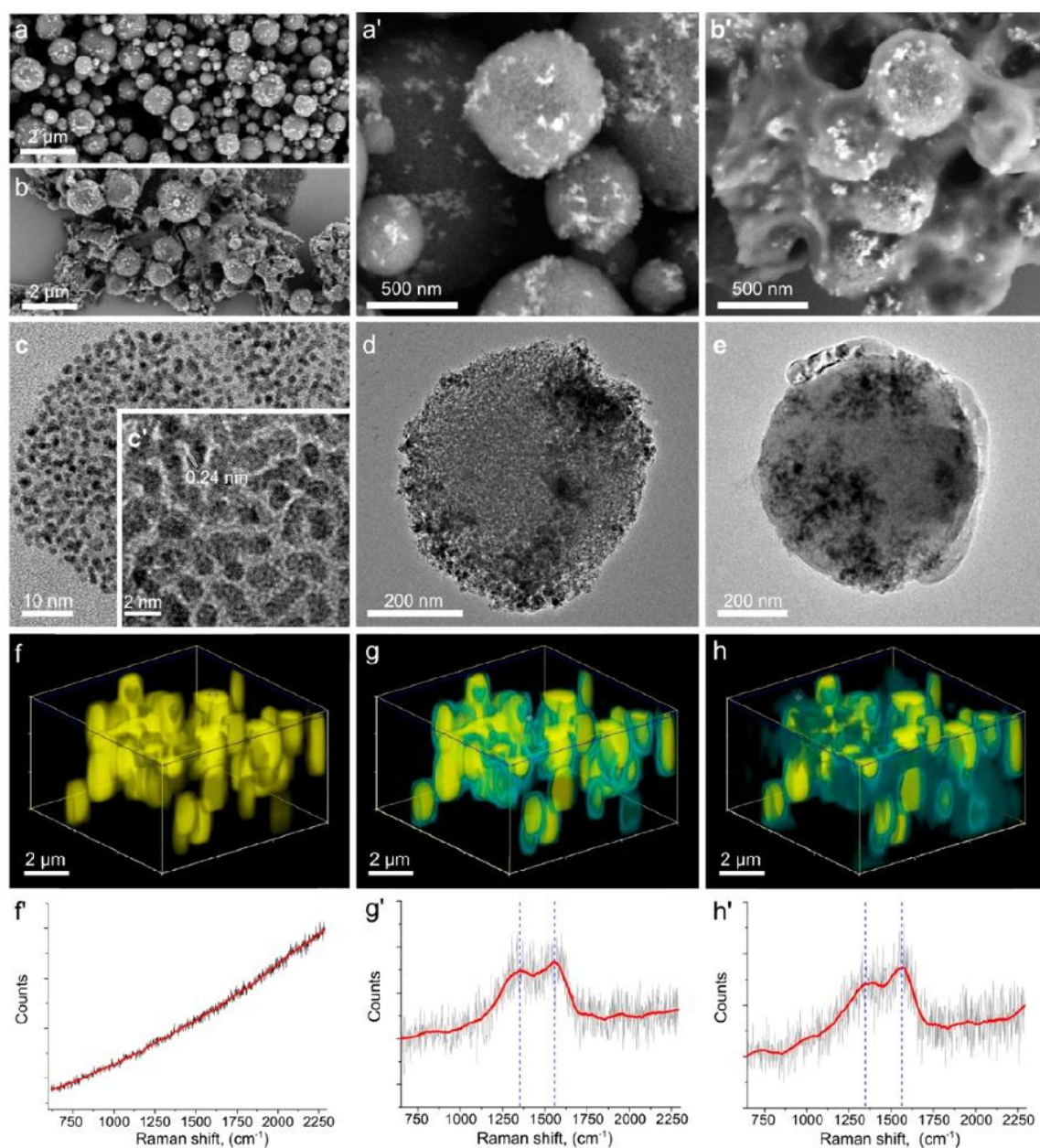


Figure 3. Images of the mSGP composite. SEM micrographs of (a and a') mSB and (b and b') mSGP. HRTEM micrographs of (c and c') GQDs, (d) mSB, and (e) mSGP. 3D Raman images and Raman spectra of (f and f') mSB, (g and g') mSB/GQDs, and (h and h') mSGP (Video SV1).

cm^{-1} in spectra shows the asymmetric stretching and symmetric vibrations of C–H.²⁴ The well-defined peak at 1565 cm^{-1} is related to bending vibrations of C=C group.²⁹ The peaks at 1685 , 1380 , and 1061 cm^{-1} were assigned to the C=O, C–O (carboxy), and C–O (alkoxy) functional groups, respectively.²⁹ The band at 1356 cm^{-1} belongs to C–N stretching modes. For the mSGP composite, and 1204 , 1068 , and 928 cm^{-1} are related to the characteristic peaks of PPy suggested the successful coating of polymer.³¹ Figure S2 shows the IR spectrum of GQDs/PPy which includes the main characteristic peaks of GQDs (beside peaks of PPy) that proves the presence of carboxylic group to conjugate with magnetic silica beads.

XPS technique was used for further confirmation of the functional groups in the GQDs, mSB, and mSGP composite, and the results are given in Figure 2d. As can be seen, C 1s and O 1s signals were observed at 284 and 530 eV for GQDs.³² XPS spectra for mSB and mSGP composite show Si 2p peaks at 99.7 and 103.9 eV (belong to $2p_{3/2}$ and $2p_{1/2}$ and SiO_2 ,³³ respectively) and Si 2s peaks around 151 eV .³⁴ N 1s peak at 400 eV was obtained beside C 1s and O 1s at 284 and 530 eV , which implies the incorporation of mSB and PPy. Also, N 1s peak intensity of composite is higher than that of mSB, which can be attributed the formation of PPy. The high-resolution C 1s spectrum of GQDs, mSB and mSGP were also performed and shown in Figure S3. GQDs show four peaks at 284 , 285.0 , 287.4 , and 288.7 eV corresponding to C=C, C–C, C–O, and

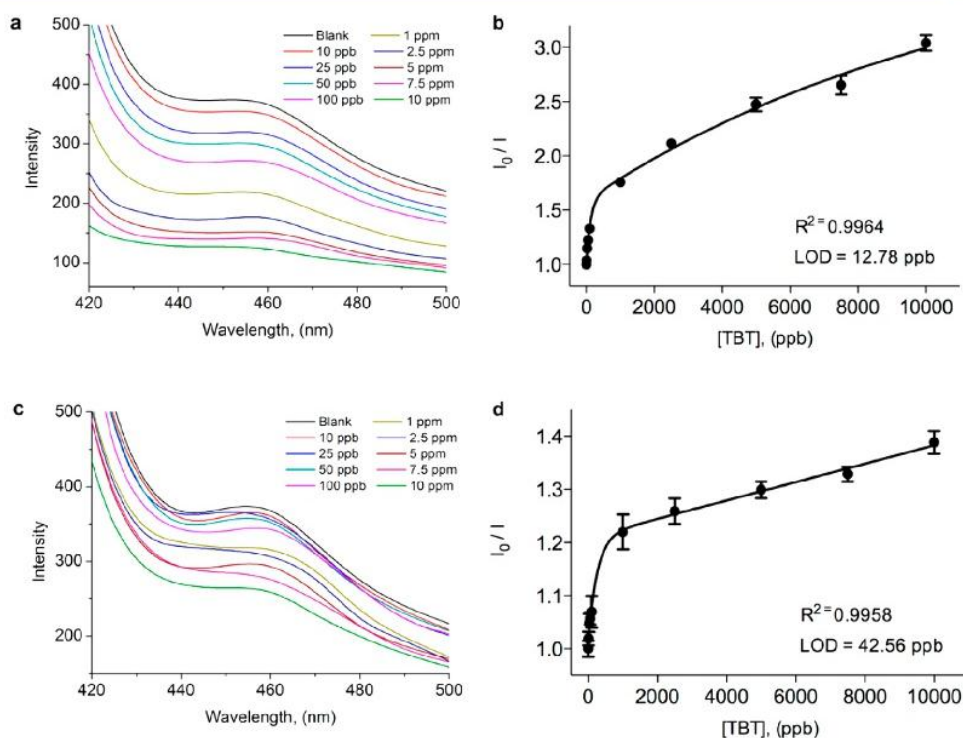


Figure 4. Behavior of the GQDs-based photoluminescent sensor. Spectral change of mSGB in the presence of TBT at different concentrations (0.0–10 ppm) in (a) pure water and (c) seawater. Nonlinear calibration curves (two phase association) for (b) pure water and (d) seawater analysis. The error bars represent the standard deviation of three parallel experiments.

COOH groups, respectively (Figure S3a). As shown in Figure S3b, mSB has two peaks at 284.5 and 285.7 eV that belong to C–C and C–N, respectively. For mSGP (Figure S3c), C 1s is deconvoluted into five unit moieties: C=C/C–C with a binding energy at 283.9 eV, C–N and C–O at 285.7 and 286.8 eV, C=O at 287.2 eV, and N–C=O at 288.5 eV, proving the chemical reaction of EDC/NHS. These results support the presence of composite and are consistent with the other spectroscopic results.

3.1.3. Scanning Electron Microscopy (SEM) and High-Resolution Transmission Electron Microscopy (HRTEM) Analysis. SEM and HRTEM were used to examine the structure of GQDs, mSB and mSGP. mSB exhibit a diameter size ranging from 200 nm to 1.2 μm (manufacturer's data, approximate values). Figure 3a,a' and 3b,b', respectively, show the SEM micrographs of mSB that has a porous appearance and of mSGP which exhibits a smooth appearance well-covered by polymer and GQDs. This coating can be explained by the interaction of positively charged Py molecule in its nitrogen (N) site with the negative charged GQDs due to the abundant oxygen groups such as –COOH and –OH on its edge as observed from the FTIR spectrum shown in Figure 2c.³⁵ Figure 3c,c' show HRTEM micrographs of the GQDs with different magnifications. Figure S4 exhibits the size distribution of GQDs, which is uniform with an average diameter of 2.37 ± 0.39 nm. GQDs have crystallinity with lattices of 0.24 nm which are sp^2 clusters in GQDs (Figure 3c').^{26,36,37} As shown in Figure 3d, mSB has a spherical shape and a porous surface. After in situ polymerization and GQDs linkage around the mSB surfaces, the porosity disappeared due to the encapsulation of mSB by polymer matrix and GQDs (Figure 3e) indicating the

formation of mSGP. Figure S5 shows the AFM image acquired in air under tapping mode and height profile of GQDs. The thicknesses of the GQDs are about 1.2 nm depicting that they assume the same structure.

3.1.4. Confocal Raman Analysis. In the following study, confocal Raman measurements were recorded in order to analyze the 3D shape of the composite material. Figure 3f,f' display the resulting 3D Raman image of the mSBs, which are nearly ball-shaped in yellow color, and the Raman spectrum, respectively. As can be seen in Figure 3g, mSBs are surrounded by GQDs which are shown in phase with turquoise color and the corresponding Raman spectrum (the marked point with star in the figure) shows D and G bands at 1351 and 1560 cm^{-1} , which are characteristic bands for GQDs as previously reported in the literature (Figure 3g').^{38,39} The peak of D band refers to the defects and disorder in hexagonal lattice, whereas G-band is due to the vibration of sp^2 bonded carbon atoms in the 2D hexagonal lattice. The calculated I_D/I_G ratio is 0.86 which express the atomic ratio of sp^2/sp^3 carbons. The corresponding Raman image and Raman spectrum for mSGP are shown in Figure 3h,h'. The blue colored cloud-shaped material belongs to the occurring polymer with the combination of GQDs (Video SV1). The Raman spectrum shows four different peaks at around 1000, 1332, 1388, and 1566 cm^{-1} . The peaks at 1332 and 1566 cm^{-1} refer to the characteristic D and G bands of GQDs. It should be mentioned that these bands of mSGP are similar to those of GQDs which can be ascribed to the fact that the polymeric part may also have GQDs due to the in situ polymerization process. In addition, the small and broad peak around 1000 cm^{-1} can be attributed to the characteristic peak of PPY which is due to the

bipolaron ring deformation and polaron symmetric C–H in plane bending vibration and the peak at 1388 cm^{-1} is ascribed to the ring stretching mode of PPy.⁴⁰ The calculated I_D/I_G ratio is 0.80.

3.2. Performance of the mSGP Multifunctional Composite As a Sensing Platform. **3.2.1. Sensing Principle, Optimization, and Sensitivity.** The proposed sensing platform is based on energy transfer.^{41–43} Thus, the analyte, being an organometallic compound, is expected to quench the photoluminescence (PL) of the GQDs embedded within the composite in order to interrogate the absence/presence of the analyte. Aiming at researching the analytical performance of the engineered sensing platform under optimal conditions, a judicious selection of the monomer amount and the analyte incubation time was carried out. Figure 4a shows PL spectra recorded to investigate the interaction between TBT and mSGP under the optimized conditions; (1) monomer amount which concentration was chosen to be 50 mM owing to the observation of total quenching due to energy transfer and (2) incubation time that was selected as 1h because the PL intensity quenched within 45 min and after that remained almost stable (Figure S6a,b). The emission peak at 460 nm gradually decreased upon addition of increasing amounts of TBT (0.0–10 ppm) into the suspension of mSGP. The emission profile of mSGP as a function of TBT concentration was obtained as shown in Figure 4b, which exhibits a nonlinear calibration curve for increasing concentration of TBT. Limit of detection (LOD, i.e., the interpolation of the mean of the blank signal plus 3 times its standard deviation into the fitting curve) and limit of quantification (LOQ, i.e., the interpolation of the mean of the blank signal plus 10 times its standard deviation into the fitting curve) were estimated as 12.78 and 42.60 ppb.

3.2.2. Specificity. Specific and sensitive detection in practical applications of sensors is also one of the most important goals.⁴⁴ In order to confirm the ability of the sensing platform to display a selective and specific analytical performance, other organotin compounds such as monobutyltin (MBT) and dibutyltin (DBT) were chosen as interfering compounds. Figure S6c shows a series of PL spectral experiments carried out to investigate the interference of MBT and DBT. As shown in Figure S6d, no significant change (a negligible enhancement) was observed for emission intensity in the presence of MBT, while it decreased around 8.2% with the addition of 10 ppm of DBT. It is clear that mSGP had a strong response to TBT, which caused a significant change in PL intensity with a high quenching degree that is more than MBT and DBT. In addition to PL spectra, EDX of TEM proves the absence (Figure S7a) and presence of TBT as a result of attachment in the composite, as given in Figure S7b.

3.2.3. Seawater Analysis. TBT is considered one of the most toxic compounds introduced into the marine environment.¹ To prove the robustness and the potential utility of the developed sensing platform, we carried out a series of photoluminescence measurements in seawater in the presence of TBT at different concentrations, and the results are shown in Figure 4c. The emission peak at 460 nm gradually decreased with the increasing amount of TBT (0.0–10 ppm), whereas the peak was not totally quenched and the emission profile of mSGP as a function of TBT concentration is shown in Figure 4d. LODs and LOQs were calculated as 42.56 and 141.86 ppb in seawater. The coefficient of variation of the proposed seawater analysis ranges from ca. 1 to ca. 3%. On the other hand, the recovery ranges from ca. 92 to ca. 114% (Table S1,

Supporting Information). Overall, the results proved that this multifunctional composite material-based photoluminescent sensor was successfully applied in the detection of TBT even in a complex medium such as a real sample of seawater without any sample treatment.

4. CONCLUSIONS

We have developed a new simple and rapid approach for sensitive and selective optical sensing systems taking advantage of the proposed multifunctional composite material. The synthesized composite material has been characterized in detail using several imaging and spectroscopic techniques. The sensing approach is based on; (1) molecularly imprinted polypyrrole that selectively captures the analyte; (2) magnetic silica beads serving as a separation mechanism (3) water dispersibility that enables a liquid-phase-based assay and (4) graphene quantum dots which lead to an optical transducing system upon analyte recognition. In this respect, we have successfully determined the organic toxic compound TBT in water and seawater with a LOD of 12.78 and 42.56 ppb, respectively. This optical sensing concept can be extended to other small compounds as a simple platform that is capable of analyzing complex samples such as seawater without any sample treatment.

■ ASSOCIATED CONTENT

Supporting Information

The Supporting Information is available free of charge on the ACS Publications website at DOI: 10.1021/acsami.5b05838.

Zeta potential measurements, details on XPS spectra, the size distribution of GQDs, the effect of monomer amount and incubation time on PL quenching, recovery of the proposed sensing system (analysis in seawater), EDX in the absence and presence of TBT as a result of attachment in the composite (PDF)

Video SV1: 3D Raman imaging video recorded to show each material and the corresponding/individual Raman spectrum (AVI)

■ AUTHOR INFORMATION

Corresponding Author

*E-mail: arben.merkoci@icn.cat.

Author Contributions

[▽]The manuscript was written through contributions of all authors. All authors have given approval to the final version of the manuscript. These authors contributed equally.

Notes

The authors declare no competing financial interest.

■ ACKNOWLEDGMENTS

This work was supported by The European Commission Program, FP7-OCEAN, SMS Project (613844). ICN2 acknowledges support from the Severo Ochoa Program (MINECO, Grant SEV-2013-0295).

■ REFERENCES

- (1) Goldberg, E. D.; Bertine, K. K. Beyond the Mussel Watch — New Directions for Monitoring Marine Pollution. *Sci. Total Environ.* **2000**, *247*, 165–174.
- (2) Barbieri, R. F.; Lester, P. J.; Miller, A. S.; Ryan, K. G. A Neurotoxic Pesticide Changes the Outcome of Aggressive Interactions

between Native and Invasive Ants. *Proc. R. Soc. London, Ser. B* **2013**, *280*, 20132157–20132157.

(3) Beketov, M. A.; Kefford, B. J.; Schäfer, R. B.; Liess, M. Pesticides Reduce Regional Biodiversity of Stream Invertebrates. *Proc. Natl. Acad. Sci. U. S. A.* **2013**, *110*, 11039–11043.

(4) Matthews, G. *Pesticides: Health, Safety and the Environment*; 1st ed.; Wiley-Blackwell: Oxford, U.K., 2006.

(5) Aragay, G.; Pino, F.; Merkoçi, A. Nanomaterials for Sensing and Destroying Pesticides. *Chem. Rev.* **2012**, *112*, 5317–5338.

(6) Brown, M. C. Antibodies: Key to a Robust Lateral Flow Immunoassay. In *Lateral Flow Immunoassay*; Wong, R.; Tse, H., Eds.; Humana Press: Totowa, NJ, 2009; pp 1–16.

(7) Whitcombe, M. J.; Chianella, I.; Larcombe, L.; Piletsky, S. A.; Noble, J.; Porter, R.; Horgan, A. The Rational Development of Molecularly Imprinted Polymer-Based Sensors for Protein Detection. *Chem. Soc. Rev.* **2011**, *40*, 1547–1571.

(8) Merkoçi, A.; Alegret, S. New Materials for Electrochemical Sensing IV. Molecular Imprinted Polymers. *TrAC, Trends Anal. Chem.* **2002**, *21*, 717–725.

(9) Lautner, G.; Kaev, J.; Reut, J.; Öpik, A.; Rappich, J.; Syrtiski, V.; Gyurcsányi, R. E. Selective Artificial Receptors Based on Micro-patterned Surface-Imprinted Polymers for Label-Free Detection of Proteins by SPR Imaging. *Adv. Funct. Mater.* **2011**, *21*, 591–597.

(10) Shutov, R. V.; Guerreiro, A.; Moczko, E.; de Vargas-Sansalvador, I. P.; Chianella, I.; Whitcombe, M. J.; Piletsky, S. A. Introducing MINA—The Molecularly Imprinted Nanoparticle Assay. *Small* **2014**, *10*, 1086–1089.

(11) Gravagnuolo, A. M.; Morales-Narváez, E.; Longobardi, S.; da Silva, E. T.; Giardina, P.; Merkoçi, A. In Situ Production of Biofunctionalized Few-Layer Defect-Free Microsheets of Graphene. *Adv. Funct. Mater.* **2015**, *25*, 2771–2779.

(12) Morales-Narváez, E.; Merkoçi, A. Graphene Oxide as an Optical Biosensing Platform. *Adv. Mater.* **2012**, *24*, 3298–3308.

(13) Zor, E.; Bingol, H.; Ramanaviciene, A.; Ramanavicius, A.; Ersoz, M. An Electrochemical and Computational Study for Discrimination of D- and L-Cystine by Reduced. *Analyst* **2015**, *140*, 313–321.

(14) Morales-Narváez, E.; Hassan, A. R.; Merkoçi, A. Graphene Oxide as a Pathogen-Revealing Agent: Sensing with a Digital-like Response. *Angew. Chem., Int. Ed.* **2013**, *52*, 13779–13783.

(15) Liu, Y.; Dong, X.; Chen, P. Biological and Chemical Sensors Based on Graphene Materials. *Chem. Soc. Rev.* **2012**, *41*, 2283–2307.

(16) Ye, R.; Peng, Z.; Metzger, A.; Lin, J.; Mann, J. A.; Huang, K.; Xiang, C.; Fan, X.; Samuel, E. L. G.; Alemany, L. B.; Marti, A. A.; Tour, J. M. Bandgap Engineering of Coal-Derived Graphene Quantum Dots. *ACS Appl. Mater. Interfaces* **2015**, *7*, 7041–7048.

(17) Nurunnabi, M.; Khatun, Z.; Reeck, G. R.; Lee, D. Y.; Lee, Y. Photoluminescent Graphene Nanoparticles for Cancer Phototherapy and Imaging. *ACS Appl. Mater. Interfaces* **2014**, *6*, 12413–12421.

(18) Son, D. I.; Kwon, B. W.; Park, D. H.; Seo, W.-S.; Yi, Y.; Angadi, B.; Lee, C.-L.; Choi, W. K. Emissive ZnO-graphene Quantum Dots for White-Light-Emitting Diodes. *Nat. Nanotechnol.* **2012**, *7*, 465–471.

(19) Liu, J.-J.; Zhang, X.-L.; Cong, Z.-X.; Chen, Z.-T.; Yang, H.-H.; Chen, G.-N. Glutathione-Functionalized Graphene Quantum Dots as Selective Fluorescent Probes for Phosphate-Containing Metabolites. *Nanoscale* **2013**, *5*, 1810–1815.

(20) Shen, J.; Zhu, Y.; Yang, X.; Li, C. Graphene Quantum Dots: Emergent Nanolights for Bioimaging, Sensors, Catalysis and Photovoltaic Devices. *Chem. Commun.* **2012**, *48*, 3686.

(21) Li, M.; Wu, W.; Ren, W.; Cheng, H. M.; Tang, N.; Zhong, W.; Du, Y. Synthesis and Upconversion Luminescence of N-Doped Graphene Quantum Dots. *Appl. Phys. Lett.* **2012**, *101*, 103107.

(22) Zhou, Y.; Qu, Z.; Zeng, Y.; Zhou, T.; Shi, G. A Novel Composite of Graphene Quantum Dots and Molecularly Imprinted Polymer for Fluorescent Detection of Paranitrophenol. *Biosens. Bioelectron.* **2014**, *52*, 317–323.

(23) Antizar-Ladislao, B. Environmental Levels, Toxicity and Human Exposure to Tributyltin (TBT)-Contaminated Marine Environment. A Review. *Environ. Int.* **2008**, *34*, 292–308.

(24) Dong, Y.; Shao, J.; Chen, C.; Li, H.; Wang, R.; Chi, Y.; Lin, X.; Chen, G. Blue Luminescent Graphene Quantum Dots and Graphene Oxide Prepared by Tuning the Carbonization Degree of Citric Acid. *Carbon* **2012**, *50*, 4738–4743.

(25) Ramanavicius, A.; Kausaitė, A.; Ramanaviciene, A.; Acaite, J.; Malinauskas, A. Redox Enzyme – Glucose Oxidase – Initiated Synthesis of Polypyrrole. *Synth. Met.* **2006**, *156*, 409–413.

(26) Zheng, X. T.; Than, A.; Ananthanaraya, A.; Kim, D. H.; Chen, P. Graphene Quantum Dots as Universal Fluorophores and Their Use in Revealing Regulated Trafficking of Insulin Receptors in Adipocytes. *ACS Nano* **2013**, *7*, 6278–6286.

(27) Tetsuka, H.; Asahi, R.; Nagoya, A.; Okamoto, K.; Tajima, I.; Ohta, R.; Okamoto, A. Optically Tunable Amino-Functionalized Graphene Quantum Dots. *Adv. Mater.* **2012**, *24*, 5333–5338.

(28) Dai, Y.; Long, H.; Wang, X.; Wang, Y.; Gu, Q.; Jiang, W.; Wang, Y.; Li, C.; Zeng, T. H.; Sun, Y.; Zeng, J. Versatile Graphene Quantum Dots with Tunable Nitrogen Doping. *Part. Part. Syst. Charact.* **2014**, *31*, 597–604.

(29) Qu, D.; Zheng, M.; Du, P.; Zhou, Y.; Zhang, L.; Li, D.; Tan, H.; Zhao, Z.; Xie, Z.; Sun, Z. Highly Luminescent S, N Co-Doped Graphene Quantum Dots with Broad Visible Absorption Bands for Visible Light Photocatalysts. *Nanoscale* **2013**, *5*, 12272–12277.

(30) Zor, E.; Saglam, M. E.; Akin, I.; Saf, A. O.; Bingol, H.; Ersoz, M. Green Synthesis of Reduced Graphene Oxide/nanopolypyrrole Composite: Characterization and H₂O₂ Determination in Urine. *RSC Adv.* **2014**, *4*, 12457.

(31) Zhang, J.; Zhao, X. S. Conducting Polymers Directly Coated on Reduced Graphene Oxide Sheets as High-Performance Supercapacitor Electrodes. *J. Phys. Chem. C* **2012**, *116*, 5420–5426.

(32) Qu, D.; Zheng, M.; Zhang, L.; Zhao, H.; Xie, Z.; Jing, X.; Haddad, R. E.; Fan, H.; Sun, Z. Formation Mechanism and Optimization of Highly Luminescent N-Doped Graphene Quantum Dots. *Sci. Rep.* **2014**, *4*, 5294.

(33) Radvanyi, E.; De Vito, E.; Porcher, W.; Jouanneau Si Larbi, S. An XPS/AES Comparative Study of the Surface Behaviour of Nano-Silicon Anodes for Li-Ion Batteries. *J. Anal. At. Spectrom.* **2014**, *29*, 1120.

(34) Yao, Y.; Liu, N.; McDowell, M. T.; Pasta, M.; Cui, Y. Improving the Cycling Stability of Silicon Nanowire Anodes with Conducting Polymer Coatings. *Energy Environ. Sci.* **2012**, *5*, 7927.

(35) Chen, L.; Guo, C. X.; Zhang, Q.; Lei, Y.; Xie, J.; Ee, S.; Guai, G.; Song, Q.; Li, C. M. Graphene Quantum-Dot-Doped Polypyrrole Counter Electrode for High-Performance Dye-Sensitized Solar Cells. *ACS Appl. Mater. Interfaces* **2013**, *5*, 2047–2052.

(36) Tang, L.; Ji, R.; Li, X.; Teng, K. S.; Lau, S. P. Size-Dependent Structural and Optical Characteristics of Glucose-Derived Graphene Quantum Dots. *Part. Part. Syst. Charact.* **2013**, *30*, 523–531.

(37) He, P.; Sun, J.; Tian, S.; Yang, S.; Ding, S.; Ding, G.; Xie, X.; Jiang, M. Processable Aqueous Dispersions of Graphene Stabilized by Graphene Quantum Dots. *Chem. Mater.* **2015**, *27*, 218–226.

(38) Li, Y.; Zhao, Y.; Cheng, H.; Hu, Y.; Shi, G.; Dai, L.; Qu, L. Nitrogen-Doped Graphene Quantum Dots with Oxygen-Rich Functional Groups. *J. Am. Chem. Soc.* **2012**, *134*, 15–18.

(39) Li, Y.; Hu, Y.; Zhao, Y.; Shi, G.; Deng, L.; Hou, Y.; Qu, L. An Electrochemical Avenue to Green-Luminescent Graphene Quantum Dots as Potential Electron-Acceptors for Photovoltaics. *Adv. Mater.* **2011**, *23*, 776–780.

(40) Lim, S. P.; Pandikumar, A.; Lim, Y. S.; Huang, N. M.; Lim, H. N. In-Situ Electrochemically Deposited Polypyrrole Nanoparticles Incorporated Reduced Graphene Oxide as an Efficient Counter Electrode for Platinum-Free Dye-Sensitized Solar Cells. *Sci. Rep.* **2014**, *4*, 5305.

(41) Stewart, M. H.; Huston, A. L.; Scott, A. M.; Oh, E.; Algar, W. R.; Deschamps, J. R.; Susumu, K.; Jain, V.; Prasuhan, D. E.; Blanco-Canosa, J.; Dawson, P. E.; Medintz, I. L. Competition between Förster Resonance Energy Transfer and Electron Transfer in Stoichiometrically Assembled Semiconductor Quantum Dot-Fullerene Conjugates. *ACS Nano* **2013**, *7*, 9489–9505.

(42) Somers, R. C.; Bawendi, M. G.; Nocera, D. G. CdSe Nanocrystal Based Chem-/bio- Sensors. *Chem. Soc. Rev.* **2007**, *36*, 579–591.

(43) Algar, W. R.; Stewart, M. H.; Scott, A. M.; Moon, W. J.; Medintz, I. L. Quantum Dots as Platforms for Charge Transfer-Based Biosensing: Challenges and Opportunities. *J. Mater. Chem. B* **2014**, *2*, 7816–7827.

(44) Baaske, M. D.; Foreman, M. R.; Vollmer, F. Single-Molecule Nucleic Acid Interactions Monitored on a Label-Free Microcavity Biosensor Platform. *Nat. Nanotechnol.* **2014**, *9*, 933–939.

Supporting Information

Graphene Quantum Dots-based Photoluminescent Sensor: A Multifunctional Composite for Pesticide Detection

*Erhan Zor,^{§,§,‡,†} Eden Morales-Narváez,^{§,†} Alejandro Zamora-Gálvez,[§] Haluk Bingol,[‡]
Mustafa Ersoz,[±] Arben Merkoçi^{§,†} **

[§]ICN2 – Catalan Institute of Nanoscience and Nanotechnology, Campus de la UAB, 08193
(Bellaterra) Barcelona, Spain

E-mail: arben.merkoci@icn.cat

[§]Science and Technology Department, A.K. Faculty of Education, Necmettin Erbakan
University, Konya, 42090, Turkey

[†]Department of Chemistry, Institute of Science, Selcuk University, Konya, 42030, Turkey

[‡]Department of Chemistry, A.K. Education Faculty, Necmettin Erbakan University, Konya,
42090, Turkey

[±]Advanced Technology Research and Application Center, Selcuk University, Konya, 42030,
Turkey

[†]ICREA – Catalan Institution for Research and Advanced Studies, Barcelona, 08010, Spain

[†]These authors contributed equally to this work.

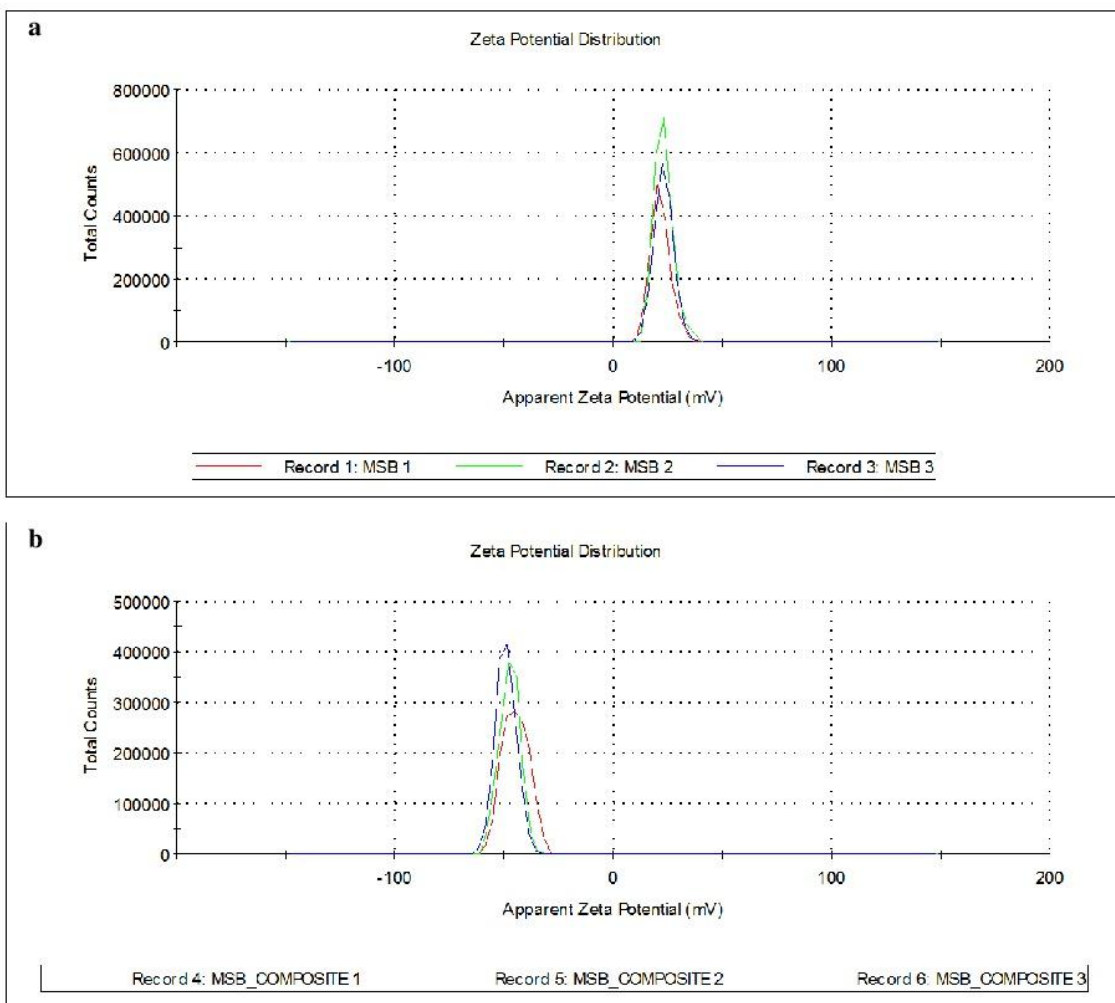


Figure S1. The zeta potential measurements of mSB (**a**) and mSGP (**b**).

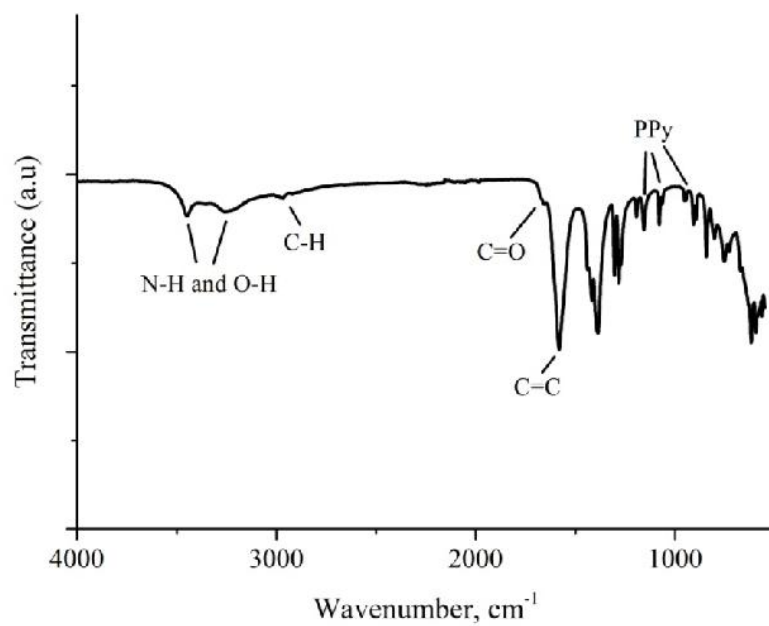


Figure S2. FT-IR spectrum of GQDs/PPy.

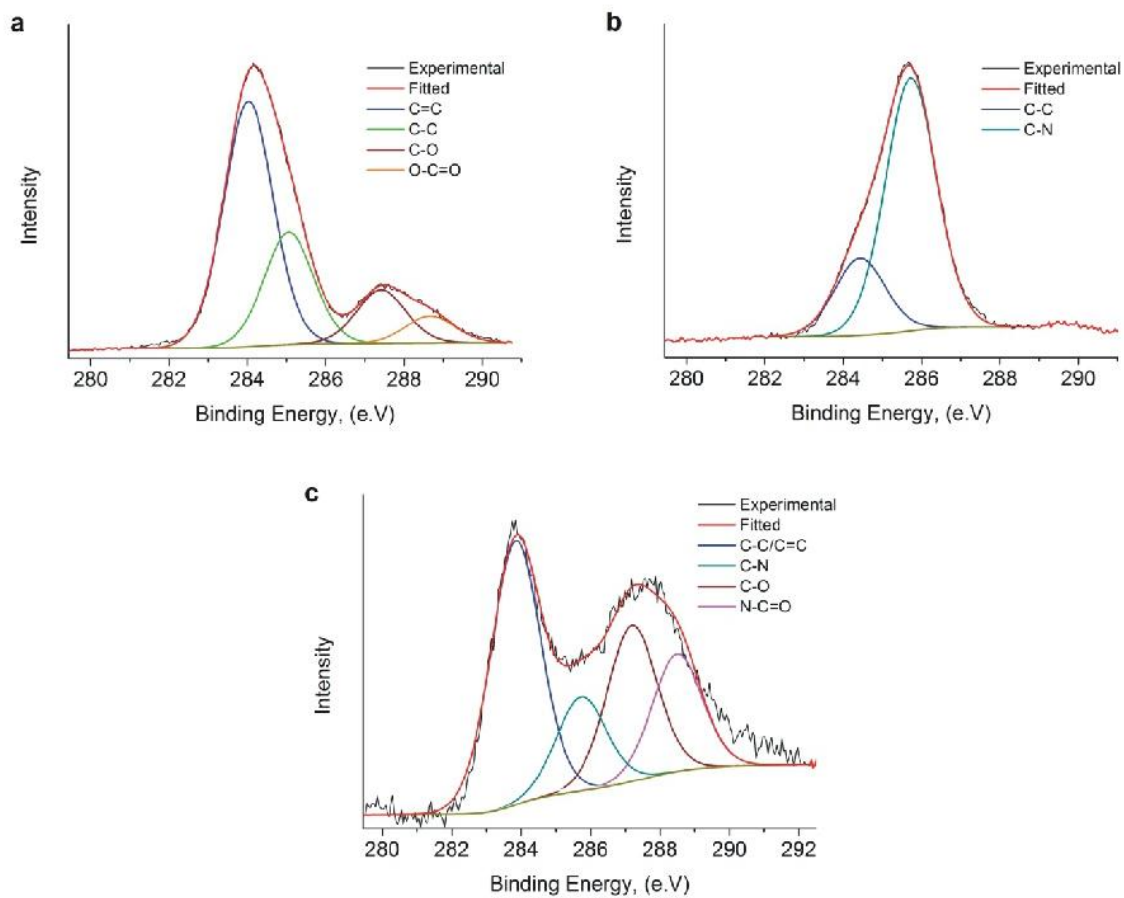


Figure S3. C1s XPS spectra of GQDs (a), mSB (b) and mSGP (c).

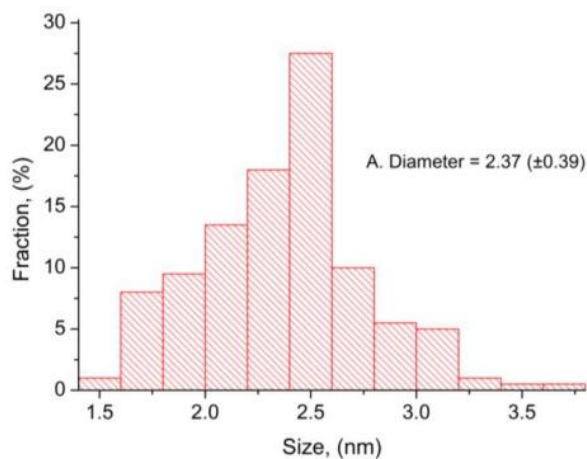


Figure S4. The size distribution of GQDs.

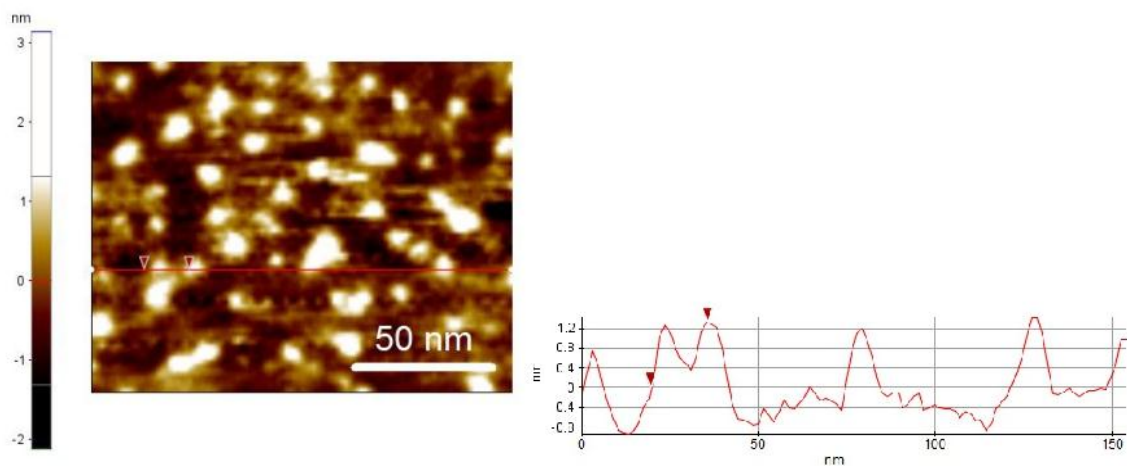


Figure S5. AFM image acquired in air under tapping mode and height profile of GQDs.

The thicknesses of the GQDs are about 1.2 nm depicting that they assume the same structure. It should be pointed out that the AFM images were acquired in air using a tapping mode, thus the thicknesses of GQDs are deviated from their true thickness (≈ 0.34 nm)^{1,2}.

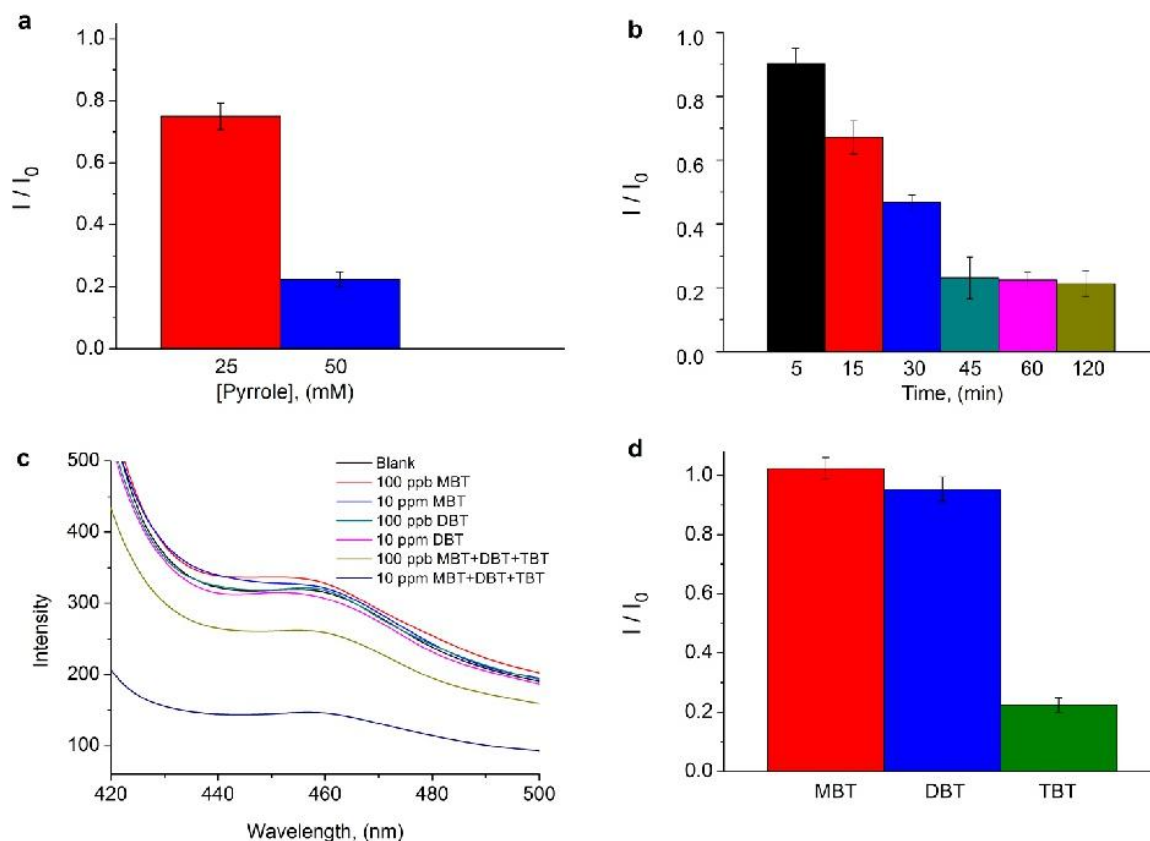


Figure S6. The effect of monomer amount (a) and incubation time (b) on PL quenching. PL spectra of mSGP in the presence of possible interferences; MBT and DBT (c) and the comparison of the corresponding PL quenching for MBT, DBT and TBT (d).

Table S1. Recovery of the proposed sensing system (analysis in seawater). The range includes expected values that are greater than the obtained limit of quantification, i.e. 141.86 ppb.

Expected Value (ppb)	Recovery
1000	93 %
2500	114 %
5000	104 %
7500	92 %
10000	103 %

Measured values are obtained by interpolating the data (PL intensity of the blank / PL intensity of the assayed sample) in the corresponding calibration curve (Figure 4). Recovery is estimated as the mean of the measured values ($n = 3$) divided into the expected value.

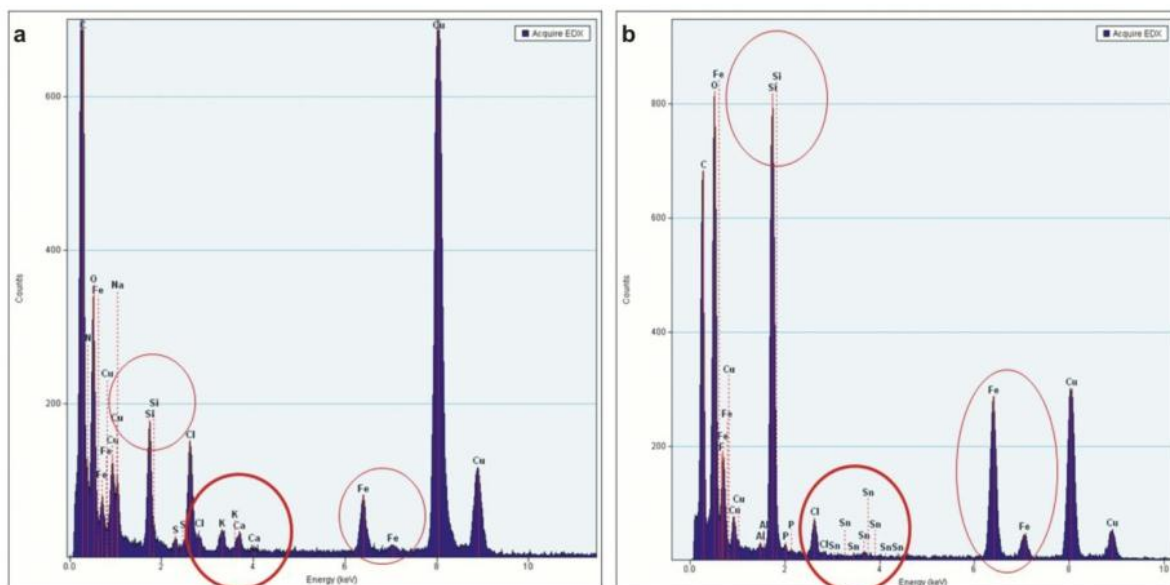


Figure S7. EDS of TEM in the absence (a) and presence (b) of TBT as a result of attachment in the composite.

Video SV1. 3D Raman imaging video recorded to show each material and the corresponding / individual Raman spectrum.

SUPPORTING REFERENCES

- (1) Zhou, X.; Zhang, Y.; Wang, C.; Wu, X.; Yang, Y.; Zheng, B.; Wu, H.; Guo, S.; Zhang, Photo-Fenton Reaction of Graphene Oxide: A New Strategy to Prepare Graphene Quantum Dots for DNA Cleavage, *ACS Nano* **2012**, *6*, 6592–6599.
- (2) Wu, C.; Wang, C.; Han, T.; Zhou, X.; Guo, S.; Zhang, Graphene: Insight into the Cellular Internalization and Cytotoxicity of Graphene Quantum Dots, *Adv. Healthc. Mater.* **2013**, *2*, 1613–1619.

Graphene-Based Biosensors: Going Simple

Eden Morales-Narváez, Luis Baptista-Pires, Alejandro Zamora-Gálvez, and Arben Merkoçi*

The main properties of graphene derivatives facilitating optical and electrical biosensing platforms are discussed, along with how the integration of graphene derivatives, plastic, and paper can lead to innovative devices in order to simplify biosensing technology and manufacture easy-to-use, yet powerful electrical or optical biosensors. Some crucial issues to be overcome in order to bring graphene-based biosensors to the market are also underscored.

1. Introduction

Technologies facilitating diagnostics, drug discovery, food safety, defense, security, and environmental monitoring are of great interest to industry, government initiatives, and research scientists. Biosensing has become an important approach within these technologies, particularly those biosensors integrating highly desirable characteristics such as specificity (suitably identifying the target analyte), high sensitivity (determining low levels or the lack of the analyte), fast results (from minutes to hours), extended shelf life, and easy-to-operate capabilities. However, when it comes to cost-efficient devices these features are often conflicting. Interestingly, nanomaterials enable us to engineer and manipulate unprecedented biosensing systems based on transducing phenomena occurring at the nanoscale. Thus, the outstanding features and new possibilities offered by nanomaterials are opening the way to exciting opportunities to overcome this challenge. In addition, we believe that flexible, abundant and low-cost substrates, that is, plastic and paper can boost such opportunities and their simplicity.

Given their advantageous properties and functionalities, graphene derivatives are two-dimensional nanoscale materials that are under active research, and the research community has devoted great effort and many resources to the development of graphene-based biosensors. In fact, a myriad of analytes including bacteria, viruses, proteins, oligonucleotides, small molecules, and metal ions have been successfully detected using graphene-based biosensors at the cutting

edge.^[1-2] Due to the excellent properties of graphene derivatives – such as excellent capabilities for direct wiring with biomolecules, a heterogeneous chemical and electronic structure, the possibility to be processed in aqueous suspension, and the ability to be tuned as insulator, semiconductor, or semi-metal; graphene-based biosensors possess a plethora of advantages over other nanomaterial-based sensors, facilitating unique biosensing approaches, which will be discussed throughout this essay.

One should not be misled into thinking that graphene is a single material enjoying always the same properties and performance. On the contrary, graphene has a wide family of materials that offers a myriad of behaviors. In general, graphene derivatives possess high specific surface area ($>470 \text{ m}^2 \text{ g}^{-1}$) and broad chemical-modification capabilities. However, it should be remarked that their specific mechanical, electrical, and optical properties depend on different parameters such as their purity degree, structural defects, lateral size, number of layers, and oxidation level, which are strongly related to their production method. Hence, graphene derivatives exploited in biosensing are expected to be judiciously selected according to the targeted application and different questions may arise; for instance, what are the most common graphene derivatives in electrical/optical biosensing; and how do the aforementioned parameters affect biosensing behavior? We will critically address these questions and expose our perspective on the integration of graphene derivatives into plastic- and paper-based substrates (Figure 1).

for instance, what are the most common graphene derivatives in electrical/optical biosensing; and how do the aforementioned parameters affect biosensing behavior? We will critically address these questions and expose our perspective on the integration of graphene derivatives into plastic- and paper-based substrates (Figure 1).

2. Graphene Derivatives and their Properties facilitating Biosensing Platforms

Pristine graphene, polycrystalline graphene, graphene quantum dots (GQDs), and (reduced) graphene oxide are the most common graphene derivatives used in biosensing. Pristine graphene is a flawless lattice of sp^2 -bonded carbon atoms, that is, without defects throughout its honeycomb-like pattern, and it is a single-crystalline grain.^[6] Polycrystalline graphene is composed of single-crystalline graphene grains of distinct orientations with a mosaic-like organization denoted by grain boundaries, which leads to topological defects such as dislocations.^[7] GQDs are nanocrystals of graphene that are tiny, sufficient to trigger exciton confinement and the quantum size effect (generally GQDs show diameters of less than 20 nm). As a result, GQDs have photoluminescent properties that can be tuned according to their size and surface chemistry. Graphene oxide (GO) is a lattice of sp^2 -bonded carbon atoms incorporating defects since it is disrupted by sp^3 carbon bonds

Dr. E. Morales-Narváez, L. Baptista-Pires,
A. Zamora-Gálvez, Prof. A. Merkoçi
Catalan Institute of Nanoscience and
Nanotechnology (ICN2)
CSIC and The Barcelona
Institute of Science and Technology
Campus UAB, Bellaterra
08193 Barcelona, Spain
E-mail: arben.merkoci@icn2.cat

Prof. A. Merkoçi
ICREA
Pg. Lluís Companys 23, 08010 Barcelona, Spain



DOI: 10.1002/adma.201604905

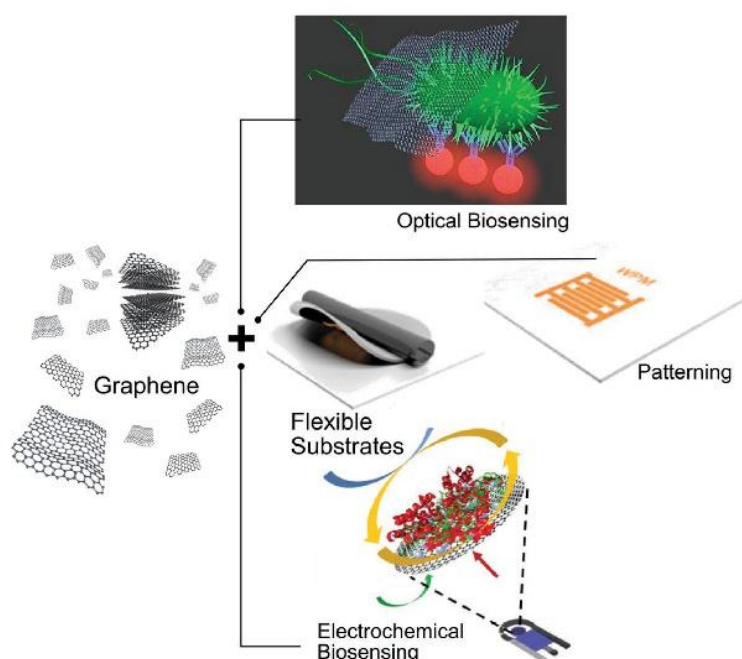


Figure 1. Integration of graphene derivatives into plastic- and paper-based substrates as a biosensing platform. We envision a new generation of biosensing devices based on the synergy between flexible, lightweight, easy-to-use, versatile, and cost-effective materials (paper and plastic) and the outstanding properties of graphene derivatives. Patterning image: Adapted with permission.^[1] Copyright 2016, American Chemical Society. Electrochemical biosensing image: Adapted with permission.^[4] Copyright 2016, Elsevier; Optical biosensing image: Adapted with permission.^[5] Copyright 2013, Wiley-VCH.

and possesses oxygen-containing groups – carboxyl groups exposed on the edges and hydroxyl and epoxy groups on the basal plane.^[8] Hence, GO often has some hydrophilic islands onto its basal plane according to its oxidation degree.^[9] Reduced graphene oxide (rGO) is composed of GO after being reduced through either a chemical or physical method. Depending on the predominance of the aforementioned hydrophilic islands, GO and rGO can be endowed with water-dispersibility properties. Therefore, GO and rGO micro-/nanosheets can be manipulated and applied in the form of a water-based suspension, which is often crucial in biosensing. Importantly, binding interactions between graphene derivatives and biomolecules such as single-stranded DNA are influenced by the C/O ratio of the employed graphene derivative – high C/O ratios promote stronger binding to biomolecules than low C/O ratios.^[10] Moreover, the lateral size of the graphene derivatives modulates the kinetics and the capacity of biomolecules adsorption.^[11]

Graphene derivatives incorporate inherent features, such as purity degree, defects, and functional groups according to their synthesis route, which are directly related to their performance and production cost. For instance, pristine graphene has remarkable properties based on its perfect crystalline structure. On the other hand, its production is hardly scalable and with high production cost. Hence, a balance between production cost and performance is of major importance for industrial applications and to implement graphene-based

devices in daily-life technologies. This serious concern has been deeply discussed in the literature.^[12–14]

2.1. Electrical-Based Platforms

Heterogeneous electron transfer (HET) in graphene derivatives is correlated with the oxygen content, the amount of defects, the edge-like architecture, the thickness, and the impurities. Unlike pristine graphene or polycrystalline graphene, GO is highly disordered and contains different functional groups according to its production method. rGO, reduced either chemically, thermally, or electrochemically, can still have oxygen-containing functional groups and can suffer from a higher level of disorder or defect areas due to the reduction process. The increase of the number of defects in the structure increases HET, whereas the presence of oxygen functional groups decreases HET. Hence, effective reduction approaches are an important feature in graphene-based thin films. Laser-scribed reduction, for instance, is highly effective and, in addition, increases the number of edge-like structures available within the produced foam-like structure with high surface area.^[15] The reduction process not only can induce different structures, which can increase the surface area, but also the printing methods.

Vacuum-filtration-based thin films are characterized by their well-oriented GO-sheet thin films, whereas drop-casting or ink-jet printing induces a higher number of edge-like structures by the drop spontaneous drying process. On the other hand, in vacuum filtration, the printing of GO-based films over rough substrates tends to change the film structure; furthermore, printing rGO using the same technique results in an increase in the number of edge-like structures possibly due to the rGO suspended sheets in solution that tend to aggregate or have different mechanical and hydrophobic properties, in comparison with GO.^[13,16] In the literature, it is hard to define different graphene-based structures in electrical biosensing platforms due to the lack of surface characterization; however, increased surface areas and number of defects have been widely described in a myriad of graphene-derived sensors to perform better than planar or defect-free structures such as pristine graphene.^[17,18]

Electrochemical sensors can be read-out using voltammetric, impedimetric, or potentiometric techniques. In voltammetric measurements, the electrode potential is controlled to drive an electron-transfer reaction with a measured current associated to it. This can be done taking advantage, for example, of $[\text{Fe}(\text{CN})_6]^{3-}$ or metals where the shift is associated to a quantitative perturbation. Impedimetric measurements monitor changes in the interfacial properties of the electrode surface and do not require labels generating signals to detect biorecognition events.^[2] The potentiometric technique also

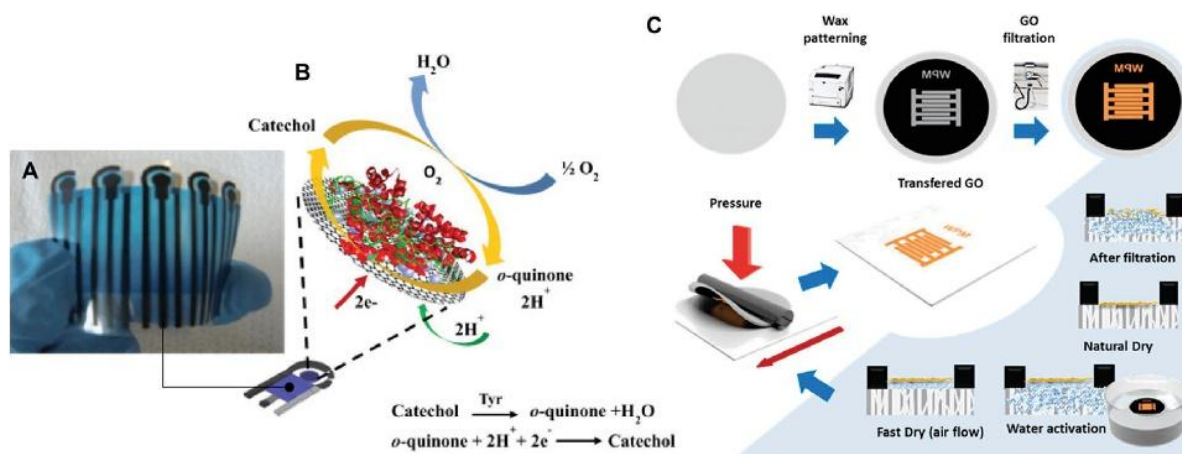


Figure 2. A,B) Electrodes printed on plastic (PET) via screen-printing method (A), and modified with graphene (B). A) Adapted with permission.^[22] Copyright 2014, Elsevier. B) Adapted with permission.^[4] Copyright 2016, Elsevier. C) Simple patterning of graphene. Adapted with permission.^[3] Copyright 2016, American Chemical Society.

is an important tool in graphene biosensors due to the high mobility of either electrons and holes in graphene. The semi-metallic behavior of graphene enables charge carriers to be tuned from electrons to holes using external electric fields enabling the Dirac point and the doping type of graphene field-effect transistors (FET) to be determined. This is very important in biosensors for DNA analysis or protein detection, where the attachment of DNA or proteins can lead to a shift in the Dirac point enabling quantitative detection of loaded molecules. This is attributed to a change in the surface charge, which can be related to the presence of a protein at a certain pH or to the length of the targeted DNA, inducing a higher or lower charge density resulting from the doping of these charged compounds to graphene. This methodology has been used for pH sensors, cell-based sensors, or cancer-biomarker sensing platforms. Solution-gated FETs have been reported using pristine or polycrystalline graphene, and recently RGO has been tested, reporting characteristics similar to polycrystalline or pristine graphene.^[19–21] This could be a step-forward in the development of low-cost graphene-based devices.

The plethora of scientific literature on graphene electrochemistry relies on GO- or rGO-based-suspensions which are drop-cast or electrodeposited onto underlying electrodes, where basically the oxidized graphene derivatives act in synergy with the underlying electrodes, producing summative electrochemical effects. This has also been achieved for a myriad of electrochemical (bio)sensors that are graphene-modified using screen-printed carbon electrodes (SPCE), gold, or indium tin oxide (ITO). For plastic-based biosensors, our research group has also studied this kind of sensor, reaching advantageous tunable electrochemical properties in an SPCE modified with GO and rGO for enzyme immobilization (e.g., tyrosinase) and drug detection, respectively, (Figure 2A,B).^[4,22] Similarly, in paper-based electrochemical biosensors, rGO has been used for tuning the electrochemical properties of microfluidic paper-based analytical devices for the detection of four different cancer biomarkers.^[23] This was achieved using

photoresist-patterned paper followed by screen printing of carbon and Ag/AgCl, and additionally the drop-casting of graphene and nanoparticles. Despite the low cost described by the authors, the fabrication process can be seen as a time and labor-consuming method.

Electrical biosensors exploiting rGO as a transducer are also able to exhibit an advantageous performance, either in plastic or paper architectures. In fact, rGO-based flexible FETs printed on plastic exhibit a performance comparable with those based on pristine graphene, which represents a good alternative for scalable bioapplications of rGO thin-film transistors.^[20] In general, electrical biosensors based on the combination of GO or rGO and plastic are making an evolution in performance and production cost. However, polycrystalline-graphene-based biosensors are making one step forward for portable and wearable biosensors that, until now, could not be observed in GO or rGO electrochemical biodevices with implemented human-machine interfaces and enabling theranostics.^[24,25]

In the paper-based field, ink-jet printing is playing an important role for device production, which could be related to the opportunity to pattern GO- or rGO-based inks without changing the features of the paper in a simple fashion and enabling the improvement of the conductivity via UV-pulsed-laser irradiation.^[26] Other deposition techniques, involving pressure, are prone to changing the paper thickness and its fluidics. It is worth mentioning that, in spite of the large surface roughness of conventional printing paper, graphene-based (opto)electronic devices can also be fabricated using this substrate, which could be of interest for innovative biosensing. In fact, multilayer graphene (growth via chemical vapor deposition) has been demonstrated to be transferred to conventional paper, taking advantage of the hydrophobic character of multilayer polycrystalline graphene.^[27]

The production of graphene-based thin films is of major importance to a wide variety of applications, such as electrical and electrochemical sensors. Their low cost and simplicity could improve the fast integration and abundance of graphene-based devices. Recently our research team reported a simple way to

transfer GO patterned structures to target substrates by simple water activation and pressure using wax printed membranes, (Figure 2C).^[3] Since wax printing is a cheap and versatile technique, one can produce unlimited shapes and structures, and the control over the thickness provided by the vacuum filtration vertically nanometer-sized films to be printed. This represents an interesting alternative to existing patterning technologies such as screen-, gravure-, and inkjet-printing, microcontact stamps, and lithography. In fact, we are able to print over paper, textile, or plastics, opening venues for low-cost and flexible all-graphene-based biosensors, overall in cases where the size of the sample to be analyzed is not a major issue.

2.2. Optical-Based Platforms

Graphene derivatives are optically omnivorous, that is, their fluorescence-quenching capabilities are virtually universal, and they are able to quench any fluorescence wavelength via energy transfer. It is noteworthy that not only does their number of layers determine the efficiency of their fluorescence-quenching ability,^[28] but also their oxidation degree affects their quenching factor – the more the utilized GO is oxidized, the less efficient it becomes in terms of fluorescence-quenching capability.^[10] In addition, long-range energy transfer is also known to occur in graphene derivatives, which is observable up to 30 nm.^[5]

Oxidized graphene derivatives undergo a recombination of electron-hole pairs localized within an sp² carbon domain embedded within an sp³ matrix, resulting in photoluminescent properties. Their maximum emission wavelength can be modulated from the blue region to the near-infrared region in

accordance with their oxygen-containing moieties,^[29] lateral size,^[30] and oxidation degree.^[31] Although the synthesis of photoluminescent graphene derivatives endowed with high quantum yield (e.g., >70%) has been scarcely developed, nitrogen doping has been reported to be an effective route to address this paucity and improve such an important parameter.^[32]

The most common graphene-based optical biosensing principle relies on the interaction between single-stranded DNA (ssDNA) and graphene derivatives, which is facilitated by hydrophobic interactions and the strong π - π stacking interaction between the hexagonal cells of the graphene derivatives and the ring structures in nucleotides. This leads to a simple, yet sensitive and versatile optical biosensing mechanism: in the absence of an analyte, a fluorescent-dye-labeled ssDNA is complexed and quenched via the interaction with the graphene derivative, whereas the complex dye-ssDNA/graphene is detached in the presence of an analyte. Consequently, the dye-labeled ssDNA recovers its fluorescence as the graphene derivative weakly interacts with the rigid structure of double-stranded DNA or aptamer-target complexes. QDs, and r/GO micro- and nanosheets are the most common graphene derivatives in optical biosensing, whereas graphene-based optical biosensing mainly capitalizes on the aforementioned photonic phenomenon.

Our research group has explored the photoluminescence-quenching capabilities and the oxygenated two-dimensional network of GO in order to exploit it as a pathogen-revealing agent.^[5] To this aim, we used a conventional glass-slide-based microarray system, whose limit of detection is 760 times more sensitive than a conventional immunoassay, though expensive, relatively time-consuming, and not particularly amenable to portability (Figure 3A). We then demonstrated an innovative

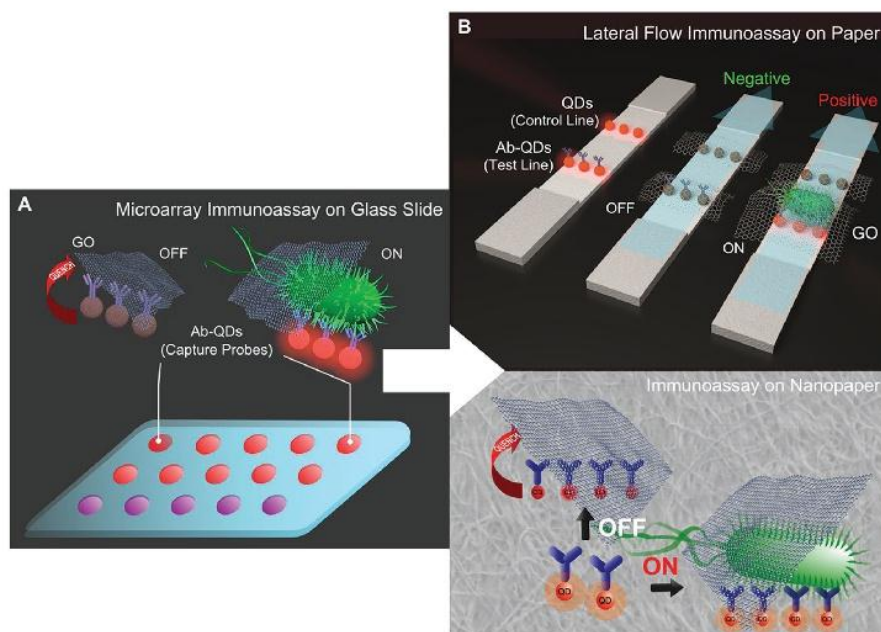


Figure 3. Graphene oxide as a pathogen-revealing agent. A) Microarray immunoassay revealed by GO on a glass slide. Adapted with permission.^[5] Copyright 2013, Wiley-VCH. B) Upper part: lateral flow immunoassay revealed by GO on paper. Adapted with permission.^[33] Copyright 2015, American Chemical Society. Lower part: immunoassay revealed by GO on bacterial cellulose nanopaper. Adapted with permission.^[34] Copyright 2015, American Chemical Society.

technological platform that transfers the previous microarray-based platform into a paper-based lateral flow immunoassay for bacteria detection – in particular *Escherichia coli*, as a model pathogen. This biosensing approach eliminates the use of secondary antibodies and is revealed by the photoluminescence quenching capability of GO. The sensing principle is based on the energy-transfer phenomenon that occurs between photoexcited quantum dots (QDs) and GO while being in close proximity. The analyte is selectively attached onto the test line of the strip (which contains antibody-decorated QDs) leading to a highly specific and sensitive sensing phenomenon that is clearly observable up to 10 CFU mL⁻¹ in standard buffer and 100 CFU mL⁻¹ in bottled water and milk (CFU = colony-forming unit). The control line of the strip containing bare QDs is always quenched upon GO addition, indicating the correct operation of the system (Figure 3B, upper part). As a cost-effective and easy-to-use approach, this device is appealing for portable and automated diagnostics applications that may include other similar sized analytes with interest for diagnostics.^[33] Furthermore, we successfully transferred this nanoenabled approach to another flexible, lightweight, and optically transparent substrate, i.e., bacterial-cellulose nanopaper (Figure 3B, lower part).^[34]

We have also exploited GQDs to engineer an innovative composite material targeting the detection of small molecules, such as pesticides (e.g. tributyltin (291 Da)). The hybrid material consists of magnetic silica beads encapsulated by GQDs embedded within molecularly imprinted polypyrrole. Thus, the mSGP composite is endowed with: i) magnetic properties, which are useful for separation and pre-concentration of the toxic compound; ii) water dispersibility, which is important to perform a liquid-phase-based assay; iii) selectivity, which is crucial to detect exclusively the target analyte; and iv) photoluminescence as an optical transducing system that is quenched via energy transfer upon analyte binding. Gathering these features, such a GQD-based sensing platform enables a rapid, simple, and sensitive approach for small-molecule detection, even in complex media, e.g., marine water, without any sample treatment.^[35]

3. Simple Biosensors based on the Integration of Graphene Derivatives into Low-Cost, Lightweight, and Flexible Substrates: Discussion and Future Outlook

Graphene derivatives compete with other well-known materials (e.g. silicon, germanium, and ITO). However, this novel family of materials is likely to find its best opportunities in innovative areas, that is, functions, applications, products, or technologies not dominated by other conventional materials.^[36] Aside from this, currently, the graphene market is mainly focused on production of graphene derivatives, whereas some opto-/electronic devices such as FETs, magnetic sensors, and photodetectors have also been launched. In contrast, the development of final products involving graphene-based biosensors is an emergent area. Thus, in the mid-term, graphene-based biosensors are

likely to find excellent opportunities and a great market niche within this context.

Well-established technologies allowing diagnostics, drug discovery, food safety, defense, security, and environmental monitoring often require bulky infrastructure, conventional electrical supply, time-consuming and labor-intensive procedures, and qualified personnel. Aiming at simplifying such technologies and manufacturing easy-to-use, yet powerful and innovative biosensing devices, we envisage a new generation of biosensing devices based on the synergy between flexible, lightweight, easy-to-use, versatile, and cost-effective materials (paper and plastic) and the outstanding properties of graphene derivatives.

When graphene derivatives are combined with cheap, lightweight, and flexible substrates, interesting opportunities arise. Flexibility facilitates advantages in terms of size and weight of the engineered biosensor. Moreover, flexibility obviates bulky architectures, facilitates assembly processes, and allows the generation of wearable and implantable devices. Aside from their flexibility, abundance, and low-cost, plastic and paper can be readily modified to create breakthrough devices using suspensions of graphene derivatives and a myriad of deposition techniques, including drop-casting, dip-coating, spraying, spin-coating, inkjet printing, screen printing, high-volume roll-to-roll gravure printing, pressure-based mechanisms, etc. Among these innovative biosensors created through the combination of graphene derivatives and flexible substrates, we could find advantageous theranostic platforms, point-of-care devices, wearable devices, and omnipresent biosensors targeting different tasks involved with diverse applications like healthcare, therapy, diagnostics, agriculture, environment, food safety, and security. The tuning with new electronic and photonic functions in flexible substrates might be a future in new technologies based on graphene derivatives for autonomous biosensing devices with integrated photonics, electronics, and microfluidics. On the other hand, we believe there is still much to discover and develop within the field of this kind of biosensor. For instance, GO or rGO membranes, also termed as GO or rGO papers, are making a step forward in the supercapacitor field.^[37] These membranes have also been tested for molecular sieving, which could be applied in the generation of breakthrough biosensing architectures.^[38,39] Although analytical lab-on-a-chip (LOC) applications capitalizing on the properties of graphene derivatives are not widely reported in the literature, one can find encouraging approaches facilitating electrochemical amplification mechanisms, multiplexed optical-detection strategies, and a novel crystallographic analysis,^[40–42] which provide excellent examples of how the thickness, conductivity, and transparency offered by graphene derivatives represent a powerful tool for lab-on-a-chip development.

Integration of graphene into LOC applications, lateral flow (LF), and general point-of-care (POC) devices, including wearables or implantables, is a critical issue. As already mentioned, electrical, optical (fluorescent, colorimetric etc.), or other transduction techniques, thanks to the advantageous graphene properties, can be integrated. Future development of the different systems/devices are strongly related to the analyte (e.g., chemical or biological molecules) to be detected, as well as the objective of the device: disposable (one use only) or for

multiuse/continuous monitoring. While disposable devices, such as LF, would require a certain “shelf life” (variably influenced by storage conditions, such as exposure to heat, light, and moisture), LOC and other POC devices for continuous monitoring would definitively require long-term stability of graphene while working in a real environment. All the mentioned issues should be carefully considered case by case, depending also on the application (health or environment monitoring, safety and security, or any other industrial quality monitoring), requested analytical performance (reproducibility, detection limit, sensitivity, selectivity, operation range, etc.) or threshold values (ON–OFF sensing applications), beside others.

Solving real-world problems through simple – albeit powerful, safe, and robust – biosensors based on the integration of graphene derivatives into cheap and flexible substrates will enforce the successful transition of these innovative devices to the market. Moreover, the novel insulating, semiconducting, and optoelectronic properties provided by other exciting 2D materials (hexagonal boron nitride, metal dichalcogenides, black phosphorus) and their combination is also expected to bring breakthrough approaches solving real-world problems through biosensing. However, overall commercialization of graphene-based biosensors will imply overcoming diverse technical, production, and market issues. Here we identify some of these crucial issues:

- i) Relevant stakeholders in the biosensing field demand different challenging characteristics, including but not limited to miniaturization potential, low power-budget ($\approx \mu\text{W}$ to mW), robust shelf and operational lifetime stability, recalibration capabilities (as they may suffer from temperature or relative-humidity drifts), and mechanical shock resistance.
- ii) The performance reproducibility of graphene-based biosensors strongly depends on the homogeneity of the quality of the involved graphene derivatives, whose manufacturing scalability is not particularly easy to control, above all when it comes to devices relying on a single flake, such as bio-FETs. Moreover, sensitivity and specificity (overall in clinical diagnostics), which are seldom reported in the literature in relation to biosensors, should be systematically determined in terms of percentage of false negatives and positives, respectively.^[43]
- iii) Graphene-deposition techniques yield different coating qualities in terms of surface coverage and interconnection between graphene flakes, which should be judiciously considered along with substrate roughness and morphology of the individual flakes; especially in electrical approaches, where conductivity is heavily affected by these features. Firstly, single layers undergo a folding and wrinkling effect to prevent collapse into multilayers.^[38,39] Secondly, some graphene-deposition techniques tend to promote an extreme degree of such a folding and wrinkling effect (e.g., drop-casting and spin-coating, which reduce surface coverage and increase the roughness, deteriorating the electrical performance). In contrast, other graphene-deposition techniques are amenable to performing a large-area monolayer of flakes with much higher surface coverage, leading to conducting thin films.^[44]
- iv) Although thoroughly systematic and well-designed experiments reveal encouraging guidance for the use of

graphene in biological environments,^[45,46] the toxicity of graphene derivatives is still under debate overall in the case of wearable platforms.

- v) Corresponding/right validation and evaluation in real settings and ongoing proficiency-testing of graphene-based biosensors are crucial to demonstrate advantages over well-known sensing technologies, in terms of simplicity, sensitivity, specificity, operating time, or cost.

All in all, graphene-based biosensing performance heavily depends on purity degree, lateral size, number of layers, oxidation level, distribution of oxygen-containing moieties, and/or defects of the employed graphene derivatives, since these features often modulate electrical conductivity, fluorescence-quenching capabilities, photoluminescence, binding interactions (between graphene derivatives and biomolecules) and kinetics, and capacity of biomolecules adsorption. Hence, scientists and technologists working with graphene-based biosensors are strongly encouraged to consider and characterize all these features judiciously with the aim to standardize the quality of graphene derivatives in biosensing and ensure reproducibility of this novel type of biosensors.

Getting their best opportunities in applications not dominated by conventional materials, simple graphene-based biosensors will lead to breakthrough solutions for the real world.

Acknowledgements

The authors acknowledge the support from H2020-EU (INTCATCH Project, Ref. 689341), MINECO (Spain, MAT2014-52485-P, RTC-2014-2619-7 and Severo Ochoa Program, Grant SEV-2013-0295) and Secretaria d'Universitats i Recerca del Departament d'Economia i Coneixement de la Generalitat de Catalunya (2014 SGR 260).

Received: September 12, 2016

Revised: October 26, 2016

Published online: November 29, 2016

- [1] E. Morales-Narváez, A. Merkoçi, *Adv. Mater.* **2012**, *24*, 3298.
- [2] A. Ambrosi, C. K. Chua, N. M. Latiff, A. H. Loo, C. H. A. Wong, A. Y. S. Eng, A. Bonanni, M. Pumera, *Chem. Soc. Rev.* **2016**, *45*, 2458.
- [3] L. Baptista-Pires, C. C. Mayorga-Martínez, M. Medina-Sánchez, H. Montón, A. Merkoçi, *ACS Nano* **2016**, *10*, 853.
- [4] S. Kurbanoglu, L. Rivas, S. A. Ozkan, A. Merkoçi, *Biosens. Bioelectron.* **2017**, *88*, 122.
- [5] E. Morales-Narváez, A.-R. Hassan, A. Merkoçi, *Angew. Chem., Int. Ed.* **2013**, *52*, 13779.
- [6] L. Rodríguez-Pérez, M. Á. Herranz, N. Martín, *Chem. Commun.* **2013**, *49*, 3721.
- [7] O. V. Yazzev, Y. P. Chen, *Nat. Nanotechnol.* **2014**, *9*, 755.
- [8] D. R. Dreyer, S. Park, C. W. Bielawski, R. S. Ruoff, *Chem. Soc. Rev.* **2010**, *39*, 228.
- [9] S. Eigler, A. Hirsch, *Angew. Chem., Int. Ed. Engl.* **2014**, *53*, 7720.
- [10] B. J. Hong, Z. An, O. C. Compton, S. T. Nguyen, *Small* **2012**, *8*, 2469.
- [11] J. Lee, Y. Yim, S. Kim, M.-H. Choi, B.-S. Choi, Y. Lee, D.-H. Min, *Carbon N. Y.* **2016**, *97*, 92.

- [12] K. S. Novoselov, V. I. Fal'ko, L. Colombo, P. R. Gellert, M. G. Schwab, K. Kim, *Nature* **2012**, *490*, 192.
- [13] W. Ren, H.-M. Cheng, *Nat. Nanotechnol.* **2014**, *9*, 726.
- [14] A. Zurutuza, C. Marinelli, *Nat. Nanotechnol.* **2014**, *9*, 730.
- [15] M. F. El-Kady, R. B. Kaner, *Nat Commun* **2013**, *4*, 1475.
- [16] W. J. Hyun, O. O. Park, B. D. Chin, *Adv. Mater.* **2013**, *25*, 4729.
- [17] K. Griffiths, C. Dale, J. Hedley, M. D. Kowal, R. B. Kaner, N. Keegan, *Nanoscale* **2014**, *6*, 13613.
- [18] A. Salehi-Khojin, D. Estrada, K. Y. Lin, M.-H. Bae, F. Xiong, E. Pop, R. I. Masel, *Adv. Mater.* **2012**, *24*, 53.
- [19] R. X. He, P. Lin, Z. K. Liu, H. W. Zhu, X. Z. Zhao, H. L. W. Chan, F. Yan, *Nano Lett.* **2012**, *12*, 1404.
- [20] Q. He, H. G. Sudibya, Z. Yin, S. Wu, H. Li, F. Boey, W. Huang, P. Chen, H. Zhang, *ACS Nano* **2010**, *4*, 3201.
- [21] S. Liu, X. Guo, *NPG Asia Mater* **2012**, *4*, e23.
- [22] L. Baptista-Pires, B. Pérez-López, C. C. Mayorga-Martinez, E. Morales-Narváez, N. Domingo, M. J. Esplandiu, F. Alzina, C. M. S.-Torres, A. Merkoçi, *Biosens. Bioelectron.* **2014**, *61*, 655.
- [23] Y. Wu, P. Xue, Y. Kang, K. M. Hui, *Anal. Chem.* **2013**, *85*, 8661.
- [24] H. Lee, T. K. Choi, Y. B. Lee, H. R. Cho, R. Ghaffari, L. Wang, H. J. Choi, T. D. Chung, N. Lu, T. Hyeon, S. H. Choi, D.-H. Kim, *Nat. Nanotechnol.* **2016**, *11*, 566.
- [25] M. S. Mannoer, H. Tao, J. D. Clayton, A. Sengupta, D. L. Kaplan, R. R. Naik, N. Verma, F. G. Ormenetto, M. C. McAlpine, *Nat Commun* **2012**, *3*, 763.
- [26] S. R. Das, Q. Nian, A. A. Cargill, J. A. Hondred, S. Ding, M. Saei, G. J. Cheng, J. C. Claussen, *Nanoscale* **2016**, *8*, 15870.
- [27] E. O. Polat, H. B. Uzlu, O. Balci, N. Kakenov, E. Kovalska, C. Kocabas, *ACS Photonics* **2016**, *3*, 964.
- [28] Z. Chen, S. Berciaud, C. Nuckolls, T. F. Heinz, L. E. Brus, *ACS Nano* **2010**, *4*, 2964.
- [29] R. M. , A. M. , C. N. , S. K. Ray, *Nanotechnology* **2014**, *25*, 495704.
- [30] M.-H. Jang, H. D. Ha, E.-S. Lee, F. Liu, Y.-H. Kim, T. S. Seo, Y.-H. Cho, *Small* **2015**, *11*, 3773.
- [31] Q. Mei, J. Chen, J. Zhao, L. Yang, B. Liu, R. Liu, Z. Zhang, *ACS Appl. Mater. Interfaces* **2016**, *8*, 7390.
- [32] J. Sun, S. Yang, Z. Wang, H. Shen, T. Xu, L. Sun, H. Li, W. Chen, X. Jiang, G. Ding, Z. Kang, X. Xie, M. Jiang, *Part. Part. Syst. Charact.* **2015**, *32*, 434.
- [33] E. Morales-Narváez, T. Naghdi, E. Zor, A. Merkoçi, *Anal. Chem.* **2015**, *87*, 8573.
- [34] E. Morales-Narváez, H. Golmohammadi, T. Naghdi, H. Yousefi, U. Kostiv, D. Horák, N. Pourreza, A. Merkoçi, *ACS Nano* **2015**, *9*, 7296.
- [35] E. Zor, E. Morales-Narváez, A. Zamora-Gálvez, H. Bingol, M. Ersoz, A. Merkoçi, *ACS Appl. Mater. Interfaces* **2015**, *7*, 20272.
- [36] M. Peplow, *Nature* **2013**, *503*, 327.
- [37] R. Raccichini, A. Varzi, S. Passerini, B. Scrosati, *Nat Mater* **2015**, *14*, 271.
- [38] B. Mi, *Science* **2014**, *343*, 740.
- [39] J. Gaughran, D. Boyle, J. Murphy, R. Kelly, J. Ducreé, *Microsystems Nanoeng.* **2016**, *2*, 16008.
- [40] Y. Ueno, K. Furukawa, K. Matsuo, S. Inoue, K. Hayashi, H. Hibino, *Anal. Chim. Acta* **2015**, *866*, 1.
- [41] L. Syedmoradi, M. Daneshpour, M. Alvandipour, F. A. Gomez, H. Hajghassem, K. Omidfar, *Biosens. Bioelectron.* **2017**, *87*, 373.
- [42] S. Sui, Y. Wang, K. W. Kolewe, V. Srajer, R. Henning, J. D. Schiffman, C. Dimitrakopoulos, S. L. Perry, *Lab Chip* **2016**, *16*, 3082.
- [43] W. C. W. Chan, B. Udugama, P. Kadhiresan, J. Kim, S. Mubareka, P. S. Weiss, W. J. Parak, *ACS Nano* **2016**, *10*, 8139.
- [44] L. J. Cote, F. Kim, J. Huang, *J. Am. Chem. Soc.* **2009**, *131*, 1043.
- [45] K. Kostarelos, K. S. Novoselov, *Science* **2014**, *344*, 261.
- [46] D. A. Jasim, C. Ménard-Moyon, D. Bégin, A. Bianco, K. Kostarelos, *Chem. Sci.* **2015**, *6*, 3952.

Label-Free Impedimetric Aptasensor for Ochratoxin-A Detection Using Iridium Oxide Nanoparticles

Lourdes Rivas,^{†,‡,||} Carmen C. Mayorga-Martinez,^{†,||} Daniel Quesada-González,[†] Alejandro Zamora-Gálvez,[†] Alfredo de la Escosura-Muñiz,[†] and Arben Merkoçi^{*,†,§}

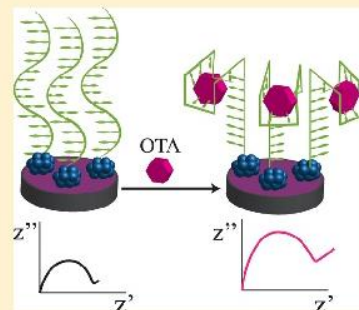
[†]ICN2 – Nanobioelectronics & Biosensors Group, Institut Catala de Nanociencia i Nanotecnologia, Campus UAB, 08193 Bellaterra (Barcelona), Spain

[‡]Departament de Química, Universitat Autònoma de Barcelona, 08193, Bellaterra (Barcelona), Spain

[§]ICREA – Institutio Catalana de Recerca i Estudis Avançats, 08010 Barcelona, Spain

Supporting Information

ABSTRACT: In this article, a novel aptasensor for ochratoxin A (OTA) detection based on a screen-printed carbon electrode (SPCE) modified with polythionine (PTH) and iridium oxide nanoparticles (IrO₂ NPs) is presented. The electrotransducer surface is modified with an electropolymerized film of PTH followed by the assembly of IrO₂ NPs on which the aminated aptamer selective to OTA is exchanged with the citrate ions surrounding IrO₂ NPs via electrostatic interactions with the same surface. Electrochemical impedance spectroscopy (EIS) in the presence of the [Fe(CN)₆]^{-3/-4} redox probe is employed to characterize each step in the aptasensor assay and also for label-free detection of OTA in a range between 0.01 and 100 nM, obtaining one of the lowest limits of detection reported so far for label-free impedimetric detection of OTA (14 pM; 5.65 ng/kg). The reported system also exhibits a high reproducibility, a good performance with a white wine sample, and an excellent specificity against another toxin present in such sample.



Ochratoxin A (OTA) is a mycotoxin generated by different fungi species such as *Aspergillus* and *Penicillium* during their growth. This toxin is a hazardous contaminant present in a great number of agricultural products such as cereals, coffee beans, dried fruits, cocoa, nuts, beer, and wine, causing economic losses to agricultural trade.^{1–4} Moreover, OTA has been reported in the literature as a nephrotoxic, teratogenic, immunotoxic agent,^{5,6} and it is also considered as possible human carcinogen (class 2B) by the International Agency for Research on Cancer.⁷

International organizations have established regulatory levels for OTA in food. In this context, the World Health Organization (WHO) has been set a tolerable weekly intake (TWI) of 100 ng/kg of body weight,⁸ and the European Union (EU) through Commission Regulation (EC) 1881/2006 has established the TWI in 120 ng/kg of body weight, specifying the maximum permitted levels of OTA in different foodstuff such as raw cereals (5 µg/kg), soluble coffee (10 µg/kg), wine (2 µg/kg), and baby food (0.5 µg/kg).⁹ Different methods are routinely used for analysis of mycotoxins, such as chromatography,¹⁰ enzyme-linked immunosorbent assay (ELISA), and lateral flow assays (LFA).^{11,12}

Aptamers are an emerging class of synthetic molecules which have several advantages compared to antibodies, including their high affinity and specificity for a wide range of targets, their thermal and chemical stability, and their low-cost production.¹³

Nowadays, the interest for label-free technologies is increasing because they are experimentally simpler and offer

direct information about the interaction of the target with the sensing element by measuring changes on physical properties such as mass, refractive index, or electrical resistivity produced by this binding. In addition, it allows the real-time measurement of kinetics of biomolecular interactions.^{14,15}

Impedimetric biosensors for label-free detection offer new opportunities to mycotoxin analysis due to their high sensitivity, easy use, and possible miniaturization and portability, which are vital requirements for point-of-care (POC) applications.^{16,17} Moreover, several label-free impedimetric aptasensors for OTA detection using different electrotransducers, for example, gold electrodes,¹⁸ indium–tin oxide (ITO) coated glass¹⁹ and screen-printed carbon electrodes (SPCEs),^{20,21} have been reported. Label-free impedimetric (bio)sensors require uniform and low resistive electrotransducer surfaces. Thus, electropolymerization is an alternative technique for improving the electrical conductivity on the surface of irregularly shaped electrodes.²² Conductive dyes such as thionine can be electropolymerized, producing stable redox-active coatings on the electrode surfaces, and they have been extensively used for biosensing applications thanks to their electrochemical properties.^{23–26}

Received: December 16, 2014

Accepted: April 22, 2015

Published: April 22, 2015

On the other hand, it is well-known that nanomaterials represent a powerful tool for modifying electrode surfaces thanks to their high surface-to-volume ratio and good conductivity, which make them useful for proposing novel electrochemical biosensors or greatly improving the existing ones.^{27,28} Iridium-oxide-based materials (in films and nanoparticle form) are attractive because of their catalytic activity, biocompatibility, and outstanding chemical and thermal stability, which have been used for applications in pH sensors,²⁹ neural stimulation,^{30,31} and environmental biosensors.³²

In this work, the development of an OTA aptasensor that takes advantage of electropolymerized thionine films onto SPCE and iridium oxide nanoparticles (IrO₂ NPs) is shown. Electrochemical impedance spectroscopy is used to monitor each step in the aptasensor development and also to detect OTA. The charge transfer resistance (R_{ct}) increases proportionally to the concentration of OTA in a linear range of 0.01–100 nM. This system shows also good reproducibility, sensitivity, and selectivity. To the best of our knowledge, this sensitive aptasensor exhibits one of the lowest limits of detection (LoD = 14 pM) reported so far for electrochemical detection of OTA.

EXPERIMENTAL SECTION

Materials and Apparatus. HPSF (high purity salt free) purified 3'-aminated aptamer selective to OTA, previously reported by Cruz and Penner³³ (5'-GATCGGGTG-TGGGTGGCGTAAAGGGGAGCATCGGACAAAAA-NH₂-3') was purchased from Isogen Life Science (Spain).

Ochratoxin A from *Aspergillus ochraceus* (C₂₀H₁₈ClNO₆), zearalenone fungal mycotoxin (C₁₈H₂₂O₅), potassium hexachloroiridate (IV) (K₂IrCl₆), sodium hydrogen citrate sesquihydrate (Na₂C₆H₆O₇·1.5H₂O), sodium hydroxide (NaOH), sodium chloride (NaCl), sulfuric acid (H₂SO₄), ethanolamine (C₂H₇NO), thionine acetate salt (C₁₂H₉N₃S₂C₂H₄O₂), potassium chloride (KCl), Trizma hydrochloride (NH₂C(CH₂OH)₃·HCl), EDTA disodium salt (C₁₀H₁₄N₂Na₂O₈·2H₂O), and CaCl₂ anhydrous were purchased from Sigma-Aldrich (Spain). Potassium hexacyanoferrate (II)-(K₄[Fe(CN)₆]·3H₂O) and potassium hexacyanoferrate (III)-K₃[Fe(CN)₆] were purchased from Panreac (Spain). The stirrer used was a TS-100 Thermo shaker (BioSan, Latvia). A Veriti 96-well Thermal Cycler (Applied Biosystems, U.S.A.) was used in PCR experiments. The electrochemical transducers used were homemade screen-printed carbon electrodes (SPCEs), and the impedance measurements were performed in an Autolab 302 potentiostat/galvanostat/frequency-response analyzer PGST30, controlled by GPES/FRA Version 4.9 (Eco-chemie, The Netherlands).

Solutions. The phosphate-buffered saline solution (PBS) consisted of 0.1 M phosphate buffer, 1.37 M NaCl, and 0.03 M KCl (pH 6.5). Tris-EDTA (TE) buffer pH 8.0 was used for dissolving the aptamer and consisted in 0.1 M Trizma and 0.001 M EDTA. Binding buffer at pH 7.0–7.2 was used for OTA recognition and consisted of 0.01 M Trizma, 0.12 M NaCl, 0.005 M KCl, and 0.02 M CaCl₂. Milli-Q water, produced using a Milli-Q system (>18.2 MΩ/cm) from Millipore, was used for the preparation of all solutions. White wine was purchased from García Carrion's cellar (Spain).

Screen-Printed Carbon Electrodes (SPCEs) Fabrication. The electrochemical transducers used were homemade screen-printed carbon electrodes (SPCEs), consisting of three electrodes: working electrode (WE), reference electrode (RE),

and counter electrode (CE) in a single strip fabricated with a semiautomatic screen-printing machine DEK248 (DEK International, Switzerland). The reagents used for this process were the following: Autostat HTS polyester sheet (Mc Dermid Autotype, U.K.) and Electrodag 423SS carbon ink, Electrodag 6037SS silver/silver chloride ink, and Minico 7000 Blue insulating ink (Acheson Industries, The Netherlands). The full size of the sensor strip was 29 mm × 6.7 mm, and the WE diameter was 3 mm. The fabrication of the SPCEs was carried out in three steps. First, a graphite layer was printed onto the polyester sheet, using the screen-printing machine with the stencil (where it is the electron pattern). After curing for 15 min at 95 °C, an Ag/AgCl layer was printed and cured for 15 min at 95 °C. Finally, the insulating ink was printed and cured at 95 °C for 20 min.

Synthesis of Iridium Oxide Nanoparticles (IrO₂ NPs).

Iridium oxide nanoparticles were synthesized following a reported procedure.³⁴ Briefly, 30 mg of K₂IrCl₆ was added to 50 mL of solution of sodium hydrogen citrate 3.8 M. The resulting solution was adjusted to pH 7.5 using NaOH solution 0.25 M and then refluxed with constant stirring for 30 min. After this, it was cooled at room temperature and followed for the pH adjustment, stirring, and refluxing, which were repeated until obtaining a constant value of pH 7.5. To obtain the suspension of IrO₂ NPs, the solution was additionally refluxed for 2 h with oxygen bubbling through it. The IrO₂ NPs dispersion was stored at 4 °C.

The nanoparticles used in the following experiments showed a homogeneous size distribution of (12.5 ± 2.5 nm), which were composed by smaller nanoparticles of (1.5 ± 0.3 nm). Detailed characterization including UV-vis and X-ray photoelectron spectroscopy (XPS) were conducted as stated in our previous work.³⁵

Aptasensor Development. First, SPCEs were activated after dropping 50 μL of H₂SO₄ 0.1 M and applying a fixed current of 3 μA for 2 min. Then, they were washed with Milli-Q-water and PBS 0.1 M, pH 6.5.

For thionine film electrodeposition onto the working electrode (WE) of SPCE, 50 μL of thionine salt 0.5 mM in PBS 0.1M, pH 6.5, were dropped and potential cycling with a triangular wave (20 cycles between 0.1 and -0.55 V versus the Ag/AgCl reference electrode at a 50 mV/s scan rate) was used. After thionine film electrodeposition, the electrodes were washed with milli-Q water and were allowed to dry completely. Then, 8 μL of IrO₂ NPs dispersion was deposited on the WE surface and allowed to dry (around 30–45 min). For removing the excess of nanoparticles over the surface, the SPCEs were washed with water and dried at room temperature. After this, 8 μL of 3'-amino aptamer 5 μM in binding buffer was deposited onto the modified WE and then incubated overnight at 4 °C.

Before immobilization, aptamers were denatured by heating at 95 °C for 5 min and then ice-cooled for 5 min. After incubation, the SPCE was washed with water, and 8 μL of aqueous solution of ethanolamine 10 mM used as blocking agent was deposited onto the working electrode surface and left for 90 min at room temperature. The limitation related to the relative high incubation time is overcome by the disposability, single-use, and low-cost characteristics of the SPCEs, which allow us to do a set of a high number of experiments in parallel. Unbounded EA was then removed by washing twice with binding buffer. Immediately, OTA at different concentrations in binding buffer (8 μL) or in white wine samples (for the spike and recovery experiments) were deposited onto the WE and

incubated for 90 min. The washed electrodes with milli-Q water were ready for immediate impedimetric measurements. The same experimental procedure was performed for ZEA analysis (specificity studies).

Impedimetric Measurements. Impedimetric measurements were performed using an Autolab 302 potentiostat/galvanostat/frequency-response analyzer PGST30, controlled by GPES/FRA Version 4.9 (Eco-chemie, The Netherlands). The measurements were done in a frequency range of 100 kHz–0.1 Hz, using a sinusoidal AC potential perturbation of 0.01 V (rms) superimposed onto the formal potential of the redox couple, $[\text{Fe}(\text{CN})_6]^{-3/-4}$ (0.24 V vs Ag/AgCl) was also applied. All measurements were performed in an aqueous solution of 1 mM $[\text{Fe}(\text{CN})_6]^{-3/-4}$ with 0.1 M KCl.

RESULTS AND DISCUSSION

Impedimetric Studies of the Modified SPCE Surface.

The aptasensor for OTA detection is prepared modifying the WE surface of SPCEs by electropolymerization of thionine (Figure S1) and adsorption of IrO_2 NPs. After this, immobilization of aptamer selective to OTA is conducted through electrostatic interactions produced by the attraction between the negatively charged citrate groups surrounding IrO_2 NPs and the positively charged amino groups of the amino-modified aptamer at neutral pH. It is important to point out that probably not only electrostatic but also hydrophobic forces are involved in the aptamer– IrO_2 NP interaction, contributing to the robustness of the prepared biosensor. As an example, in a previous work, antibodies were easily connected to citrate-capped IrO_2 NPs by simple adsorption, giving rise to very stable conjugates.³⁵ Next, blocking steps are carried out so as to avoid unspecific adsorptions before the OTA impedimetric detection (Figure 1).

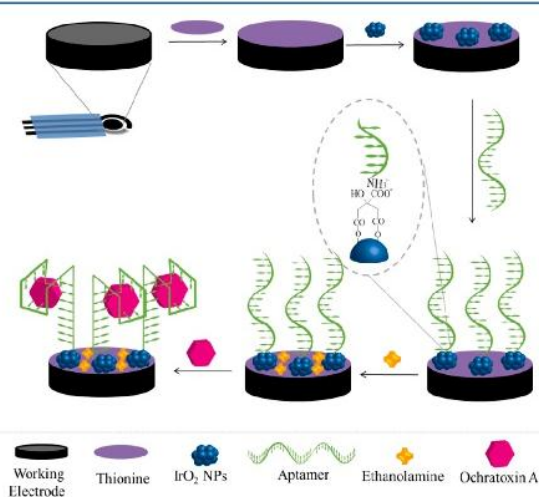


Figure 1. Schematic illustration of the fabrication steps and working principle of the developed impedimetric aptasensor for ochratoxin-A (OTA) detection. Experimental conditions as described in the text.

The electrochemical characterization of the sensor surface at each fabrication step is conducted through EIS using $[\text{Fe}(\text{CN})_6]^{-3/-4}$ as redox probe. Impedance spectra (Nyquist plots) for each surface functionalization step are shown in Figure 2. The interface is modeled using the Randle model modified with Warburg impedance (Z_w) (see model in Figure

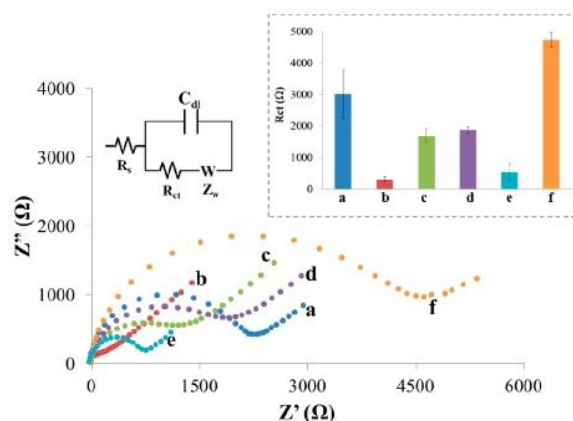


Figure 2. Nyquist plots for the aptasensor obtained after each fabrication step recorded in 1.0 mM $[\text{Fe}(\text{CN})_6]^{-3/-4}$ in 0.1 M KCl solution by applying bias potential of 0.24 V vs pseudo Ag/AgCl reference electrode and an AC amplitude of 10 mV in a frequency range of 100 kHz to 0.1 Hz: (a) Bare SPCE; (b) SPCE/PTH; (c) SPCE/PTH after its modification with IrO_2 NPs; (d) the aptamer immobilization onto SPCE/PTH/ IrO_2 NPs; (e) SPCE/PTH/ IrO_2 NPs/aptamer/EA; and (f) OTA (100 nM) interaction with the aptamer. Inset: R_{ct} values corresponding to each fabrication step. Other experimental conditions as described in the text.

2). The Nyquist plots show a semicircle in which diameter corresponds to the charge-transfer resistance (R_{ct}) and straight line corresponds to the Warburg-impedance (Z_w). Different R_{ct} values are obtained for each fabrication step (see inset in Figure 2). It can be seen that the R_{ct} value of the bare SPCE (a curve) remarkably decreases around 1 order of magnitude when conductive polythionine (PTH) films are deposited (b curve). Thionine is a redox dye able to reduce the impedance of the SPCE, but it also has capacitive behavior, as shown in Figure 2, where the Nyquist plot is almost a straight line. After IrO_2 NPs adsorption onto the SPCE/PTH, the charge transfer is more efficient, and it is well-adjusted to the equivalent circuit, probably due to an enhancement in the electrode effective area.

On the other hand, IrO_2 NPs are known as a redox active material,³⁶ which probably contributes to the increase of the charge transfer. Nevertheless, the negative charge from the citrate groups surrounding the IrO_2 NPs acts as an electrostatic barrier between SPCE/PTH and the redox probe. Moreover, their biocompatibility and their ability to increase the number of biomolecules attached to the citrate groups (surrounding the IrO_2 NPs) make these a useful nanoparticle-based electrode surface modifier.

Once the amino-modified aptamer selective to OTA is connected to the IrO_2 NPs adsorbed onto the electrode (d curve), the R_{ct} increases due to the additional negative charge from the phosphate backbone of aptamers.¹⁸ Ethanolamine was chosen as blocking agent, and its effect increases the electron transference, as explained in Supporting Information (see Figures S2 and 2, e curve). In addition, in the presence of 100 nM OTA the R_{ct} significantly increases (f curve). This phenomena could be explained by the ionization of the phenolic and carboxylic moieties in the OTA molecule at neutral pH,³⁷ which increases the negative charge onto the electrode surface. The high stability of the electrostatic interaction between citrate-capped IrO_2 NPs and aminated aptamer is confirmed by the presence of the aptamer onto the IrO_2 NPs surface after multiple washing steps, which in turn is

experimentally evidenced through the R_{ct} value obtained after its subsequent interaction with OTA.

Prior to OTA detection, different concentrations of aptamers were evaluated (data not shown), finding the optimum response for an aptamer concentration of 5 μM . The optimization for blocking agents was also performed (see Figure S2) so as to improve the sensitivity of the assay.

The other parameter considered for improving the OTA detection is the effect produced by the presence of divalent cations in the binding buffer, especially with calcium ions (Ca^{2+}) which greatly enhance the binding between the OTA and the aptamer.³³ Possibly, OTA forms a complex with Mg^{2+} or Ca^{2+} with the aid of the carboxyl and hydroxyl groups both present on the toxin, and this complex may enhance the binding to the aptamer.³³ This hypothesis is supported by previously reported works describing the influence of the concentration of $[\text{Ca}^{2+}]$ in the binding buffer, which is optimum at 20 mM.¹⁸

In addition, the role of the IrO_2 NPs in the impedance response percentage of this aptasensor is evaluated (see Figure S3) following eq 1:

$$\% \text{ Relative Response} = \frac{(R_{ct\text{aptamer}} - R_{ct\text{toxin}})}{R_{ct\text{aptamer}}} \times 100 \quad (1)$$

where, " R_{ct} aptamer" corresponds to the average of the charge transfer resistance measured in three different systems of SPCE/PTH/ IrO_2 NPs modified with aptamer and blocked with ethanolamine. Moreover, the " R_{ct} toxin" corresponds to charge transfer resistance measured after OTA interaction with the SPCE/PTH and SPCE/PTH/ IrO_2 NPs modified with aptamer and blocked with ethanolamine. In the presence of IrO_2 NPs the aptasensor response is higher due to the fact that the protonated amine group located at 3'-tail of the aptamer is linked through electrostatic interactions with negative charged citrate groups surrounding the IrO_2 NPs surface (see inset in Figure 1). SEM images of bare SPCE and SPCE/PTH/ IrO_2 NPs/OTA-aptamer are shown in Figure S3B and S3C, respectively. The presence of IrO_2 NPs adsorbed onto the electrode surface as bright dots (Figure S3C inset) using backscatter electrons mode is observed, due to an enhancement of the contrast between heavy and light elements present onto the electrode surface.

Impedimetric Detection of OTA. Once the aptasensor is optimized, different OTA concentrations are incubated for 90 min. Experimental results show that net R_{ct} increases as the OTA concentration increases in a logarithmic way in a wide range between 0.01 to 100 nM (Figure 3) (graph in decimal scale is shown in Figure S4), due to the extra negative charge that is provided by OTA at neutral pH, as stated before. This behavior is in agreement with other reports.^{18,20,37,38}

The linear regression equation was adjusted to $R_{ct} (\Omega) = 470.46 \ln[\text{OTA}] (\text{nM}) + 2150$ ($r = 0.98$) with an estimated LoD of 14 pM (5.65 ng/kg), calculated as the concentration of toxin corresponding to the 3 times " s/m " ratio, where " s " is the standard deviation of the blank impedance signal (three replicates) and " m " is the slope of the related calibration curve.³⁹

The relative standard deviation (RSD) is around 17%. This value represents the mean RSD obtained from five different OTA concentrations, where three different modified SPCE are used as replicates for each concentration (Figure 3). The obtained values of r and RSD including the wide range of

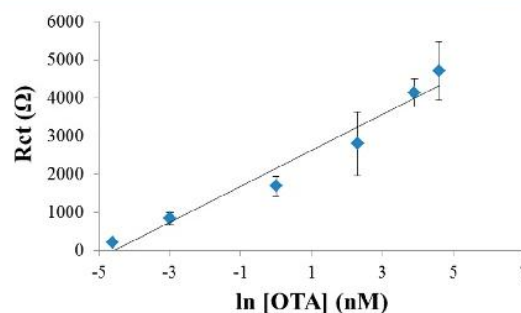


Figure 3. Calibration curve obtained by plotting the R_{ct} values vs \ln of OTA concentration in the range of 0.01 to 100 nM. Experimental conditions as described in the text.

response demonstrate the good performance of this proof-of-concept approach. Further improvements are previewed so as to get better repeatability between the different electrodes.

This aptasensor for OTA detection presents high analytical performance in terms of linear range, sensitivity, and LoD. Although more sensitive electrochemical approaches based on rolling chain amplification (RCA) procedures followed by methylene blue (MB) intercalation and differential pulse voltammetric detection have been recently reported,⁴⁰ our approach presents clear advantages. We reach a very low limit of detection without the need of neither amplification, nor MB intercalation, taking advantage of a novel nanostructured impedimetric platform. As result, our approach is simpler and cheaper, allowing us to achieve the widest range of response and one of the lowest LoD reported so far for label-free impedimetric detection of OTA (Table 1).

Table 1. Comparison of Lineal Range and Limit of Detection of Different Label-Free Impedimetric Aptasensors for OTA

transducer	linear range (nM)	LoD (nM)	ref
Langmuir–Blodgett films of polyaniline (PANI)–stearic acid (SA) prepared on ITO-coated glass plate	0.25–24.8	0.25	19
gold electrode surface	0.1–100	0.12–0.40	18
electrografted binary films via click chemistry onto SPCE	0.003–1.24	0.006	20
Au electrode modified with AuNPs stabilized on hyper-branched polymer film	0.1–100	0.02	38
Au electrode modified with Ag nanoparticles decorated with macrocyclic ligand	0.3–30	0.05	41
SPCE modified with thionine and IrO_2 NPs	0.01–100	0.014	this work

Specificity of OTA Aptasensor. The specificity of the developed aptasensor is evaluated by incubating the aptasensor with *zearalenone* (ZEA) of different concentrations during 90 min. ZEA was selected because it is reported to simultaneously coexist with OTA in plants and foods,⁴² representing a potential interference in the detection of OTA. As shown in Figure 4, impedance responses corresponding to 0.01, 1, 2, and 50 nM of both toxins are evaluated, finding that high specificity of the selected aptamer for OTA allows to discriminate between both mycotoxins in the entire range of concentrations assayed. No significant signals are observed for ZEA concentrations in the lower range of the immunosensor

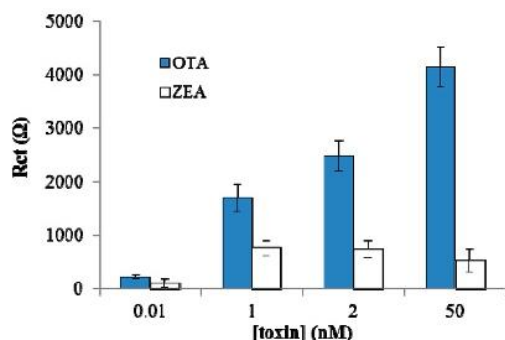


Figure 4. R_{ct} values for the selectivity of the impedimetric OTA aptasensor against ZEA for different toxin concentrations. Experimental conditions as described in the text.

response (0.01 nM). The almost constant value of signal background of around 500 Ohm obtained for ZEA concentrations higher than 1 nM is probably related to a combination of both low unspecific recognition by the aptamer and adsorption onto the electrode surface. It is important to highlight that starting from 2 nM of toxin, the value of ZEA signal represents less than 20% of that of the OTA (less than 12% for 50 nM). This is of special relevance because the European Community suggests that the maximum OTA concentration in wine, which is the sample selected for real analysis in our approach, should be 2 nM (European Commission no. 1881/2006). Considering this, we can ensure that the proposed method is able to detect OTA in the presence of ZEA in a real scenario.

Recovery Performance in Wine Samples. The performance of the aptasensor in a real complex matrix such as white wine is also evaluated. This kind of sample is selected due to the presence of very low levels of OTA in white wine caused by the wine processing methodology.⁴³ As stated before, the maximum OTA levels in wine established by the European Community should not be more than 2 nM, which perfectly fits with the performance of this optimized biosensor (LoD: 14 pM). Wine analysis without any pretreatment (i.e., without adjusting the pH to 7) and its comparison with the performance of the system for the standard solutions at the optimum pH is very representative for evaluating the real effect of the wine sample matrix in this biosensing approach.

Recovery experiments are performed for this evaluation, according to Guidance for Industry Bioanalytical Method Validation of FDA.⁴⁴ Wine samples spiked with OTA at levels between 0.01 and 50 nM are evaluated. The obtained analytical signals and their comparison with those obtained in binding buffer are included in Table 2. As shown in the table, recoveries of around 125% for all the assayed concentrations are obtained. It must be pointed out that the recoveries are above 100%, which is probably due to the fact that unspecific adsorptions of

Table 2. Recovery Assay Data^a

spiked OTA (nM)	R_{ct} in buffer (Ω)	R_{ct} in wine (Ω)	recovery (%)
0.01	221 ± 37	295 ± 47	133
1	1160 ± 174	1370 ± 219	118
50	4140 ± 662	5200 ± 780	125

^aThe study is done by spiking 0.01, 1, and 50 nM of OTA in a white wine sample ($n = 3$ for each sample) and the percentage of recovery is obtained as comparing with binding buffer.

components of the wine matrix on the electrode surface are increasing its impedance.

The deviation of wine signals of around 25% with respect to those obtained in buffer is probably related to such interferences of the wine matrix, including its acidity. These findings are in agreement with very recent works reporting aptamer-based OTA detection in which a similar deviation was obtained for wine analysis without any pretreatment in comparison with buffer media.⁴⁵

These results demonstrate that our technology can be considered as a promising alternative for the determination of OTA in a real scenario.

CONCLUSIONS

A novel nanostructured platform based on IrO₂ NPs is presented as an alternative to improve the performance of carbon-based electrodes used in impedimetric biosensors. The developed impedimetric aptasensor is based on SPCE modified with conductive films of polythionine and citrate-capped IrO₂ NPs. Electrochemical impedance spectroscopy studies were conducted in order to characterize each fabrication step of the aptasensor and also for OTA detection. In addition, these studies reveal that SPCE/PTH/IrO₂ NPs/aptamer sensor shows a wide linear range of 0.01 to 100 nM for OTA detection with a high reproducibility. The developed aptasensor shows the widest range of response and one of the lowest limit of detection (14 pM; 5.65 ng/kg) found in the literature for label-free impedimetric detection of OTA, which makes it useful for future applications in OTA analysis. The system is highly specific against a toxin (ZEA) that could interfere in the detection of OTA in white wine samples. Furthermore, relatively low matrix effects are found when analyzing a white wine sample, demonstrating the ability of the sensing system to perform analysis in real scenarios.

The nanostructured electrode presented in this work represents a novel and universal platform that may be of interest for various diagnostic applications that require very low limits of detection in addition to a highly robust and cost/efficient system, especially for those to be used directly in field.

ASSOCIATED CONTENT

Supporting Information

Additional information as noted in text. The Supporting Information is available free of charge on the ACS Publications website at DOI: 10.1021/acs.analchem.5b00890.

AUTHOR INFORMATION

Corresponding Author

*E-mail: arben.merkoci@icn.cat. Tel: (+34)937374604.

Author Contributions

[†]These authors contributed equally to this work (L.R. and C.C.M.-M.).

Notes

The authors declare no competing financial interest.

ACKNOWLEDGMENTS

The authors acknowledge support of the Spanish MINECO under Project MAT2011–25870 and through the Severo Ochoa Centers of Excellence Program under Grant SEV-2013-0295. L.R. also acknowledges Universitat Autònoma de Barcelona for her predoctoral grant.

REFERENCES

- (1) Food and Agricultural Organization (FAO). *Manual on the application of the HACCP system in mycotoxin prevention and control*; FAO: Rome, 2001; p 124.
- (2) Meulenbergh, E. P. *Toxins* **2012**, *4*, 244–266.
- (3) Anfossi, L.; D'Arco, G.; Baggiani, C.; Giovannoli, C.; Giraudi, G. *Food Control* **2011**, *22*, 1965–1970.
- (4) Covarelli, L.; Beccari, G.; Marini, A.; Tosi, L. *Food Control* **2012**, *26*, 347–356.
- (5) Benford, D.; Boyle, C.; Dekant, W.; Fuchs, R.; Gaylor, D. W.; Hard, G.; McGregor, D. B.; Pitt, J.; Plestina, R.; Shepard, G.; Solfrizzo, M.; Verger, P. J. P.; Walker, R. *Joint FAO/WHO Expert Committee on Food Additives: Ochratoxin A*; World Health Organization (WHO): Geneva, Switzerland, 2001; Vol. 47.
- (6) Denli, M.; Pérez, J. F. *Toxins* **2010**, *2*, 1065–1077.
- (7) International Agency for Research on Cancer (IARC). *Monographs on the evaluation of carcinogenic risks to humans. Some naturally occurring substances: Food items and constituents, heterocyclic aromatic amines and mycotoxins*; IARC: Lyon, France, 1993; Vol. 56, p 609.
- (8) Joint FAO/WHO Expert Committee on Food Additives. *Evaluation of certain mycotoxins in food*; World Health Organization (WHO): Geneva, Switzerland, 2002; p 74.
- (9) European Union (EU). *Commission Regulation (EC) No 1881/2006 of 19 December 2006 setting maximum levels for certain contaminants in foodstuffs*; EU: The Netherlands, 2010; pp 1–26.
- (10) Gilbert, J.; Anklam, E. *TrAC-Trend Anal. Chem.* **2002**, *21*, 468–486.
- (11) Krska, R.; Welzig, E.; Berthiller, F.; Molinelli, A.; Mizaikoff, B. *Food Addit. Contam.* **2005**, *22*, 345–353.
- (12) Shephard, G. S. *Chem. Soc. Rev.* **2008**, *37*, 2468–2477.
- (13) *Aptamers in Bioanalysis*; Mascini, M., Ed.; Wiley-Interscience: Hoboken, NJ, 2009; p 325.
- (14) Skládal, P. *Electroanalysis* **1997**, *9*, 737–745.
- (15) Cunningham, B. T. In *Label-free Biosensors: Techniques and Applications*; Cooper, M. A., Ed.; Cambridge University Press: NY, 2009; p 300.
- (16) Katz, E.; Willner, I. *Electroanalysis* **2003**, *15*, 913–947.
- (17) Willner, I.; Zayats, M. *Angew. Chem., Int. Ed.* **2007**, *46*, 6408–6418.
- (18) Castillo, G.; Lamberti, I.; Mosiello, L.; Hianik, T. *Electroanalysis* **2012**, *24*, 512–520.
- (19) Prabhakar, N.; Matharu, Z.; Malhotra, B. D. *Biosens. Bioelectron.* **2011**, *26*, 4006–4011.
- (20) Hayat, A.; Sassolas, A.; Marty, J.-L.; Radi, A.-E. *Talanta* **2013**, *103*, 14–19.
- (21) Hayat, A.; Haider, W.; Rolland, M.; Marty, J.-L. *Analyst* **2013**, *138*, 2951–2957.
- (22) Cosnier, S. *Anal. Bioanal. Chem.* **2003**, *377*, 507–520.
- (23) Gao, Q.; Cui, X.; Yang, F.; Ma, Y.; Yang, X. *Biosens. Bioelectron.* **2003**, *19*, 277–282.
- (24) Dempsey, E.; Diamond, D.; Collier, A. *Biosens. Bioelectron.* **2004**, *20*, 367–377.
- (25) Yang, T.; Hu, Y.; Li, W.; Jiao, K. *Colloid. Surface. B* **2011**, *83*, 179–182.
- (26) Jiang, S.; Hua, E.; Liang, M.; Liu, B.; Xie, G. *Colloid. Surface. B* **2013**, *101*, 481–486.
- (27) *Biosensing Using Nanomaterials*; Merkoçi, A., Ed.; John Wiley & Sons: Hoboken, NJ, 2009; p 499.
- (28) Liu, G.; Mao, X.; Gurung, A.; Baloda, M.; Lin, Y.; He, Y. In *Trace Analysis with Nanomaterials*; Pierce, D. T., Zhao, J. X., Eds.; Wiley-VCH: New York, 2010; p 418.
- (29) Huang, W.-D.; Cao, H.; Deb, S.; Chiao, M.; Chiao, J. C. *Sens. Actuators, A* **2011**, *169*, 1–11.
- (30) Lu, Y.; Wang, T.; Cai, Z.; Cao, Y.; Yang, H.; Duan, Y. Y. *Sens. Actuators, B* **2009**, *137*, 334–339.
- (31) Göbbels, K.; Kuenzel, T.; van Ooyen, A.; Baumgartner, W.; Schnakenberg, U.; Bräunig, P. *Biomaterials* **2010**, *31*, 1055–1067.
- (32) Mayorga Martinez, C.; Pino, F.; Kurbanoglu, S.; Rivas, L.; Ozkan, S.; Merkoçi, A. *J. Mater. Chem. B* **2014**, *2*, 2233–2239.
- (33) Cruz-Aguado, J. A.; Penner, G. J. *Agrig. Food Chem.* **2008**, *56*, 10456–10461.
- (34) Harriman, A.; Thomas, J. M. *New J. Chem.* **1987**, *11*, 757–762.
- (35) Rivas, L.; de la Escosura-Muñiz, A.; Pons, J.; Merkoçi, A. *Electroanalysis* **2014**, *26*, 1287–1294.
- (36) Nakagawa, T.; Bjorge, N. S.; Murray, R. W. *J. Am. Chem. Soc.* **2009**, *131*, 15578–15579.
- (37) Radi, A.-E.; Muñoz-Berbel, X.; Lates, V.; Marty, J.-L. *Biosens. Bioelectron.* **2009**, *24*, 1888–1892.
- (38) Evtugyn, G.; Porfireva, A.; Stepanova, V.; Kutyreva, M.; Gataulina, A.; Ulakhovich, N.; Evtugyn, V.; Hianik, T. *Sensors* **2013**, *13*, 16129–16145.
- (39) *Development and validation of analytical methods*; Riley, C. M., Rosanske, T. M., Eds.; Elsevier Science: New York, 1996.
- (40) Huang, L.; Wu, J.; Zheng, L.; Qian, H.; Xue, F.; Wu, Y.; Pan, D.; Adeloju, S. B.; Chen, W. *Anal. Chem.* **2013**, *85*, 10842–10849.
- (41) Evtugyn, G.; Porfireva, A.; Sitdikov, R.; Evtugyn, V.; Stoikov, I.; Antipin, I.; Hianik, T. *Electroanalysis* **2013**, *25*, 1847–1854.
- (42) Li, Y.; Zhang, B.; He, X.; Cheng, W.-H.; Xu, W.; Luo, Y.; Liang, R.; Luo, H.; Huang, K. *Toxins* **2014**, *6*, 1177–1192.
- (43) Otteneder, H.; Majerus, P. *Food Addit. Contam.* **2000**, *17*, 793–798.
- (44) *Guidance for Industry. Bioanalytical Method Validation*; U.S. Department of Health and Human Services, Food and Drug Administration (FDA), Center for Drug Evaluation and Research (CDER), Center for Veterinary Medicine (CVM): Rockville, MD, 2001.
- (45) Prieto-Simón, B.; Samitier, J. *Anal. Chem.* **2014**, *86*, 1437–1444.

